Investigation of Mining Subsidence Prediction Under Tectonic Influences

Von der Fakultät für Geowissenschaften, Geotechnik und Bergbau

der Technischen Universität Bergakademie Freiberg

genehmigte

DISSERTATION

zur Erlangung des akademischen Grades

Doktor - Ingenieur
(Dr.- Ing.)

vorgelegt von   M.Sc. Aleksandra Babaryka

geboren am   19. November 1994 in Russland

Gutachter: Prof. Dr. Jörg Benndorf,
Technische Universität Bergakademie Freiberg
Deutschland

Dr.-Ing. habil. Jan Blachowski
Wrocław University of Science and Technology
Poland

Tag der Verleihung: 12. Dezember 2023

Inhalt

List of tables and figures

1   Introduction

Subsidence refers to the gradual sinking or settling of the ground surface. Anthropogenic-induced subsidence poses significant risks to various types of infrastructure, including buildings, gas and water pipelines, and transportation systems. Excessive groundwater extraction in China, for instance, has resulted in subsidence-related incidents, such as building and bridge collapses and disruption to transportation networks (Tzampoglou et al., 2023). Similarly, in Katowice, Poland, a subsidence rate of 450 mm per year, between 1997 and 2011, caused substantial damage to buildings, roads, and pipelines (Kowalski, 2020), while Gliwice experienced a subsidence rate of 340 mm per year, leading to infrastructure deterioration, flooding, and groundwater issues in some areas (Przyłucka et al., 2022). The magnitude of the subsidence can reach over 30 m and exceed the predicted magnitude on 30% in Walbrzych (Poland) (Blachowski, 2016). The assessment of subsidence effects is crucial, as demonstrated in the Starobin potash deposit in Belarus, where InSAR-based subsidence monitoring by Konovalov (2019) revealed a subsidence rate of 73 mm per year in the central region of the deposit. Caro Cuenca and Hanssen (2008) utilised persistent scatterer interferometry to investigate the subsidence (3 m) and uplift (0.1 m) caused by coal mining near Wassenberg (Germany), in the area influenced by the 'Meinweg' fault. In another example of coal mining in Germany, maximum ground subsidence reached 4.2 m (Hegemann, 2020). These examples highlight the destructive consequences of subsidence. Accurate prediction of subsidence patterns is essential for mitigating potential risks and damages and for ensuring the safety, stability, and effective management of structures in subsidence-prone regions.

The development of subsidence prediction methods leads to better protection of civilians and state property. Accurate subsidence prediction enables the categorisation of surface objects based on their risk levels and allows further analysis and effective risk mitigation management (Grün, 1995). For instance, a report by DMT (2016) indicated that 4560 objects with varying risk levels are currently under observation, including 90 objects in category I and 1407 in category II, until the year 2317, to mitigate the potential risks and damages caused by subsidence.

Improvements in monitoring techniques and the abundance of data facilitate the identification of deviations between projected subsidence patterns and observed measurements (Benndorf, 2021; Przyłucka et al., 2022). Current geo-monitoring technologies, such as Interferometric Synthetic Aperture Radar (InSAR) and Light Detection and Ranging

(LiDAR), provide high-resolution measurements of surface deformation, allowing for real-time monitoring of subsidence (Caro Cuenca and Hanssen, 2008). By combining the available information with Global Navigation Satellite System (GNSS) data, these methods enable precise monitoring of ground deformation, facilitating the detection of deviations from expected subsidence, in terms of form, magnitude, and timing. Comparing prediction models with measured data not only enables the recognition of discrepancies but also presents opportunities for refining and enhancing the accuracy of subsidence predictions.

The detection of subsidence deviations from the expected values, so-called anomalies, has been observed for a long time and in various forms, such as subsidence asymmetry, uplifts, compression, and tension locations, among others. In particular, uplift and cohesion anomalies, instead of the expected tension areas, have been detected in coal (Awershin, 1947) and polymetallic mining (Sashurin, 1999) in Russia. Other examples are: unexpected tension appearing in Spain (Sanmiquel et al., 2018); an uplift area occurring parallel to the main fault in Germany (Busch, 2014, 2017); changes in subsidence parameters due to stress release activities in China (Xia et al., 2016, 2017); the asymmetrical shape of the subsidence trough not being related to the geometry of mining in Poland (Vušović et.al., 2021). To gain a deeper understanding of subsidence processes, numerical models are often used (Peng, 2020). For example, Suchowerska et. al., (2016) studied the influence of Young's modulus on the subsidence magnitude, numerically; void closure in coal mining in Australia was numerically studied by Keilich et al. (2006); and Villegas et al. (2011) numerically studied the effect of stress relaxation and gravity on hanging wall displacement. Most of the referenced anomalies appear to be related to excessive horizontal stress areas; however, the direct influence of stress condition contribution on ground subsidence anomalies has yet to be investigated. This study is aiming to fill the gap.

Therefore, the objective of this thesis is to discover how stress conditions influence ground subsidence, assuming that the stress conditions are the prime reason for the aforementioned anomalies. The investigation begins with a comprehensive review of the relevant literature, to identify research gaps and the appropriate methodology. This is followed by a numerical experiment using the Finite Element Method, via the FLAC 3D 7.0 software, generating valuable, unbiased data on the subsidence process. The results are then validated against established and newly developed empirical models, incorporating insights from notable researchers. Finally, these findings are applied and tested in a real-world case study involving the ETZEL cavern group's storage caverns, to validate the findings and demonstrate the research's practical relevance.

2 State of the art

Advances in subsidence research are driven by the use of extensive monitoring data and numerical modelling techniques to understand the underlying factors and to predict the magnitude and timing of subsidence phenomena. However, differences between predicted and observed measurements persist, particularly in areas of excessive horizontal stress. This underlines the importance of continued research efforts and improvements in subsidence prediction methods. This chapter provides a comprehensive review of subsidence prediction methods, with a particular focus on empirical approaches, to elucidate their mathematical limitations in the context of the studied anomalies, observed during subsidence monitoring. The chapter emphasises the influence of stress conditions and concludes by identifying research gaps, objectives and targets for further investigations in this field.

2.1 Subsidence prediction methods

This chapter provides a brief description of the subsidence prediction approaches, highlighting their accuracy, reliability and practical applications.

Empirical methods focus on measurement interpretation and apply mathematical functions to observed subsidence data, in order to predict profiles under analogous geological conditions (Whittaker and Reddish, 1989). The accuracy of these methods is based on extensive historical data, and geological and mining similarities. Hazen and Sargand (1988) confirmed that subsidence measurements were consistent with the predictions of empirical methods but emphasised the reduced accuracy of strain values. Zhang et al. (2022) stated that empirical methods are accurate in certain scenarios but are not universally applicable. The methods are economically efficient, optimal for regions with extensive historical data, and can potentially be improved by integrating numerical or physical methods or interpretations, to increase prediction accuracy (Li et al., 2022). Limitations arise from a lack of historical data or unique geological and mining conditions, making them unsuitable for unique or complex geological settings. In conclusion, empirical methods are best applied in areas with abundant historical data and similar geological and mining conditions. The main advantages of the method are its ability to capture a global pattern of subsidence and its simplicity. The historical matching and low data requirements make the method applicable overall.

Numerical methods, including finite element methods (FEM) and discrete element methods (DEM), are used to simulate mine subsidence through complex mathematical equations (Sidki-Rius et al., 2022). Their accuracy depends on the quality of the input data, the selection of the mathematical model and the modelling assumptions (Peng, 2020). Despite their accuracy and modelling flexibility, these methods are resource intensive, requiring extensive computational resources and expertise. They are typically used in complex geological settings or for hypothesis testing. While they are less capable of predicting surface movement than empirical methods, they excel at identifying and analysing movement mechanisms (Marwan, 2008). The chosen numerical method has the ability to accurately capture local deformation and displacement features. However, the scale of real mine subsidence presents significant data requirements for the practical implementation of this method. In this case, the challenge in applying numerical methods was parameter estimation, for real subsidence prediction tasks have more parameters to estimate than available data. On the other hand, simplification of the task can increase the error exponentially. As a result, these numerical methods are often used to study small-scale cases rather than for practical applications.

In contrast to numerical and empirical methods, **Physical analytical methods** use physical properties and laws to estimate subsidence on a large scale. Like numerical modelling, they are limited to local areas. They require less data but cannot capture a local feature in large-scale predictions. Self-analytical physical subsidence solutions are usually restricted to the elastic interpretation of the rock mass and are severely limited in their implementation (Ike, 2019), e.g. Berry's physical analytical solution is limited to depths up to 70 m (Berry, 1963), which is a rare case for underground mining. To solve the task of subsidence prediction, physical methods are used to understand the patterns and logic of the underlying mechanisms. This understanding is often used to develop an empirical model (Litwiniszyn, 1994) or to relate empirical parameters to certain physical properties. For this reason, the methods that use analytical physical methods will not be discussed.

Hybrid methods combine prediction approaches (empirical, physical and numerical) to optimise the accuracy and applicability of subsidence prediction (Liu et al., 2019; Heib et al., 2001; Aksoy et al., 2004). For example, an empirical model could be used to predict subsidence over a large area and a numerical model could be used to predict subsidence in a local area, where a particular pattern is suspected (e.g. geological structure, fault or other problem). Hybrid methods, which exploit the strengths of several techniques, offer improved accuracy, adaptability to different geological conditions and data availability. However, they require significant expertise and resources to implement. They are most effective when single methods do not provide good enough results and the complexity of the problem requires a

combination of methods. For the time being, as most cases deal with specific local issues, hybrid methods need to be developed and applied for each particular case. As the method does not provide a global picture, it will not be discussed in the following chapters.

A **machine learning** approach is also applicable. For example, Zhang et al. (2019) used an artificial neural network (ANN) to synergize the effects of different methods, including empirical, FEM and DEM. Their ANN-based hybrid method outperformed individual methods, reporting prediction errors of less than 5%. However, the method is a 'black box' and does not allow interpretation of the results to further the understanding of the subsidence process or application to other mines, so this approach is not discussed in this thesis.

Each subsidence prediction method has unique strengths and weaknesses that affect its suitability under specific geological and mining conditions. Empirical methods derive results from limited data and capture the global pattern of subsidence (Marwan, 2008), while numerical methods are typically used where abundant data are available, or for case studies (Sidki-Rius et al., 2022; Aurelio, 2000) to investigate the influence of natural factors on subsidence parameters (Suchowerska et. al., 2016). A detailed description of empirical and numerical methods is given below.

2.1.1 Empirical subsidence prediction method overview

The main objective of the empirical method is to predict subsidence in conditions of limited data. The method can analyse subsidence by studying the statistical distribution of subsurface displacement (Litwiniszyn, 1994). The main differences between the empirical methods relate to the form of the distribution, which is defined by the influence function, Equation 1.

$$dS(r) = c \cdot f(r) \cdot dV \tag{1}$$

where c is the correction coefficient that ensures the volume under the influence function equals one; dV is an underground shrinking volume; $f(r)$ is an influence function; and a is a transmission coefficient, representing the part of the underground shrinking volume transmitted into the subsidence volume (Figure 1).
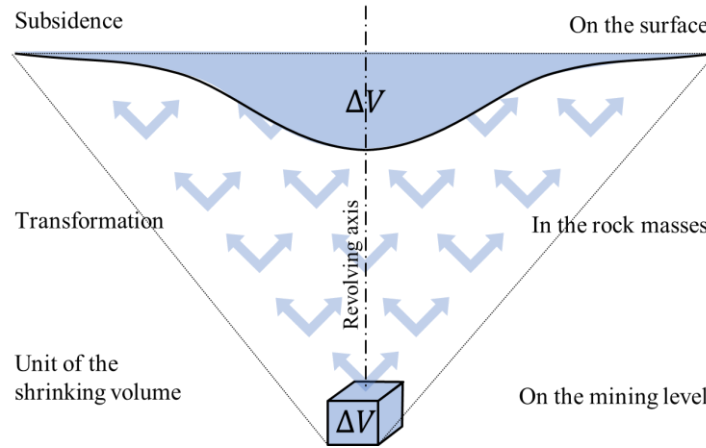
Figure 1. Illustration of the distribution of the underground unit of shrinking volume at the surface.

Litwiniszyn (1994) introduced the description of subsidence of an incompressible medium at a fixed level as a Gaussian distribution. The hypothesis was supported by physical modelling of the displacement of dry sand. Litwiniszyn's results showed that the subsidence of the incompressible medium follows a normal distribution for individual elements. Knothe (1953) obtained the same solution by correlating geometric parameters that can be determined by geodetic measurements. This method has been widely accepted by mining companies (e.g. Kratzch, 2013; Sroka, 2001) and implemented in various computer software applications (Kwinta and Gradka, 2018). There are many other influence functions, some of which are listed in Table 1 and illustrated in Figure 2.

Table 1. Influence functions (adopted and extended from Sroka and Wittkopf, 1992 and Chi et al., 2021).

Author	Subsidence model
Bals	$\dfrac{1}{1+\dfrac{r^2}{H^2}}$
Knothe (1953)	$\exp\left(-\dfrac{\pi r^2}{R^2}\right)$
Kochmański (1955)	$\exp\left(-\left(\dfrac{r}{R}\right)^b\right)$, where $b=\dfrac{5-1.120\log H}{1+0.672\log H}$
Ruhrkohle	$\exp\left(-k\dfrac{r^2}{R^2}\right)$, where $k=-ln(0.1)$
Geertsma (1973)	$\dfrac{1}{(r^2+H^2)^{3/2}}$
Whittaker and Reddish (1989)	$\exp\left(-6.65\left(\dfrac{r}{R}\right)^2\right)$
Ramírez and Rambaud (1986)	$\exp\left(-\pi\left(\dfrac{r}{k_R H}\right)^2\right)+n\cdot\exp\left(-\pi\left(\dfrac{r}{2k_R H}\right)^2\right),$

Author	Subsidence model
	where n and k_R are two parameters that characterise the ground and allow the shape and magnitude of the subsidence trough to be adjusted. k_R defines the 0 position relative to H, which is used as an equivalent of R.
Eikermejer (2005)	$exp\left(-\pi\xi^{\frac{\delta}{2}}\dfrac{r^\delta}{R^\delta}\right)$
Boltzmann function	$\dfrac{\exp(-\frac{r}{R})}{\left(1+\exp\left(-\frac{r}{R}\right)\right)^2}$

*where r – horizontal distance between excavated element and point on the surface;
H – the vertical distance between element and surface; R – influence radius, specified for the processes $R = H \cot \gamma$; b – landshaft characteristic; γ - influence angle; δ - chape parameter; ξ - parameter that controls the maximum subsidence
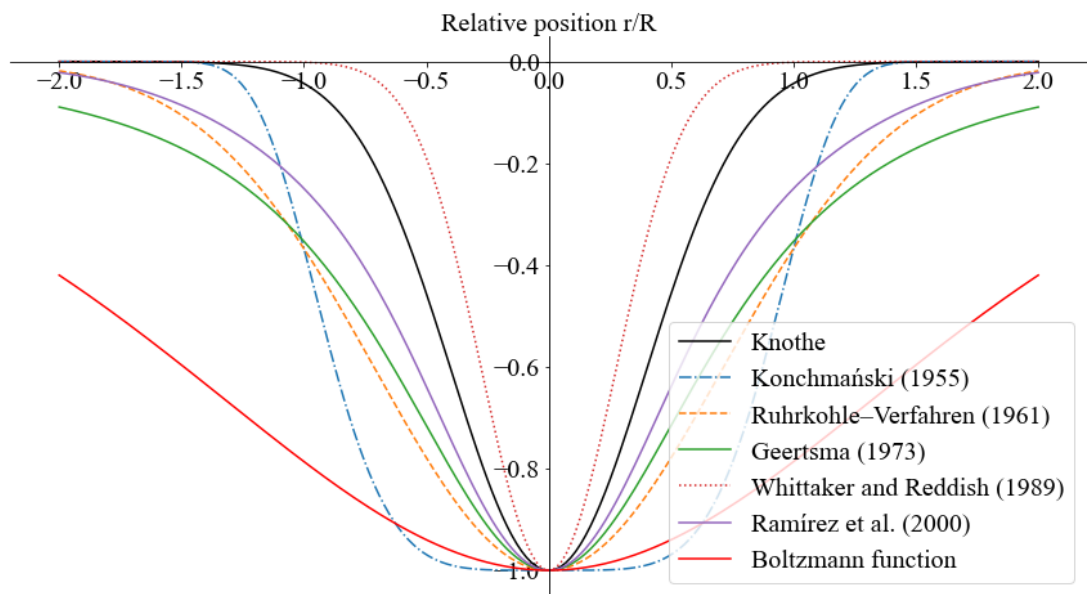
Figure 2. Illustration of different subsidence influence functions. N.B. all models are normalised to their absolute maximum values.

Figure 2 and Table 1 show that the influence functions are symmetric and retain their shape, regardless of the input data, with the exception of the Kochmański and Ramírez functions, which take shape deviation into account. Despite the limitations discussed in the following chapter, these influence functions are widely used in practice and provide relatively good results.

Another key point of the empirical method is the accuracy of the underground volume shrinkage or convergence. The accuracy of the data depends on the mining method. For example, in mechanical mining (e.g. coal mining), direct measurements of convergence can be obtained. In contrast, in the case of drainage-induced subsidence, the underground volume shrinkage can only be estimated indirectly (Guzy et al., 2021). In the field of cavern energy

storage, the high costs associated with direct measurements of volume shrinkage limit the frequency of data acquisition, while the complexity of the volume-shrinking process (Wei et al., 2016) reduces the quality of the physical or numerical solution. According to Equation 1, the accuracy of the volume shrinkage data proportionally affects the quality of the prediction.

In some cases, geology may impose specific requirements on the influence functions, leading to the development of extensions to the classical solution. Thus, Knothe (2005) wrote "the real profile of the trough is usually asymmetric", when he suggested that the asymmetric curve comprised two functions of normal distribution, with a different influence radius in the outer and inner parts of the subsidence trough, concluding that the result of this prediction has more accurate values of displacements and deformations. Other extensions dealing with asymmetry (e.g. Quasnitza (1989)) covered the phenomenon by representing influence angle as a function of planometrical direction (as discussed in Section 4).

In order to improve the quality of the subsidence prediction, parameter estimation is one of the methods of choice. The availability of measured data allows the application of parameter estimation, which has a positive effect on the accuracy of future predictions (Tajduś et al., 2021a ; Eickemeier, 2005). In general, parameter estimation benefits from having more data points (measurements) than parameters to be estimated. This advantage reduces the risk of overfitting which, in turn, leads to more reliable and stable parameter estimates. Thus, a high ratio of data points to parameters often increases the applicability and validity of empirical models, compared to methods that require a large number of parameters. However, there are approaches, such as the Bayesian parameter estimation, that effectively deal with situations where the number of data points is relatively small compared to the number of parameters. This is largely due to the ability of the Bayesian framework to incorporate prior information.

In conclusion, the empirical models capture the global trend of the subsidence process and, with limited data, allow the prediction of subsidence with relatively high quality. The quality of the prediction depends on the parameter values and the mathematical representativeness of the influence function of the subsidence distribution. The simplicity of the approach and the manageable number of parameters facilitates the development of the method and the application of advanced statistical techniques to improve the quality of future predictions, avoiding overfitting.

2.1.2 Numerical methods for subsidence prediction

Mining-induced subsidence, which involves the deformation of overlying rock strata, can be predicted and assessed using numerical modelling methods (Lo et al., 2022; Tajduś et al., 2021a). Recent studies have focused on developing more efficient and accurate numerical models for simulating mining-induced subsidence, utilising methods such as the finite element method (FEM), finite difference method (FDM), boundary element method (BEM), and discrete element method (DEM) (Yin and Yang, 2019; Sidki Rius et al., 2022; Alam et al., 2022).

In FEM, the domain is divided into a finite number of subdomains or elements, interconnected at specific points called nodes. The governing differential equations are approximated over each element by interpolating the solution using shape functions. However, this method requires significant computational effort and may yield inaccurate results with large mesh sizes (Alam et al., 2022). On the other hand, FDM discretises the domain by dividing it into a grid of equally spaced points. The governing differential equations are approximated by finite difference equations, relating the values of the solution at discrete grid points. While FDM offers easier implementation and lower computational requirements, it sacrifices accuracy and flexibility in modelling complex scenarios (Zienkiewicz et al., 2013). BEM, which only solves deformation equations on the boundary, is suitable for simple geometries and homogeneous materials but may lack accuracy for complex scenarios (Gaul et al., 2003; Bahuguna et. al., 1992). DEM models individual particle deformations and interactions and is effective for granular materials but requires substantial computational resources for large-scale applications (Yin and Yang, 2019). Different combinations of coupled numerical methods can also be applied. In the field of subsidence engineering, coupling DEM and FEM has been employed to simulate subsidence processes and provide greater accuracy (Vyazmensky et al., 2007).

Numerical methods are sensitive to boundary conditions, constitutive models, grid spacing, and input data, requiring a high level of expertise to obtain accurate results. Another challenge to consider is the requirement for substantial computational resources. The challenges make it impractical for full-scale subsidence predictions in many cases. Furthermore, parameter estimation presents difficulties in subsidence prediction using numerical methods, due to the requirement to estimate parameters for every element. In a full subsidence case, the number of parameters exceeds the available measurements, which leads to a mathematically ill-posed problem.

The use of numerical cases is driven by the need to solve complex problems where a controlled environment is required. Thus, the implementation of numerical methods for subsidence is mainly limited to research cases. For example, numerical studies have been carried out to analyse subsidence behaviour in European mining regions, e.g. in a coal mining study. Numerical simulations were used to investigate subsidence patterns, including the relationship between maximum subsidence and factors such as depth, tensile and compressive strain (Holla and Barclay, 2000), as well as the relationship between maximum subsidence and slope, as a function of the width-to-depth ratio of the face (Keilich et al., 2006). In a study of the hard rock mining region in Kiruna (Sweden), numerical simulations investigated the effect of rock properties on subsidence behaviour, highlighting the role of variations in rock strength and stiffness in generating asymmetric subsidence patterns (Villegas et al., 2011). Similarly, a study in the Ruhr coal mining region of Germany investigated the influence of mining-induced stress changes on subsidence behaviour, emphasising the importance of the direction of maximum horizontal stress, particularly in regions with complex geological structures (Villegas, 2008). The influence of mine and mine flooding parameters on uplift was investigated by Zhao et al. (2021). Through numerical simulations, Suchowerska et. al., (2016) demonstrated the dependence of the magnitude of subsidence on variations in the synthetic Young's modulus. Thus, applying numerical methods provides valuable tools to investigate the mechanisms of the subsidence process.

In general, numerical methods provide valuable tools for understanding mining-induced subsidence. However, considering the aforementioned cases and limitations, the use of numerical methods in subsidence prediction is primarily limited to research cases, where a closed and controlled environment is required, for example, to understand the pattern of the process or the underlying causes. The choice of numerical method depends on the specific problem, the geometry and size of the mine, and the desired accuracy and computational efficiency. In any case, the application of numerical methods requires a high level of expertise, careful consideration, and a thorough understanding of the specific problem.

2.2   Subsidence monitoring methods

The prediction and understanding of subsidence is based on observations. Over time, a variety of observational techniques have been developed for this purpose. This chapter examines subsidence monitoring techniques, with particular emphasis on their development and application.

2.2.1 Observation methods

Subsidence monitoring methods typically fall into two distinct categories: in-situ measurements and remote measurements, although different methods provide different information about ground movement; some of them are only able to measure vertical differences, while others are only planimetric.

In-situ measurements

This group involves the use of measuring instruments directly at the site of interest. The advantages are high temporal resolution, continuous measurement, and on-site knowledge due to self-collecting data; however, the observations are made manually from point to point and, as a consequence, require accessibility to the objects (Pawlik et. al., 2023). Here are some key methods in this group:

- Levelling. This technique measures height differences between points using the principle of levelling, down to the remarkable accuracy of a millimetre scale (Li et al., 2014), and limited to the vertical measurements. This type of measurement is not continuous and offers low temporal resolution.

- Global Navigation Satellite Systems (GNSS). This technology estimates the geographic position of a point on or near the Earth's surface by processing signals from satellites. Depending on the approach (discussed in Chapter 4), they provide varying levels of accuracy; the accuracy of vertical observations is significantly lower than that of planimetric measurements. GNSS is only partially suited for monitoring vertical displacements, primarily due to its limited precision in the vertical dimension.

- Tacheometry. The method estimates the horizontal and vertical difference between points using triangulation principles and angle and distance measurements, covering vertical and planometric measurements. This type of measurement is not continuous and offers low temporal resolution.

Remote measurements group

This group includes the use of instruments positioned at a distance from the measurement field. Advantages and disadvantages vary but, in general, the method covers a large observation area, which could depend on the measurement conditions (such as direction or atmospheric conditions) (Pawlik et al., 2023). The main methods in this group include:

- Interferometric Synthetic Aperture Radar (InSAR). This technique uses two or more synthetic aperture radar (SAR) images to create surface deformation maps or digital elevation models (Gabriel et al., 1989). This method is used to measure vertical deviation more precisely than planimetric deviation.

- Photogrammetry. The method interprets photographs taken from different angles of the measured field to obtain coordinates. The camera can be installed on different platforms. For example, using unmanned aerial vehicles (UAVs), Gasperini et al. (2014) achieved precision displacement measurements, up to ten centimetres vertically and one centimetre horizontally. Due to the low precision of vertical measurements, this method is usually used for planimetric measurements.

- Light Detection and Ranging (LiDAR). This method uses pulses of light to measure ranges, or variable distances, to the Earth, generating precise, three-dimensional information about the shape of the Earth and its surface characteristics (Hurtado-Pulido, 2023). It yields more precise vertical measurements than planimetric measurements.

- Terrestrial Laser Scanning (TLS). This technique involves firing laser beams towards the surface, then measuring the time taken for the beam to be reflected back to the scanner, in order to determine distances and produce detailed three-dimensional models. The technique is not suitable for ground movement monitoring because it provides a snapshot of the surface at a specific point in time and requires repeated setups at the same location for temporal comparison, making it challenging to detect subtle, gradual changes in terrain that are characteristic of ground movement or subsidence.

2.2.2 Interplay and evolution of techniques

The choice of methodology for subsidence monitoring historically depends on the quality and capabilities of the techniques that are available. Over time, these methods have evolved, improving in quality and expanding in applications. The following is a historical overview of the development of subsidence monitoring methods, contrasted with their current applications.

Mid-19th – 20th century: manual and large-scale measurements

In the mid-19th century, levelling and inclinometers were first used to monitor slope stability and subsidence. This period was characterised by meticulous manual measurements.

Nowadays, the levelling method is usually used for small-scale projects, to measure vertical displacement to the nearest millimetre. Inclinometers are now only used for special cases of subsidence monitoring, providing measurements at a scale of 10^{-6} m/s^2 at specific locations (Li et al., 2014).

Later, in the early 20th century, the need for large-scale ground monitoring and the development of photography introduced a technique for measuring distances and creating maps and models of real-world objects and environments using photographs. This technique made it possible to measure changes in the earth's surface, including subsidence, but the accuracy is low compared to levelling. Today, photogrammetry itself provides an accuracy that varies from 2 to 16 cm in the vertical direction (Cai et al., 2023), while the potential of using unmanned aerial vehicles separately for subsidence monitoring is assessed with an accuracy of 10 cm, for the estimation of vertical displacement, and one cm, for horizontal measurements (Gasperini et al., 2014). Better subsidence measurement results were reported by Pal et al. (2020), who achieved an accuracy of 0.5-4.0 centimetres for vertical measurements, by applying classical photogrammetry in combination with an unmanned aerial vehicle (UAV). In principle, UAV photogrammetry is based on the same mathematical principles as traditional photogrammetry. However, there are differences in the application due to the quality, speed and orientation of the cameras mounted on the UAVs. According to subsidence measurements in Italy (Gasperini et al., 2014) and in New South Wales (Australia) (Ge et al., 2016) using unmanned aerial vehicles (UAVs), total stations, and laser imaging detection and ranging (LIDAR) measurements, showed similar accuracy between the methods.

In the middle of the 20th century, the range of tools available was further enriched by the introduction of extensometers. These instruments, capable of measuring changes in the distance between two anchored points, provided another lens through which subsidence could be observed with an accuracy of 0.001 to 0.100 mm for specific cases (Gambolati and Teatini, 2021). The implementation is limited to the deformation of rock masses for geomechanical tasks.

21st century: GNSS and InSaR

The 21st century brought the advent of Global Navigation Satellite Systems (GNSS), including the familiar GPS and InSAR techniques.

Satellite positioning itself began with the very first artificial satellite, Sputnik I, launched by the Soviet Union in 1957 (Skinner, 1984). In 1994, in response to the growing number of satellites and the widespread use of receivers, the European Commission, the

European Space Agency and Eurocontrol proposed the creation of the Global Navigation Satellite System (GNSS), which is now widely used for geomonitoring (Czaplewski and Goward, 2016). However, GPS was used for subsidence monitoring even earlier. In 1993, in Italy, the GPS network was implemented to control subsidence with high accuracy; planimetric errors were estimated within the order of 1.2 cm, and height to about 1.5 cm (Bitelli et al., 2000). Later, Wang (2022) used a network of GNSS reference stations, with the ability to continuously measure and analyse data, to achieve an accuracy of 4-8 mm in the vertical direction, which is a new level of accuracy for GNSS observations. However, in casual mine cases, the methods do not use the receiver network and they are not used for subsidence monitoring, due to the low accuracy of vertical measurements.

With the advent of large-scale satellite monitoring, interferometric synthetic aperture radar (InSAR) techniques were introduced in the 1970s (Braun, 2021). The technique does not measure absolute values, only the rate of movement. Gabriel et al. (1989) pioneered the use of Synthetic Aperture Radar (SAR) imagery to measure subsidence movements to within 1 cm, with a spatial resolution of 10 m over a 50 km area. By 1997, InSAR technology had become popular for subsidence monitoring in mining (Stow and Wright, 1997). Today, the technique is widely used to estimate surface subsidence with high accuracy over large areas. According to John (2021), the accuracy of subsidence estimates using this method can be less than a millimetre, using a special corner reflector and, in general, it is on a millimetre scale. Despite its insensitivity to surface displacement in the direction of satellite flight, this limitation can be mitigated by combining it with other data sources. For example, InSAR techniques have been integrated with the offset tracking method to monitor mining-induced large-gradient subsidence and subsidence along both the line of sight (LOS) and azimuth directions (Chen et al., 2020).

Different types of InSAR techniques are used today, such as dual-polarisation SAR (DInSAR), quad-polarisation SAR and bistatic SAR, etc. Their main differences are based on the number and types of polarisations used in the transmission and reception of the radar signal (Ratudu and Vlad-Sandru, 2023). Until 2003, classical InSAR and DInSAR techniques were widely used for subsidence monitoring but had the aforementioned problem with vegetation, etc.

In modern InSAR applications, full time series analysis (enabled by Persistent Scatterer Interferometry (PSI), Small Baseline Subset (SBA), and Time Series Interferometric Synthetic Aperture Radar (TS-InSAR) techniques) provides a robust solution to overcome the challenges previously mentioned (Ratudu and Vlad-Sandru, 2023).

PSI makes use of stable ground features, identified by point-like targets on the surface known as 'persistent scatterers'. These scatterers reflect radar signals consistently over time,

effectively bypassing the decorrelation problems caused by dense vegetation cover (Colesanti et al., 2005).

SBA strategically selects a subset of image pairs with small temporal and spatial baselines (Bru et al., 2022). This selection process is designed to minimise the effects of decorrelation and atmospheric artefacts, thereby increasing the reliability of the resulting data.

TS-InSAR provides insight into long-term deformation patterns, allowing the detection of subtle movements that occur over months or years (Khodaei et al., 2023).

Conclusion

Various methods are employed to gather information on subsidence, with the choice of method depending on the specific objectives of the research or project. For a comprehensive understanding of the subsidence process, it can be beneficial to integrate different available monitoring methods into a single Earth observation network. This combination of methods can either increase the overall image of the subsidence or improve the quality of the information obtained.

For example, in-situ monitoring data were used as ground control points for unmanned aerial vehicle (UAV) measurements, thereby improving the quality of these measurements (Lian et al., 2021). In another case, measurements were used to correct results estimated by InSAR technology (Tang, 2011). Differential interferometric synthetic aperture radar (D-InSAR) and terrestrial laser scanning (TLS) technology were combined to monitor subsidence, with a mean difference of 23.1 mm, compared to subsidence obtained by levelling (Chen et al., 2013). In Europe, integrated monitoring has combined terrestrial laser and radar technology with spaceborne and airborne remote monitoring methods. This approach allows continuous, highly automated identification and monitoring of mining-induced ground movements (Czerwonka-Schröder and Klonowski, 2019). Another interesting example is a combination of DInSaR and in-situ measurements at several points of a subsidence trough, to decrease the relative error from 68 to 8.3% (Hong-dong et al., 2014). Wang et al. (2022) used a mixture of monitoring techniques (SBAS-InSAR, DInSAR and UAV) and interpolation techniques (Kriging) to extract the surface subsidence caused by an underground coal mine, to construct a complete and high-precision surface subsidence field. These examples show the potential for using a combination of difference techniques to achieve greater results, which are not limited to the monitoring method combinations.

The evolution of subsidence monitoring methods, from small-scale manual observations to large-scale, high-precision, comprehensive subsidence imaging, has greatly improved the quality and quantity of observational data. As a result, this progress has led to

improved identification of subsidence anomalies although, in general, levelling is still the method of choice, due to its reliability and precision.

2.3   Subsidence anomalies

Despite the variety of subsidence prediction methods and models, subsidence predictions can deviate significantly from reality. Unexpected or unpredictable ground surface movement patterns or magnitudes are called 'subsidence anomalies'. These anomalies are influenced by various factors, including the properties of the mine, rock mass, and the nature of surrounding rock formations. Several common types of subsidence anomalies can be identified, as follows:

• Convergence and magnitude-related anomalies are characterised by the under or overestimation of the ground subsidence magnitude due to under or overestimation of the convergence or other processes. This type of anomaly is difficult to estimate because it can be mathematically covered, leading to potential confusion with parameter estimation problems.

• Asymmetric subsidence and subsidence trough shape anomalies are related to the proportion of the distribution and its shape in general. The shifting of the maximum subsidence is excluded from this anomaly type.

• Uplift can be characterised differently, e.g. as uplift due to the elastic kinematic energy on the periphery of the subsidence trough or as curves on the subsidence timelines.

These different types of anomalies are detected around the world and are connected to various factors, ranging from mining methods and geology to topography and surface structural factors (Speck and Bruhn, 1995). In the case of longwall mining, the distortion of predicted subsidence can be induced by failures in pillars, which deviates the stress distribution (Speck and Bruhn, 1995). In Pennsylvania, uplift was identified in the direction of retreat, leading to subsidence asymmetry in the periphery (tension zone) (Bruhn and Speck, 1985). In Russia, unexpected cohesion, tension, shape deviations, asymmetry, and uplifting zones were identified in coal (Awershin, 1947) and polymetallic (Sashurin, 1999) mines. The authors have connected these anomalies with the stress field and faults. In China, stress release activities increased the area of subsidence influence by 10% on one side, resulting in asymmetry of the subsidence (Xia et al., 2016, 2017). In Poland, wider subsidence troughs, combined with an asymmetric shape, led to an overestimation of subsidence magnitude in the central part of subsidence trough and underestimation of the periphery (Vušović et al., 2021). In another publication, significant deviation of predicted and observed subsidence (inclusive

asymmetry and shape deviation) in the Upper Silesian Coal Basin were connected with the activation of old goafs, which have impacted the distribution of the deformation probability (Sikora, 2021). Sheorey et al. (2000) presented different cases of coal mines in India, where the observed subsidence distribution showed asymmetrical patterns, without an explanatory reason. In Germany, correlation of the anisotropy of the subsidence trough and uplift with tectonic fault direction was detected (Busch, 2014, 2017). A complex structured system of blocks and faults dominated by extensional tectonics in the region of the Upper Rhine Graben (Germany) was the reason for an uplift of 34 cm over 3 years (Lubitz et al., 2013). Near-surface ground properties can also lead to shape-related subsidence anomalies. Shadbolt (1972) noted the tendency of moist unconsolidated soils to increase the influence angle and, consequently, decrease the maximum subsidence. Magnitude and convergence related anomalies were detected near Alborz (Iran), the anomalies being present in a wide variety of subsidence rates (ranging from 9-25 cm per year) in the region within 32 km (Pirouzi and Eslami, 2017). Various investigations have studied anomalies due to groundwater extraction or drainage, particularly for gas pipeline risk analysis, including uplift (Guzy and Witkowski, 2021; Guzy et al., 2021). These processes have a strong influence on stress conditions and the subsidence process. The discussed anomalies and their reasons are presented in Figure 3, which combines the above-referenced articles.
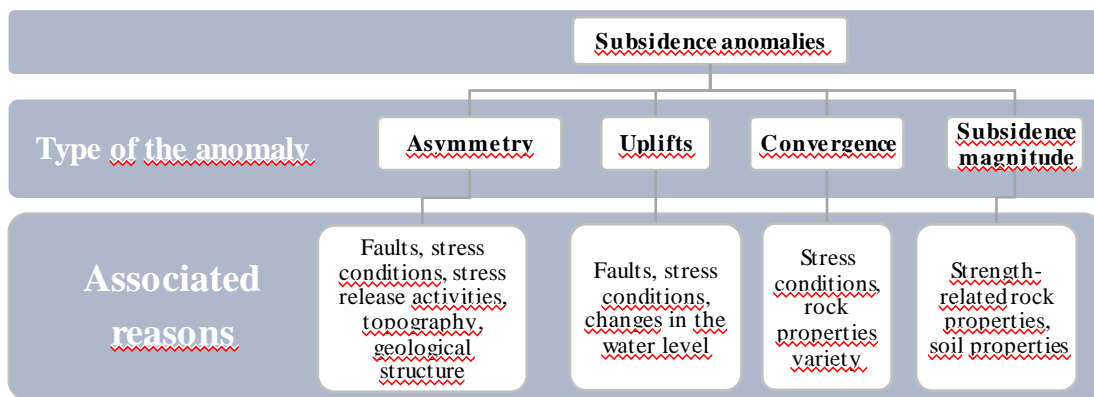
Figure 3. Overview of subsidence anomalies.

The anomaly cases discussed are directly or indirectly related to the distribution and magnitude of the stress field. For example, faults that occur under regional tectonic activity can influence the stress field and changes in topography and water levels can indirectly affect the stress field and balance, consequently influencing subsidence patterns. The properties of the rock, specifically its strength-related properties, describe its reaction to stress and cannot be investigated without considering the stress field. Empirical methods, on the other hand, capture a general picture of the stress distribution and average the stress influence. The

experiments conducted by Litwiniszyn (1994) (in a homogeneous medium) and the measurements by Knothe (1953) (in the Upper Silesian Coal Basin) were based on models and locations where stress is primarily a result of the material weight. This suggests that anomalies may arise due to the underestimation of the influence of stress distribution.

In conclusion, subsidence anomalies in mining areas can manifest in various ways, including asymmetry, uplift, and unexpected magnitudes. The factors mentioned in the references primarily affect subsidence through their influence on the stress conditions. However, the direct influence of stress conditions on subsidence is not investigated. The following chapter will provide an overview of the in-situ stress field.

2.4   In-situ-stress field

In a mining context, the main stress directions are commonly characterised as vertical (parallel to the force of gravity) and horizontal (perpendicular to it). The vertical stress is defined as the weight of the overlying masses (Equation 2), while the horizontal stress arises as a consequence of the elastic behaviour of rock mass under vertical stress (Moravwietz et al., 2020) and external stresses, e.g. tectonic (Equation 3).

$$\sigma_v = \gamma \cdot z \qquad\qquad (2)$$

$$\sigma_h = \sigma_v \lambda + \sigma_{external} \qquad\qquad (3)$$

where: γ is the weight of the rock; z is the depth of the overlying rock; $\lambda = \frac{v}{1-v}$ represents a coefficient that shows how much applied stress is redistributed in the perpendicular direction; and v is Poisson's ratio (Terzaghi, 1936; Skempton, 1960).

In a rock mass, Poisson's ratio varies from 0.05 to 0.40 (Vasarhelyi, 2009) and, according to the aforementioned equations, the horizontal stress induced by vertical stress redistribution is in the range 10-66% of vertical stress. The external part of in situ horisontal stress can exceed vertical stress itself, by several times (Bulin, 1971). Hergert (1974) observed that, in 75% of measured cases (45 measurements in the USA, Scandinavia, Ottawa, North Bay, Mount Isa, Tasmania, South Africa, Zambia, British Columbia, East Iceland, Ireland and Spitzbergen), the horizontal stress exceeded the vertical stress, based on measurements from the World Stress Map project, a finding confirmed by other researchers, such as Adams and Bell (1991), and Martin and Chandler (1993). The measurement of the stresses versus depth are demonstrated in Figure 4, where part (a) presents the distribution of vertical stress against depth, and part (b) presents the vertical to horizontal stress ratio against depth. A green area highlights the value of stress ratio related to the vertical stress redistribution. The same

distribution range of external stress was observed in a crustal stress field in Germany, made by Ahlers et al. (2022).

A general assumption in geomechanics is that the vertical stress component increases linearly with depth, while the ratio of horizontal stress to vertical stress depends on the inverse depth (Amadei and Stephansson, 1997). Local deviations from this assumption are not uncommon, arising from geological features or tectonic activity (Herget, 1974, 1986). Ahlers et al. (2022) emphasised that exceeding the horizontal stress can change its orientation by up to 25 degrees from the mean values and its absolute magnitude by 12 MPa, which is comparable to an average vertical stress of 500 m.
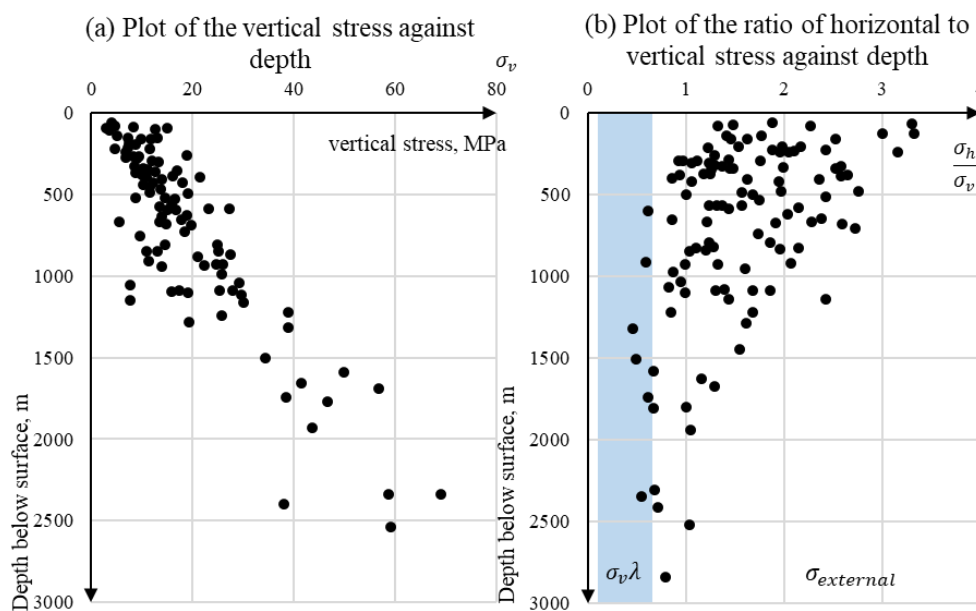
Figure 4. (a) Plot of the vertical stress against depth; (b) variation of average horizontal stress to vertical ratio with depth (adopted from Amadei and Stephansson, 1997). The blue area is the area of horizontal stress as a consequence of the elastic behaviour of the rock mass under vertical stress.

The stress field can be influenced by various types of inhomogeneity, which can be categorised into different orders, based on their scale of influence:

- First-order stress sources, such as plate boundary forces like ridge push or slab pull, can impact the stress field over hundreds or thousands of kilometres (Richardson, 1992; Zoback, 1992).

- Second-order sources, such as mountain chains, have an influence on the stress field over hundreds of kilometres (Zoback, 1992).

- Local stress sources, including faults, diapirs, and detachment zones, contribute to third or fourth-order deviations (Yale, 2003). Some of the sources of the third category deviations have been identified as a reason for subsidence anomalies in Chapter 2 (State of the art), e.g. the aforementioned anomalies in China where stress release activity resulting in asymmetry. The effect of horizontal stress on the deformation process can be well evidenced by the effect of core disking, which indicates that stress distribution is intricately involved in the deformation process and cannot be disregarded when considering the distribution of subsidence.

Despite the aforementioned investigations, there are enough areas where the features of the stress field are not significant for the subsidence to be processed; however, ignoring them leads to anomalies (as referenced in Chapter 2.3). Classifications of regions regarding their influence of the stress field do not exist. However, there are classifications of stress regimes, which would give an overview of the field of the research interest. One of them is Anderson's classification (Anderson, 1951), which is presented below, with new extension-related measurements and locations (in the classification, $\sigma_{h\,max}$ and $\sigma_{h\,min}$ mean maximum and minimum horizontal stress, respectively):

- Normal faulting region, $\sigma_v > \sigma_{h\,max}$ ($\sim 0{,}6\,\sigma_v$), for example: Central Greece (Tsanakas, 2019), Illinois, Indiana, United States; The Pennines (Okal, 2009));

- Strike-slip faulting region, $\sigma_{h\,max} > \sigma_v > \sigma_{h\,min}$ ($0{,}6 \sim 1{,}6\,\sigma_v$), for example: The Philippines (Aurelio, 2000); Nova Scotia; The Atacama Desert, Chile; Turkey (Okal, 2009));

- Reverse faulting region, $\sigma_{h\,min}, > \sigma_v$ ($1{,}6 \sim 4{,}6\,\sigma_v$) (Hooker et al., 1972), for example: South Island, New Zealand (Gledhill et al., 2000), The Kinki region of Japan (Shikakura et al., 2014), The Alps, Europe (Okal, 2009).

The global pattern of regional tectonic stress is systematically documented by the World Stress Map Project (World Stress Map Project, n.d.) up to 2011. This project utilises stress indicators to characterise stress regimes and directly measures stress data to compile a comprehensive database of stress distribution worldwide. However, not only the magnitude can be different but the distribution of stress can as well. According to Herget (1993) and Voight (1966), tectonic stresses can exhibit both uniform and non-uniform distributions over large areas, e.g. 10,000 km^2 or local areas. Non-uniform distribution of stress can be identified if the stress differs on opposite sides of a considered area.

Non-uniform stress distribution can be induced by mining and subsidence itself. The stress appears due to the 'residual' stresses. Residual stresses are formed by the loading history of rock masses and, due to the lack of self-equilibration, persist within a structure even after the external forces and moments are removed (Voight, 1966). During rock mass deformation

or displacement, these locked-in stresses can be released in the form of displacement, fracturing or deformation.

In summary, in mining applications, horizontal stress is often underestimated, the actual data of horizontal stress may exceed the vertical stress by several times. Since horizontal stress influences the deformation process, it should be considered in subsidence. The location and sensitivity of subsidence to horizontal stress has not been investigated. However, there are several sources of stress conditions that can be taken as an indicator of potential deviations (second-order and local stress sources). The classification of stress regimes can be used as a basis for investigation. Another part that should be considered is the distribution of stress through the subsidence area, obviously the symmetrical conditions cannot lead to asymmetry.

2.5   Subsidence prediction methods for anomalies

This chapter describes the prediction method developed to cover the subsidence anomalies. The anomalies of the subsidence profile can be related to parameter underestimation, asymmetry, uplift and shape deviation. Each of them is a challenge that requires a different approach to deal with. This chapter describes different approaches to solving these problems, grouped by anomaly type.

Parameter estimations

These types of anomalies appear when the parameter for subsidence prediction deviates from expectations. The problem is solved by using different techniques, e.g. the parameter estimation or neural network application.

The parameter estimation techniques are based on the difference between a subsidence prediction model and measured data, using different techniques (as discussed in Chapter 4) to find the parameters set with the smallest difference, e.g. inverse modelling could be applied to estimate the convergence (Fokker, 2002). Parameter optimisation (Differential Evolution Adaptive Metropolis) and InSAR data is used to define a distribution of rock mass parameters for subsidence prediction in Smith and Knight (2019). Gazzola et al. (2021) used a variance-minimising estimator in the geomechanical modelling of subsidence prediction, to reduce numerical uncertainty.

The neural network method involves estimating the hidden function between the conditions and parameters of an empirical model using various techniques. Mine area

information is plotted against parameters and then fitted. These functions are summarised for each parameter and weighted, to minimise deviations between predicted and training data. As an output, the parameters of the empirical model can be estimated, based on the different mine area information. The main idea and the different approaches were described by My et al. (2014). For example, the regression method Extreme Learning Machine (ELM) neural network was used to estimate parameters for an empirical model based on geological and mining data (Chi et al., 2023). In another application, the implementation of Artificial Neural Network (ANN) on the basis of 5 years of training data, achieved the absolute difference level of 10 cm between subsidence prediction and the measured data (Turk and Ambrožič, 1999). This approach can also be used conversely; for example, Blachowski (2016) used GPS data to estimate the parameters of mining conditions for detected subsidence. The anomalies that cannot be covered by parameter variation belong to the shape deviation anomalies, including uplift.

Shape deviation and uplifts

The shape deviation is a deviation that cannot be mathematically resolved by the empirical model. The problem is partially covered by using different empirical subsidence models, as presented in Table 1 and Figure 2. There are several models that cover the shape deviation by some additional parameters, e.g. Eickeimeier (2005), Kochmański (1955), Ramírez et al. (2000). Li et al. (2014) proposed to use a sum of two distribution functions to cover the shape deviation observed in the mining field near the city of Huainan. Later, Chi et al. (2021) proposed to use the same superposition principle but for a Boltzmann function to obtain the shape deviation Equation 4.

$$S(r) = \frac{(1-P)\exp\left(-\frac{r}{R_1}\right)}{R_1\left(1+\exp\left(-\frac{r}{R_1}\right)\right)^2} + \frac{P\exp\left(-\frac{r}{R_2}\right)}{R_2\left(1+\exp\left(-\frac{r}{R_2}\right)\right)^2} \tag{4}$$

where P is supposed to be below 1.

This solution requires several remarks (Figure 5):

a.   The numerically estimated integral of the function is not constant for different values of P;

b.   The ability to take into account uplifts when P is negative;

c.   The distribution of the Boltzmann function is much wider than R. For example, in Figure 5, R1 and R2 have been taken to be 100 and 200, respectively, but the influence extends much further.
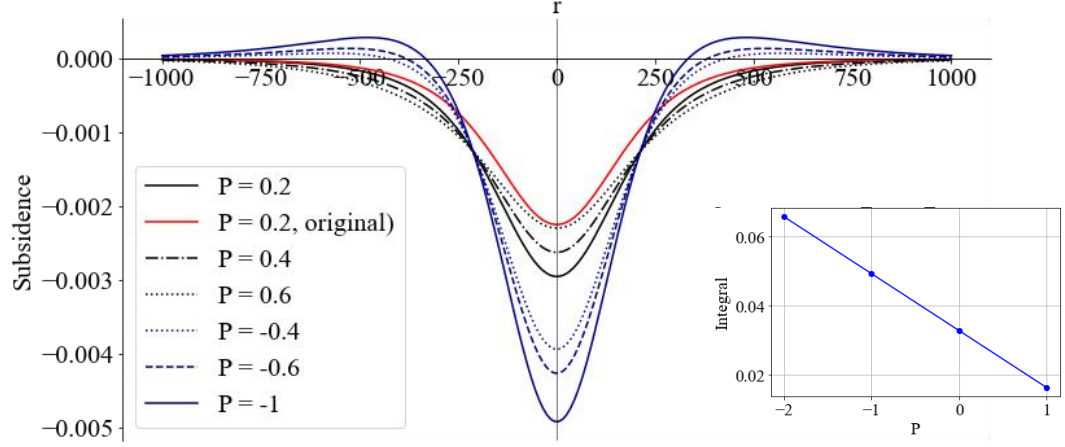
Figure 5. Influence function with basic Boltzmann distribution. The red line represents the original solution.

The solution is reminiscent of the approach of Ramírez et al. (2000) but, if this approach is based on the Boltzmann distribution, Ramírez et al. (2000) was based on Gaussian distribution. An adaptation of the above idea for the normal distribution solution could be made in the form of Equation 5, Figure 6.

$$S(r) = \frac{(1-P)\exp\left(-\pi\left(\frac{r}{R}\right)^2\right)}{(R)^2} + \frac{P\exp\left(-\pi\left(\frac{r}{Rk}\right)^2\right)}{(Rk)^2} \tag{5}$$
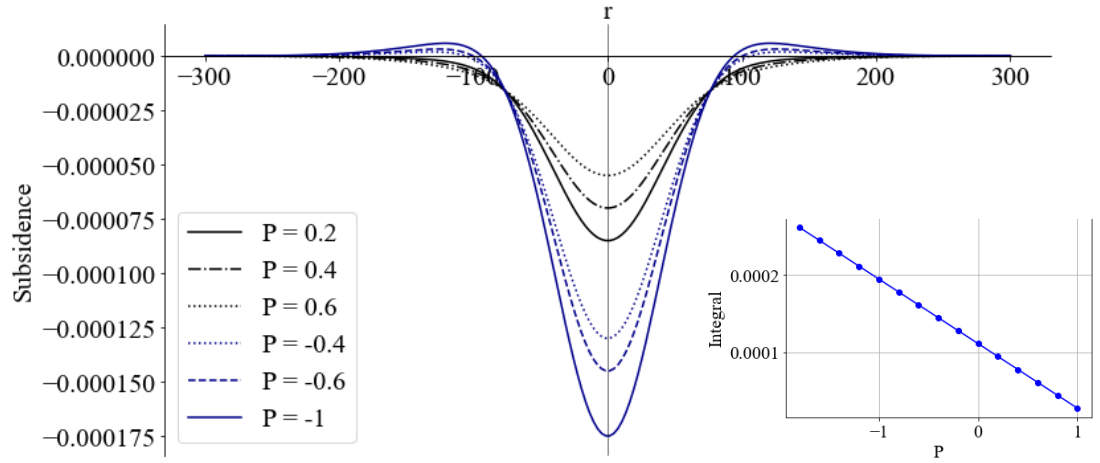
Figure 6. The adoption of Chi et al. (2021)'s solution to a normal distribution.

A similar assumption was proposed by Asadi et al. (2005) (Equation 6) and the solution was applied to a coal mine in India. The solution requires more variables but does not include asymmetry or uplift.

$$dS(r) = S_{max}\left[c * \exp\left(-f\left(-\frac{r}{R_1}\right)^g\right) + d * \exp\left(-p\left(\frac{r}{R_2}\right)^q\right)\right] \tag{6}$$

where the variables *g, q, f and p* are variable profile constants obtained in the field, and coefficients c and d ensure volume balance between convergence and subsidence.

Other approaches suggest varying the power of the relative positions to cover the shape deviation (Eickemeier (2005) and Kochmański (1955)). This approach does not cover uplifts and has the same problem of volume balance, but has a clearer relationship between shape and shape coefficient (Eickemeier, 2005); the influence function will be discussed in Chapter 4.

Uplift phenomena can occur in the form of a time function or, as mentioned above, at the periphery. For the time function, the maximum subsidence first increases and then begins to decrease, often associated with mine watering (Rosner et al., 2014; Kessler et al., 2020; Zhao et al., 2021).

Asymmetry

Asymmetry of the subsidence trough can be described as the deviation of distribution that depends on the planimetric direction. As mentioned above, Knothe (2005) assumed that the asymmetry is common for a subsidence trough and proposed to use the weighted sum of two normal distribution functions with different weights (similar to the aforementioned shape deviation solution of Chi et al. (2021) but with a shifted centre for one of the distributions. In the publication by Polanin (2015), this was called the 'bimodal method' and was implemented for the Upper Silesian coal basin with a higher degree of agreement. The author emphasised that the solution is not applicable for high levels of asymmetry.

In Zhao et al. (2022), the methodology proposed to estimate the influence angle depends on the thickness of the rock and the thickness of the soil, with the integrated coefficient being different for different cases. It can be assumed that the subsidence asymmetry can be covered by the difference in the properties of the rock layers when they are different across the field. In this way, the asymmetry does not belong to the distribution, but to the parameters of the angle of influence from element to element. This is contrary to Quasnitza (1988), where the asymmetry was evaluated by the influence angle in different directions and presented in the influence function itself (see Chapter 4). Yan et al. (2022) considered a non-symmetrical maximum subsidence velocity position, which can lead to a temporary asymmetrical shape of subsidence trough, covering this kind of asymmetry decreases deviations on 7%. In this method, the asymmetry belongs to the subsidence rate distribution, which is taken to be a Weibull function.

Much earlier, the analysis of subsidence above inclined seams suggested that the presence of a seam gradient not only shifts individual subsidence troughs to the dip side, but also causes asymmetry of the trough itself (Equation 7), in the cases where different values of P provide different widths of distribution in the x and y direction (Lin et al., 1992). In the solution, similar to Quasnitza (1988), the influence angle is assumed to vary in the x and y direction. In the same direction, Luo (2015) continued the investigation by using the influence angle difference in the lower and upper side.

$$dS(\Delta x, \Delta y) = \frac{S_m S_{cx} S_{cy}}{\Delta h^2 \tan(\gamma_x) \tan(\gamma_y)} \exp\left(-P_x \left(\frac{\Delta x - \Delta h^2 \tan(\phi)}{\Delta h^2 \tan(\gamma_x)}\right)^2\right) \cdot \exp\left(-P_y \left(\frac{\Delta y}{\Delta h^2 \tan(\gamma_y)}\right)^2\right) \qquad (7)$$

where ϕ is an angle of shift of the maximum subsidence; P is the maximum-slope calibration coefficient, and $\Delta h^2 \tan(\gamma_x)$ defines the shifting distance of an underground point in the dip direction.

Saeidi et al. (2013) proposed covering the asymmetry variation by varying the influence angle from element to element; in other words, the influence angle should depend on its location. In the article, different influence angles at opposite edges of a mine cave were used to obtain an asymmetric shape. The same approach was used by Sikora (2021) to cover the asymmetry of the subsidence distribution due to the old goaf activations in the Upper Silesian Coal Basin. In this particular case, the Cellular Automaton method was used by the numerical modelling principle; an analogy of the influence angle was used to estimate the slope of the subsidence distribution through each cell and the volume of deformation. The maximum deviation from the FDM model in this case study was 200 mm (11%).

Zhang et al. (2021) suggested using a rotation function instead (a function of x and y), the idea being to differentiate the influence radius (R) in that direction to create anisotropic asymmetry in the form of an ellipsoid (Equation 8). The published solution only covers the asymmetry in one direction; in order to cover the orientation of the anisotropy in another direction, the coordinates have to be transformed.

$$dS(\Delta x, \Delta y) = \frac{1}{R_x R_y} \exp\left(-\pi\left(\frac{\Delta x}{R_x}\right)^2 + \left(\frac{\Delta y}{R_y}\right)^2\right) \qquad (8)$$

In conclusion, addressing subsidence anomalies involves a multi-pronged approach. Parameter underestimation can be improved with machine learning techniques and parameter estimation methods, while shape deviation and uplift demand the use of diverse empirical subsidence models, each with their own advantages and limitations. Asymmetry management includes different strategies, including the use of weighted sums of normal distribution functions, dividing the element's strategy, determination of influence angle either as a function or as two different influence angles in the x and y direction. Different techniques have their own advantages and disadvantages that limit their particular applications.

2.6   Conclusions

Of the different approaches to subsidence prediction, the empirical model is more applicable in practice and gives the global picture of subsidence. These models can be extended to cover asymmetry differently. However, they need to be further developed to be universally applicable, in particular, to include local features such as horizontal stress. On the other hand, numerical models are valuable tools for studying the response of subsidence to different parameters and conditions. Consequently, numerical investigations can provide a basis for understanding the subsidence process and developing empirical models.

Despite the variability of empirical subsidence prediction models, the difference between prediction and reality is still present. The deviation in the form of asymmetry and shape deviation is found in the regions where stress is expected to be unusual (mountain chains, faults, stress release activities, etc.). However, the effect of the stress field on the subsidence process is not detected and existing models only partially cover the anomaly.

As mentioned above, the ratio of horizontal stress to vertical stress is inversely related to depth (Amadei and Stephansson, 1997), making its influence particularly important for deformation above 1500 m depth. The horizontal stress scenario, geology, hydrology and mining methods vary from case to case, so the influence cannot be generalised empirically. However, numerical methods are suitable for these cases. In practice, the main source of excess horizontal stress is assumed to be the stress from secondary and local stress sources, which can potentially be used as an indicator of the high probability of subsidence anomalies.

The combination of the above prerequisite, related to the mathematical limitations of empirical models, and the investigation of anomalies, defines the aims and objectives of the thesis to improve subsidence prediction methods in the field, under tectonic influence.

3   Goals and objectives

Understanding and accurately predicting subsidence remains a crucial challenge in the field of mining impact assessment. Various factors, including stress conditions, significantly influence subsidence, making prediction a complex task. This thesis aims to address this challenge, particularly focusing on the role of horizontal stress in subsidence. The core goal is to increase the precision of subsidence prediction methods by accounting for the influence of in-situ stress conditions, thereby mitigating the risks associated with inaccurate predictions.

Goal: The primary aim of this thesis is to enhance the accuracy of subsidence prediction methods by incorporating the impact of horizontal stress, while preserving the practicality of empirical methods.

To accomplish these goals, the following objectives have been identified:

1. **Developing a comprehensive understanding about the state of the art.**

The main question for the objective relates to the identified research gap, which is the inclusion of stress conditions in subsidence prediction models.

According to the investigation, excessive horizontal stress induces asymmetry and shape deviation in the subsidence profile. To address these deviations, different approaches and strategies have been reviewed in Chapter 2 - 'State of the art'. The reviewed methods cover various patterns but they are not unified, to address all of them together.

The state of the art provided a clear roadmap for the research:

a) Numerical investigation of the causal relationship between horizontal stress and the subsidence profile;

b) Identification of the causality with subsidence profile parameters, anomalies, and their magnitude;

c) Development and application of an empirical subsidence prediction model that incorporates the features discovered in the numerical study;

d) Statistical analysis of the results.

2. **Establishing the foundations for the research.**

This objective aligns with Chapter 4, 'Foundations', which outlines the roadmap for developing a new subsidence prediction model. The chapter starts with the basic concepts of subsidence prediction and the construction requirements of the model, critically comparing advantages, disadvantages, and the potentials of different models. A substantial focus is put on the numerical investigation method, emphasising crucial choices, such as grid size, boundary conditions, and constitutive models, which significantly affect experimental

outcomes. The final section introduces tools for model validation and experimental result verification.

3. Designing a comprehensive research methodology.

Based on the foundations and the state of the art, a methodology for the research is developed. The methodology provides a workflow for the whole of the research. It is useful to get an overall impression of the results and to identify the potential problems and opportunities of the research.

4. Investigating subsidence profiles under different stress conditions using numerical methods.

This is covered in Chapter 6 – 'Numerical investigation'. Results related to the different parameters are provided. In the analysis, different techniques are used to identify causality, since the relationships are non-linear. Each result is discussed in the context of the subsidence parameter that is included or should be included, according to its influence on the subsidence profile in the experiment results and observed in real cases anomalies.

5. Developing a subsidence prediction model that covers the subsidence profile patterns related to the stress conditions.

This is covered by Chapter 7 – 'Adaptation of an empirical model to the discovered features'. In this part, the model discussed in the foundation is adapted to the main patterns estimated by numerical experiment and to the requirements established in the foundations. In the last part, a unifying solution is presented that can be reduced to the classical solution or to cover the discovered patterns separately or all together.

6. Evaluating the performance of the new model.

The objective is covered by Chapter 8, which presents the case used to evaluate the model and data and techniques used. In conclusion, comprehensive statistical analysis is used to evaluate a new solution and contribution to the subsidence prediction method covering the various features.

The thesis has a narrow focus on the development of the subsidence influence function to cover the subsidence deviation related to the stress conditions, out and in-scope of the work presented in Table 2.

Outline

Each chapter of the thesis is dedicated to one objective; the following is the outline of the thesis:

Chapter 1: Introduction

This introduces the motivation behind advancing the field of subsidence prediction, by showcasing various subsidence cases from around the world.

Chapter 2: State of the art. Objective 1: Develops a comprehensive understanding of the state of the art. This section describes various studies pertinent to the research theme.

Chapter 3: Goals and objectives. Summarises the research structure and outlines the goals and objectives identified from the literature review.

Chapter 4: Foundations. Objective 2: Establishes the foundation for the research. This chapter provides in-depth information about the methods and techniques that are, or can be, employed in the research.

Chapter 5: Methodology. Outlines the structured approach of the research.

Chapter 6: Numerical investigation. Objective 3: Generates subsidence profiles under stress conditions using numerical modelling. This chapter delves into the details of numerical modelling, its results, and their interpretation.

Chapter 7: Adaptation of an empirical model to discover subsidence profile patterns. Objective 4: Develop a subsidence prediction model that addresses the patterns in subsidence profiles related to stress conditions.

Chapter 8: Application to a full scale. Objective 5: Evaluates the performance of the new model. This chapter discusses the model's implementation, its results compared to real-world data, and its performance against other models.

Table 2. Limitations and content of the thesis.

In-Scope	Out-of-Scope:
Numerical modelling of subsidence under different stress conditions for different rock properties.	Developing or comparing the results of different numerical methods and approaches, measurements and analysis of rock properties.
Interpretation of numerical experimental results in the context of subsidence profile parameters.	3D subsidence trough, dynamic analysis of the subsidence process and its interpretation.
Development of an empirical model for subsidence prediction based on polar coordinates, covering subsidence asymmetry and shape deviation.	Integration of a method based on cell automation or Cartesian coordinates, etc., and their comparison. Rate of the subsidence process.
Parameter estimation for different subsidence shape types and validation of the results.	Development of parameter estimation or validation methods. Comparing the results of the parameter estimators.
Statistical analysis of the residual subsidence and its interpretation.	Development of a statistical evaluation tool.

4   Foundations

This chapter aims to provide enough information to understand the underlying principles guiding our investigation, the rationale behind each choice, and the methodology. It provides the knowledge necessary to replicate the study, thereby ensuring the transparency and reproducibility of our research.

The chapter provides a foundation for:

- Empirical subsidence prediction methods.
- Numerical simulation of the depth, grid size, boundary conditions, and the various constitutive models specifically used for mine subsidence modelling.
- Validation and evaluation of the results.

4.1 Empirical subsidence prediction methods

Given the current trend of closing coal mines in Europe (Dudek et al., 2022) and the growing interest in using salt caverns as energy storage units (Thoms and Gehle, 2000), this chapter focuses on subsidence prediction above salt cavern energy storage. However, those methods and developed method in Chapter 7 are applicable to all types of mining.

A cavern is an artificially constructed cavity that can be used as storage for liquids and gas. The mining method involves drilling a well into the rock salt with a diameter of $d < 1$ m. Several pipes are installed in this well and bonded to the surrounding rock with cement. During the solution mining process, water is injected to dissolve the salt. The brine produced is then transported to the surface (Moseley and Garche 2014). The void constructed during the leaching process, and later used for energy storage, leads to a destruction of the force balance in the surrounding rock mass and results in deformation manifested by the cavern convergence.

In contrast to classical mining, leaching mining is a speciality, in terms of its geometry and depth, exploitation, and other factors, such as the cycles and phases of gas storage caverns due to leaching and filling processes, high geological uncertainty, and surrounding mass creep (Ye et al., 2022). Despite the difference, the general approach for subsidence prediction remains the same as for a classical mining method: i.e. a product of influence function, convergence and correction coefficient (Chapter 2.1.1, Equation 1, Figure 1).

To determine the exact expression of convergence, transmission coefficient and influence function, various methods are available, including numerical modelling and physical solutions. In the following subchapter, these themes are discussed.

4.1.1 Convergence

The International Society for Rock Mechanics (ISRM) defines 'convergence' in rock mechanics as the 'time-dependent closure of a fractured rock mass under compressive stress, typically observed following excavation and usually measured perpendicular to the excavation face' (Ulusay, 2015). This closure results in the volume deficit within the subsurface, determining the volume of the subsidence trough. With respect to a cavern, its unique geometry results in significant displacement, not only in the roof and floor (as in the case of longwall mining), but also along the sides. Consequently, the concept of convergence expands to encompass volumetric changes in the context of a cavern.

Convergence within a cavern is a multifaceted process, influenced by many factors. On one side, it is the operating cycle, comprising stages such as low-pressure operation, gas injection and pressurisation, high pressure operation, and gas recovery and depressurisation (Figure 4). On the other side, complex geomechanical conditions, including the creep process, significantly impact the process. The description of the creep process varies across different models and depends on a range of factors like the microstructure and NaCl content within the rock mass. A summary of different factors affecting the creep process is outlined in Table 3. Given the complexity of the convergence process, measurement is typically the preferred method; however, there are high associated expenses in the context of salt cavern energy storage.

Table 3. General tendency of salt characteristics on the creep model (Zhang et al., 2021; Holdsworth, 2008) where ε defined the strain.

| Characteristic	Influence
Confining pressure	An increase in stress increases strain rate over time $\frac{d\varepsilon}{dt}$; however, when confining pressure exceeds 4MPa, the creep behaviour of salt rock is independent of confining pressure.
Temperature	1. The higher the temperature (T), the faster the creep rate. 2. When the other conditions remain unchanged, the higher the temperature, the faster the creep rate, the larger the creep strain, and the shorter the creep life. In geomechanics, creep life refers to the amount of time it takes for a material to deform or fail under a constant load or stress.

Characteristic	Influence
NaCl content	The decaying creep rate and steady creep rate of salt rock increases with increasing NaCl content.
Water	Water can form near to the grain structure, which can promote the release of elastic energy stored in salt rock and accelerate the creep development process.

The empirical method for quantifying the convergence volume is generally expressed in an exponential form (Eickemeier, 2005; Tajduś et al., 2021). However, it can be simplified to a percentage of the cavern volume relative to a previous period (Tajduś et al., 2021a). Tajduś et al. (2021a) suggested that the annual volume reduction could be as high as 2% and depends on the exploitation phase (Figure 7). Equation 9 can be used to calculate the volume reduction of the cavern over a given period.

$$\Delta V_{[t_1,t_2]} = V(t_0) \cdot \left(e^{-c(t_1 - t_0)} - e^{-c(t_2 - t_0)} \right) = \sum_{i=t_1}^{t_2} \mu \cdot V(t_i) \tag{9}$$

where $(t_2 - t_1)$ is a time period; c is the time influence coefficient (of the order 10^{-2}); $V(t_0)$ is the initial cavern volume; $V(t_i)$ is a convergence volume at the time t_i in years; and μ is a percentage of the convergence per year.
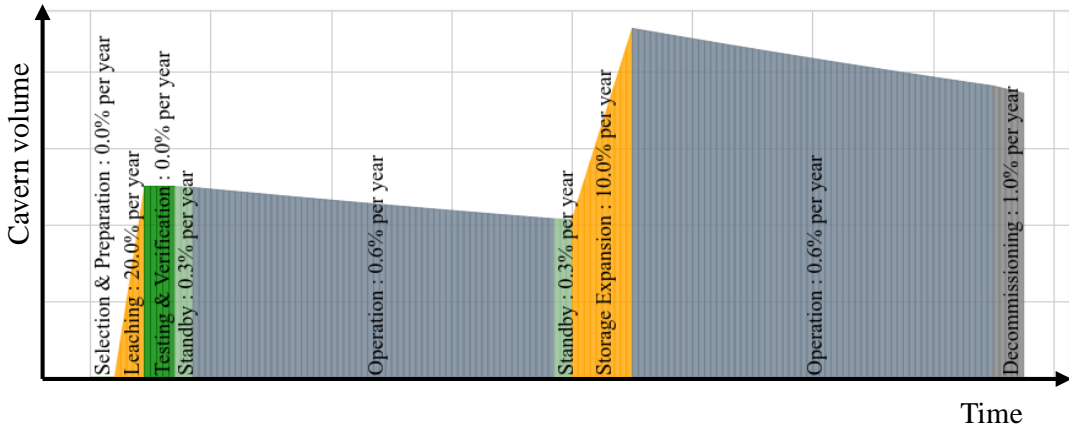
Figure 7. The schema of the typical cycle of the cavern volume changes, due to different exploitation phases.

4.1.2 Transmission coefficient

The transmission coefficient is a parameter that quantifies the proportion of the convergence volume that ultimately contributes to the volume of ground subsidence (V_s) over an infinite time horizon. It can be mathematically defined by Equation 10.

$$a = \frac{V_s}{\Delta V} \tag{10}$$

The influence of the transmission coefficient and the convergence rate on the subsidence process can strongly overlap. The accurate estimation of the transmission coefficient can only be achieved when subsidence is fully completed. However, in practical terms, this condition cannot be met during the exploitation period and even years after it. Therefore, in the subsequent analysis, the transmission coefficient is assumed to be one, as stated by Tajduś et al. (2021).

4.1.2   Influence factor

The influence factor represents the part of the convergence volume unit that results in subsidence at a particular point on the surface. This is influenced by the distance from the point and the distribution of deformation described by the influence function f(r) (Figure 8).
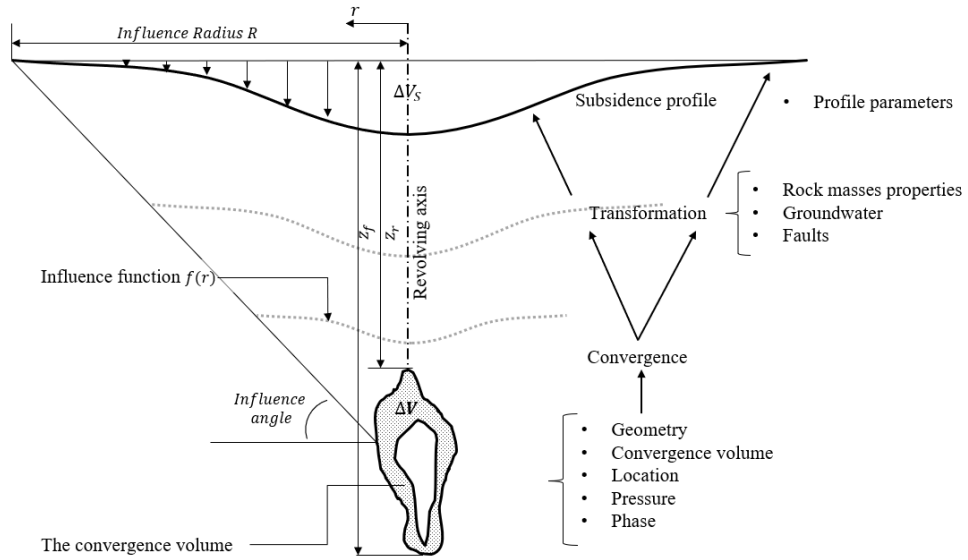
Figure 8. Ground subsidence above a salt cavern, where z_r and z_f are the depths of the roof and floor of the cavern and ΔV is convergence volume.

The fundamental principle behind the influence function is the concept of 'volume balance,' where the volume of convergence (ΔV) and the volume of subsidence (V_s) should be equal. This is expressed mathematically by Equation 11.

$$\Delta V = V_s \tag{11}$$

The volume of subsidence can be determined by solving the integral under the surface of the influence function, as given in Equation 12. Solving this equation allows the influence function to be weighted in a way that satisfies the volume balance condition.

$$\int_0^{2\pi} \int_0^{\infty} f(r,\varphi)\, r\, dr\, d\varphi = \Delta V \tag{12}$$

where φ is a horizontal angle between vector r and geographical North.

Sroka and Schober (1982) applied the subsidence solution of Knothe (1953) and Litwiniszyn (1994) to a salt cavern (Equation 13). In this solution, ground observations such as geometric levelling are used to estimate the parameters of the influence function. This approach does not reference any specific physical parameters.

$$S(r,t) \cong \frac{\Delta V(t)}{R^2} exp\left(-\frac{\pi r^2}{R^2}\right) \tag{13}$$

where R is defined as a radius of maximum influence and $R = \sqrt{z_f z_r \cot^2 \beta}$; β is the so-called angle of main influences. In a later publication by Tajduś et al. (2021a), an adjustment to the influence radius of the roof is introduced by incorporating the influence of the cavern roof characteristic, denoted as c, and a surface factor, denoted as n. The adjusted influence radius, denoted as $R_r(z)$, is calculated as $R_r(z) = R\left(\frac{z - z_r + c}{z_r - z_f + c}\right)^n$

Eickermeier (2005) proposed significant changes by introducing the parameter δ, which represents the power of the relative position (r/R), to define the shape and inclination of the subsidence trough wings. The implementation of this parameter poses difficulties due to the lack of analytical solutions for arbitrary values of δ in the solution of the volume balance (Equation 12). Eickermeier (2005) addressed the volume balance problem using the approach described in Equation 14, but this solution is only valid around specific exact values, as shown in Figure 9.

$$S(t,r) = -\frac{\xi\,\delta}{2\pi^{1-\frac{2}{\delta}} R^2 \Gamma\left(\frac{2}{\delta}\right)} exp\left(-\pi \xi^{\frac{\delta}{2}} \frac{r^{\delta}}{R^{\delta}}\right) \cdot V \cdot z(t) \tag{14}$$

The author referred to ξ as "a parameter to consider a time effect". In the Praxis, programme should be used for a fine calibration of the maximum subsidence; δ is a form parameter that describes a change in the curvature of the influence function (ranging from 1.5-3.0); and Γ is a gamma function that normalises the function, with respect to the convergence volume. The effects of the variables on the subsidence can be seen in Figure 9.
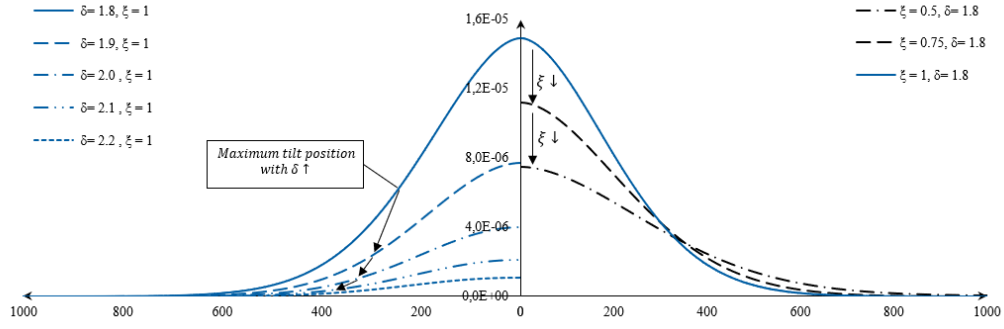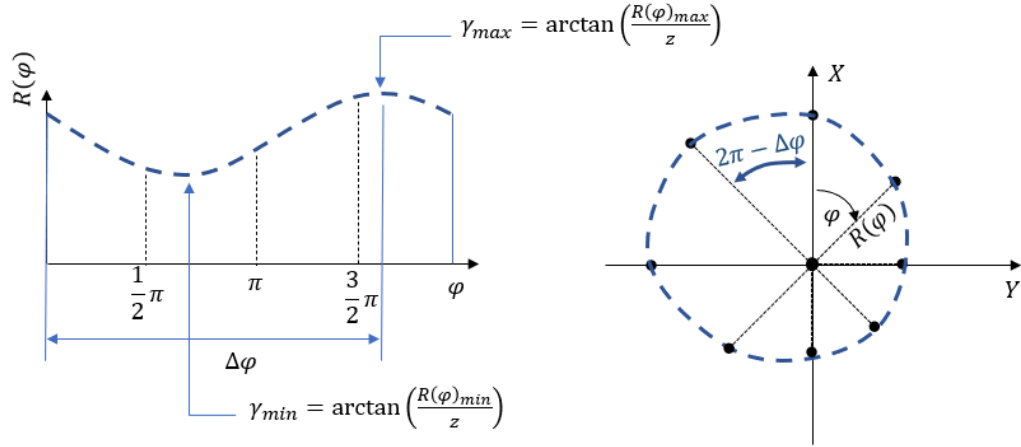
Figure 9. Demonstration of the influence of ξ and δ parameters on the influence function, according to Eickemeier (2005).

Figure 9 illustrates the effects of the proposed parameters and shows that the solution gives different volumes, which is unacceptable for an influence function. However, an appropriate compensation for the deviation of the δ parameter can provide flexibility in regulating the wings of the influence function. This aspect is often considered as a motivation for the development of new influence functions, as highlighted by Sroka et al. (2015) and Zhang et al. (2022).

Quasnitza (1988) proposed a mathematical approach to achieve an asymmetric shape for subsidence troughs, based on the subsidence trough solution introduced by Sroka and Schober (1982). This solution represented the radius of maximum influence R as a function of the horizontal angle φ, which represents the angular difference between the profile line and geodetic north and is represented as a sine function. Consequently, the volume of the shape depends on the function $R(\varphi)$. However, the originally proposed solution (Equation 15) does not accurately address the balance between the convergence and subsidence volumes (Equation 12). For demonstration purposes, Figure 10 shows the distribution of the influence angle over the horizontal angle for a given function, while Figure 11 compares this distribution with the solution proposed by Sroka and Schober (1982).

$$S(r,\varphi) = \frac{a\,\Delta V}{z_r z_f \cdot ctg\,\gamma_{max}\,\cdot ctg\,\gamma_{min}}\,e^{-\frac{\pi r^2}{R^2(\varphi)}} \tag{15}$$

where γ_{max} and γ_{min} are influence angles in the direction of asymmetry (in the context of the influence radius shown in Figure 10).

Figure 10. Schema of distribution of the influence radius across horizontal angles, according to Quasnitza (1988).
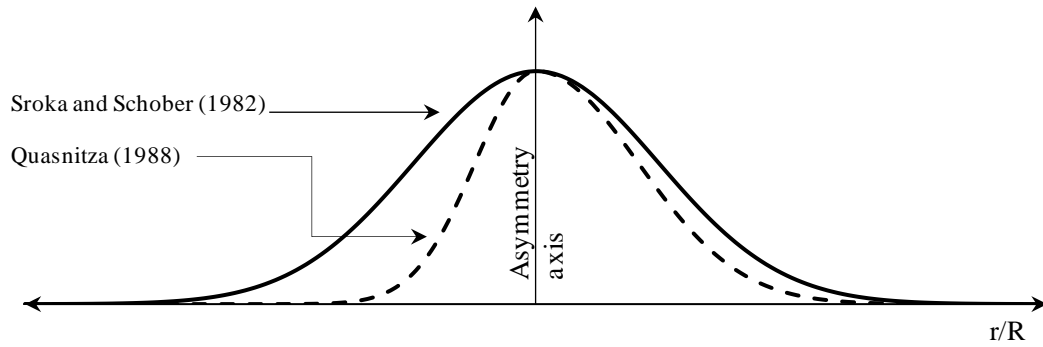
Figure 11. Demonstration of asymmetry according to Quasnitza (1988) and Sroka and Schober (1982).

Based on the information provided, it is indeed possible to use the approach proposed by Sroka and Schober (1982) as a basis for incorporating both the shape extension method proposed by Eickermeier (2005) and Quasnitza (1988). This integration, with appropriate adjustment, can improve the adaptability of symmetric models by allowing shape adjustments and effectively covering asymmetric subsidence phenomena. This adaptation of the empirical model will be presented and discussed in Chapter 7.

4.2   Numerical models for subsidence case

Numerical models simulate the response of the cavern boundaries, adjacent strata, and overburden (Peng, 2020; Van Smeek, 2015). Such models must take into account a range of

factors including initial geology, exploitation, mechanical behaviour of the rock mass, and hydrogeological parameters (Arson, 2020).

The Finite Element Method (FEM) is widely used in the subsidence modelling of caverns for research purposes, such as proving a new concept or predicting convergence. In this regard, Li et al. (2022) noted its ability to accurately represent complex geometric structures. By partitioning the domain into smaller components, it enables detailed representation of complex shapes such as the caverns and surrounding rock formations (Keilich et al., 2006). The ability of FEM to assign different properties to each element makes it competent to deal with the inherent heterogeneity of geological materials, thereby allowing a more credible simulation of rock behaviour. FEM's methodology of solving the governing equations for each element, while taking into account interactions with neighbouring elements, ensures the efficiency of the numerical model, which depends largely on the accuracy with which physical phenomena are expressed mathematically (Cremonesi, 2020). To ensure model accuracy, it is crucial to incorporate the stress-strain relationship of rocks under varying loading conditions, and their time-dependent deformation, failure criteria, etc. These requirements emphasise the need for an accurate representation of material behaviour, which is the role of the constitutive model (Arson, 2020).

Constitutive models mathematically characterise the strain-stress relationship under different conditions (Stewart, 2007). The constitutive model must take into account the mechanical behaviour of the rock, recognising complexities such as non-linear elasticity, plasticity and damage. However, the selection or development of an appropriate constitutive model presents significant challenges. This is mainly due to the high heterogeneity and anisotropic behaviour of natural materials such as rock, where properties differ in different directions (Stewart, 2007). This chapter provides a basic understanding of the constitutive models commonly used in subsidence prediction, to ensure the correct choice of constitutive model, grid size and boundary conditions.

4.2.1 Grid size for subsidence case

In numerical modelling, the grid size determines the spatial resolution and accuracy of a simulation (Cremonesi, 2022). Essentially, grid size refers to the dimensions of cells in the computational mesh. A larger grid size implies greater approximation errors and decreased accuracy (Jurisch, 1990).

When predicting subsidence, a phenomenon influenced by regional geological conditions, consistent grid size is critical. Varying grid sizes can lead to misrepresentation of the subsurface and a skewed stress and strain distribution, resulting in distorted subsidence predictions.

To achieve accurate results (Bi, 2019; Kikuchi, 1987):

- Define a baseline grid size considering prior knowledge, computational constraints, and required detail.

- Simulate using the baseline, recording and analysing the results.

- Increase the grid size incrementally, keeping all other factors constant.

- Compare results across different grid sizes, quantifying the impact using statistical analysis and checking for result convergence.

It is necessary to assess the computational resources required for each grid size and strike a balance between accuracy and computational efficiency. In addition to adjusting the grid size, sensitivity analysis can be performed by varying other model parameters. Finally, whenever possible, the model's results should be validated against experimental or benchmark data. This cross-checking ensures the accuracy of the model, taking into account the grid size. However, in subsidence modelling, data limitations can sometimes prevent thorough validation.

4.2.2   Boundary conditions

The mathematical models used to predict subsidence require the specification of boundary conditions that describe the behaviour at the edges of the area being modelled. Boundary conditions are mathematical constraints used in models to define how the ground and subsurface interact with the surrounding environment at the limits of the study area (Arson, 2020). They represent the behaviour of the subsurface and the earth's surface at these boundaries, which can be vertical (the sides of the model) or horizontal (the top and bottom of the model).

The choice of boundary conditions has a significant effect on the results of subsidence predictions. Boundary conditions can be broadly categorised into the following types (Zeitoun and Wakshal, 2013):

- Fixed or Dirichlet boundary conditions. These conditions fix the displacement at the boundary to a specific value. For example, the surface can be considered fixed (zero displacement) if the depth of interest is much less than the depth to the surface. Fixed boundary

conditions can lead to an underestimation of subsidence, for example, if the actual boundary is not perfectly rigid. They often require additional spatial modelling to minimise the influence of the boundary conditions on the results (Keilich et al., 2006).

- Free or Neumann boundary conditions. These conditions specify the flux or gradient across the boundary. In subsidence models, this could be a condition where there is no shear stress on the boundary. Free boundary conditions can lead to an overestimation of subsidence if the actual boundary is not completely free to move.

- Mixed or Robin boundary conditions. These are a combination of Dirichlet and Neumann boundary conditions and can represent more complex interactions at the boundary.

The choice of appropriate boundary conditions is, therefore, critical and typically requires expert judgement based on the specifics of the case. The influence on the results can be estimated in the same way as for the mesh size.

4.2.3   Constitutive models

Hoek (2016): "In the field of engineering, it is greatly appreciated to have a classification of the rock properties as some measurable numeric value to calculate deformation, although the task of real geologist is more complicated". Rock properties are used to quantify the response of a rock sample to applied stress, a critical element in solving the 'stress - deformation - failure' puzzle.

A stress-strain curve illustrates the response of the material to applied stress (Figure 12), which depends on the material model used (constitutive model). Despite this variability, some properties, such as Poisson's ratio and Young's modulus, are generally observed. These properties are typically obtained from uniaxial unconfined compression tests, where deformation is measured in two perpendicular directions. The deformation parallel to the applied stress indicates the Young's modulus property of the material, while the Poisson ratio is determined as the ratio of the perpendicular deformation to the parallel deformation.

Other parameters and rock properties are influenced by the specific constitutive model used. No single model is superior to others; rather, different models are found to be more suitable for specific tasks.

In the present study, three models are commonly used: the Elastic, Mohr-Coulomb and Hoek-Brown models, which are commonly used in subsidence engineering. Each model

has common and unique characteristics, parameters or criteria that are relevant to the rock or rock mass, which will be further explored in the following discussion.

Elastic, isotropic model

The simplest form of constitutive model is the elastic isotropic model. At the molecular level, when a material undergoes elastic deformation, its crystalline structure undergoes a slight stretching or contraction along the direction of the applied stress (whether in tension or compression). This type of deformation is temporary, meaning that when the stress is removed, the atoms return to their original positions and reconnect in the same way. However, if the stress applied to the material exceeds the Young's modulus, plastic deformation will occur. This type of deformation involves the breaking of bonds with neighbouring atoms and the formation of new bonds. In order to dissipate the energy applied during deformation, plastic deformation occurs through a slip process, which involves the movement of dislocations within the material.

The elastic, isotropic model describes the reversible deformation of the material based on Hooke's law. Certain parameters are required to apply this model:

- Density ρ is a measure of the mass of the material per unit volume. For homogeneous rocks, it is a ratio of total mass to total volume. In heterogeneous materials, the density varies between different regions of the object.

- Young's modulus E is a measure of the elasticity of a material. Specifically, it measures the ability of a material to resist deformation when subjected to tensile or compressive forces. The determination of Young's modulus involves tracing the secant on a stress-strain curve, starting from the point of origin of the stress and extending to a point corresponding to the applied test load. This process is illustrated in Figure 12 (part of the elastic deformation). The numerical value of Young's modulus depends on the maximum stress applied to the material. It is calculated as the ratio of the tensile stress to the axial strain, which represents the proportional deformation experienced by the material. This modulus is commonly used to determine the stiffness of a given material. In simple terms, it quantifies the amount of stress required to produce a unit of deformation in the material.

- Poisson ratio v is a measure of the ratio of lateral to longitudinal strain in a material and is only applicable to elastic deformation. For rocks, values typically range between 0.05 and 0.40. The deformation described by Poisson's ratio is known as volumetric strain and is described by the generalised Hooke's law (Equation 16).

$$\varepsilon_v = \frac{1 - 2v}{E}(\sigma_x + \sigma_y + \sigma_z)$$ (16)

where E is Young's Modulus, σ is the unconfined compressive strength, k is a coefficient used for mixed fractures, which can be derived from various approximations, such as $\sqrt{3/2}$ for a maximum criterion and one for a maximum energy release criterion, and v is Poisson's coefficient.
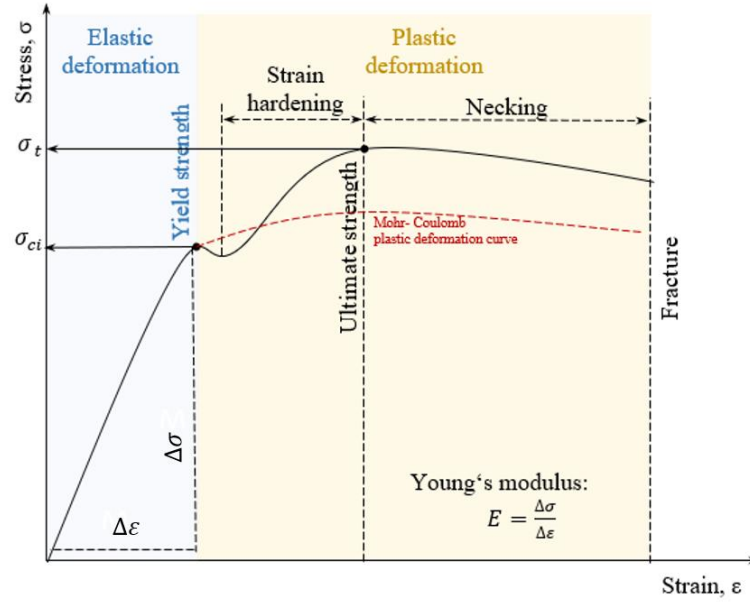
Figure 12. The stress-strain ratio and the processes associated with it.

Mohr-Coulomb model (elastic – perfectly plastic)

The Mohr-Coulomb model is a classical model that describes the strength of a material as a function of the normal stress (σ_n) and the shear stress (τ) acting on a plane (Figure 13). The behaviour of the material is identical to an elastic isotropic model until failure occurs. It is a two-parameter model that is based on the Mohr-Coulomb failure criterion, which states that failure occurs when the shear stress on a plane exceeds a certain value. The value is determined by the normal stress, cohesion and friction coefficients of the material. The Mohr-Coulomb failure envelopes the failure shear stress. This model is recommended for large strains and is relatively simple to use (Stewart, 2007). The model can be described in terms of the principal stress, by Equations 17-20.

$$\sigma_1 = \sigma_c + N_\phi\, \sigma_3 \tag{17}$$

$$N_\phi = \frac{1 + \sin \phi}{1 - \sin \phi} \tag{18}$$

$$\phi = \sin^{-1}(\frac{1 - v}{1 + v}) \tag{19}$$

In accordance with plasticity theory, this envelope is converted into a shear yield function as follows:

$$f^s = \sigma_1 - \sigma_3 N_\phi - 2c\sqrt{N_\phi} \tag{20}$$

The Mohr Coulomb model includes a tension cut-off. The tension yield function is given in Equation 21.

$$f^t = \sigma^t - \sigma_3 \tag{21}$$

For a Mohr-Coulomb material, with both cohesion and friction, the maximum tensile strength may not exceed σ_{max}^t which is given in Equation 22.

$$\sigma_{max}^t = \frac{c}{tan\phi} \tag{22}$$

The tensile strength is set to zero (instantaneous softening) when tensile failure occurs. It should be noted that the Mohr-Coulomb criterion assumes the intermediate principal stress and has no effect upon the failure load. Failure occurs when f ≥ 0; if f < 0, then the material is still within an elastic state. Once the material fails, plastic flow occurs and the total strain increment Δε is the sum of the recoverable elastic and non-recoverable plastic strain components.
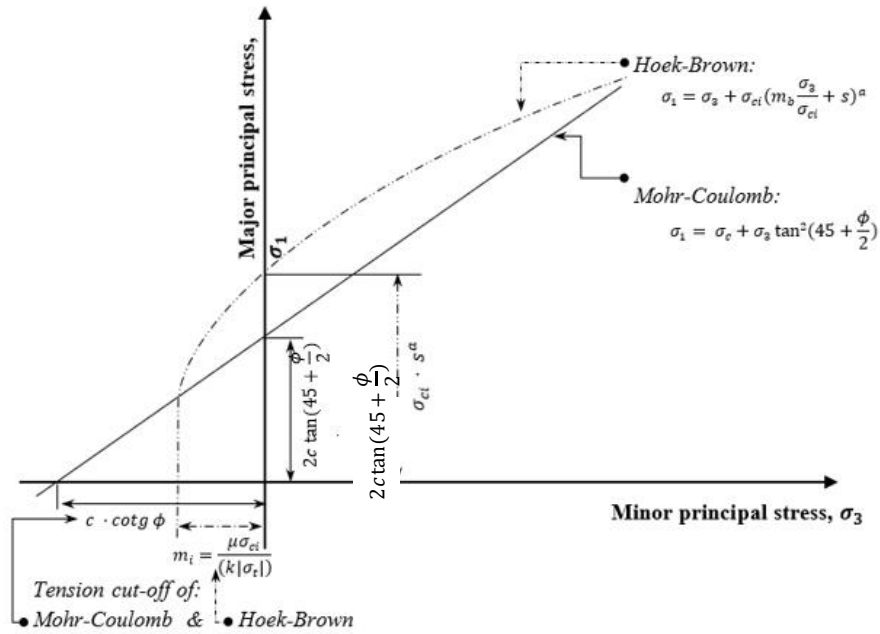
Figure 13. Hoek-Brown and Mohr-Coulomb failure criterion, where σ_1, σ_3 are the major and minor principal stress, respectively; and $m_b, s,$ and a are the rock mass material constants.

The Hoek-Brown model

The Hoek-Brown model is a more advanced model that was developed by geologists for a precise estimation of the behaviour of rock masses under stress. It includes a number of parameters that take into account the properties of the rock masses, such as the joint system, etc. It is a three-parameter model that describes the strength of a material as a function of the normal stress (σ_n), the shear stress (τ), and the rock mass properties (such as the uniaxial compressive strength, the shape of the rock mass, etc.). It is a more consistent model for small strains and more precise to determine the failure criterion for rock masses. The model predicts the strength of a rock mass as a function of the intact rock strength, the joint spacing and the rock mass structure.

- The intact Hoek-Brown failure criterion is based on major and minor principal stresses. The failure criteria are given by the definition of the stress component at failure for an intact rock (Equations 23-24). Dividing the principal minor stress by the compressive strength makes the parameter dimensionless (Stewart, 2007). For a fractured material, the generalised Hoek-Brown failure criterion is defined by Equation 23.

$$\sigma_1' = \sigma_3' + \sigma_{ci} \left(m_i \frac{\sigma_3'}{\sigma_{ci}} + 1 \right) \tag{23}$$

where σ_1' is a major effective principal stress at failure, σ_3' is a minor effective principal stress at failure, σ_{ci} is a uniaxial compressive strength of intact rock determined from a 50 mm diameter specimen of 1:2 diameter to length ratio, and m_i is a constant, depending on the rock type.

$$\sigma_1' = \sigma_3' + \sigma_{ci} \left(m_b \frac{\sigma_3'}{\sigma_{ci}} + s \right)^a \tag{24}$$

where m_b is a material constant m for a case of broken material under conditions of disturbance of the jointed rock mass, s is an exponential function of rock mass conditions (provided in Equation 18), and a is an exponent linked to the geological strength index (GSI), ranging from 0.5 for intact rock (GSI = 100) to 0.62 for GSI = 5. All of these parameters belong to the rock mass:

- The uniaxial compressive strength σ_{ci} is a measurable strength parameter, defined by the maximum compressive stress applied to a cylindrical specimen before failure. It was chosen according to its availability in the rock mechanics literature (Hoek and Brown, 1980a). It is either obtained from uniaxial compression tests or, where cores of suitable size for compression testing were not available, calculated using correlations from point load test results.

- The intact material constant m_i depends on fracture initiation and propagation and determines the curvature of the Hoek-Brown failure envelope. The constant reflects the mineral composition, grain packing pattern, nature of the cementing matrix, degree of inter-particle interlock, grain size and angularity (Hoek and Brown, 1980a, 1980b). Variability in the factor results in variation in the material constant m_i. Table 4 gives the material constant for intact rock when $\sigma_1 = \sigma_3 = \sigma_t$. The ratio can vary widely, so it is recommended that m_i be used as an empirical curve fitting parameter (Hoek and Brown, 1980a). The effect of increasing the intact material constant m_i on intact Hoek-Brown envelopes is shown in Figure 14.

$$m_i = -\frac{\sigma_{ci}}{\sigma_t} \qquad (25)$$

where σ_t is a tension strength and σ_{ci} is a uniaxial compressive strength.
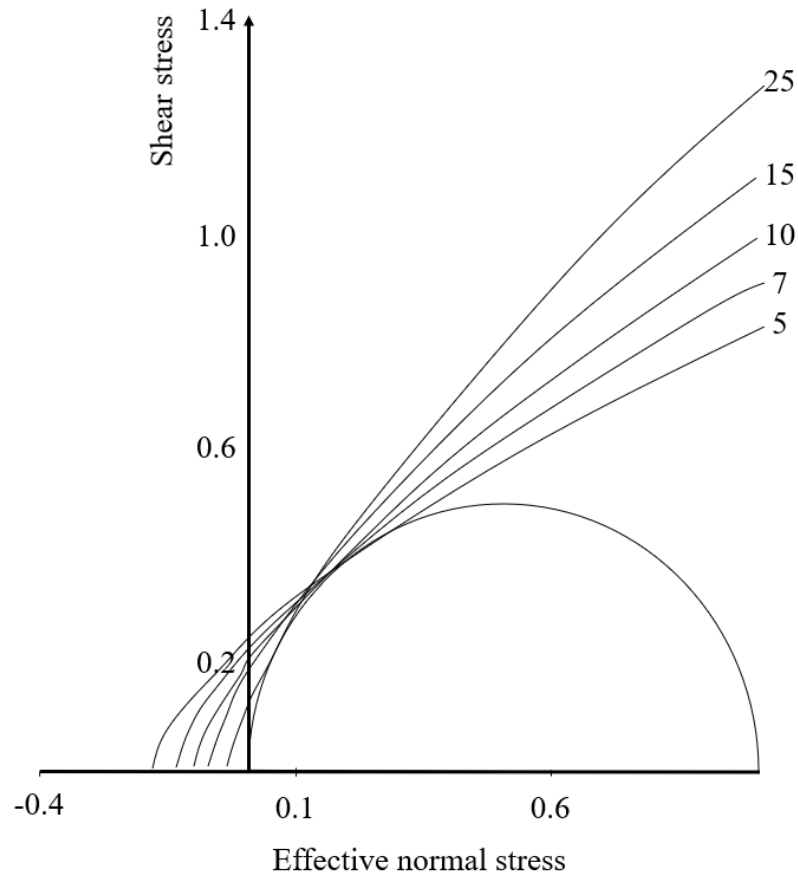
Figure 14. Effect of increasing m_i on intact Hoek-Brown envelopes (adapted from Stewart (2007)).

Table 4. Values of the constant m_i for intact rock, by rock group (adopted from Stewart (2007)).

Rock Type	Class	Group	Texture			
			Coarse	Medium	Fine	Very fine
Sedimentary	Clastic		Conglomerates Breccias	Sandstones 17 ± 4	Siltstones 7±2 Greywackes 18±3	Claystones 4±2 Shales 6±2 Marls 7±2
Sedimentary	Non-Clastic	Carbonates	Crystalline Limestone 12±3	Sparitic Limestones 10±2	Micritic Limestones 9±2	Dolomites 9±3
Sedimentary	Non-Clastic	Evaporites		Gypsum 8±2	Anhydrite 12±2	
Sedimentary	Non-Clastic	Organic				Chalk 7±2
Metamorphic	Non-Foliated		Marble 9±3	Hornfels 19 ± 4 Metasandstone 19±3	Quarzites 20±3	
Metamorphic	Slightly Foliated		Migmatite 29 ± 3	Amphibolites 26 ± 6	Gneiss 28±5	
Metamorphic	Foliated **			Schists 12±3	Phyllites 7±3	Slates 7±4
Igneous	Plutonic	Light	Granite 32±3 Granodiorite 29±3	Dolerite 16±5		
Igneous	Plutonic	Dark	Gabbro 27±3 Norite 20±5	Dolerite 16 ± 5		
Igneous	Hypabyssal		Porphyries 20±5		Diabase 15±5	Peridotite 25 ± 5
Igneous	Volcanic	Lava		Rhyolite 25 ± 5 Andesite 25±5	Dacite 25±3 Basalt 25±5	
Igneous	Volcanic	Pyroclastic	Agglomerate 19 ± 3	Breccia 19±5	Tuff 13 ± 5	

- The Hoek-Brown exponent *a* does not correspond to any physical characteristic of the rock mass. "The justification for choosing this particular criterion over the numerous alternatives lies in the adequacy of its predictions of observed rock fracture behaviour, and the convenience of its application to a range of typical engineering problems"

(Hoek, 1983). For intact rock, it is equal to 0.5, according to the experimental data fitting (Stewart, 2007).

- The Hoek-Brown rock mass failure criterion. The criteria for rock masses according to their structure and destruction differ from the data for intact rock. To predict the strength of rock masses, Hoek et al. (2002) developed new parameters: m_b, s and a (Equations 26–28). m_b is a constant for a fractured rock or broken material, developed from the m_i constant (for intact rock) due to the condition and disturbance of the jointed rock mass.

$$m_b = m_i \, exp \left(\frac{GSI - 100}{28 - 14D} \right) \tag{26}$$

$$s = \, exp \left(\frac{GSI - 100}{9 - 3D} \right) \tag{27}$$

$$a = \frac{1}{2} + \frac{1}{6} (e^{-\frac{GSI}{15}} - e^{-20/3}) \tag{28}$$

where GSI = Geological Strength Index (Hoek and Marinos, 2000), and D is the disturbance factor (0 < D < 1), a parameter which quantifies the effect of disturbance on the rock mass (e.g. blasting, stress relaxation, etc.) (Hoek et al., 2002). If the disturbance is minimal, then D equals 0, otherwise poor quality of blasting provides a D equal to 0.8.

- The Geological Strength Index (GSI) is an index that quantifies the effect of block structure and defects on rock mass strength. GSI data was published by Marinos and Hoek (2001). In the case of heterogeneous rock masses, an extension was published by Marinos and Hoek in 2001, but it does not play a role in this research.

4.3 Validation

The main aim of the validation process is to assess the reliability and accuracy of theoretical results by comparing them with empirical data. This comparison requires, on the one hand, empirical data of known accuracy to serve as a benchmark for evaluating theoretical predictions and, on the other hand, a mathematically integrated hypothesis capable of generating predictions.

In the context of this thesis, patterns of asymmetry and shape deviation are expected to appear in the stress conditions. Thus, successful validation will be an improvement of the prediction results made on the basis of the features adopted in this model, in comparison to the basic solution. To compare the results, statistical tools are used in the comparative aspect of validation, to quantify the degree of agreement between the theoretical predictions and the

empirical data. This statistical analysis provides an objective and quantifiable measure of the accuracy of the model.

The basis for each step of the validation process, from measurement to statistical analysis, is discussed in detail in this subsection.

4.3.1 Observation methods

This subchapter provides a description of differential geodetic observation methods to highlight their applicability for subsidence monitoring. This description covers the specific details of each observation method, along with their potential sources of error and types of measurements. Finally, the observation methods are summarised in Table 5, to illustrate the differences between the methods in related aspects such as cost, precision, etc.

- **Levelling** measures the height difference between two distinct points. Unlike some methods that measure distances or angles, levelling is unique to capturing height disparities. This method has, historically, been a classic choice for subsidence measurements due to its exceptional accuracy.

The precision of levelling can be susceptible to cumulative errors. To mitigate this, the application of geodetic network optimisation is recommended to enhance estimation accuracy (Cross and Thapa, 1979; Yetkin et al., 2009). Grafarend (1974) identified four distinct design challenges related to the geodetic network: relative reference systems, network configurations, observation weights, and the incorporation of supplementary observations to refine an existing network.

The levelling technique boasts significant precision, often reaching accuracy levels up to a millimetre. The approach to solving design issues across different orders typically employs an error minimisation method (Díaz-Fernández et. al., 2010; Alizadeh-Khameneh, 2015). While levelling is precise, it lacks support for ongoing monitoring (Zhang et al., 2019). Large-scale projects that require high-frequency measurements can render the method costly. Despite its high accuracy, levelling does not offer measurements of distances or angles.

- **Tacheometry**, on the other hand, measures horizontal and vertical relative positions as angles and distances. In terms of precision, tacheometry can achieve a high degree of accuracy, although it may not reach the precision of levelling (Ghilani and Wolf, 2012). However, tacheometry has the advantage of being more efficient for large projects, as measurements can be made for many points from the same station. Laser scanning uses the

same base to produce a point cloud, which increases the density of the measurements, but also the cost of the instrument. This method is not usually employed for subsidence measurements.

- **Photogrammetry** is another method used to create a 3-dimensional cloud of points with a high degree of accuracy. This technique uses images taken from different positions to define the coordinates of points.

The process starts with high-resolution cameras moving over the area of interest and taking a series of overlapping images. Once these images have been captured, they are processed using specialised software to perform a number of tasks, including matching points between images, adjusting the position of the camera and generating a dense cloud of points. The end result of this process is a high-resolution model of the terrain, which can take the form of a digital surface model or a digital elevation model.

The accuracy of photogrammetry for a specific case study can reach up to 28 mm (in planimetric) and 24 mm (in a vertical direction) by a combination of terrestrial and aerial imagery (Petschko et al., 2022). The overall accuracy will depend on the quality and resolution of the images, the accuracy of the camera calibration and the quality of the image matching and modelling processes. The smaller the pixel sizes, the more detailed models and higher quality point matching can be achieved. The speed of the drone can also affect the quality of the images, thus impacting the results of the photogrammetry process. Despite its challenges, careful photogrammetry can yield highly accurate terrain models (Ghilani and Wolf, 2012). However, the minimal height variation during drone photography reduces the precision in height estimation.

- **Global Navigation Satellite Systems** (GNSS) are used to measure the coordinates of a surface point by transmitting signals from satellites orbiting the Earth to receivers on the ground. The receiver calculates its distance from each satellite by measuring the time it takes for the signal to travel from the satellite to the receiver. Thus, the effectiveness of GNSS depends on environmental conditions and lack of interference from obstructions (Huang et al., 2023). With signals from at least four satellites, the receiver can determine its precise three-dimensional position. However, due to the geometry of the satellite configurations, GNSS systems inherently provide better horizontal than vertical accuracy. This is why they are not applicable for subsidence measurements but are used for real-time landslide monitoring.

Two key positioning methods of GNSS are used: Real Time Kinematic Positioning (RTK) and Precise Point Positioning (PPP).

RTK provides high-precision positioning, often down to the centimetre level (Petschko et al., 2022), by using a reference station or base station established at a known location (Eyo et al., 2014). This base station communicates with mobile receivers, also known

as rovers, which provide real-time corrections to improve the accuracy of position estimates. However, the accuracy of RTK decreases with increasing distance from the base station, which limits the measurement area. The cost of setting up and maintaining a reference station and high accuracy GNSS receivers makes this method more expensive than PPP.

PPP is generally less expensive and does not require a reference station. Instead, it uses external data, often referred to as 'correction data' or 'external products', which include precise satellite orbit and clock data, atmospheric delay models and other factors (Zhang et al., 2017). These data are used to correct for various sources of error in GNSS measurements. PPP typically has a longer processing time for each point (convergence time). This time is used to stabilise and reach full accuracy of measurements.

- **Interferometric Synthetic Aperture Radar** (InSAR) is a remote sensing technique using satellites, which can measure deformation over large areas with high accuracy, by analysing radar images (Crosetto et al., 2016; Bitelli et al., 2015; Zhang et al., 2023). This involves taking two or more radar images of the same location from a satellite at different times. Each pixel in a SAR image contains amplitude and phase information. The amplitude represents the strength of the radar reflection from the ground. The phase is related to the distance the radar signal travelled from the satellite to the ground and back. The phase difference values in the interferogram are initially 'wrapped' in the range $-\pi$ to π radians. This wrapped phase is used to calculate the absolute difference in distance between the two SAR acquisitions. This difference is used to produce a type of map known as an interferogram, which estimates the ground movement (Goldstein and Zebker, 1987). InSAR requires a series of SAR images, a satellite in a stable orbit, and precise image co-registration.

Advanced InSAR techniques (like SBAS - Small Baseline Subset) and PSI (Persistent Scatterer Interferometry) have been developed to address the limitations of conventional InSAR. SBAS aims to reduce the atmospheric and temporal decorrelation by using a subset of image pairs with small temporal and perpendicular baselines (Bru et al., 2022). On the other hand, PSI focuses on the analysis of individual scatterers that remain coherent over longer time periods. PSI allows for more accurate deformation measurements in urban or infrastructure environments, where there are many stable reflective objects, by analysing these persistent scatterers throughout a stack of SAR images (Colesanti et al., 2005).

Despite these advancements, InSAR still faces challenges. Error sources can include atmospheric delays, orbital errors, temporal decorrelation (changes in the ground surface between image acquisitions), and noise in the radar signal. Moreover, pixel size impacts the quality of InSAR measurements. While a smaller pixel size (higher spatial resolution) allows for more detailed ground surface information, it also averages the radar signal over fewer

reflective objects, or ground scatterers, which can increase noise and lead to decorrelation in the InSAR measurements (Simons and Rosen, 2015).

Conclusions

In summary, the selection of an appropriate geodetic observation method for subsidence monitoring depends on the specific requirements of the project, including precision, scale, cost and frequency of observations. Traditional methods such as levelling offer high precision, but are limited by the scale and time density of the project's measurements. Photogrammetry, using drones and high-resolution imagery, provides detailed three-dimensional terrain models at moderate cost, but the accuracy is lower. While InSAR allows for continuous monitoring of deformation over large areas, it is more expensive than other methods. Therefore, the optimal method depends on the balance between the project requirements and the advantages and limitations of each method.

Table 5. An overview of the measurement types and their specifics

| Method	Measurement types	Precision, mm		Space density	High error sources	Costs as the service
		Δh	Δd			
Levelling	Relative heights	~1	–	+	Performing and network design	+++
Tacheometry	Distances, angles	~3-5	~5	+		+++
GNSS	Geographic coordinates	~30	~5	+	Atmosphere and multipath	+++
Photogrammetry	Distances	~50	~20	+++	Image quality and incorrect matching	++
InSAR	Vertical and horizontal changes	~1	~2	+++	Atmosphere and temporal decorrelation	+

4.3.2 Parameter estimation

The ultimate goal of parameter estimation is to find the parameter values that yield a solution that is closest to the real data, thus ensuring the fidelity of the model (Nocedal and Wright, 2006).

The L2 or L1 norm is commonly used to quantify the closeness between the estimated values and the observed data (Hastie et al., 2009). The L2 norm measures the squared difference between the estimated values and the observed data, while the L1 norm represents

the absolute difference. These norms serve as objective measures to assess the quality of parameter estimates and guide the optimisation process.

Different methods are used to find the optimal parameters, taking into account factors such as the approach chosen, the characteristics of the input data and the number of parameters involved. The nature of the problem determines the specific function and parameter set to be estimated (González-Rodríguez et al., 2007), as well as the approach used (forward or inverse modelling, as shown in Figure 15) and the type of method used (global or local search).
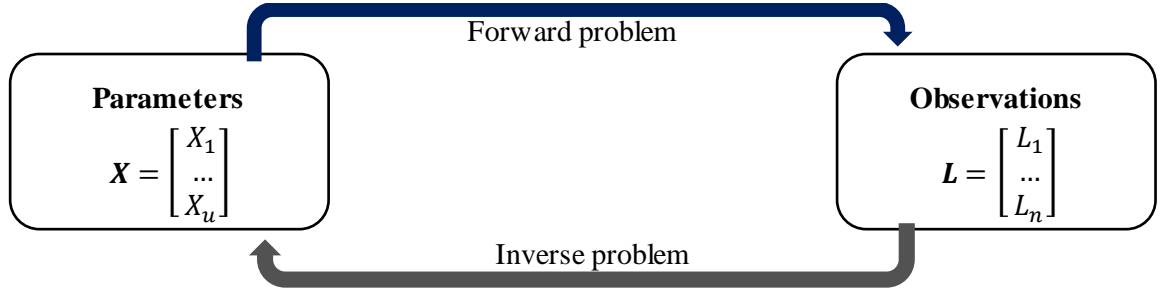
Figure 15. Parameter estimations methods.

In forward modelling, the known input parameters are used to predict the output response of the system, allowing simulation or prediction. Conversely, inverse modelling estimates the unknown input parameters based on observed output responses. This inverse approach is particularly useful when the underlying system is complex or when the input parameters are difficult to measure directly.

The estimation of the ratio between the number of observations (n) and the number of unknown parameters (u) approaches limits:

- when $n > u$, the problem is over-determined and can be resolved by adjusting the observation method.
- when $n = u$, the problem is uniquely defined and can be solved by finding a solution to an equation system.
- when $n < u$, the problem is under-identified and the use of a Bayesian approach is required.

In subsidence prediction cases, where there are usually less than 10 parameters and more than 100 measurements, the adaptation of the observation method is the appropriate approach for parameter estimation.

4.3.3 Global parameter estimation

Global parameter estimators are used in the case of multiple local optima. The complexity of the task increases exponentially with the number of parameters and their possible values. Different algorithms can be used to identify the global optimum:

- The basic concept of **basin hopping** is to move the optimisation process away from local minima by taking large, random steps in the parameter space. The algorithm essentially 'hops' from one 'basin' to another, hence its name. Each basin corresponds to a local minimum in the solution space. After each step, the new local minimum is accepted or rejected based on an acceptance criterion, typically the Metropolis criterion from statistical mechanics, which accepts worse solutions with a probability that decreases as the new solution becomes worse (Wales and Doye, 1977) (Figure 16 (a)).

- **Evolutionary algorithms**, such as genetic algorithms, use combinations of parameters for evaluation. The combinations that produce the best solutions are selected and certain parameters are swapped, leading to the generation of new solutions by crossing over from the first generation. To avoid losing superior solutions, the best pair is kept in the new generation. Next, a mutation phase is implemented in which a single parameter is randomly changed. This generation is taken as the starting point and the algorithm is iterated until the desired solution is found or the iteration limit is reached (Slowik and Kwasnicka, 2020) (Figure 16 (b)). **Simulated annealing** is a probabilistic method for finding a globally optimal solution. The algorithm decides whether to accept or reject a solution based on the probability of that solution, which is defined by an exponential function of the difference between two solutions (Kirkpatrick et al., 1983). If the second solution is better, the probability approaches one; otherwise, a lower probability is estimated. This is then compared to the exception probability of the solution. While this method does not require initial parameters, it does require defined parameter bounds. The method is run until a specified number of iterations have been completed (Figure 16 (c)).
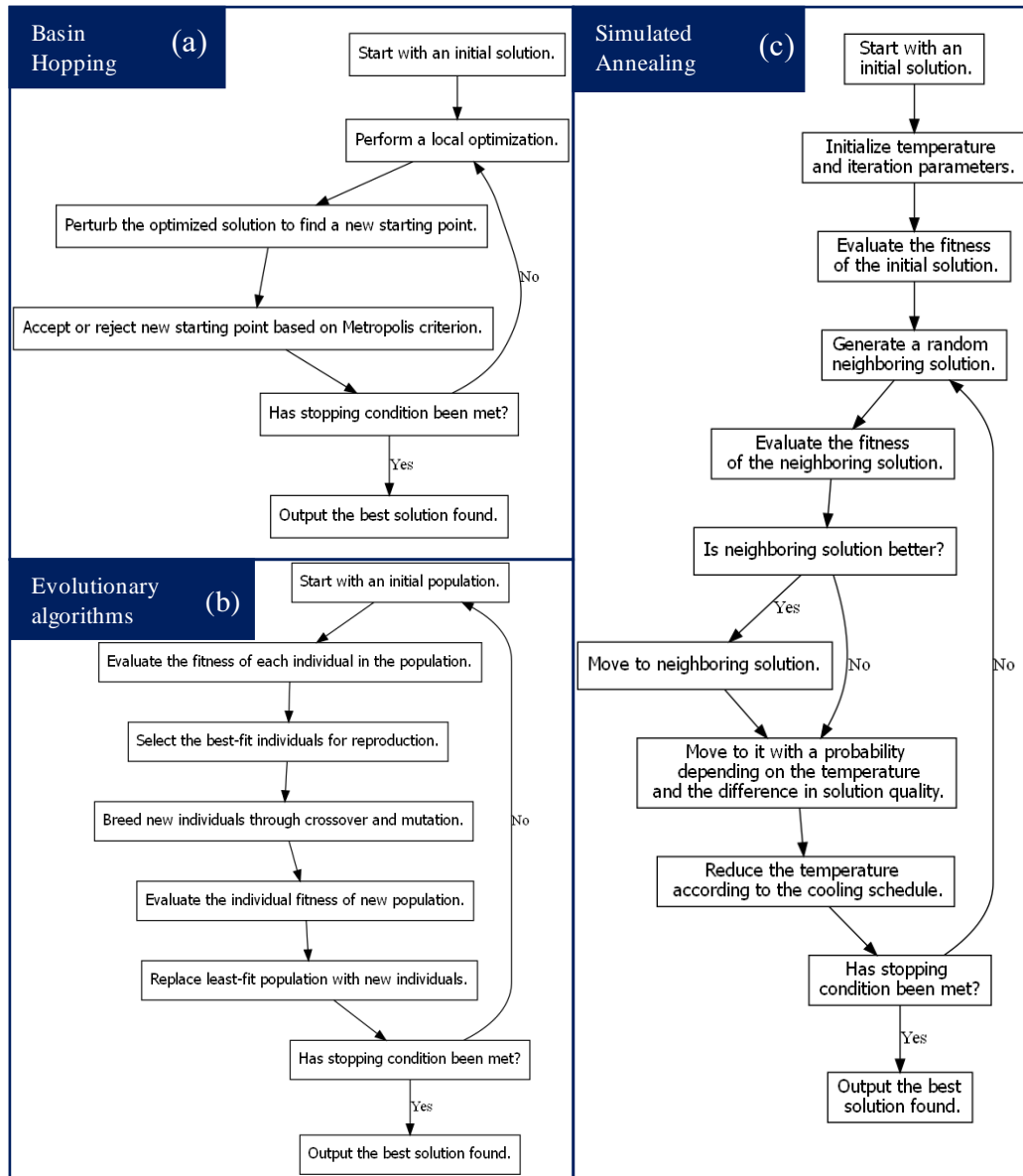
Figure 16. Algorithms for global optima searching.

4.3.4   Local parameter estimation

Local optimisation focuses on finding optimal solutions in a localised region of parameter space. However, the goal is to find the most optimal solution within a defined neighbourhood of parameter values, rather than in the global parameter space. This can be more computationally efficient in scenarios where the global solution is not of paramount importance, or where the local region around the global solution is relatively smooth and well

behaved. Some important local optimisation algorithms include gradient descent, Newton's method and quasi-Newton's method (Figure 17).
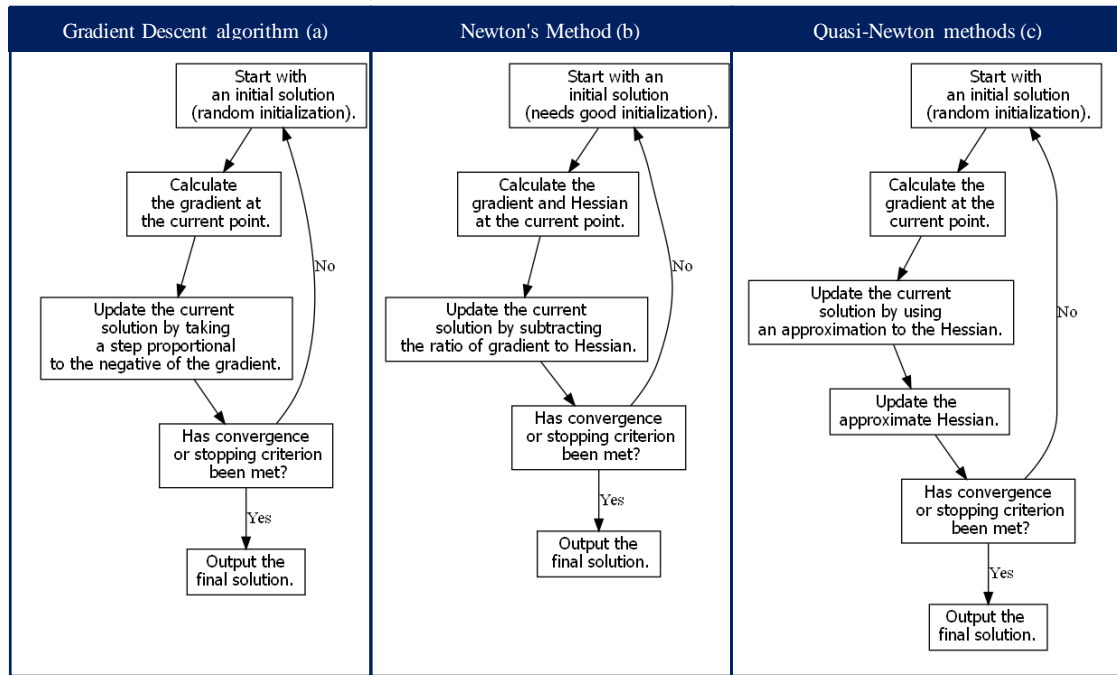
Figure 17. Algorithms for finding a local optimum.

The description of the algorithm presented in Figure 17 is provided below:

• **The gradient descent algorithm** iteratively adjusts the parameters to move along the direction of steepest descent, which is defined by the negative gradient. The parameters are updated until a stop condition is met, such as when the improvement in function value is less than a predefined threshold. The learning rate, which determines the size of each step, plays a critical role in the performance of the algorithm (Park and Sandberg, 1991; Nocedal and Wright, 2006).

• **Newton's method**, also known as the Newton-Raphson method, is an iterative optimisation algorithm that uses the concept of quadratic approximation to the objective function to find its minimum. It uses both first and second derivative (Hessian) information to guide the search for a minimum. The inclusion of second order information allows Newton's Method to converge faster than Gradient Descent when near the minimum. However, this method can be computationally expensive and is not guaranteed to converge for non-convex functions (Ryaben'kii and Tsynkov, 2006).

• **Quasi-Newton methods**, such as the Broyden-Fletcher-Goldfarb-Shanno (BFGS) method, are optimisation algorithms that build up an approximation of the Hessian, using gradient evaluations. They can converge faster than gradient descent and are less

computationally expensive than Newton's Method, as they do not require the computation and inversion of the Hessian at each and every iteration. These methods have been successfully applied to various optimisation problems (Nocedal and Wright, 2006).

4.3.5 Quality measures for result valuation and validation

Comparison of the results means that the analysis of the residual distribution provides an insight into whether the model has systematically missed any trends. Residuals should ideally be independent and identically distributed. Plotting real (observed) against modelled (predicted) values provides a visual means to evaluate the model's performance. The points should ideally fall along a 45-degree line, indicating perfect prediction. Deviations from this line suggest the residuals from the predictions. To ensure that residuals are normally distributed, the Quantile-Quantile (QQ) Plot can be used (Makkonen, 2008). This plot compares the distribution of the prediction errors to the standard normal distribution. If the points in the QQ plot fall along a straight line, it suggests that the errors are normally distributed.

The numerical evaluation of the results considers some commonly used metrics (Wackerly et al., 2008):

- The MSE is a metric that measures the average squared difference between the predicted values and the actual values. It provides a measure of how well the model fits the data. MSE is calculated by taking the average of the squared differences between each predicted value and its corresponding actual value. A model with a lower MSE is generally preferred. The equation for calculating MSE is:

$$MSE = \frac{1}{n} \Sigma \left(data_{actual} - data_{predicted} \right)^2 \qquad (29)$$

where n is the number of data points, $data_{actual}$ represents the actual values, and $data_{predicted}$ represents the predicted values.

- The MAE is a metric that measures the average absolute difference between the predicted values and the actual values. It provides a measure of the average magnitude of the errors made by the model. MAE is calculated by taking the average of the absolute differences between each predicted value and its corresponding actual value. Like MSE, a lower MAE is desirable. The equation for calculating MAE is:

$$MAE = \frac{1}{n} \Sigma |data_{actual} - data_{predicted}| \qquad (30)$$

where n is the number of data points, $data_{actual}$ represents the actual values, and $data_{predicted}$ represents the predicted values.

- The STD is a measure of the dispersion or spread of a dataset. It quantifies the average amount of variation or deviation from the mean. STD is calculated by taking the square root of the average of the squared differences between each data point and the mean of the dataset. A lower STD suggests more consistency in the errors, which is generally a good thing. The equation for STD is:

$$STD = \sqrt{\frac{1}{n-1} \Sigma(data - mean)^2} \tag{31}$$

- The R2 score, also known as the coefficient of determination, is a statistical measure that indicates the proportion of the variance in the dependent variable that is predictable from the independent variable(s). It is commonly used to evaluate the performance of regression models. In simpler terms, the R2 score represents the proportion of the total variation in the dependent variable that is explained by the independent variable(s). It ranges from 0 to 1, with 1 indicating a perfect fit where the model explains all the variability, and 0 indicating that the model does not explain any variability. The R2 score is calculated using the following equation:

$$R2 = 1 - \left(\frac{SSR}{SST}\right) \tag{32}$$

where SSR (Sum of Squared Residuals) is the sum of the squared differences between the predicted values and the actual values, and SST (Total Sum of Squares) is the sum of the squared differences between the actual values and the mean of the dependent variable.

Evaluating the results of these analyses requires considering all the metrics and plots together. A model that performs well on one metric but poorly on others might not be the best choice. It is essential to consider the nature of the data, as well as the specific requirements of the analysis.

Not only does the accuracy of the model play a role but also its complexity. To evaluate that, the Akaike Information Criterion (AIC) and Bayesian Information Criterion (BIC) are used (Stoica and Selen, 2004). Both are used for model selection among a finite set of models, the model with the lowest AIC or BIC being preferred.

AIC is an estimator of the relative quality of statistical models for a given set of data. Given a collection of models for the data, AIC estimates the quality of each model, relative to each of the other models. The lower the AIC value, the better the model. The AIC is generally used for model selection, where several competing models are in consideration and is calculated as follows:

$$AIC = -2 \cdot log(Likelyhood) + 2k \tag{33}$$

where k is the number of parameters in the model and n is the number of data points.

BIC is a criterion for model selection among a finite set of models. It is based on the likelihood function and is derived from Bayesian probability. The BIC is similar to the AIC but includes a stronger penalty for models with more parameters. BIC is calculated as follows:

$$BIC = -2 \cdot log(Likelyhood) + k \cdot log(n) \tag{34}$$

where n is the number of observations and k is the number of parameters in the model.

The primary goal of both AIC and BIC is to penalise complex models, i.e. models with more parameters. This is due to the principle of parsimony, which suggests that simpler models should be preferred, unless the increased complexity provides a significant improvement in fit.

5   Methodology

Based on the gaps identified in the previous literature review and state of the art analysis, this study aims to assess the impact of stress conditions on subsidence profiles. Specifically, it aims to understand how stress conditions affect the subsidence profile. According to the objectives of this research, the following tasks have to be solved:

1. **Preliminary Estimation and Requirements Setting:** Conduct a pre-estimation using a simplified model to test the hypothesis and establish experimental requirements.

2. **Design of the Main Experiment**:
   a. **Input Data:** Specifying the necessary data to be used in the experiment.
   b. **Numerical model and simplifications:** Developing a detailed numerical model and identifying any required simplifications for the purpose of the experiment.

3. **Numerical investigation:** Establish the relationship between subsidence parameters and rock mass properties.

4. **Developing a new functional model:** Identification of the features should be covered and implemented in the model.

5. **Validation of results against real data:** Validate findings by comparing them with real-world data.

This study follows the workflow represented in Figure 18, which outlines each step and its corresponding goal in a linear progression. The process begins with the estimation of the problem and its foundational aspects, to determine the appropriate tools and strategies for the proposed solution (steps 1-3). Subsequently, numerical modelling is designed to ensure reliable results from the experiments (steps 4-6). The collected numerical results are then analysed using various methods, ranging from visual investigation to statistical interpretation (step 7). The identified subsidence patterns are mathematically integrated into a predictive model, which is then tested to assess whether these features enhance the model's predictive quality compared to baseline models that do not account for these characteristics (step 8). Finally, a real-world testing field is selected for the validation phase, which involves integrating the model and comparing the results (in the conclusion).

1. Literature review and gap identification:

Comprehensive review of existing literature to identify knowledge gaps in the field of subsidence processes.

6. Conducting the numerical experiment:

Implementation of the developed numerical model to conduct a more detailed experiment.

7. Statistical analysis of results:

Analysis and interpretation of the experimental data, with a focus on statistical representation.

2. Focused exploration of identified gaps:

Detailed investigation into the identified areas of knowledge gaps.

5. Development of a numerical model:

Design and development of a comprehensive numerical model for detailed simulation.

8. Selection of an appropriate subsidence prediction method for validation:

Choosing a suitable method from existing subsidence prediction models to validate the experimental results.

3. Formulation of hypothesis and experiment requirements:

Development of a research hypothesis based on the identified gaps and setting requirements for the subsequent experiment.

4. Preliminary numerical simulation:

Conducting a simplified numerical simulation to generally validate the proposed hypothesis.

9. Validation of results in a real field study:

Application and validation of the results in a real-world subsidence field to verify the predictive power of the model.

Figure 18. Investigation Flowchart.

6 Numerical investigation

6.1 Preliminary investigation

The aim of this section is to investigate the hypothesis that stress conditions have a fundamental effect on subsidence profiles. In the preliminary investigations, the symmetric stress conditions are used as the basis for our assessments. The result of this investigation will form the cornerstone for future investigations, serving as a basis for exploring theoretical implications, setting stress condition limits, justifying its incremental steps and evaluating the significance of the expected patterns for subsidence engineering.

6.1.1 Method

Numerical modelling (implemented via the FLAC 3D software) was selected as the primary method for this study, to limit external influences and investigate within a controlled environment. Such an approach is requisite, given that the uncertainties associated with real-world input parameters may exceed the tolerable limits of output error.

There are inherent limitations associated with numerical simulations that should be acknowledged. Investigations relying on numerical experiments must consider the approximations within the numerical methods (Helmut, 2008). Even though numerical solutions are regarded as highly reliable, the results remain susceptible to the researcher's decisions and the simplifications and interpretations embedded in the material model (Gargani et al., 2006). These limitations, primarily related to the numerical method itself, are beyond the scope of this research, other approximations of induced errors are discussed further.

6.1.2 Choice of constitutive model

The essence of any constitutive model rests on the interdependence of stress and strain. Under standard conditions in rock mechanics, the form of this function can be divided into elastic and plastic sections. For initial investigation purposes, classically used in mining

tasks, the Mohr-Coulomb constitutive model is deemed suitable owing to its simplicity and time-tested results, notwithstanding its inability to adequately represent the cracking process and relative stress distribution (Lekhnitskii, 1981).

The 'Mohr-Coulomb Tension' constitutive model, as incorporated in the FLAC 3D software, was selected for this study, due to its proficiency in addressing tensile failure and considering the effects of tensile crack closure.

6.1.3   Model and input data

The choice of the fixed boundary conditions defines the geometrical ratios of the model: the relative parameters of depth, width, and height were set at a ratio of ~40:10:1 for the hypothetical experiment. The influence of these boundary conditions has been found to be negligible (less than 0.1%), as established by increasing the distance to the borders and comparing the results (the detail is described in Chapter 4).

The input parameters for the experiment are shown in Table 6. They are representative parameters for a hypothetical sedimentary rock type. Tectonic conditions were implemented in the form of a stress ratio σ_v/σ_h, where σ_v is the vertical stress and σ_h is the horizontal stress. To prevent overestimation of the stress contribution to subsidence troughs, due to extreme and infrequent values, the stress ratio was limited to 0.43~1.66, with cases evenly distributed around the case 1 scenario.

Table 6. Rock mass characteristics

Characteristic	Magnitude		Characteristic	Magnitude	
Density	1600	kg/m^3	**Tension**	2000	N/m^2
Bulk	$4 \cdot 10^7$	Pa	**Stiffness-normal**	$4 \cdot 10^8$	N/m
Shear	$3 \cdot 10^7$	Pa	**Stiffness-shear**	$4 \cdot 10^8$	N/m
Cohesion	$1 \cdot 10^{20}$	Pa	**Friction**	30	degree

6.1.4 Preliminary investigation results

The results of modelling subsidence, for the hypothetical case of sedimentary rock under different tectonic conditions, are presented in Figure 19. Figures 20 and 21 show the relative volume of subsidence, maximum subsidence, influence angle, tilt and exploitation coefficient changes due to the applied stress conditions. On the figures, the bars and lines are

labelled 'Case', with a number related to the stress ratio $\frac{\sigma_v}{\sigma_h} \in$ (Case 0.43; 0.71; 1; 1.33; 1.66). In other words, the number after 'Case' is the stress ratio and the results are presented in relation to Case 1.
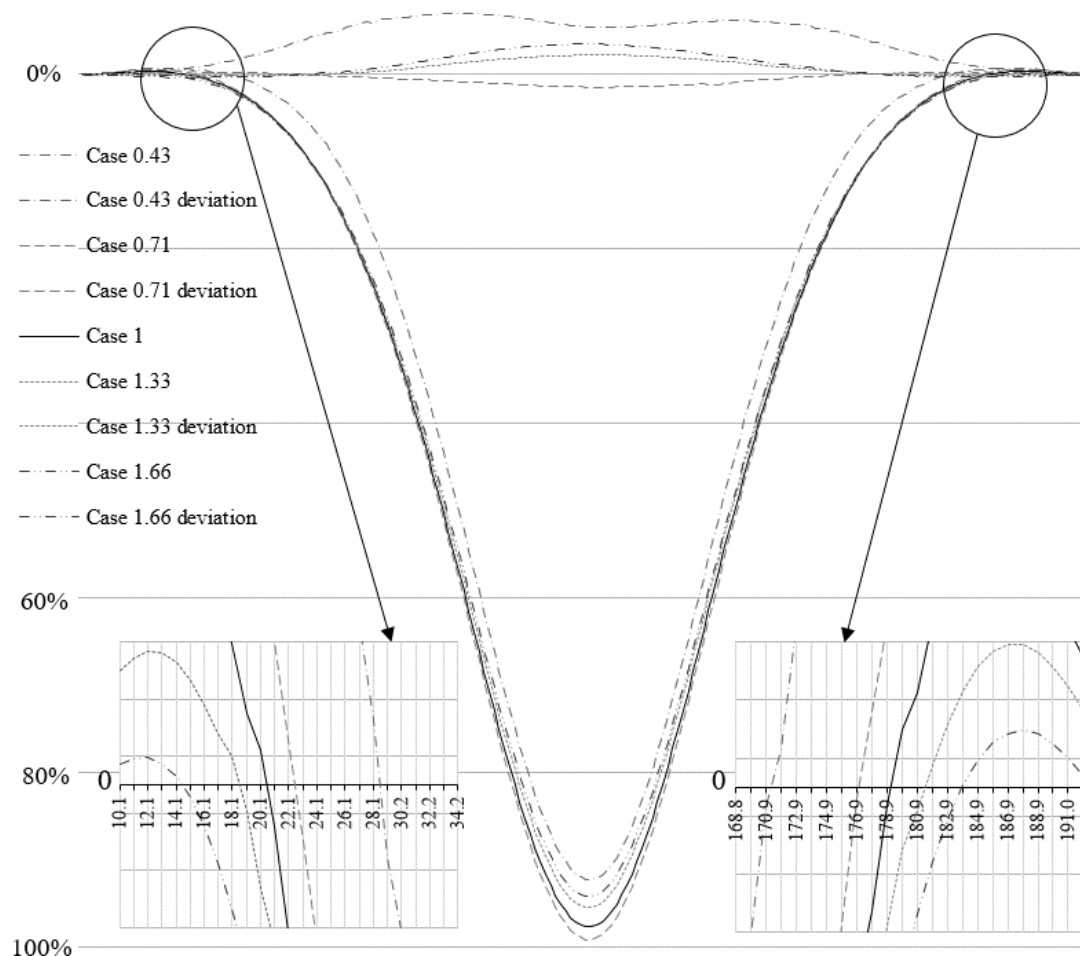
Figure 19. Results of preliminary investigation

	Case 0.43	Case 0.71	Case 1	Case 1.33	Case 1.66
■ Volume of subsidence, %	87,73%	101,17%	100,00%	98,05%	97,00%
▦ Max of subsidence,%	94,48%	101,51%	100,00%	97,77%	96,47%
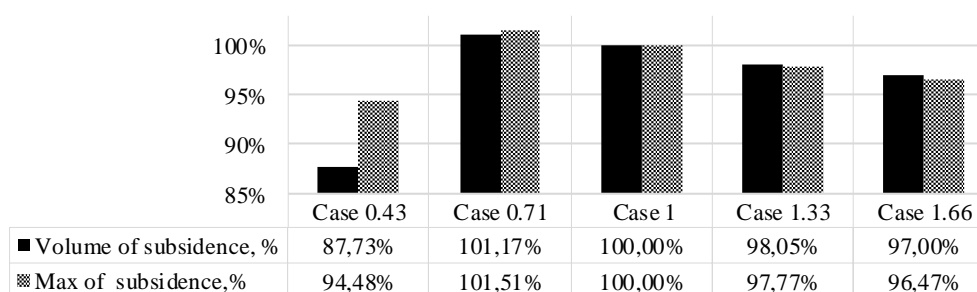
Figure 20. Changes of maximum subsidence and value of subsidence relative to Case 1

	Case 0.43	Case 0.71	Case 1	Case 1.33	Case 1.66
■ Deformation, %	103,3%	104,9%	100,0%	95,6%	93,0%
▫ Tilt, %	101,8%	102,6%	100,0%	98,0%	96,6%
▨ Angle%	109,0%	102,3%	100,0%	97,8%	94,5%
◫ Exploitation coefficient - a, %	88,2%	102,0%	100,0%	98,0%	96,7%
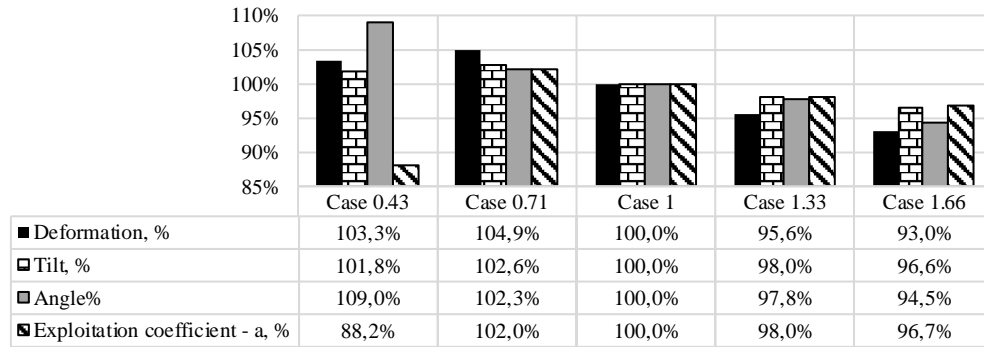
Figure 21. Changes in deformation and tilt for different stress influences.

The results show that all parameters change due to the variability of ratio $\frac{\sigma_v}{\sigma_h}$, up to 8% of the maximum subsidence and 12% of the influence angle.

Generally, an increase in horizontal stress results in a decrease in the radius of the subsidence trough, coupled with an increase in the total volume of subsidence. However, an unexpected deviation is observed when comparing Cases 0.43 and 0.71. This discrepancy prompts a closer examination of the influence angle γ, necessitating a denser distribution of stress conditions.

Less than one percent of the uplifts could be a result of the Mohr-Coulomb constitutive model or the boundary conditions. This suggests the need to employ a more advanced model and flexible boundary conditions.

This initial investigation, although limited to a single sample and assuming a homogeneous geological structure, still provides valuable insights into how the ratio of horizontal to vertical stress affects the situation. The findings underline the importance of stress fields in computing subsidence prediction parameters and demonstrate that tectonic conditions can significantly alter the subsidence profiles expected. As a result, further investigations are warranted, focusing on the effects of non-uniform stress fields as a potential cause for asymmetry. These investigations should be based on a more advanced constitutive model, a wider range of rock properties and flexible boundary conditions.

6.2 Design of the main experiment: non-uniform stress distribution

6.2.1 Constitutive model and input data

The Hoek-Brown model has a more complex stress-strain relationship that takes into account the properties of the rock mass (Buljak and Ranzi, 2021). As a more advanced model, the Mohr-Coulomb model provides a more reliable result at small strains and takes into account the disturbance of the rock mass.

The input parameters for the Hoek-Brown constitutive model consist of the following: Density, ρ; Young modulus, E; Poisson's ratio, v; Uniaxial strength, σ_i; and Rock mass disturbance parameter, m_b.

In order to cover different possible combinations of rock type parameters, data were taken from different sources. To ensure a wide variety of rock types and their properties, the selection included three basic classes: sedimentary, metamorphic and igneous. Sedimentary rock types were given priority due to their prevalence at depths down to 1000 m. In total, 31 different rock properties were used as input data, as shown in Appendix A. These were collected from various sources, including: Mendoza-Chavez et al. (2012); Tunnelling Experts (2013), 'Variation of Intact Rock Properties', accessed in 2021; Britannica (Britannica, n.d.); Kim and Jeon (2019); Shimada et al. (2013); Vyazmensky et al. (2010); Wong et al. (2006); and Meng et al. (2006). The distributions of the classes and their properties are shown in Figure 22.

Another aspect of the input data are the stress conditions. In this case, the stress conditions were applied as boundary conditions and as a distribution of the stress trough rock mass model (Figure 23). The boundary conditions are presented as an equavalent stress around the model, to avoid influencing the stress environment inside the model. The equavalent horizontal stresses are given by Equation 35.

$$\sigma_h = \lambda \cdot \gamma \cdot z, \tag{35}$$

where $\lambda = \frac{v}{1-v}$: v is a Poisson coefficient, z is depth and γ is the weight of the rock mass. The stress distribution is represented in the form of a linear gradient (Equation 36).

$$Sress\ gradient = \frac{\lambda \cdot \gamma \cdot z \cdot n}{2r} \tag{36}$$

where n presents the stress factor and varies between 1-14, to provide average stress ratios from 0.26-3.70, that is justified in the state of the art; r is half the wideof the whole model. Since the size of the model is constant, such a definition is appropriate.

Other strong influences on the results of the numerical modelling are the size of the grid and the size of the model. Both definitions have been checked for their influence on the results, according to the methodology provided in Chapter 4.
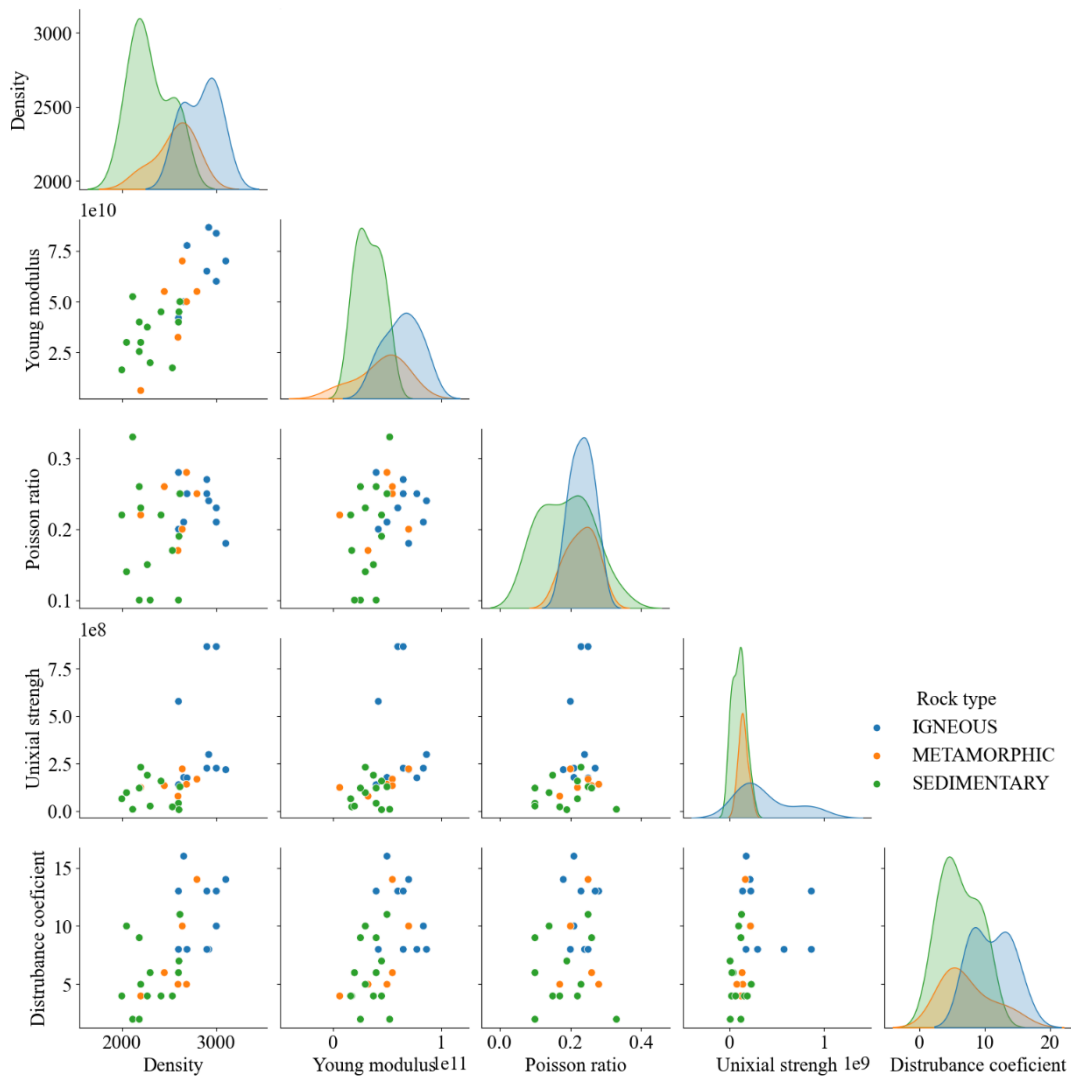
Figure 22. Distribution of the characteristic rock types used in the numerical simulation, divided by class. Green signifies igneous rocks, red signifies metamorphic rocks, and blue signifies sedimentary rocks.

Figure 23 illustrates the boundary condition, the direction of the stress gradient (as mentioned above) and the model proportions used to provide sufficient space to simulate the deflection at the periphery of the simulated subsidence trough. The model is based on the left and right soft boundary conditions. The size is chosen relative to the void dimension to ensure a complete subsidence profile. The reduction in depth is replaced by an equivalent weight at the top. The stress gradient is applied directly to the rock mass. The definition of the stress sides (input and releasing sides) will be used in the results, as a reference to the subsidence trough side of the deflection.

$$\sigma_z = \lambda\gamma(z - h)$$

Energy input side

Energy releasing side

Stress gradient

h

h

$3h$

$\sigma_x = \lambda\gamma z$

$\sigma_x = \lambda\gamma z$

$v_z = 0$
$v_y = 0$
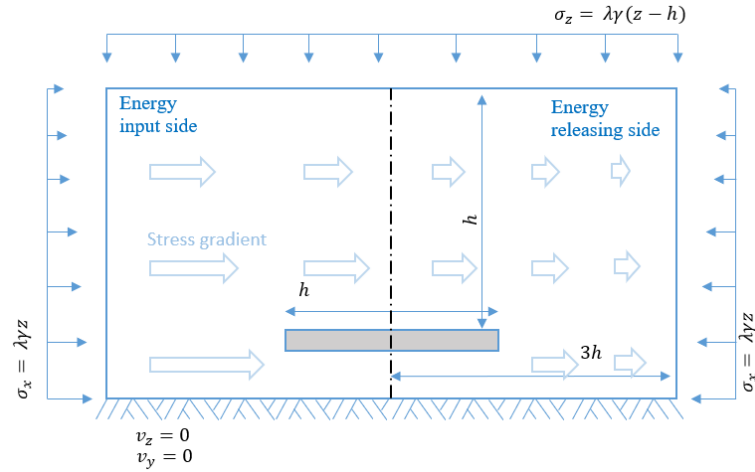
Figure 23. Boundary conditions and geometry of numerical experiment.

6.2.2 Model simplification

The simulation calculates subsidence at the surface, with a convergence of 8 m above 160 m of rock mass. Figure 24 shows how the subsidence parameters of the influence angle and exploitation coefficient change with depth. It shows the point beyond which the characteristics of the subsidence profile do not change or change linearly, which is a justification for the parameters mentioned.

The boundary conditions and geometric relationships between the elements are shown in Figure 23. In this study, a 2D model with a constant grid size of 1 x 1 m was used for the analysis. Preliminary investigations justified the use of this grid size as appropriate for the task and are discussed in Chapter 4.
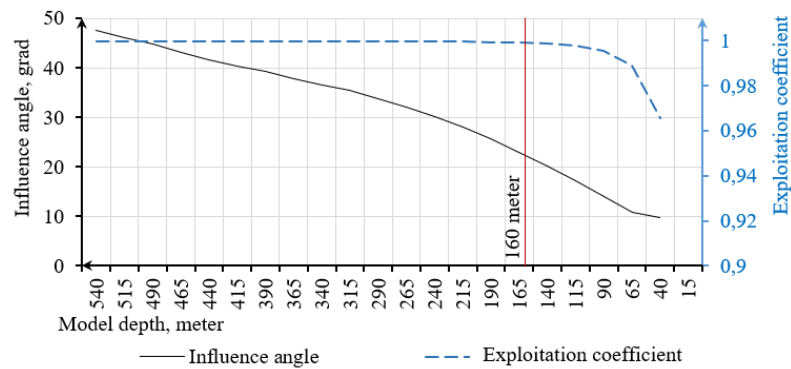
Figure 24. Influence of the depth of the prime characteristics on the subsidence prediction parameters.

6.2.3 Output data

The output is a set of points defined by the distance from the symmetry axis of the model and the magnitude of the subsidence. The points are spaced 1 m apart. The profiles represent the response of different rock masses to different stress factors (defined in the previous section, as *n* in Equation 36). The preliminary investigations showed that five subsidence profiles are not enough to explain the cumulative changes in the parameters of the subsidence profiles, therefore the stress difference has been reduced. Consequently, larger stress factors (14) were applied to each rock mass, to obtain different profiles. The exact meaning of the stress ratio depends on the other parameters, according to Equation 36.

For example, Figure 25 illustrates the subsidence profiles for stress factors from 1 to 3, for two different rock masses, schist and phyllite. The difference in the responses is visually clear. In the case of phyllite, asymmetry occurs at stress factors 2 and 3, while the magnitude of subsidence decreases within the symmetry pattern. However, schist responds in terms of symmetrical subsidence, where changes in the maximum subsidence area are visually clear. Increasing the stress, similar to the case of phyllite, results in smaller magnitudes of subsidence, although other examples (given in the 'Results' section) show the opposite response to increasing the stress factor.
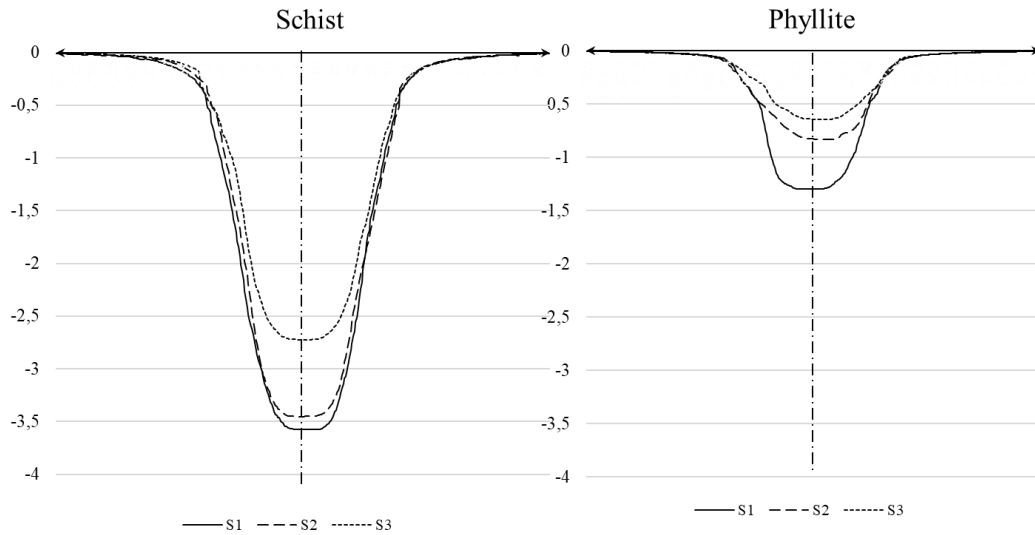
Figure 25. Subsidence profile results with different stress factors, for two examples.

The quantitative evaluation of the profile characteristics was estimated according to the following definitions (Figure 26):

- Maximum subsidence (S_{max}) and its location (in degrees from model axis).

- Skewness is a mathematical concept that refers to the degree of asymmetry of a function, defined as the difference between the maximum and minimum values of the function divided by the range of the function. A function with a skewness of zero is perfectly symmetrical, whereas a function with a large positive or negative skewness is highly asymmetrical.

$$Skewness = \frac{E[(X - \mu)^3]}{\sigma^3} \tag{37}$$

where μ is the mean (average) of the distribution, σ is the standard deviation of the distribution, E denotes the expected value, and X is a random variable from the distribution

- The inflection point is a point where the slope of the curve is at a maximum, defined as the first derivative of the subsidence with respect to distance and measured in degrees from the axis of the cavity. Influence angle (γ_{left} and γ_{right}) is the angle between the border of the cave and the border of 1% of the subsidence integral.

- The descriptive features can estimate the shape of the subsidence and the shape of the asymmetry in any context. To avoid the effect of the mathematical inconstant solution on the above parameters, the profile sets were smoothed by the mathematical moving average method, with a central Gaussian base. In other words: the correction takes into account the influence of the surrounding points, according to the normal distribution around the corrected point.
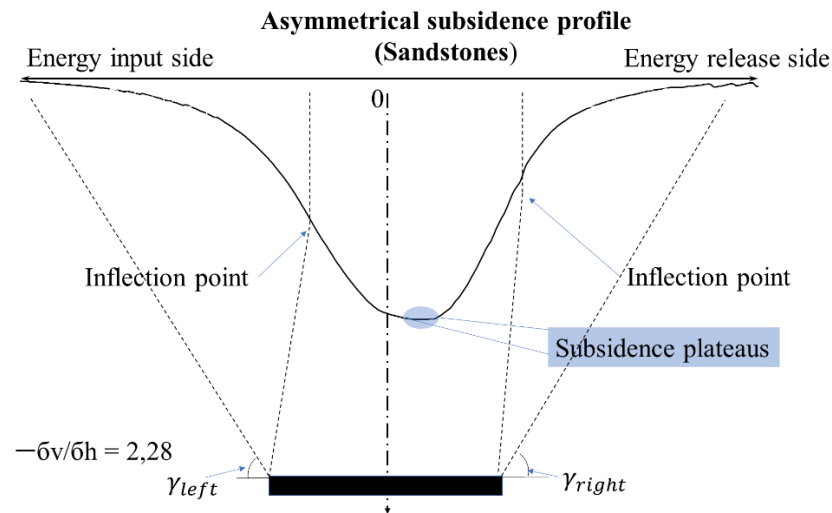
Figure 26. The subsidence profile parameters of sandstones.

6.3 Contribution of asymmetrical stress distribution

In this section, the various factors influencing subsidence deviation are explored, as revealed by the experiments. This part relates to the poor numerical results and their interpretation. By carefully analysing different patterns, the chapter aims to provide a comprehensive understanding of how stress conditions contribute to the subsidence profile. Each of the following subsections will delve into these aspects, supported by the experimental data (presented in Appendix B) and statistical analysis. The implementation of the results in an empirical model will be discussed in Chapter 7.

The analysis starts with the visual intersection of the profiles, to discover the main patterns and aspects of influence in detail and based on the statistical interpretation of those patterns, which are further discussed in the related sections. The general observations have been formulated as follows.

- There is notable variation in the shapes of symmetric and asymmetric profiles. This variation could be due to differences in angular deviation, the shape itself, or a combination of both.

- The subsidence magnitude and the position of its maximum point have a complex causation. In major cases, the maximum subsidence point deviates from the centre. Additionally, both the variations in subsidence magnitude and the location of maximum subsidence do not have a linear relationship with the applied stress. The subsidence magnitude can either increase or decrease in response to increasing stress, defying intuitive expectations.

- Visual asymmetry is frequently observed when the subsidence is below the average for a given rock type. Figure 27 illustrates the distribution of subsidence profiles with subsidence, either higher or lower than the average for the rock type. The lower subsidence magnitude is observed in areas with a stress factor between 2 and 5. The same area also shows a higher frequency of asymmetric patterns (indicated by the grey area), with a greater overlap of cases with lower or average subsidence magnitudes.

In summary, these visual findings highlight the significant influence of stress conditions on all facets of the subsidence profile. This complex influence alters the magnitude and location of maximum subsidence in different ways. Different rock types respond differently to these conditions; some exhibit asymmetric profiles and others maintain symmetry. These observations are only a basis for further discussion and analysis and will be explored in more detail in the following sections.
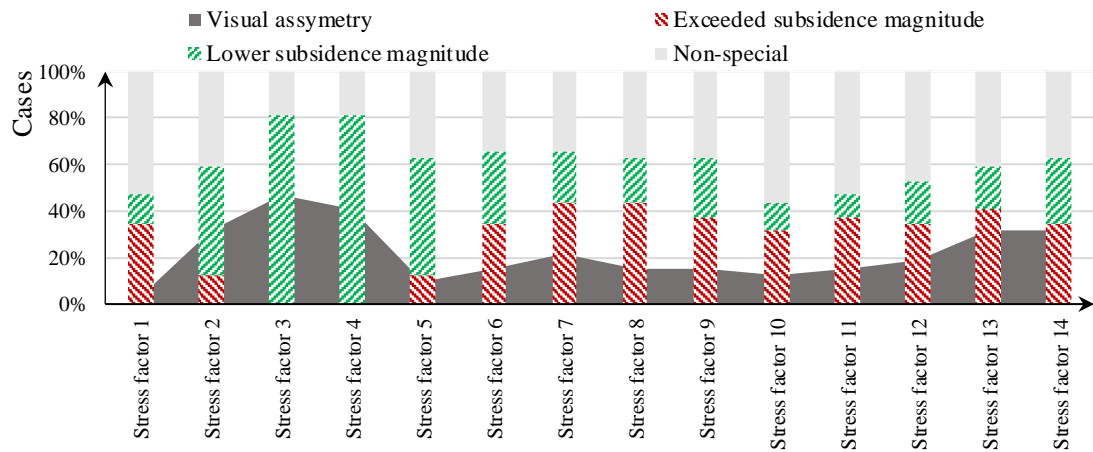
Figure 27. Distribution of relative magnitude and asymmetry in subsidence cases in response to stress factors.

6.3.1 Discussion of the basic distribution form

The shape of the subsidence profile is defined as the position of the inflection point or the maximum slope. The choice is based on the clear mathematical identification and relationship with the shape of the influence function discussed in the basics (the relationship is discovered in detail in Chapter 7). This measure of shape deviation is independent of the influence angle and the subsidence magnitude. The distribution of the inflection point position is provided in Figure 28. In the distribution, for practical and interpretative reasons, the absolute position is replaced by the position relative to the influence radius.

The result is open to several interpretations. Firstly, how it relates to the distribution shape (discussed in Chapters 2 and 4), secondly the difference between the energy input and release sides and, finally, its correlation with physical properties.

Discussion in light of the distribution shape

As discussed in the state of the art, in the case where the stress is described as a consequence of vertical stress, the subsidence profile has the shape of a Gaussian distribution (Lytwiniszyn, 1958; Knothe, 1953). In this particular case, the location of the inflection point would be around 0.39 R. The location range is covered by the distributions on the energy release side. As this side has a significantly lower additional horizontal stress, on average, it

is indirectly evident that the smaller the additional horizontal stress, the closer the shape will be to a normal distribution.
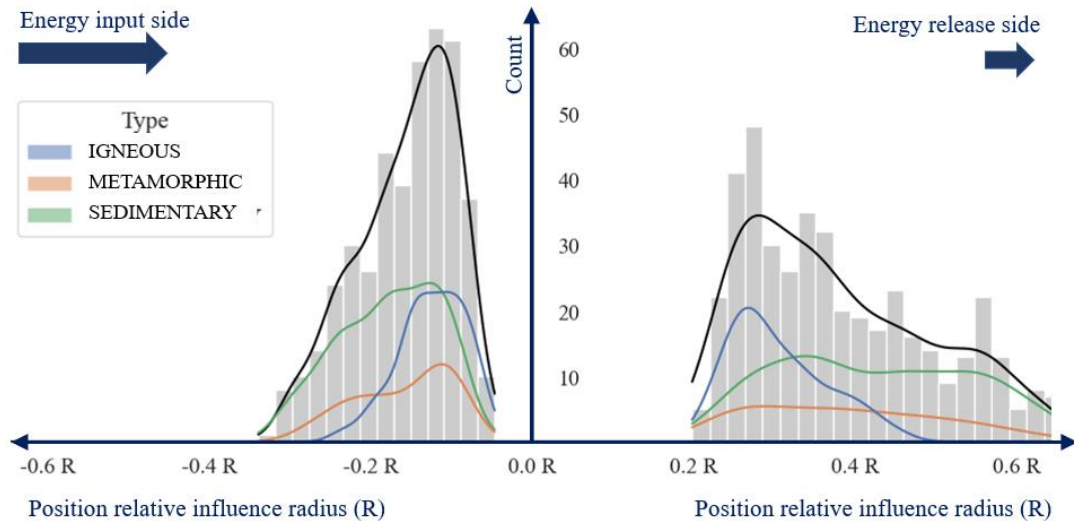
Figure 28. Histogram of inflection point locations.

Discussion in the light of asymmetry

The distribution in Figure 28 shows different shape patterns for the energy input side and the release side. The difference between the mean value of these sides (0.15 R and 0.37 R, respectively) is 60%, while the difference for the influence angles was 38.5 and 39.5 degrees, respectively (about 2.5%). This can be interpreted to mean that the stress conditions have a greater influence on the central part of the subsidence profile than on the periphery.

Correlation with physical properties

The correlation of rock properties and the inflection point were calculated. The highest correlation with Poisson's ratio is -0.48, and other properties are around 0.3; the rank correlation (Spearman's method) did not show better results. The correlation matrix can be seen in Appendix C.

In summary, the direction of the stress gradient influences the shape of the settlement profile. The stronger the stress, the more the shape deviates from the normal distribution. The central part of the subsidence profile is more sensitive to stress conditions than the periphery.

6.3.2 Discussion of maximum subsidence

The maximum subsidence is defined as the point of maximum vertical displacement in the subsidence profile, characterised by location and magnitude. However, accurately estimating this point numerically is a challenge due to the local variability that arises when applying the finite element method (FEM). To address this challenge, a polynomial function is fitted to estimate the maximum point within a specified range. The results highlight the main aspects: the magnitude of the subsidence and its evaluation with stress and the location of the maximum subsidence.

Magnitude of maximum subsidence

The scatter plots of the maximum subsidence and rock mass properties do not show a linear dependency (Figure 29). The rank correlation method was applied (Table 7) to identify the correlations. The highest rank correlation belongs to the uniaxial strength and disturbance coefficient. To investigate the relationship in more depth, a machine learning technique was employed to analyse sensitivity of the maximum subsidence to the rock mass properties.
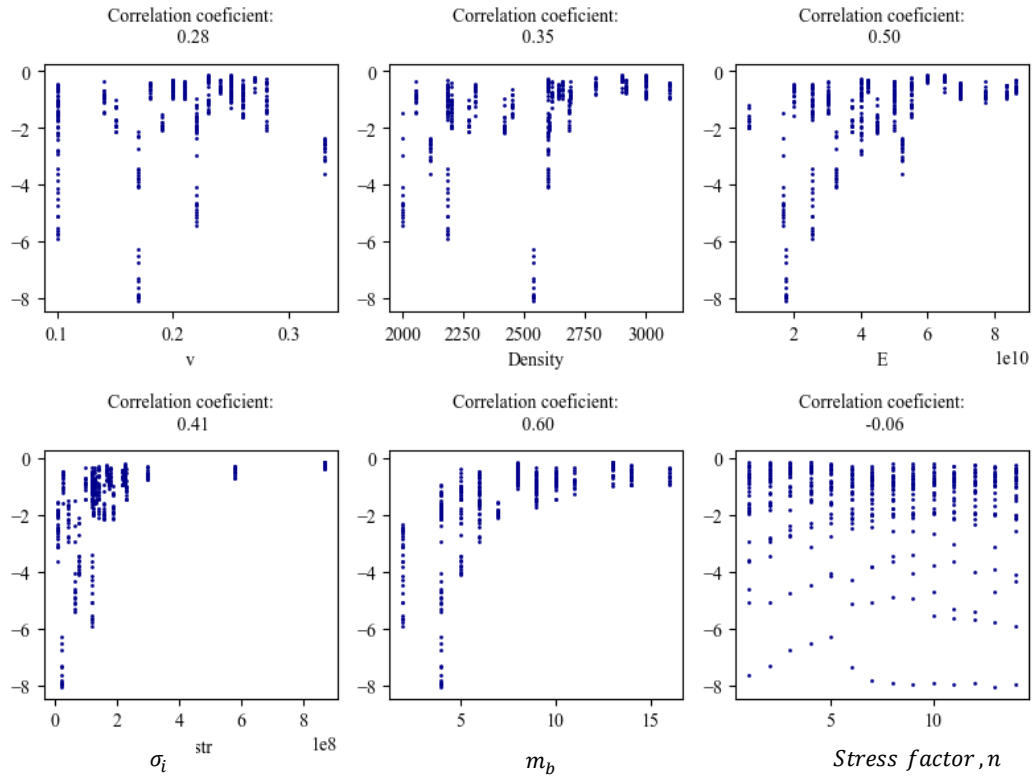
Figure 29. Scatterplot of the maximum subsidence versus rock mass properties with Pearson's correlation coefficient.

Table 7. Rank correlation of the rock mass properties and maximum subsidence (Spearman correlation coefficient).

Rock mass property	v	ρ	E	σ_i	m_b	n
Rank correlation with the maximum subsidence	0.33	0.64	0.62	0.78	0.80	-0.08

For this particular case, the statistical tool known as 'Random Forest Regression' was used (implemented by the Python library as 'sklearn', Pedregosa et al. (2011)). This technique uses multiple decision trees to create a model for qualitative prediction, dealing with non-linear patterns in the data. In this particular context, the technique is applied to define the sensitivity of various parameters.

The sensitivity is calculated by evaluating the reduction in the predictive accuracy of the model (created by the random forest regression technique) when parameters are changed. In other words, the greater decrease in the model's accuracy, the more sensitive this parameter is to the property. To ensure the reliability of the analysis, the MSE parameter must be low.

The results of the sensitivity analysis are presented in Figure 30. According to the analysis, the maximum subsidence mainly depends on the disturbance coefficient (m_b) and the uniaxial strength (σ_i). The results contribute to the sensitivity analysis and highlight the role of those parameters.

According to the results, the maximum subsidence is largely influenced by the disturbance and uniaxial strength properties, while the stress factor appears to have the smallest effect. However, the visual investigation showed the high variation of maximum subsidence within a rock type for different stress factors. For a deeper understanding of the problem, the evaluation of the maximum subsidence due to the stress condition is discussed.
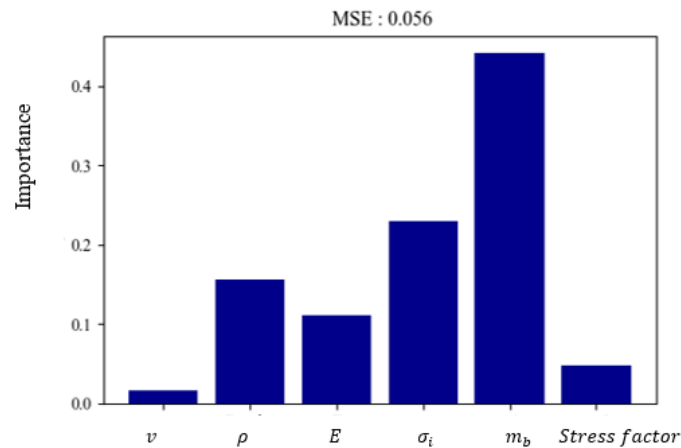
Figure 30. The sensitivity of the maximum subsidence relative to the rock mass properties.

Evaluation of maximum subsidence with stress factor variety

As already mentioned, the low correlation does not allow an estimate of the direct influence of the stress factors on the evaluation of the maximum subsidence. In order to understand this pattern, plots of maximum subsidence versus stress factor were visually observed to find a similarity. Three preliminary patterns, or clusters, were identified but, for the final analysis, those plots were clustered using a mathematical algorithm (K-means clustering) to ensure impartiality in the interpretation. The results presented in Figure 31 contribute the visually identified patterns:

Cluster 0: in general, maximum subsidence decreases with increasing stress;

Cluster 1: in general, maximum subsidence increases with increasing stress;

Cluster 2: has the smallest maximum subsidence in the area of stress factors of 2-5 and then the magnitude increases.

The statistical representation of rock mass properties does not show a significant difference between cluster 0 and 2. However, cluster 2 has a lower Young's modulus, Poisson's ratio and uniaxial strength. Related to the other subsidence properties, the cluster has a higher mean skewness. The rock type and their clusters are presented in Appendix A.
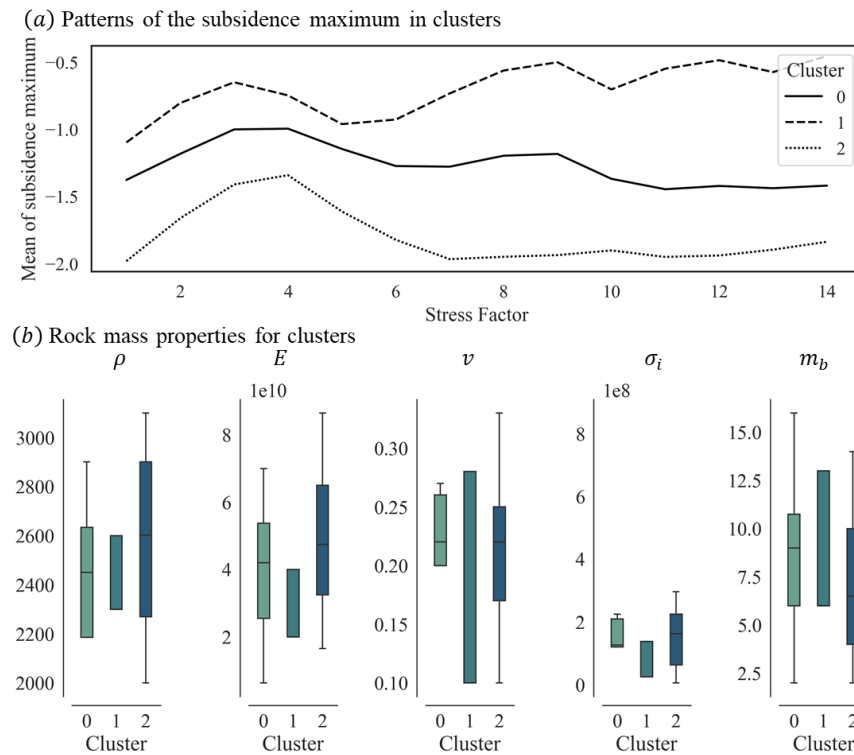
Figure 31. The geometrical representation of the maximum subsidence response to stress conditions (a) and related rock mass properties (b).

Position of the maximum subsidence

The maximum subsidence is typically located on the axis of the geometrically weighted centre of convergence. The assumption of an asymmetric shape considers the possibility of maximum subsidence deviation from the central location. Such a hypothesis is supported by numerical investigations.

The numerical experiments show that horizontal stresses can shift the maximum subsidence away from the central location. The effect of these stresses is relatively small for igneous rocks but, for sedimentary rocks, the maximum subsidence can be shifted significantly. On average, under the influence of stress, the location of the maximum subsidence shifts from the geometrical center of the void by 1.8 degrees (or 31 m for a depth of 500 m) towards the direction of energy release, with a standard deviation of 5.8 degrees (Figure 32).
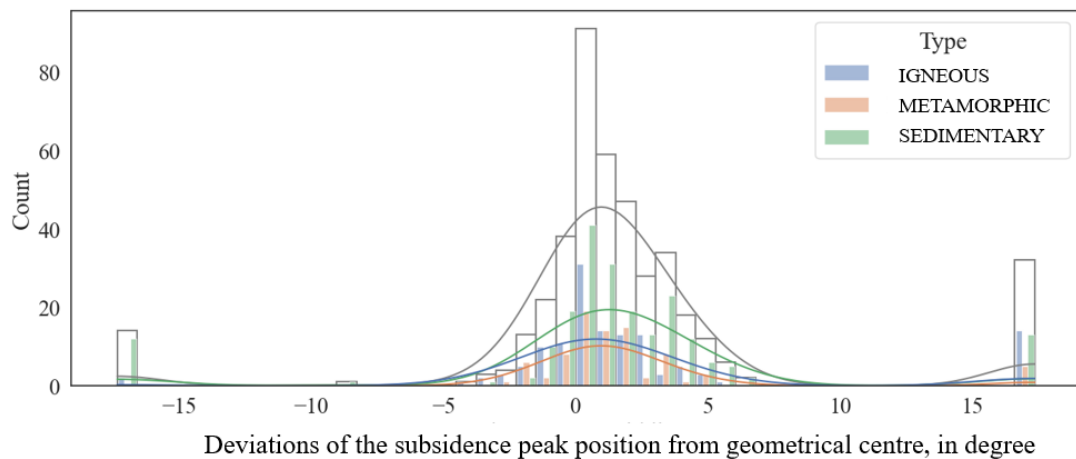
Figure 32. Histogram of the maximum subsidence deviation from the central location, in degrees.

As shown in Figure 33, the shift in the location of maximum subsidence towards the direction of energy dissipation is most likely for stress factors between 2-5 and 10-13. In other cases, the distribution is centred around 0. Igneous rocks show a reduced response due to their superior strength, while rocks with a lower Young's modulus show a more pronounced response. Therefore, the position of the subsidence peak can vary by up to 6 degrees from the central position.
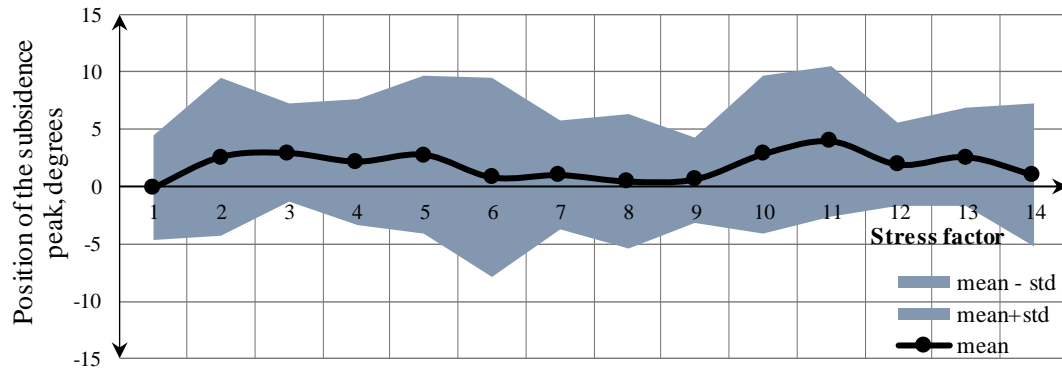
Figure 33. The maximum subsidence position (in degrees) and its standard deviation.

6.3.3   Discussion of assymetry

As mentioned, the skewness of the subsidence profile is used to identify the measure of asymmetry. Mathematically, skewness is defined as a measure of the asymmetry of the probability distribution of a real-value random variable around its mean. The skewness value can be positive, negative, or undefined. If the mean is 0, then the distribution is considered to be symmetrical. Negative or positive values of skewness indicate the left or right position of the distribution's tail, respectively.

The challenge in a quantitative investigation is estimating the numerical limit of skewness for 'true' asymmetry, particularly when local variation can lead to skewness without actual asymmetry. To determine this limit, the profiles were visually marked as either symmetrical or asymmetrical ('True' or 'False' in Figure 34, where the orange part is visual asymmetry and blue is visual symmetry) and plotted on a histogram. The histogram effectively separates the visually asymmetrical cases from the others and, based on this cut-off, the profiles with skewness below -2.13 were accepted as asymmetrical. All of the profiles are skewed, which is to be expected, according to the applied stress conditions.

Analogous to the maximum subsidence analysis, a sensitivity analysis for asymmetry was employed. The results are presented in Figure 35. According to the analysis, the skewness is more sensitive to certain parameters, namely the uniaxial strength (a correlation coefficient with this factor is 0.52), stress factor and density. In essence, changes in these parameters have a greater impact on the skewness value, indicating a higher value of sensitivity. While the sensitivity analysis offers important insights into how certain parameters influence skewness, there remains a need for a more definitive method to establish the conditions that contribute to asymmetry. This makes it usefull to apply other methods.
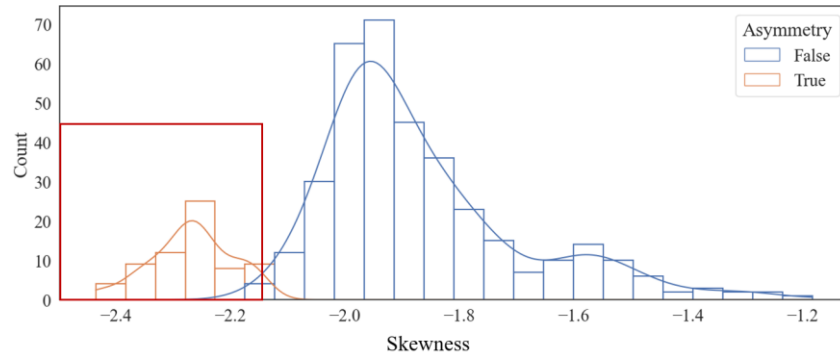
Figure 34. Skewness histogram with identification of visual asymmetry. Orange signifies visually asymmetric cases; blue signifies visually symmetric cases. The red frame highlights the skewness accepted as being asymmetric.
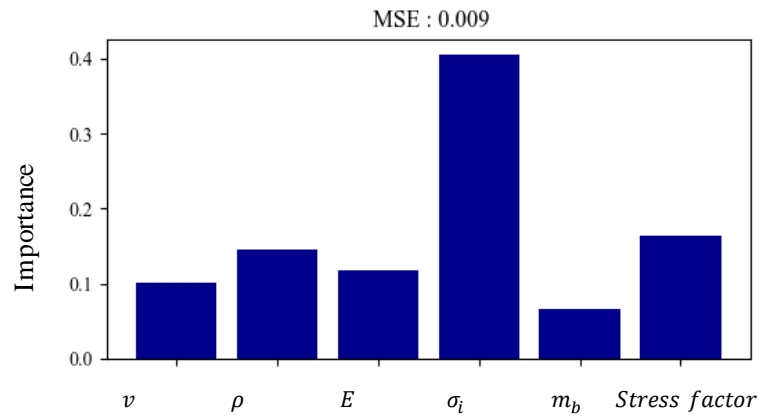
Figure 35. Rock mass parameters importance for profile skewness.

To investigate the specific rock properties and the ranges that influence symmetry and asymmetry, the decision tree classifier, that operates on the principle of minimising entropy, was employed. This approach is chosen for its effectiveness in handling complex tasks, as it mimics human decision-making processes by partitioning the feature space into more homogeneous subsets. The principle of minimal entropy is a strategic approach intended to reduce uncertainty. In this context, the classifier selects decisions or 'splits' that lead to the purest or most homogeneous subsets, thus effectively minimising entropy. The aim is to pinpoint the limits to the properties that are significant in identifying asymmetry.

In contrast to the sensitivity analysis, the decision tree implements a cutoff based on specific criteria for the optimal identification of asymmetry. Based on the analysis, the following rock properties are estimated for symmetry and asymmetry (Table 8). Given these conditions, ranges for other parameters have been identified and are presented in Figure 36.

The results suggest that the favourable conditions for asymmetry are within the range of parameters shown in Figure 36. At the same time, only the uniaxial strength shows a positive correlation with the degree of asymmetry. With respect to relative density, asymmetry only occurs in 2% of cases where the density exceeds 2400. Since other properties do not have such a defined cut-off, only high density can be used (for now) to distinguish between symmetric and asymmetric patterns in subsidence profiles.

In the patterns described, particularly the positive correlation with uniaxial strength and density cut-off, there is an apparent dependence of the asymmetry pattern on the elastic displacement potential of rock. High density rock has less capacity for rock deformation. At the same time, lower uniaxial strength reduces the asymmetry due to faster failure; however, this factor is usually associated with a lower Young's modulus, which increases the elastic deformation part. In conclusion, the asymmetry pattern forms during the elastic deformation phase of the rock. Consequently, the longer the elastic phase of deformation persists in the stress gradient field, the higher the asymmetry of the subsidence.

Table 8. The properties of rock mass identifying the symmetry and asymmetry of the subsidence profile

	Asymmetry (Figure 36 a)	Symmetry (Figure 36 b)
Properties	$\sigma_i \leq 7.9 \cdot 10^7$ & $\rho \leq 2400$	$\rho > 2400$
Cases	38/45 or 54% of all simulated asymmetrical cases	264/271 or 75% of all simulated symmetrical cases.
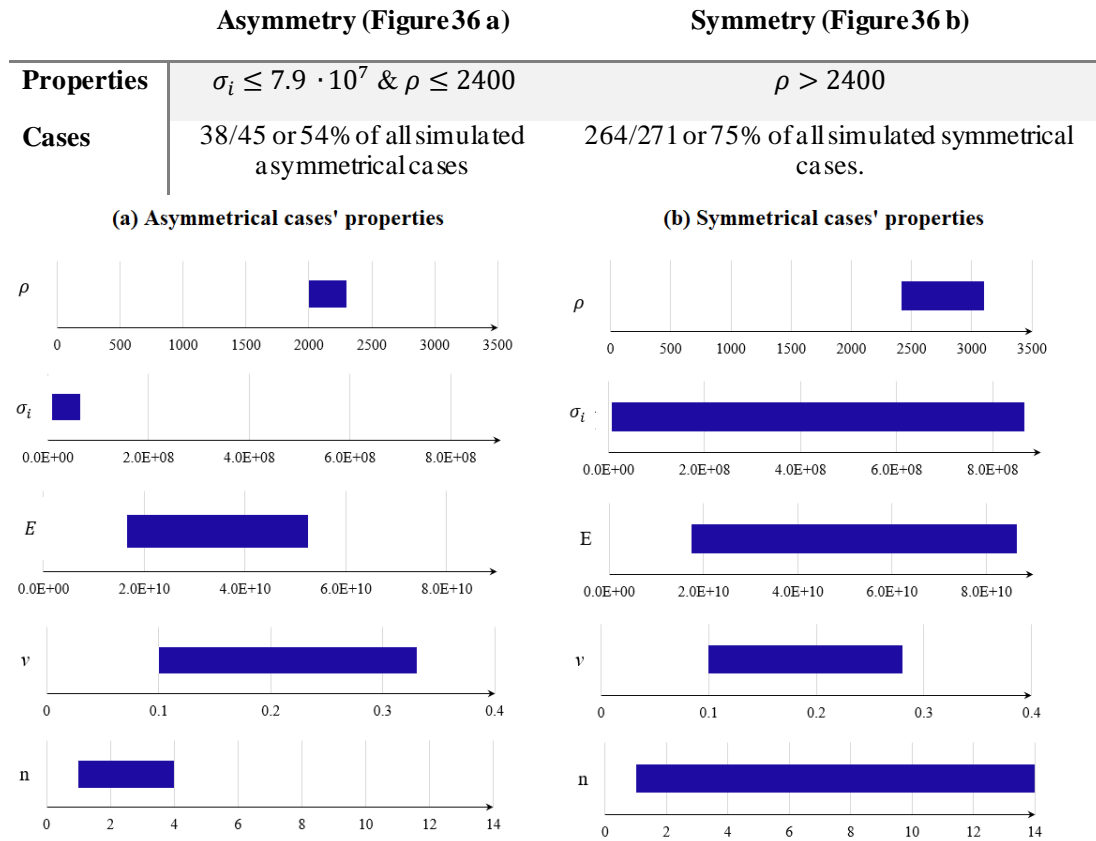
Figure 36. Rock parameters for profiles, (a) asymmetrical; (b) symmetrical.

6.3.4 Discussion of influence angle

This chapter discusses the influence angle, focusing on its relationship with depth and rock properties. The first part describes the dependence of the influence angle on depth using numerical quantification. The second part navigates through the complex interplay of rock properties to develop a predictive method for the influence angle. The results of these investigations and their implications for wider geological understanding are discussed in the following sections.

Influence of the depth

Based on Figure 24 (Chapter 6.2.2), there is a linear dependence of the influence angle on depth. To determine whether this factor needs to be included in the prediction function, the influence angle, defined as 99% of the integral, is calculated numerically (Figure 37). The plot leads to an outcome of further investigation of this dependency for wider rock mass properties and conditions.
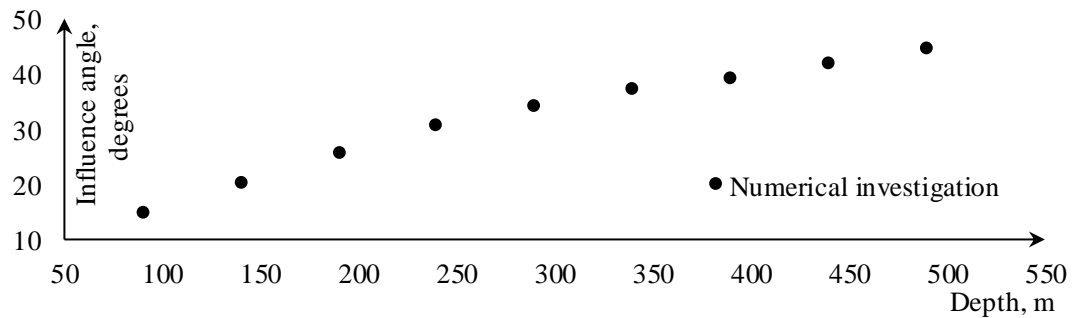
Figure 37. Difference between the changes in the influence angle caused by depth: calculated and numerically simulated.

Influence angle as a rock mass property function

The scatter plots of the rock mass parameters against the influence angle show the high variety of the data. The initial step was a visual inspection to identify the potential correlations (Figure 38). For parameters $\rho, v, E,$ and $n,$ no significant correlation was detected. Parameters m_b and σ_i, however, show patterns that indicate some kind of relationship. This is not necessarily linear; therefore, in the subsequent analysis, rank correlation has been used.

To better understand this relationship, different parameter combinations have been tried out (Figure 39). The best solution was the product of m_b, σ_i and v. The improvement of the distribution is presented on the scatter plot and the corresponding rank correlation is in Figure 38. According to the narrowing result v and the highest rank correlation of the product m_b, σ_i and v, the combination is used as the basis for further analysis.

Scatterplot analysis specified an exponential form of dependence (Figure 38). To identify the exact equation, a curve fitting based on the principle of residual minimisation was used. The additional coefficients under the exponential function were replaced by -2π on the basis of similarity. The adjustment led to the solution given by Equation 38.

$$\gamma = a \cdot exp \left(-2\pi \; \frac{m_b \cdot v \cdot \sigma_i}{10^{10}}\right) + c \tag{38}$$
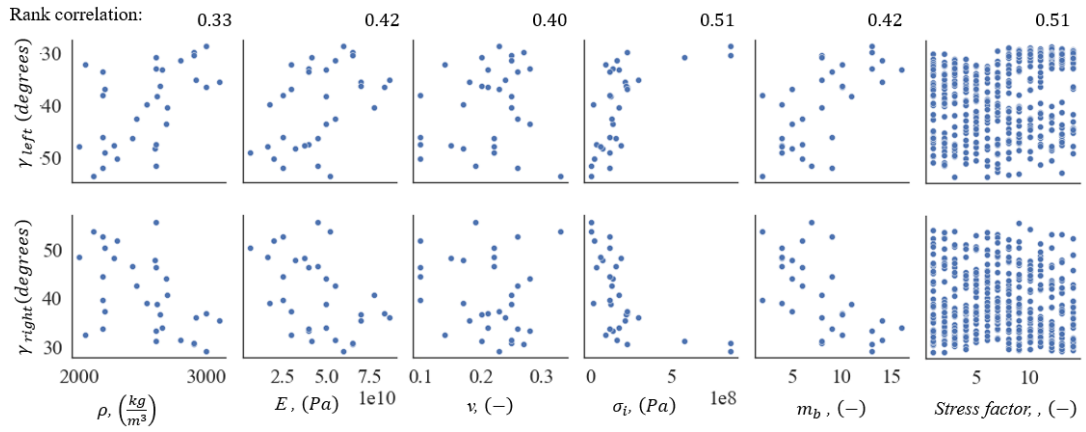
Figure 38. Scatterplots of influence angle versus rock mass properties
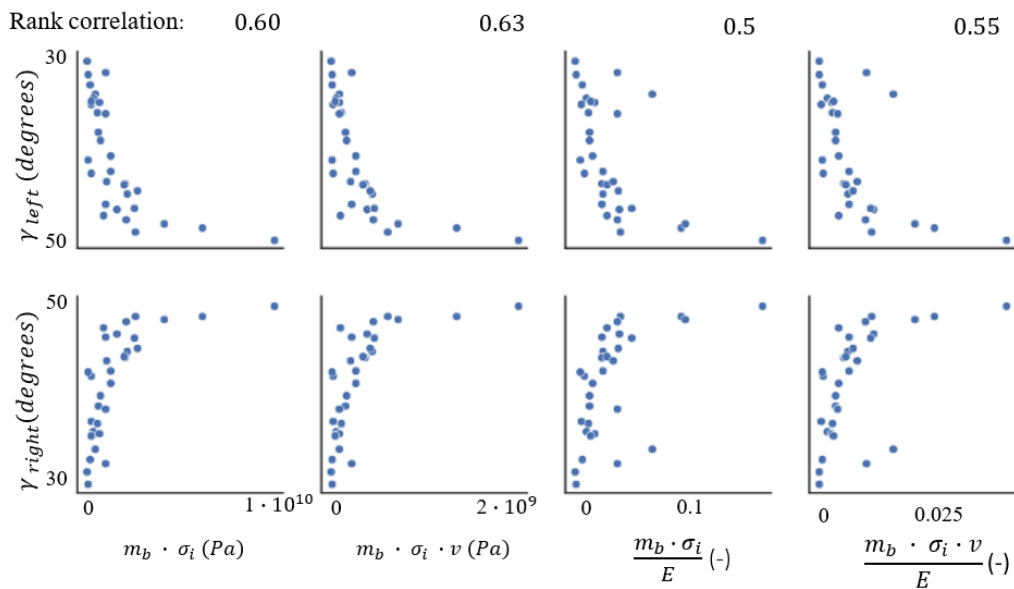
Figure 39. Narrowing results of the property multiplications.

To estimate the parameters 'a' and 'c', a correlation analysis was employed. As a result, these parameters have the highest correlation with stress: 0.93 and 0.73, respectively (Figure 40). After linear fitting, the final version (in the form of Equation 39) is proposed to identify the angle of influence in degrees.

$$\gamma = (-0.85n + 28.95) \cdot exp\left(-2\pi \, \frac{m_b \cdot v \cdot \sigma_i}{10^{10}}\right) + (0.46n + 17.85), degrees \qquad (39)$$

where n is the stress factor and the numerical coefficient depends on the type of angle measured.

According to Figure 40 and Equation 39, the stress conditions affect the influence angle by up to 12 degrees. The complexity of the equation explains the low correlation with the stress factor, despite its high influence.
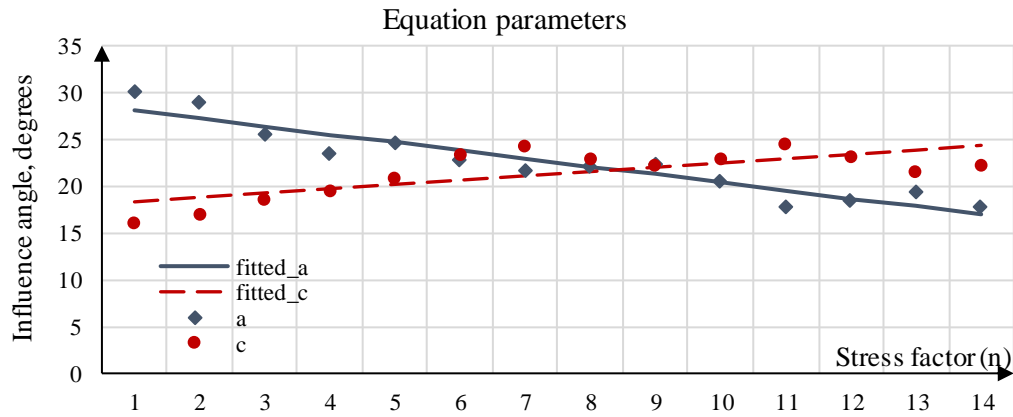
Figure 40. Parameter estimation of the influence angle function, 'a' and 'c' are coefficients from Equation 38.

6.4 Conclusions

The analysis shows that there is a non-linear relationship between the profile parameters and the rock mass properties, including the stress factor. The variation of subsidence due to the stress state has been identified in all aspects, although with different effects. The effect of the rock mass properties on the subsidence parameters are described below.

Inflection point

The shape of the subsidence profile can deviate from the normal distribution. The profile deviation occurs in the central part of the subsidence trough, where the influence angle defines the common peripheral parts. The experiment identified a significant shape variation and estimated that higher horizontal stress results in higher subsidence profile deviations, from a normal distribution. The observation suggests the need for an empirical model to cover a significant shape deviation.

Regarding the rock mass properties, the highest, but not significant correlation is estimated to be with Poisson's ratio. However, the influence is too complex to be identified by a single factor.

Maximum subsidence

The response of the maximum subsidence to stress is shown by the deviation of the centre point and the magnitude.

Relatively speaking, the deviation of the centre point was estimated to be between -4 and +7 degrees, in most cases. The specific relationships were not identified.

Regarding the maximum magnitude of the subsidence, a sensitivity analysis and the rank correlation show the highest dependence on the perturbation coefficient, followed by the uniaxial strength. The analysis of subsidence variation due to stress factors indicates that stress factors between 2 and 5 resulted in lower subsidence. However, different rock types exhibit differing reactions to increasing horizontal stress. In general, three patterns were estimated: constant decrease, constant increase and a wave pattern in the beginning, with an extremum around a stress factor equal to three and a constant high after a stress factor equal to six. This behaviour was interpreted as follows: higher stress first increases resistance to vertical displacement, resulting in a decreased subsidence magnitude. However, after reaching a certain value, it induces fracturing, causing an increase in subsidence magnitude. This interpretation also explains the high positive correlation with the disturbance coefficient.

Asymmetry

The definition of an asymmetrical pattern consists of the skewness of the subsidence profile and shows the greatest difference in the central part of the profile. Skewness is more sensitive to the uniaxial strength, stress factor and density.

The analysis shows that a symmetrical pattern is common in high-density rock (more than 2400). This factor describes 75% of the symmetrical cases of the experimental results. In

this range of density, only 2% of cases of asymmetry are identified. While symmetrical cases appear in the whole range of stress factors, significant asymmetrical cases accumulate in the range from 1 to 4. Identifying asymmetrical cases is more complex. Low uniaxial strength, density, and Young's modulus are conducive to asymmetry but do not necessarily limit its occurrence. The asymmetry pattern is interpreted as follows: the longer the elastic phase of deformation lasts, the more asymmetrical the subsidence profile becomes.

Influence angle

Influence angle changes are investigated in two directions: the influence of depth and the influence of horizontal stress and rock properties.

Regarding the depth, an increase in influence angle with increasing depth is estimated, although the conclusion is made for only one rock type, it is assumed that investigation of wider rock mass properties will result in the slope variation.

An empirical function has been estimated for the influence of rock mass properties. The function has an exponential form and depends on the product of the disturbance coefficient, the uniaxial strength and Poisson's ratio. The constants of the equation show a high correlation with the stress factor. Integration of the stress improves the solution. Based on the function of the influence angle, the role of the stress factor was estimated to be up to 25% or 12 degrees.

In conclusion, the hypothesis of asymmetry and shape deviation as a consequence of stress conditions is proven, although the exact conditions leading to asymmetry have not been estimated. In order to better understand the process, the sensitivity of the parameters to the rock mass properties has been generalised in Table 9. The generalisation shows that, despite the changes derived from the stress factor, the response depends on the combination of different factors that cannot be studied separately.

Table 9. Subsidence parameter sensitivity to rock mass properties.

	Influence angle	Inflection point	Subsidence magnitude	Skewness
Density, ρ	+	+	++	+++
Poisson's ratio, v	+	++	+	+
Young's modulus, E	+	+	++	++
Disturbance coefficient, m_b	+++	+	+++	+
Uniaxial strength, σ_i	+++	+	+++	+++
Stress factor	++	+++	+	++

7 Adaptation of an empirical model to the discovered features

The numerical investigation highlighted the potential for the improvement of subsidence prediction methods through the consideration of shape change and asymmetry. To address these aspects, the models of Eickermeier (2005), which considers shape deviation, and Quasnitza (1988), which considers asymmetry, were used and, subsequently, adjusted to the problem discussed in the fundamentals.

7.1 Subsidence asymmetry

As mentioned above, Quasnitza (1988) proposed a solution to account for bilateral asymmetry (also known as bivariate asymmetry, referring to the lack of symmetry between the two sides of a structure) by considering the influence angle as a function of direction. However, this solution only covers one particular case of direction-dependent asymmetry and does not ensure a balance between subsidence volume and volume shrinkage through correct integration (as discussed in Chapters 2 and 4).

The influence function describes the spatial distribution of subsidence and how it varies with relative distance from a cavern. The relative distance is controlled by the influence radius R, which is defined in Equation 40.

$$R = z \cot (\gamma) \tag{40}$$

where z is the depth of the cavern and γ is an influence angle.

For simplification, this thesis utilises the term 'influence radius' instead of influence angle. In practice, however, the influence angle is usually estimated because the depth of mining may vary. To introduce asymmetry, the influence function should be direction-dependent. The direction is defined as the angle φ in Equation 41, which is the horizontal angle between vector r and the north direction on the X-Y axis.

$$\varphi = arcctg\left(\frac{\Delta y}{\Delta x}\right) \tag{41}$$

To express the asymmetry of the subsidence trough, a continuous function should be implemented in R, which depends on φ and is defined between 0 and 2π, to describe a closed contour. In the symmetric case, $R(\varphi)$ is described as a constant with a constant value. For each specific asymmetric case, it is important to satisfy the volume balance requirement

between the convergence volume and the subsidence volume. The volume under the influence of the function integral, presented in Equation 42, must be solved.

$$\int_0^{2\pi} \int_0^\infty exp\left(-\pi\frac{r^2}{R(\varphi)^2}\right) r \, dr \, d\varphi = \int_0^{2\pi} \frac{R(\varphi)^2}{2\pi} d\varphi = \frac{1}{2\pi}\int_0^{2\pi} R(\varphi)^2 \, d\varphi \tag{42}$$

This equation does not limit the expression of the function $R(\varphi)$ to any function that provides a variable choice of asymmetry shape; the integration of the solution into the basic empirical model solution (Equation 42) provides a general solution for an asymmetrical case (Equation 43). The solution is appropriate for any type of asymmetry, ensuring the aforementioned volume balance.

$$S(r,\varphi) = \frac{\Delta V}{\frac{1}{2\pi}\int_0^{2\pi} R(\varphi)^2 \, d\varphi} \cdot exp\left(-\frac{\pi r^2}{R(\varphi)^2}\right) \tag{43}$$

This solution can be reduced to the Sroka and Schober (1982) solution, in the case where $R(\varphi)$ is constant. Some examples to demonstrate the flexibility of the solution are presented below.

Examples

The value of $R(\varphi)$ can be defined by any equation meeting the above-mentioned requirements. Examples of such functions are provided in Equations 44 and 45, and are illustrated in Figures 41 and 42. These examples use trigonometric and polynomic functions.

$$R(\varphi) = (1 + B \sin(\varphi) + \Delta\varphi) \cdot R \tag{44}$$

$$R(\varphi) = -A R \cdot \varphi^4 + B R \cdot \varphi^3 + C R \cdot \varphi^2 + D R \cdot \varphi + R \tag{45}$$

where R is an average mean of the influence radius, estimated by the influence angle in several directions; and $\Delta\varphi$ is an angle from the North direction, to state the direction of asymmetry, in the example $\Delta\varphi$ equals 0.

In both cases (using either a trigonometric function or a polynomial function), it is important to estimate the influence angle, in order to obtain the property of influence radius in different directions:

- **For the trigonometric function**, the influence angle should be estimated either in two directions of asymmetry: $\Delta\varphi$ and $\Delta\varphi+1/2 \pi$ or, if they are unknown (usually) in three directions. Alternatively, the difference in direction should be concluded beforehand. In this case, R represents an average of $z \cdot ctg(\gamma)$ in the two directions. In other words, for this trigonometrical case, there are two main directions of profile, one that describes asymmetry (Figure 41 with a direction of 90 degrees) and one perpendicular to that one (in the 0 direction), without an asymmetrical pattern.

- **For the polynomial function**, the influence angle should be estimated in five different directions, in order to estimate the polynomial function. The value of R, in this case, is the same as in the sin function case, i.e. an average of $z \cdot ctg(\gamma)$. In this case, the influence radius must be estimated in general directions and, for the case in Figure 41, its direction of inflection points. For this particular case, it must be estimated in five directions to estimate the polynomial of the 4th order.

To calibrate the new function according to Equation 43, Equations 44 and 45 must be solved. An analytical solution is provided in Equations 46 and 47, respectively. Both models are presented in Figure 42.

$$S(r,\varphi) = \frac{\Delta V}{\frac{1}{2\pi} \int_0^{2\pi} \left(R + RB\sin(\varphi)\right)^2 d\varphi} \cdot \exp\left(-\frac{\pi r^2}{R(\varphi)^2}\right) =$$

$$= \frac{\Delta V}{\frac{1}{2} R^2 (2 + B^2)} \cdot \exp\left(-\frac{\pi r^2}{R(\varphi)^2}\right) \tag{46}$$

$$S(r,\varphi) = \cdots = \frac{\Delta V}{\frac{1}{2\pi} \int_0^{2\pi} \left(-A R \cdot \varphi^4 + B R \cdot \varphi^3 + C R \cdot \varphi^2 + D R \cdot \varphi + R\right)^2 d\varphi} \cdot$$

$$\cdot \exp\left(-\frac{\pi r^2}{\left(R(\varphi)\right)^2}\right) \tag{47}$$
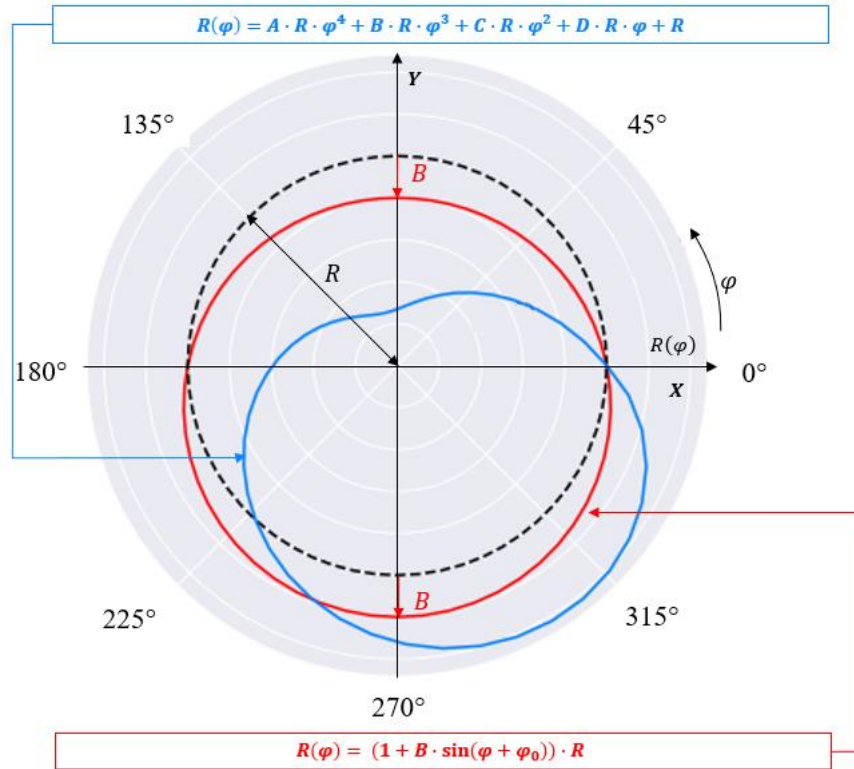
Figure 41. Definition of $R(\varphi)$ as a function and discrete relative to the mean value.

The demonstration of the aforementioned definition of $R(\varphi)$ in Equation 46 (Figure 41) is provided in Figure 42a. The demonstration of the aforementioned definition for $R(\varphi)$ in Equation 47 (Figure 41) is provided in Figure 42b.

In practice, the value of R is estimated from subsidence measurements. Pre-estimation of the shape of the trough as a simple figure with one asymmetrical direction, such as a sine function or an ellipsoid, can be applied in cases of anisotropic, uniformly distributed horizontal stress, simple anisotropies, geological structures, significant changes in the landscape, etc.

$$R(\varphi) = (1 + B \sin(\varphi)) \cdot R \qquad R(\varphi) = A R \cdot \varphi^4 + BR \cdot \varphi^3 + C R \cdot \varphi^2 + D R \cdot \varphi + R$$
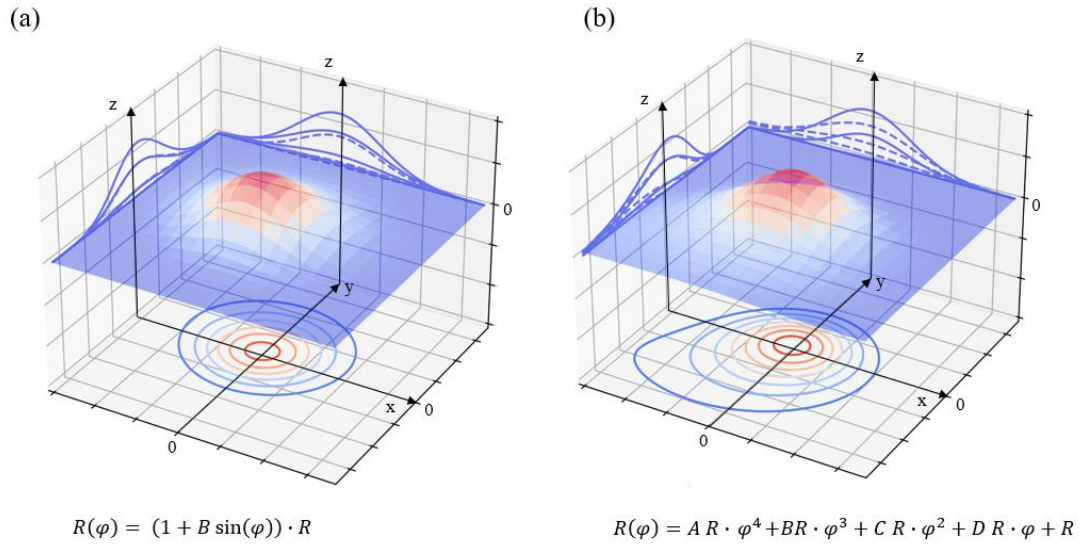
Figure 42. Subsidence trough with asymmetry on an example of the radius distribution demonstrated in Figure 41.

7.2   Subsidence shape flexibility

As mentioned in Chapter 4, the solution proposed by Eickermeier (2005) introduces a parameter δ which changes the shape of the distribution. However, this solution only satisfies the volume balance in a certain range of shape variation. To overcome this limitation, another methodology is proposed based on this idea.

In order to control the shape of the subsidence profile, Sroka and Schober's (1982) influence function $\exp\left(-\pi \left(\frac{r}{R}\right)^2\right)$ is adopted into Equation 48. To ensure the volume balance of this influence function, the function should be integrated (analogous to Chapter 7.1), but an analytical integral of such a function does not exist.

$$f_\delta(r) = \exp\left(-\pi\left(\frac{r}{R}\right)^\delta\right) \tag{48}$$

where δ is called the shape parameter and is introduced to calibrate the position of the inflection point discussed in Chapter 6, 'Numerical investigation'.

Step 1. Solution of volume balance problem

A numerical method is used to solve this problem. The ratio of the numerical estimated volume under influence functions $\exp\left(-\pi\left(\frac{r}{R}\right)^2\right)$ and the adopted influence function (Equation 48) is independent from R and has an exponential dependency from δ (Figure 43). This means that integration can be replaced with a geometrically defined function of correction coefficient: c_δ (δ) (Equation 49, Figure 43).

$$c_\delta = \frac{\pi \int_{-R}^{R}(f_2(r))^2 r\, dr}{\pi \int_{-R}^{R}(f_\delta(r))^2 r\, dr} \tag{49}$$

The absolute difference of the volumes defined by the disk method is -8,23 e-14 with R = 500, and the difference decreases with an increase in the influence radius.
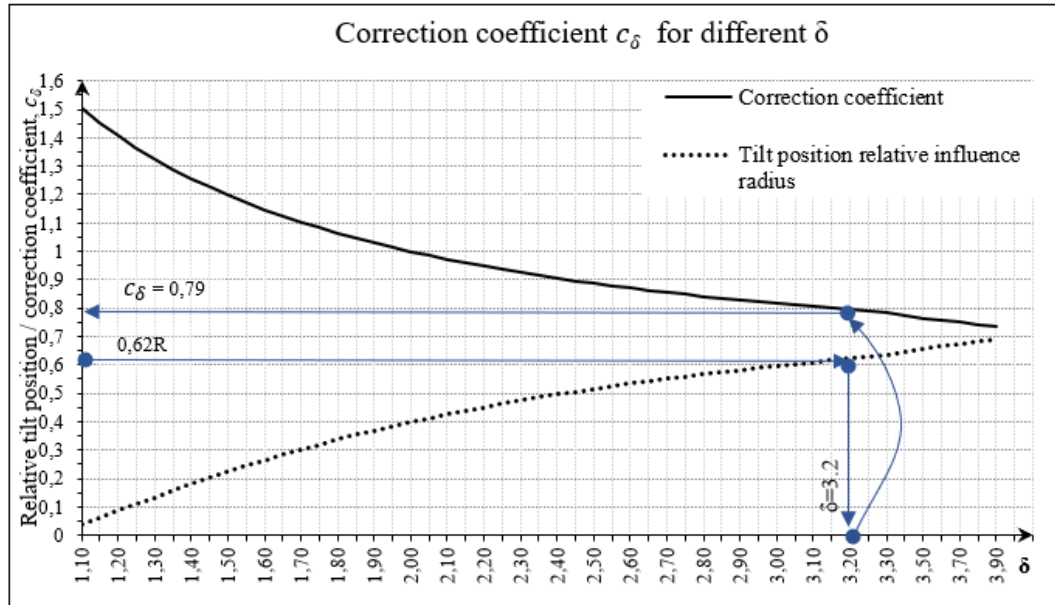
Figure 43. Definition of the shape according to the relative position of the maximum slope and the correction coefficient. The blue line shows how to use the diagram.

Consequently, instead of iterative numerical integration for each individual case, the new function can be weighted by the Sroka and Schober (1982) solution (Equation 50). The empirical solution of the shape parameter δ and the volume correction coefficient c_δ is shown

94

in the diagram (Figure 43). This introduced coefficient has been integrated into the equation for the subsidence prediction model (Equation 48). However, this presentation requires a numerical solution, which is not preferred.

$$S_\delta(r) = \frac{\Delta V c_\delta}{R^2} \exp\left(-\pi \left(\frac{r}{R}\right)^\delta\right) \tag{50}$$

Step 2. Transforming the solution to an analytical form

In order to represent the solution analytically, c_δ was plotted against δ and fitted using an exponential function (Equation 51) with an error of 10^{-11}. The result is demonstrated in Figure 44, against the numerical solution.

$$c_\delta = 2.316556800348546 \cdot e^{-\delta} + 0.6937466336515017 \tag{51}$$
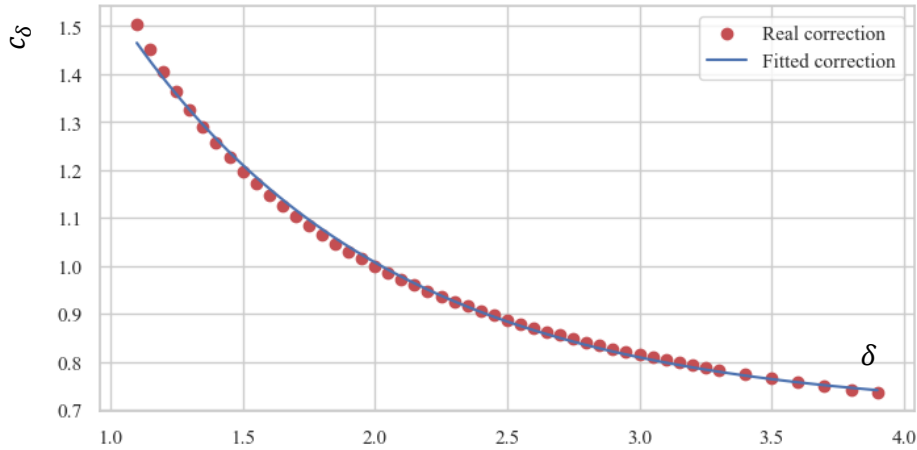
Figure 44. Fitting the correction coefficient function.

Step 3. Empirical solution

The combination of these steps leads to a general model adapted to the shape deviations, which has an empirical solution that does not depend on influence radius (Equation 52), the solution is not applicable when influence radius is a planimetric function. The solution can be reduced to a classical Sroka and Schober (1982) solution by setting $\delta = 2$. The solution is presented graphically (Figure 45) to show the changes in the subsidence profile and the location of the inflection point due to the shape parameter.

$$S(r) = \frac{2.3165568 \cdot e^{-\delta} + 0.6937466}{R^2} \exp\left(-\pi \left(\frac{r}{R}\right)^\delta\right) \tag{52}$$

In conclusion, this solution (Equation 52) can cover the shape deviation discussed in Chapter 6.3. However, this solution does not cover the asymmetric cases and is more applicable to a uniformly distributed stress area.
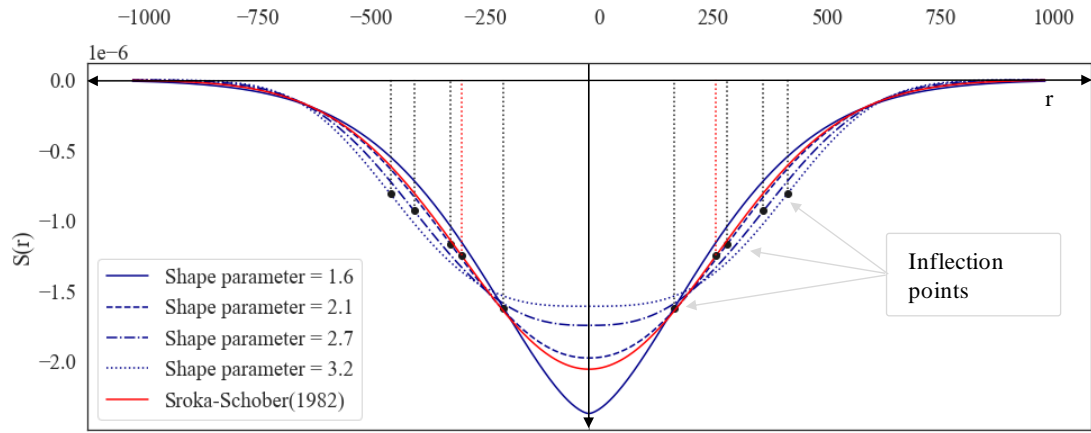
Figure 45. The Influence Function (Equation 51) demonstrated according to different shape parameters.

7.3   Unifying solution

According to the aforementioned investigation, the asymmetry and shape deviation patterns are mathematically combined in a unifying solution (provided by Equation 53).

$$S(r,\varphi) = \frac{V \cdot z(t)}{\int_0^{2\pi} \int_0^{\infty} \left(exp\left(-\pi \frac{r^{\delta}}{R(\varphi)^{\delta}}\right)\right)^2 r \, dr \, d\varphi} \cdot exp\left(-\pi \left(\frac{r}{R(\varphi)}\right)^{\delta}\right) \tag{53}$$

This unifying equation can have different implementations.

1.   When $\delta = 2$ and $R(\varphi) = const$, the solution related the assumption of symmetry and the normal distribution shape of subsidence. The integral under the volume will then be R^2 and provide a classical Sroka-Schober (1982) solution.

2.   When $\delta = 2$ and $R(\varphi) \neq const$, the solution related the assumption of asymmetry and the normal distribution shape of subsidence. In the specific case when $R(\varphi) = R_0(1 + Bsin(\varphi))$ the integral will be $\frac{1}{2}R^2(2 + B^2)$, and the solution becomes a corrected Quasnitza (1988) solution.

3.   When $\delta \neq 2$ and $R(\varphi) = const$, the solution related the assumption of symmetry but varied the subsidence distribution shape from normal, similar to the solution of

Eikermeier (2005). To solve the integral, the empirical method is suggested in the form of

$$\frac{1}{2.316556 \cdot e^{-\delta} + 0.69374}.$$

4.   When $\delta \neq 2$ and $R(\varphi) \neq const,$ there is a new combination. The solution related the assumption of asymmetry and varying the subsidence distribution shape from normal. The analytical solution of the integral does not exist and so, in this case, a numerical calculation should be applied.

7.4   Conclusion and outlook

The present adaptation of the empirical prediction model is intended to cover an observed pattern of subsidence due to stress conditions. According to the numerical results, stress conditions can lead to significant deviations in the subsidence profiles. The deviations include the magnitude of the subsidence, the degree of asymmetry, shifts in the position of maximum subsidence and changes in the angle of influence. The different patterns are sensitive to the different rock mass parameters that can be used to evaluate the potential for deviation.

According to the analysis of the empirical subsidence prediction models and numerical investigation, asymmetry and shape deviation would improve the quality of the empirical model. Thus, the chapter presents a potential for the development of subsidence prediction methodologies by incorporating considerations of shape change and asymmetry. It suggests modifications to existing models to take these factors into account, using the ideas developed by Eickermeier (2005) and Quasnitza (1988).

The solution for subsidence asymmetry proposed by Quasnitza (1988) suggests considering the influence angle as a function of direction. However, this documented solution does not take into account other types of asymmetries (non-bilateral) and does not ensure a balance between subsidence volume and volume shrinkage. To address these limitations, a new function has been introduced that can account for any type of asymmetry, based on the $R(\varphi)$ distribution, and ensures an appropriate volume balance (Equation 45).

The basic solution proposed by Eickermeier (2005) introduced a shape parameter δ that controls the shape of the function. However, this solution only satisfies the volume balance under certain limited conditions. To overcome these limitations, another method for volume balance is proposed. A new proposed empirical solution (Equation 51) considers the shape parameter (δ) variation in the volume balance and reduces the complexity of the original method by one variable (ζ).

For a subsidence case where both patterns (asymmetry and shape deviation) are expected, a unifying solution is proposed (Equation 52). This solution, depending on the parameters used, can take a form of the classical Sroka-Schober (1982) solution, adopted Eikermeier (2005) or Quasnitza (1988) solutions, or even cover a combination of them. However, the solution for a combined pattern requires a numerical solution of the integral, although computational power is not usually a critical issue, nowadays.

Looking to the future, the results of this study may lead to more accurate and comprehensive subsidence predictions. The incorporation of shape deviations and asymmetry into these methods, as well as the development of a more flexible approach to subsidence shape, represents significant advances in the field. Further investigation could be devoted to the form of asymmetry, the angle difference is probably not the best method to incorporate asymmetry. This direction of investigation implies dependence of shape parameters from a direction, which is a challenging mathematical issue.

8   Application to a full scale

8.1   General information for a salt cavern storage field

The new empirical model was applied to an energy storage cavern in a salt dome in north-western Europe. The storage field, commissioned in 1971, was designed to create oil storage caverns in a salt dome. The Zechstein salt formations in the region provide an optimal environment for cavern construction due to their low permeability and ductile nature, which facilitate self-sealing and deformation resilience.

As of 2017, the facility had 75 operational caverns (Storag Etzel, 2022b). By 2022, the total number of caverns had increased to 86 (Appendix B) and categorised into three types:

- 11 brine-filled caverns functioning as buffer volumes with capacities ranging from 16,000 to 290\000 cubic meters;
- 25 oil-filled caverns designed for crude oil storage with capacities between 5,000 and 730,000 cubic meters;
- 50 gas-filled caverns serving as storage units for natural gas with capacities varying from 440,000 to 930,000 cubic meters.

The operation of such a large-scale underground storage facility is not without its challenges. The stress conditions in the region are influenced by gravitational, tectonic, and cavern-induced stresses. The latter, triggered by cavern excavation and operation, can potentially lead to deformation and subsidence. This is where the importance of accurate subsidence prediction comes into play.

Subsidence, a significant concern for underground storage facilities, is caused by the extraction of salt during cavern construction, coupled with the cyclical injection and extraction of fluids. This can change the stress state, causing neighbouring rock strata to deform and settle. Minimal subsidence has been observed, with the highest rates recorded being less than 10 mm per year.

To evaluate and mitigate potential subsidence impacts, comprehensive monitoring and modelling efforts, including geodetic surveys, interferometric synthetic aperture radar (InSAR) analysis, and annual classical levelling data collection, are employed. These initiatives underscore the importance of ongoing research in this area, ensuring the facility's long-term stability and operational efficiency.

8.2 Estimation of the observed subsidence surface as reference

To create a surface of subsidence based on the levelling measurements, Ordinary Kriging (OK) was used. OK uses a regular subsidence grid with a resolution of 35 x 35 m and takes into account spatial correlation for parameter estimation (the input is levelling data, provided in Figure 45, where the coordinates have been changed for privacy reasons (STORAG ETZEL, 2022)).

The OK approach is advantageous over simple interpolation or irregular data because it takes into account spatial dependencies, reducing potential bias. OK is particularly suited to irregular and sparse spatial distributions of data, such as the subsidence measurements at Etzel, providing unbiased predictions and accounting for spatial autocorrelation. By accounting for spatial dependencies, OK provides accurate and reliable subsidence predictions, outperforming deterministic interpolation methods (Cheng and Lu, 2000; Oliver and Webster, 2014).

The workflow for ordinary kriging applied to subsidence estimation includes the following steps (Oliver and Webster, 2014):

1. Data collection. Gather subsidence measurements from levelling (Figure 46), STORAG ETZEL (2022);

2. Exploratory data analysis. Analyse the spatial distribution and characteristics of the collected data, identify trends or patterns, and examine the presence of outliers;

3. Variogram modelling. Calculate the experimental variogram, which quantifies the spatial dependence between pairs of data points at different separation distances (lags). Then, a theoretical variogram model is fitted to the experimental variogram, ensuring that it satisfies the conditions of positive definiteness and stationarity. For the data set of the Etzel Storage, the variogram and its model is presented in Figure 47. On the plots it seems that the secondary structure appears in the direction of 150 degrees, according to the recommendations the variogram adapted to the 'smallest' structure;

4. Ordinary Kriging interpolation. Using the fitted variogram model, estimate subsidence values at unsampled locations, by calculating a weighted average of nearby observations. The modelled variogram used nug 100, minimum 1440, median 1680 and maximum 1740. Figure 48 shows the subsidence surface for Etzel based on the levelling data and aforementioned variogram model.
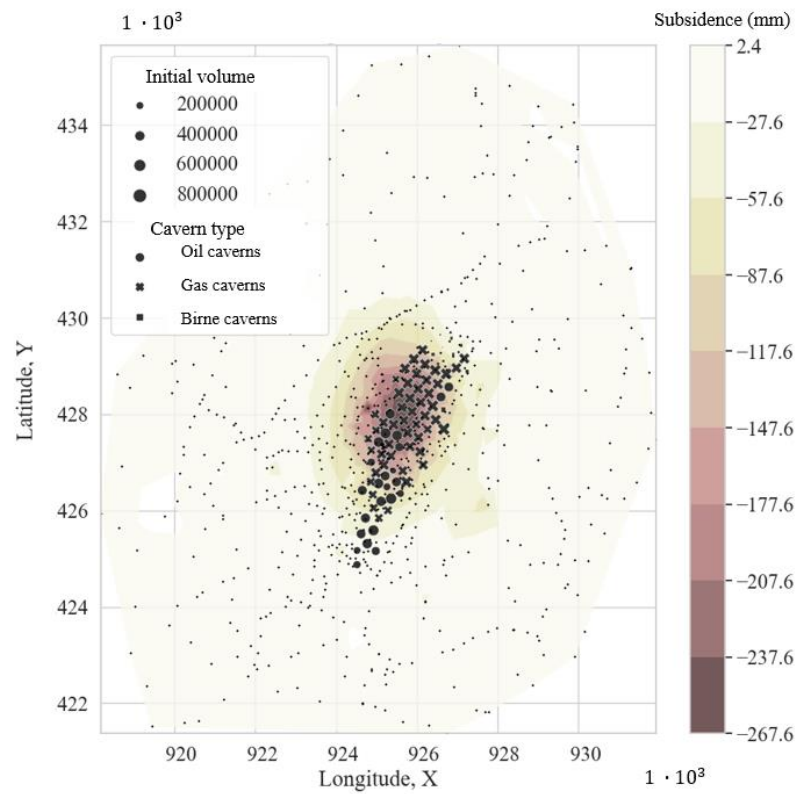
Figure 46. Initial levelling and cavern data, 2017-2022 (Storage Etzel, 2022a)
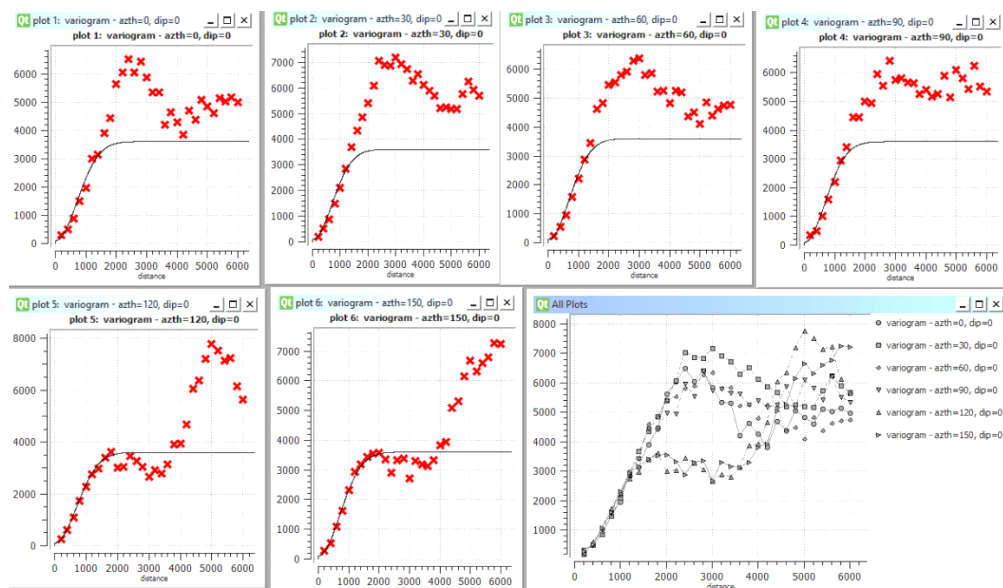
Figure 47. Variogram and variogram models with lag distance 200, lag tolerance 100 for every 30 degrees, made with the SGeMS programme, based on the levelling data for the years 2017-2022, provided by the company 'STORAG ETZEL, Energy Storage Solution'.
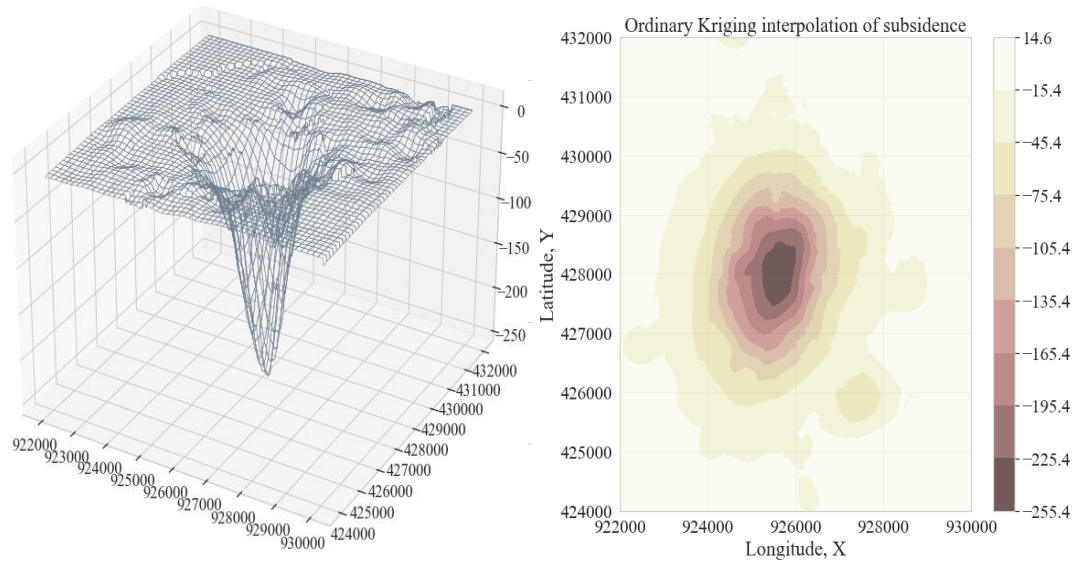
Figure 48. OK interpolation of subsidence surface from 2017-2022 for the Etzel energy storage field, based on the levelling data.

8.3   Model implementation

The implementation of the models requires both the parameters and the cavern data. The relevant cavern data, together with their descriptions, are given in Appendix C. The variation in cavern fill types can potentially affect the magnitude of convergence and, consequently, subsidence. In addition, the time influence function cannot be replaced by a constant because the caverns have different start times.

To estimate the parameters, observational data and a model are needed. The observation data consists of subsidence measurements obtained by levelling between 2017 and 2022. The use of a consistent measurement method (levelling) allows parameter estimation without the need for additional weighting data.

To validate the assumptions regarding the shape and asymmetry of the subsidence distribution, the results obtained from the classical Gaussian model and its extensions covering relative assumptions, are compared with the actual data. The unified approach (Equation 52 in the previous chapter), which includes and extends the approaches of Sroka-Schober (1982), Quasnitza (1988) and Eickermeier (2005), was implemented for four specific cases:

a.   The $\delta = 2$ and $R(\varphi) = const$ model, becoming a Sroka-Schober (1982) model. The solution related the assumption of symmetry and a normal distribution of subsidence;

b.   The $\delta = 2$ and $R(\varphi) = R_0(1 + Bsin(\varphi))$ model, becoming a corrected Quasnitza (1988) solution. The solution related the assumption of asymmetry and a normal distribution of subsidence;

c.   The $\delta \neq 2$ and $R(\varphi) = const$ model, becoming a simplified and corrected Eickermeier (2005) solution. The solution related the assumption of symmetry but varying the subsidence distribution shape from normal; and

d.   The $\delta \neq 2$ and $R(\varphi) = R_0(1 + Bsin(\varphi))$ new combination model. The solution related the assumption of asymmetry but varying the subsidence distribution shape from normal.

According to the aforementioned description of a cavern, the time influence function z must represent the relationship with time and be influenced by the filling, comprehensively. To cover the requirements, a classic time dependency function is used (Equation 4, Chapter 4).

8.3.1   Parameter estimation results

The subsidence magnitude at specific coordinates is calculated in Python by considering the cumulative impact of multiple caverns. To estimate the required parameters, such as $c, \cot\beta, \varphi_0, B$ and δ, the SciPy library's (SciPy Community, 2019) method of residuals minimisation was employed.

For global parameter estimation, the Basin-hopping approach is chosen over other methods. The advantage of Basin-hopping lies in its ability to avoid local minima through stochastic perturbations, enabling a more comprehensive search across multi-dimensional parameter spaces. This contrasts with methods like the Gauss-Newton iterative adjustment, which is more prone to getting stuck in local minima or Genetic Algorithms and introduces more randomness, requiring a larger number of function evaluations.

Other parameter estimation methods were also tested for comparison, as discussed in Chapter 4.3.3, but they either yielded similar or worse results. Utilising Python's SciPy library (SciPy Community, 2019) for this purpose is advantageous because it offers pre-optimised algorithms and functions. The parameters for models presented in Table 10 arise from the parameter estimation process. The discussion of the parameters is provided below.

Table 10. The parameters for different assumptions. dX and dY represent a dislocation of the subsidence maximum from the cavern axis.

	Model:		c_{gas}	c_{oil}	c_{brine}	γ, degree	dX, degree	dY, degree	φ_0, degree	B	δ
a	$\delta = 2$ $B = 0$	Classical solution	0.012 μ≈0.6%	0	0	33.23	15.5	0.6	0	0.00	2.00
b	$\delta \neq 2$ $B = 0$	Unifying shape	0.013 μ≈0.65%	0	0	33.86	16.0	1.7	0	0.00	0.99
c	$\delta = 2$ $B \neq 0$	Unifying asymmetry	0.023 μ≈1.1%	0.003 μ≈0.15%	0	24.06	15.5	1.7	209	0.54	2.00
d	$\delta \neq 2$ $B \neq 0$	Unifying solution	0.036 μ≈1.7%	0.005 μ≈0.25%	0	30.85	18.3	0.2	209	0.54	1.50

Convergence related parameters. The estimated parameters show that a gas cavern has a higher convergence rate, which makes sense due to the higher compaction of gas relative to oil and brine; this confirms the conclusions of other authors in the field (Tajduś et al., 2021b). The convergence of brine, estimated as 0, seems unrealistic. The value for oil caverns looks underestimated, which could be partly explained by their location: most of them are surrounded by gas caverns and have higher convergence and, in general, longer exploitation periods (the location of caverns, their volume and exploitation time can be seen in Appendix D and E). The problem with overestimating one parameter and underestimating another can be seen as a potential for the development of parameter estimation algorithms; however, for this particular research, the topic is out of scope.

Dislocation of maximum subsidence from cavern axis. For all solutions, the maximum subsidence displacement is in the northern direction, mainly around 15 degrees. This value was estimated as the critical deviation value in the numerical investigation.

Asymmetry coefficient B and its direction. According to the estimated parameters, there is a strong asymmetry in the north-west direction.

Shape deviation showed quite different results for solutions b and d. Since parameter B is high for solution d and c, it can be assumed that the shape parameter (δ) estimated for the unifying shape has been overestimated to cover the asymmetry pattern. However, the development of parameter estimation is not an aim of this thesis; therefore, this topic is not discussed in detail.

8.4   Statistical validation of models

In order to compare and evaluate the performance of different models, several evaluation metrics were used. These include the Mean Squared Error (MSE), the Mean Absolute Error (MAE), the Standard Deviation (STD), the R2 value, the distribution of the residuals and QQ-plots.

According to the statistical data presented in Table 11, both the integration of shape and asymmetry improves the results of the model. The BIC and AIC have been combined because they represent, more or less, the same parameter, balancing complexity and quality.

Table 11. The statistical values of the model solutions compared with levelling data.

Model	MSE	MAE	R2	STD	Median Deviation	AIC / BIC
Classical solution **(a)**	133	7.4	0.968	11.36	4.88	5665 5693
Unifying shape **(b)**	116	6.1	0.972	10.79	3.05	5567 5599
Unifying asymmetry **(c)**	105	6.4	0.975	10.15	4.15	5495 5532
Unifying solution **(d)**	91	5.5	0.978	9.46	3.28	5394 5435

According to the table evaluation, the best model is represented by the unifying solution, which improves the classical solution by all criteria. The introduction of shape deviation based on MSE improves the solution by 12%, asymmetry by 21% and both together by 31%. The difference in R2, AIC and BIC is not significant.

To identify the nature of the error, the QQ plot is used to analyse whether the residuals are normally distributed. The plot shows the quantiles from the theoretical distribution on the x-axis and the quantiles from the data set on the y-axis. The more the data set lies on the red line, the more it is normally distributed. On the other hand, a curved, skewed or S-shaped pattern of data would suggest that the data is not normally distributed. It could indicate skewness in the data or the presence of outliers. The deviation from the line indicates the existence of outliers, which has a significance for the pattern of the subsidence model, which is not covered.
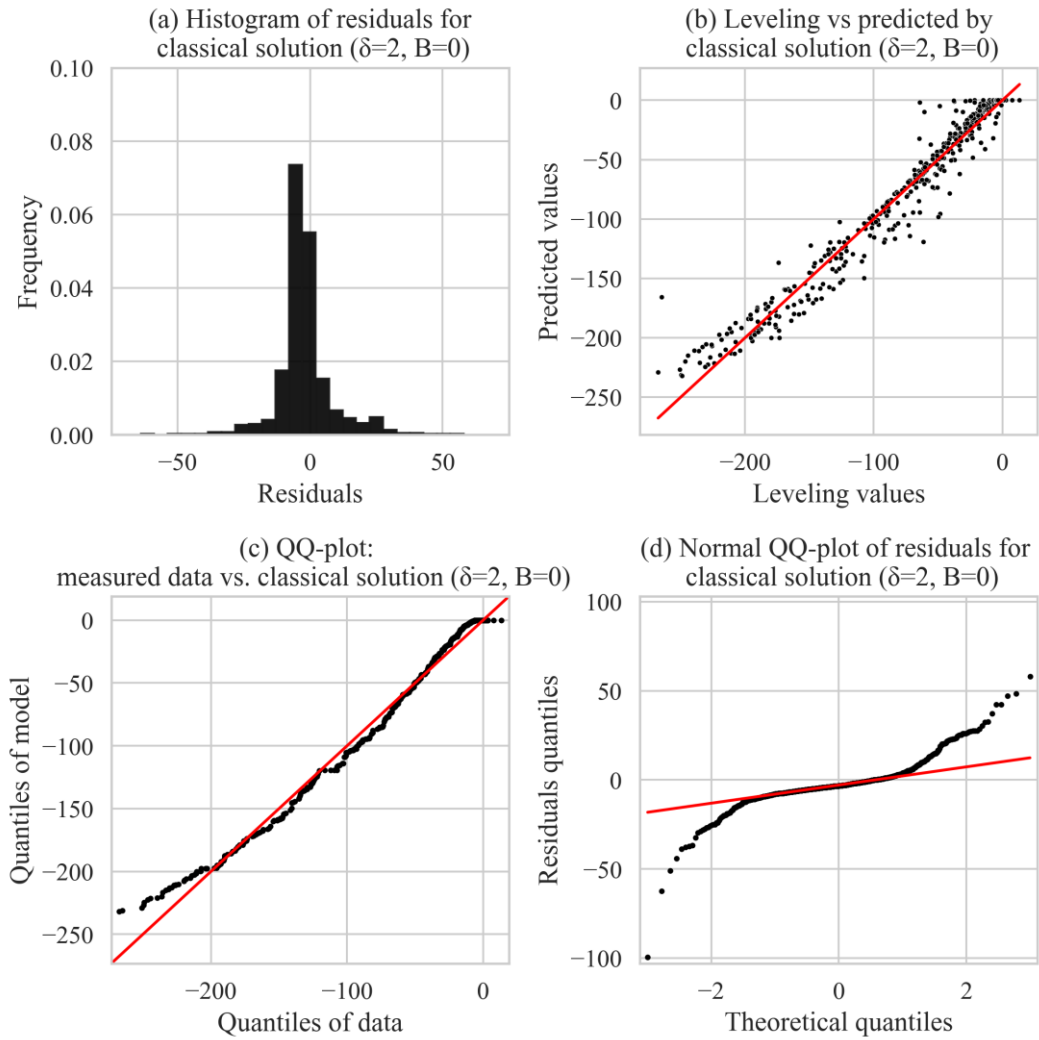
Figure 49. Statistical representation of the residuals for the classical solution (a), described in Table 10.

The statistical plots for the classical solution shown in Figure 49 represent the classical solution (a) Table 10 implementation. The solution represents a normal distribution, which shows skewness, meaning that the residuals are not normally distributed. The comparison with other models is discussed below.
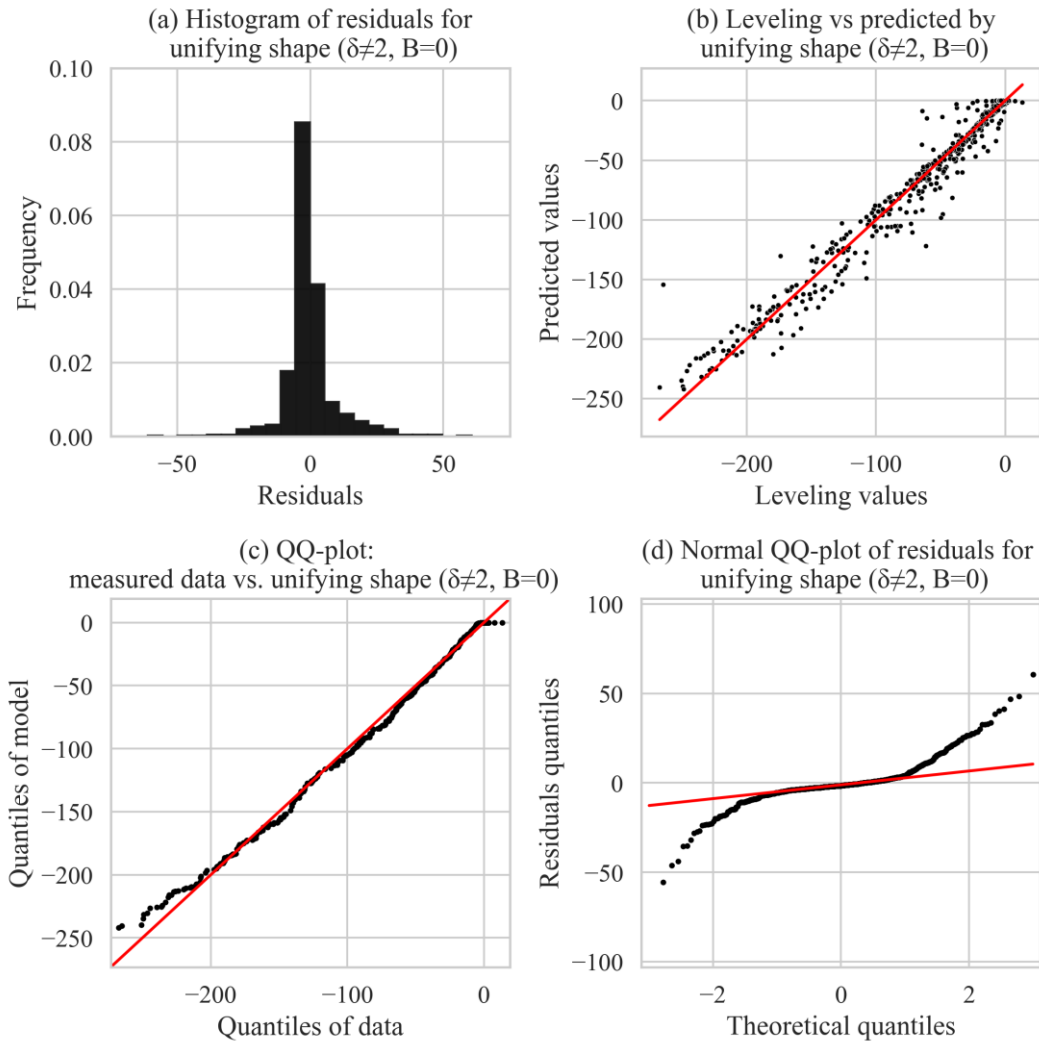
Figure 50. Statistical representation of the residuals for unifying shape solution (b), described in Table 10.

In the solution with shape adaptation, as shown in Figures 49 (a) and 50 (a), an increase in the frequency of residuals around 0 is observed, increasing from 0.72 to 0.86; this is the number of points where the residuals are around 0. In part (c) of Figures 49 and 50, skewness is evident in both cases but the integration of shape adaptation seems to mitigate this skewness according to the curvature magnitudes, as suggested by the QQ plot. A more linear character is also evident in the plot of predicted versus measured values, especially around 0, and at the maximum magnitude of subsidence, when compared to the classical solution. In conclusion, the shape fitting improves the quality of the prediction but the asymmetry is still presents on QQ plots.
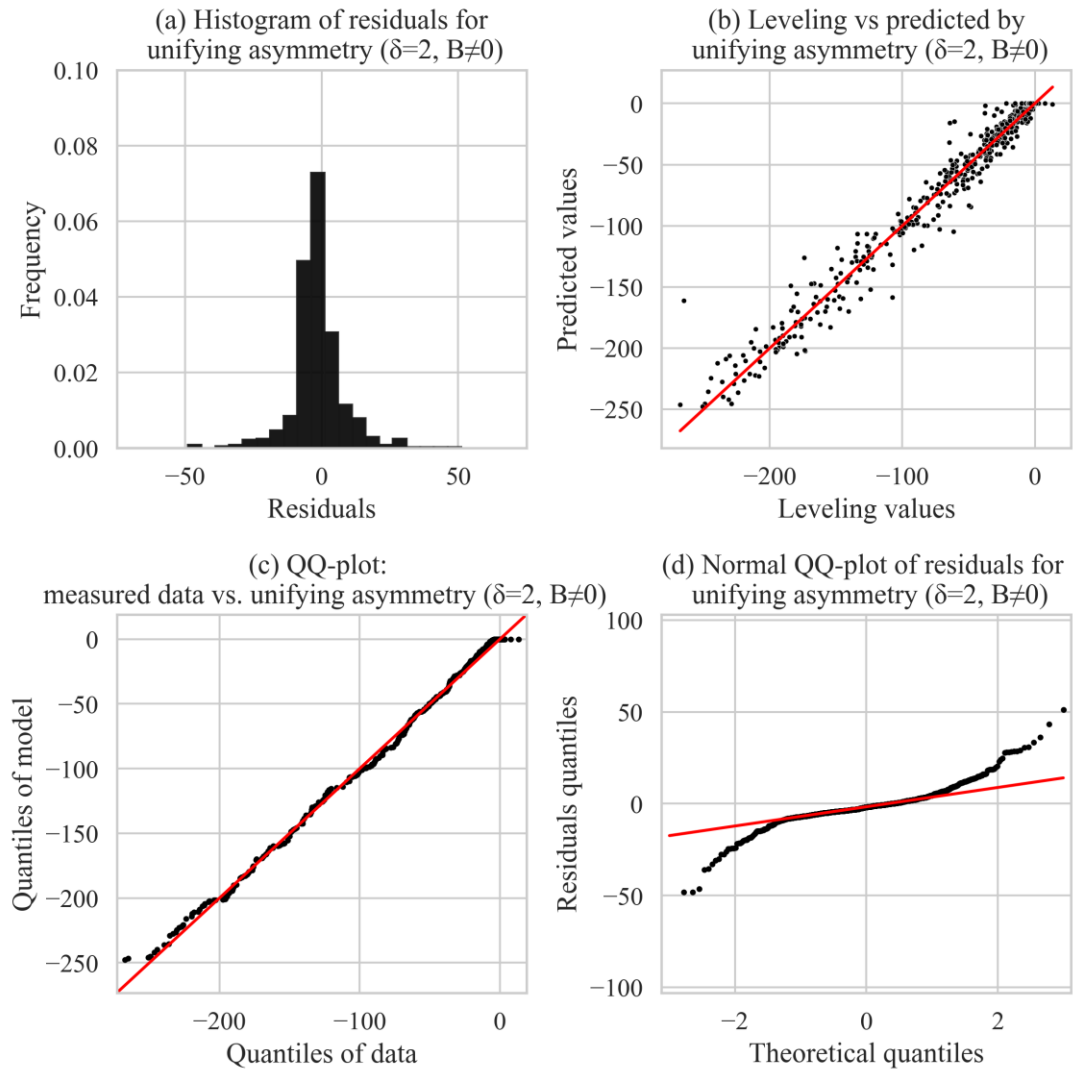
Figure 51. Statistical representation of the residuals unifying asymmetry solution (c), described in Table 10.

In the solution with asymmetry, as shown in Figure 51, the incorporation of asymmetry in the subsidence prediction model appears to narrow the histogram towards 0, compared to the classical solution (Figure 49), and reduce its skewness, compared to the classical solution and the unifying shape solution (Figure 50). However, the histogram of the residual, in this case, is wider than for the unifying shape solution (Figure 50). This trend towards the target value is also evident in the QQ plot and the plot of predicted versus measured values. The convergence to the line on the QQ plot implies that the inclusion of bilateral asymmetry in the model reduces the skewness of the residuals. The residual part of the skewness could either represent outliers or indicate a more complex asymmetrical

structure. In conclusion, the assumption of asymmetry by angle of influence covers most of the asymmetry, but does not increase the number of points where residuals are around zero.
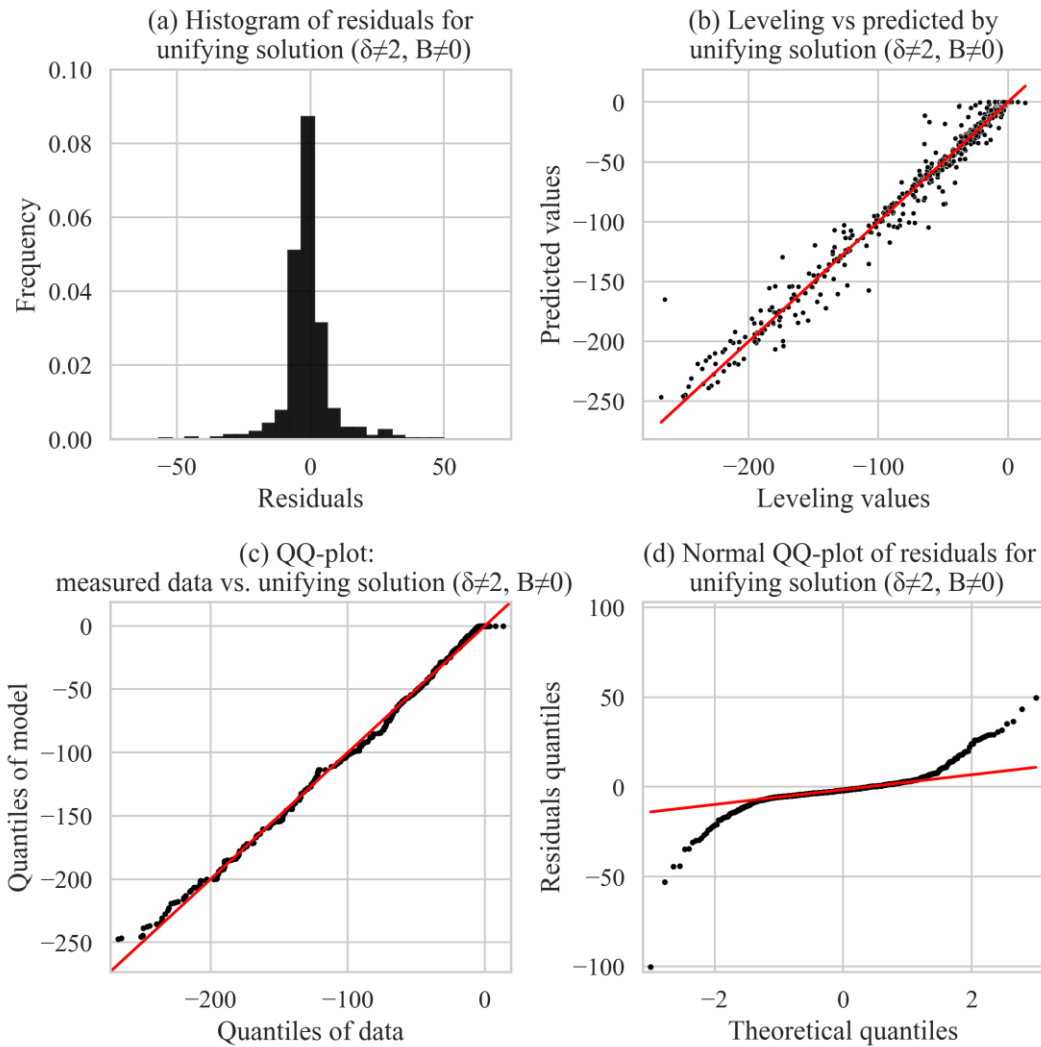
Figure 52. Statistical representation of the residuals for the unifying solution (d), described in Table 10.

For the solution with asymmetry and shape patterns shown in Figure 52, the residual histogram has the highest frequency (around 0) among the presented solutions (Figures 49-51. The skewness of the QQ plot is the same as for the asymmetry adopted solution (Figure 51). Although the unifying solution has the highest number of parameters, it still has lower AIC and BIC results (discussed in the basics), which evaluate the balance between complexity and quality of the prediction model.

In order to visualise the differences between the relative caverns, the residuals were mapped (Figure 53). These maps were constructed from the differences between the subsidence surface (based on levelling data and ordinary Kriging interpolation) and

simulations based on different cases of the unified solution. On the map, a negative difference means that the estimated subsidence is overestimated (blue) and a positive difference means that it is underestimated (red).
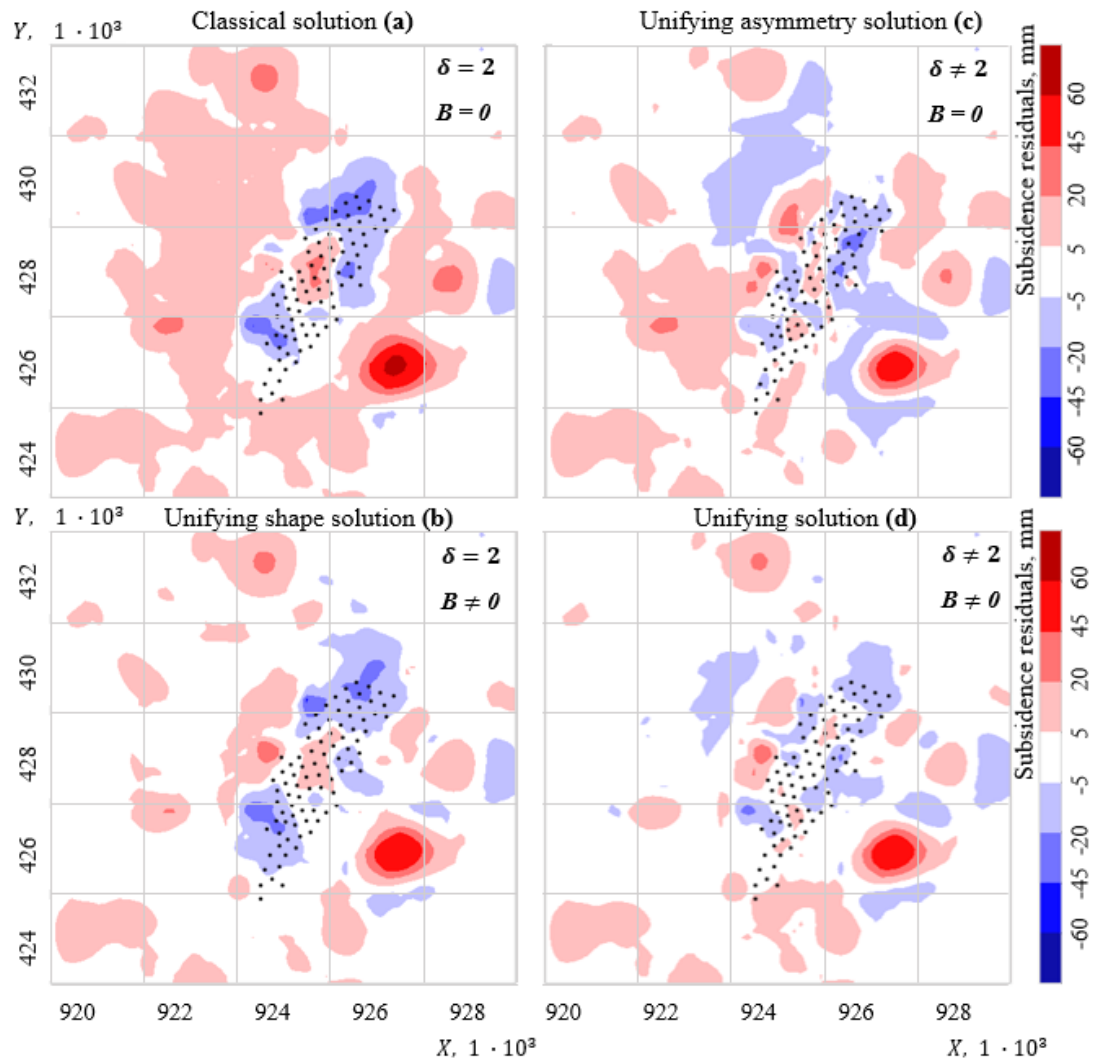
Figure 53. The residuals maps for different solutions described in Table 10. Black points represent the location of caverns.

The figure shows four residual maps where different patterns were included in the unifying solution:

a. The classical solution is a solution with a normal distribution shape and symmetric pattern (Figure 53a, Table 10). The residual distribution shows that the solution overestimates the subsidence in the central area where the caverns are located, which can be a sign of a shape deviation problem. On the other hand, in the periphery there is an oriole of underestimation that is wider in the north-west direction, emphasising the asymmetric pattern of subsidence.

b. The unifying shape solution is a solution with a non-normal distribution shape of subsidence and symmetric pattern (Figure 53b, Table 10). The model has a better solution in the central part but an underestimation in the north-west direction. The residuals are smaller, on average, resulting in a smaller MSE. The better results, compared to the classical solution, are evident in the shape deviation pattern.

c. The unifying asymmetry solution with normal distribution shape but bilateral asymmetry pattern is shown in Figure 53c (Table 10). The peripheral part of the cavern field in the solution is mainly present in the area of ± 5 mm. The central area has no significant improvements, compared to the classical solution, and looks a bit worse compared to the shape unifying solution. According to the statistical evaluation, the application of this solution for this particular case is, in general, better than shape adaptation or a classical solution.

d. The unifying solution with a non-normal distribution of subsidence profile and bilateral subsidence asymmetry patterns is shown in Figure 53d (Table 10). Among all of the implemented solutions, the unifying solution presents the best statistical and visual parameters. Due to the visual observation, most of the asymmetry pattern is covered and the central part also has lower absolute residuals. Despite the higher parameters, due to the BIC and AIK criteria, it is the best balance between quality and complicity.

In order to investigate the difference in the solution in detail, normalised subsidence profiles were plotted in different directions for the classical and unified solution (in Figure 54, this presents a plan with cavern and profile lines; Figure 55 shows profiles in different directions).
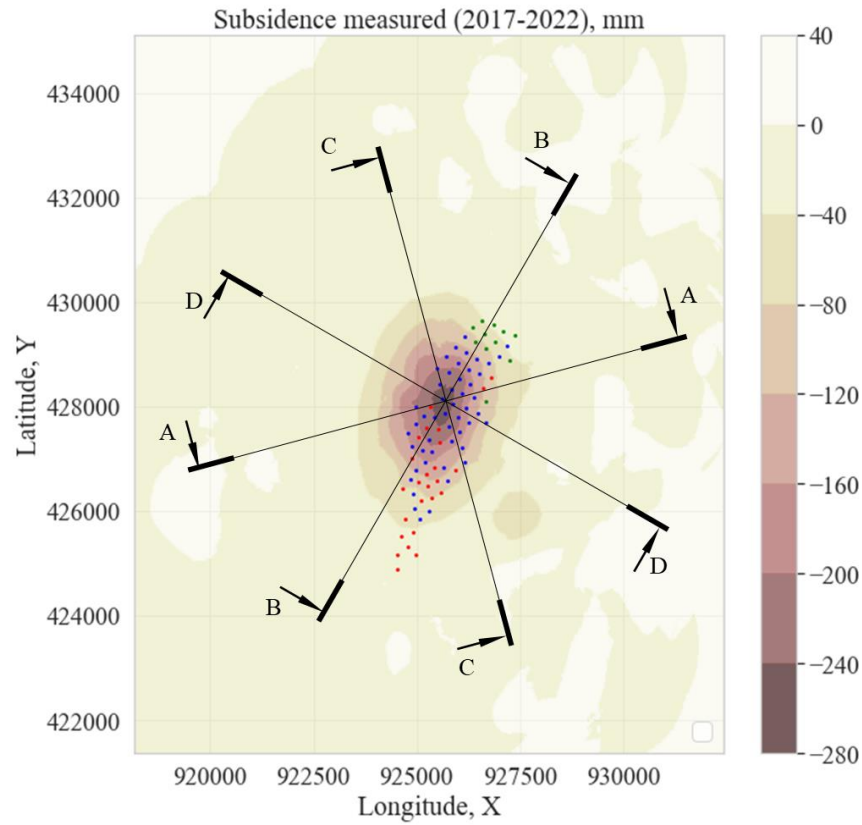
Figure 54. The subsidence prediction in the direction of symmetrical patterns.

Figure 55 shows the profiles of the measured data and those simulated by the classical solution (a) and the unifying solution (d) (Table 10) in the different directions (Figure 54). The shape deviation adaptation ensures the fitting of the maximum subsidence part with the same quality as the peripheral data. According to Figure 55 (from a to d), it is obvious that the classical solution balances between fitting the periphery and the central part of the subsidence, which is the mathematical limit of the model. The difference in precision between the left and right parts are different (a and c), which emphasises the asymmetry pattern that is not covered in the classical model. At the same time, the residuals for the unifying solution are more symmetrical. The central part the asymmetry is less valuable due to the magnitude but it can also be detected in Figure 55c and 55d.

Overall, the classical solution is able to cover either the periphery or the central parts of subsidence profile but tries to find a balance between the two, whereas, the new solution captures better the global shape of the subsidence profile.
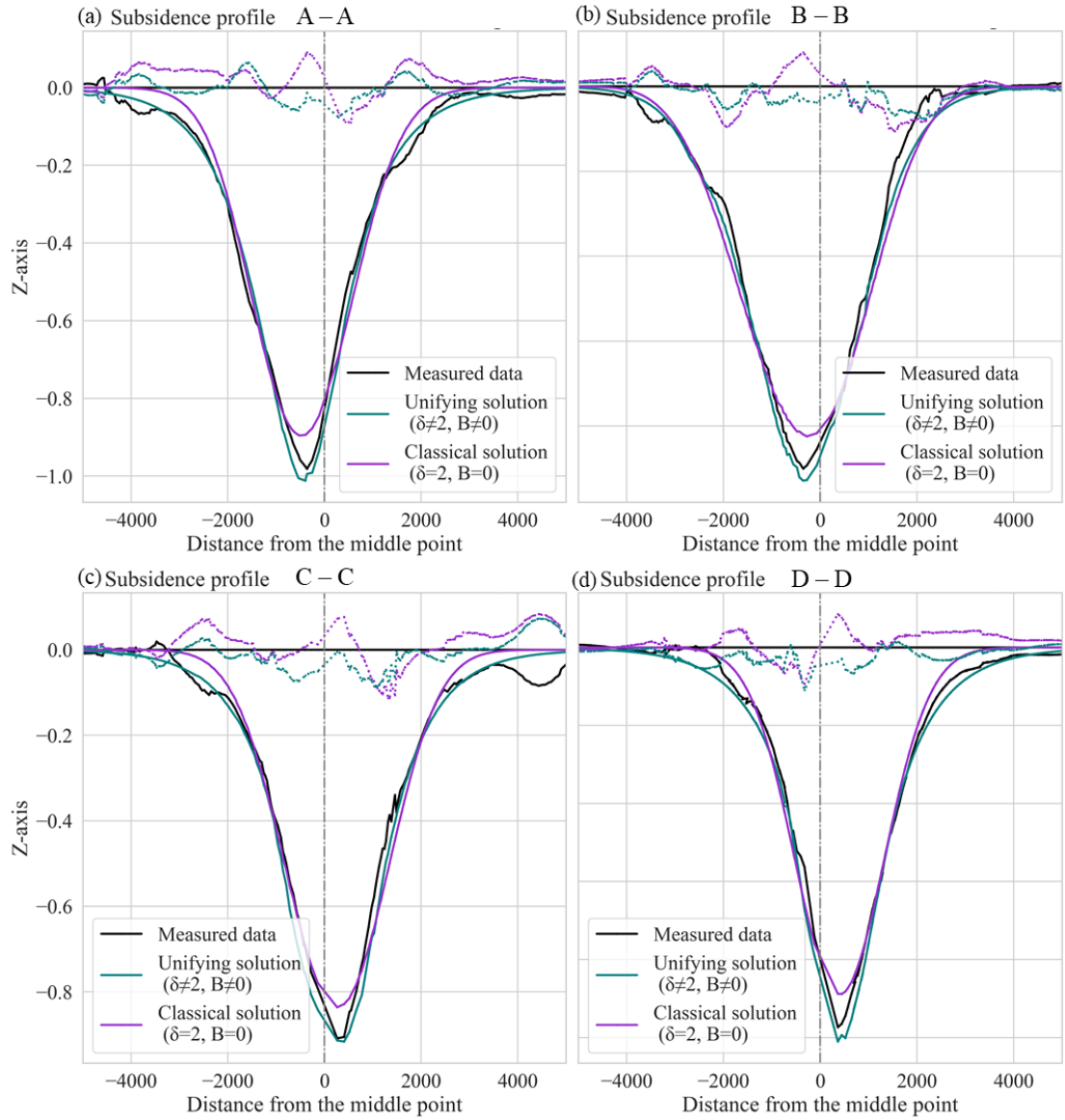
Figure 55. The subsidence profiles and residuals for classical and unifying solutions in different directions.

8.5 Conclusions

In accordance with the results obtained from the numerical experiment, it was found that stress conditions have the potential to induce asymmetry and shape deviation. In order to validate these findings, a classical Gaussian model, together with its adaptation for asymmetry and shape, was implemented in the field of salt caverns in order to estimate the subsidence over five years. The key to validation was to determine whether the inclusion of asymmetry

and shape deviation in the subsidence model could improve the accuracy of subsidence predictions. The degree of improvement was estimated based on a comprehensive statistical analysis that included the use of classical SME, MAE, and R2 parameters and residual distribution analysis.

The validation process has confirmed the initial findings by estimating that the inclusion of asymmetry and shape deviation in the subsidence prediction model, particularly in areas of high horizontal stress, can significantly improve the predictive capabilities of the model. This fact indirectly validates the results of the numerical experiments. However, since asymmetry and shape deviation exist in parallel with the subsidence process, the most effective approach is to incorporate both elements into a unified model. This approach ensures that the interaction between these two factors is adequately accounted for, thereby improving the predictive accuracy of the model. Unfortunately, an analytical solution to such a complex integral does not currently exist and can only be estimated numerically. This presents a challenge to the development of a unified model, but also opens up opportunities for future research and the application of empirical methods.

9 Conclusion

This thesis investigates the prediction of mine subsidence under tectonic influence. According to the classical understanding of subsidence, the subsidence trough is symmetrical and described as a normal distribution of the underground void. However, observations in areas of tectonic influence have shown a deviation from this picture. In these areas, subsidence with peripheral uplift occurs in an asymmetric and/or non-normal distribution. Using numerical investigations, this research comprehensively analysed subsidence profile deviation and developed an empirical model, which was able to cover it. The model is tested on a real case of subsidence and showed better results, compared to the classical method.

In the state of the art, the research gaps were identified, in relation to the connection between the studied anomalies and stress conditions and the coverage of the anomalies with the empirical subsidence prediction method. The research covered the gaps with the comprehensive analysis of a numerical experiment and an empirical model of the subsidence prediction method. With respect to the gaps, the thesis presents findings relating to:

- Coupling of rock properties with subsidence profile parameters to improve an understanding of the subsidence trough formation process.

- Development of a new influence function for the empirical subsidence prediction method covering different cases, such as normal distribution influence function, shape deviation and asymmetry.

In order to improve the accuracy of subsidence prediction methods by incorporating the effects of horizontal stress, while ensuring the plasticity of the empirical methods, research has been carried out to develop the main objectives 'step-by-step'.

The thesis started by developing a comprehensive understanding of the state of the art (the first objective). Different subsidence prediction methods were described, focusing on numerical modelling, which is commonly used for such case studies, and empirical models, which are more practical but limited to predicting global patterns. In empirical models, subsidence profiles are usually presented as a symmetrical distribution (a normal distribution in Germany and Poland). However, subsidence observations show deviations from this assumption, so-called 'anomalies'. The literature review showed that the presence of these anomalies, such as uplift, asymmetry and shape deviation, correlates with the presence of stress-related patterns. Different strategies for empirical models were developed, e.g. based on cell division, the sum of the different influence functions and the influence angle function from a geographical direction.

In conclusion, the lack of a comprehensive investigation of stress conditions on subsidence profiles, as well as a unifying solution to cover different anomaly types in one function, was identified. To cover the gaps, the following plan was proposed:

a. Employing a numerical experiment to provide an understanding of the subsidence patterns resulting from different stress conditions;

b. Developing the model that covers the patterns;

c. Comparing the residuals of new, and older models, implemented on a full-size subsidence field.

In order to implement the plan, a basic structure was set up under Objective 2. This objective had several components. It began with the introduction of empirical models for predicting subsidence. While these models share a common basic structure, they address different patterns. Notable models include Sroka and Schober's (1982) basic model, Quasnitza's (1998) asymmetry model, and Eickemeier's (2005) shape deviation model. The design of the numerical experiment was then discussed in detail. The insights gained from the results of the experiment were crucial in identifying key patterns. These patterns were then used to build a new comprehensive prediction model.

For data evaluation, observational studies are essential. Both levelling and InSAR data are suitable for this research. However, the state of the art referenced the absolute difference between these two types of data. As a result, levelling data was chosen for this investigation. These data allowed us to define the model parameters, which then lead to a comprehensive review of parameter estimation methods. In addition, statistical tools and methods were examined to compare different model implementations. The culmination of this research is the presentation of the final results.

The modelling and processing of the numerical experimental results (Objective 4) provided a deeper understanding of the main relationships between rock mass properties and subsidence profile parameters.

Firstly, the numerical investigation confirmed the assumption that subsidence asymmetry and shape deviation can occur due to stress conditions. However, the effect is different depending on the rock mass properties. The overall influence of stress state is complex and difficult to fit an empirical function to. However, statistical tools were used to estimate some of the causal relationships.

If the stress is uniformly distributed, the shape deviations are symmetrical, including the angle of influence and the maximum magnitude of the subsidence, while the non-uniformly distributed stress causes asymmetry. According to the investigation, the shape can deviate from the normal distribution, in terms of the position of the inflection point, with the inflection point moving towards the centre, in the case of compressive stress, and away from

it in the other case. However, the analysis also showed that the position of the inflection point not only depends on the stress conditions but, also, on the transformation of the deformation from a vertical to a horizontal direction and vice versa. In this sense, the different position of the inflection points leads to an asymmetry, which is measured as the skewness of the subsidence profile.

Asymmetry showed the greatest influence of uniaxial strength, density and stress factor. However, deeper analysis has shown that asymmetric shape formation occurs in the elastic phase of deformation. A longer elastic phase not only induces asymmetry but also has a relatively large influence on the maximum subsidence. During the elastic phase, the excess horizontal stress deforms the rock mass by increasing the resistance to vertical displacement, while the cracking process otherwise contributes to vertical displacement. Further increases in horizontal stress reform and deform the rock mass, narrowing the cracks which, in turn increases the above resistance. This interpretation explains the peaks in the subsidence prediction plots versus applied stress.

A particular success was the estimation of the contribution of stress to the definition of the influence angle. It was shown that stress can be a reason for a 12-degree deviation in the magnitude of the influence angle. The estimated function is in good agreement with numerical experiments, but needs to be extended to include depth effects and verified in a real subsidence case.

In conclusion, the influence of the form of asymmetry and shape deviation of the subsidence profile was confirmed and lead to the development of the empirical subsidence prediction method, which is able to cover them (Objective 5). A unifying solution, based on the different ideas and their combinations, was applied to cover the patterns of asymmetry and shape deviation estimated by numerical investigation. In particular, the ideas of Eickemeier (2005) - for shape deviation, Quasnitza (1988) - for asymmetry, and Sroka and Schober (1982) as a basis, were combined and extended.

To validate the new solution (Objective 6), the ETZEL energy storage field of a salt cavern was selected. The levelling data were used to estimate parameters for different assumed patterns: normal distribution, shape deviation, asymmetry and a combination of patterns. The predicted subsidence trough was calculated for all solutions. According to the statistical analysis, which includes the complicity and accuracy of the model, it was estimated that, in this particular case, the solution gives a better result. Based on the equally weighted combination of different statistical parameters, the unifying solution gives a 24% better statistical result than the representation of the subsidence profile as a normal distribution.

9.1   Limitations

The experimental part of the study was based on the results of numerical modelling, which assumed a degree of simplification by simulating real conditions and rock behaviour, leading to the numerical constraints. Relying on the numerical models potentially leaves gaps in the actual field data, as the approach cannot assess whether the data are representative. Despite the variety of rock masses considered, it is not clear which result is more representative of real rock mass behaviour and which is purely numerical in nature. Furthermore, the additional simplification applies to homogeneous rock masses, leaving the question of inhomogeneous rock mass behaviour unanswered. The research investigates the stress conditions, despite the geological structures or the groundwater which can modify them, although neither has been considered in this research. Furthermore, in the models presented, the stress distribution is characterised as a gradient, a representation which may vary in real cases. All of this affects the numerical experimental results. Augmenting the validation process with more field studies could address these gaps.

With regard to the proposed subsidence prediction model, although innovative, it introduces a degree of complexity due to the numerical estimation of the integral in some cases. However, with modern technological capabilities, these challenges appear to be manageable. The most resource-intensive phase is parameter estimation, especially when dealing with large data sets. However, a more serious limitation has been identified in this regard. In the prediction method, different parameters have different meanings, while parameter estimators only rely on their mathematical definition. Thus, the importance of one factor may be masked by the effects of another. This limitation can lead to a lack of understanding of the subsidence process and to the estimation of parameters that are unlikely to be reliable.

9.2   Outlook

This work presented a first step towards investigating the stress conditions that influence the subsidence profile. While the work presented a way to cover the numerically confirmed stress contribution, there are other issues that can be investigated further.

In the first place, the perspective belongs to the understanding of the subsidence process itself. In spite of the comprehensive analysis presented here, the causal relationship

can be better investigated through additional experiments, e.g. studying subsidence as a dynamic process, looking at the contribution of stress relief conditions in more detail. More detailed investigation of the cracking process and its influence on the magnitude and ratio of subsidence is also suggested.

While this work deals with the combination of influences of different rock mass parameters, a significant contribution to the understanding of subsidence trough formation could be a more specific, concentrated investigation, e.g. analysing the contribution of each factor separately and then using this knowledge to unpick the influence of the rock parameters on the subsidence profile parameters. As discussed earlier, the investigation of the changes in the angle of influence due to mining depth could contribute to the field of subsidence engineering.

As mentioned above, the stress condition is considered in terms of stress ratio and is either uniformly distributed or implemented as a gradient; the investigation of other forms of stress distribution, to understand whether the difference in subsidence troughs with stress gradients is significant, could not only be an extension of the thesis, but would also help us to understand the response of the subsidence trough to the stress difference.

With regard to the subsidence parameters themselves, it is important to have an appropriate influence function. In the state of the art, different methods are provided, which could also be developed for the discovered features. The work is limited to the polar coordinate influence function but the 3-dimensional cell-based solution may be more applicable or provide better results. The integration and comparison of different assumptions could extend this research.

As always, any solution would benefit from wider validation and comparison with other solutions on real subsidence cases. A neural network algorithm could be used to better understand the causation between observable stress sources (as described in the state of the art) and subsidence parameter deviation. Work in this direction will lead to the more mathematical topic of the development of parameter estimation techniques, in order to provide reasonable parameters.

Despite the limitations and outlook provided, the thesis presents a comprehensive study of the contribution of stress to the subsidence prediction model, resulting in a significant improvement in prediction accuracy. The implemented model has been successfully applied and validated, demonstrating its potential for universal applicability. Furthermore, the stress distribution sources provided allow the identification of areas that would benefit from model extension without the need for extensive geomechanical investigations. By covering symmetrical solutions, the proposed model provides valuable practicality.

In summary, this thesis makes a significant contribution to the understanding of subsidence prediction under tectonic influences. While acknowledging the identified limitations, the research opens up promising avenues for future investigation and advancement in subsidence prediction methodology.

References

1.   Adams, J. & Bell, J.S. (1991). Crustal Stresses in Canada. Geological Society of America, The Geology of North America, Neotectonics of North America, pp. 207-222.

2.   Ahlers, S., Röckel, L., Hergert, T., Reiter, K., Heidbach, O., Henk, A., Müller, B., Scheck-Wenderoth, M., & Anikiev, D. (2022). The crustal stress field of Germany: a refined prediction. Geothermal Energy 10, 10, https://doi.org/10.1186/s40517-022-00222-6.

3.   Aksoy, C.O., Kose, H., Onargan, T., Koca, Y., & Heasley, K. (2004). Estimation of limit angle using displacement discontinuity analysis in the Soma coal field, Western Turkey. International Journal of Rock Mechanics and Mining Sciences, 41, pp. 547-556.

4.   Alam, A.K.M.B., Fujii, Y., Eidee, S., Boeut, S. & Rahim, A. (2022). Prediction of mining-induced subsidence at Barapukuria longwall coal mine, Bangladesh. Scientific Reports, 12. 14800. https://doi.org/10.1038/s41598-022-19160-1.

5.   Alizadeh-Khameneh, M. A. (2015). On Optimisation and Design of Geodetic Networks (Thesis). https://doi.org/10.13140/RG.2.2.22724.32644.

6.   Amadei, B. and Stephansson, O. (1997). Rock Stress and Its Measurement. Springer Dordrecht. https://doi.org/10.1007/978-94-011-5346-1.

7.   Anderson, E.M. (1951) The dynamics of faulting and dike formation with application to Britain. Oliver and Boyd, 2nd Edition, Edinburgh, pp. 133-147.

8.   Arson, C. (2020). Introduction to Theoretical Geomechanics. Georgia Institute of Technology [Online]. Available at: https://emi-poromechanics.github.io/resources/Arson_geomech.pdf (Accessed: May 2020).

9.   Asadi, A., Shahriar, K., Goshtasbi, K., & Najm, K. (2005). Development of a new mathematical model for prediction of surface subsidence due to inclined coal-seam mining. Journal of The South African Institute of Mining and Metallurgy, pp. 15-20.

10.   Aurelio, M.A. (2000). Shear partitioning in the Philippines: Constraints from Philippine Fault and global positioning system data. Island Arc, 9(4), pp. 584-597. https://doi.org/10.1111/j.1440-1738.2000.00304.x.

11.   Awershin, S.G. (1947). Сдвижение горных пород при подземных разработках [Shear displacement of rocks in underground mining]. Ugletekhizdat, Moskow. 245 pages.

12. Benndorf, J. (2021) 'Geomonitoring und Markscheidewesen als integrativer Teil des Umweltmanagements in der Rohstoff-und Energiebranche - zukünftige Aufgaben', AVN - Allgemeine Vermessungs-Nachrichten. pp. 237-247. Available at: https://gispoint.de/artikelarchiv/avn/2021/avn-ausgabe-052021/7208-geomonitoring-und-markscheidewesen-als-integrativer-teil-des-umwelt-managements-in-der-rohstoff-und-energiebranche-zukuenftige-aufgaben.html?journal=2&cHash=bd3edee2605d2309e1726981c166f0e8 (Accessed: March 2022).

13. Berry, D.S. (1963). Ground movement considered as an elastic phenomenon. Min. Engr, 123(37), pp. 28-41.

14. Bi, P. (2019). Finite Element Analysis Applications: A Systematic and Practical Approach. Academic Press. 504 pages. https://doi.org/10.1016/C2016-0-00054-2.

15. Bitelli, G., Bonsignore, F., & Unguendoli, M. (2000). Levelling and GPS networks to monitor ground subsidence in the Southern Po Valley. Journal of Geodynamics, 30, pp. 355-369. https://doi.org/10.1016/S0264-3707(99)00071-X.

16. Bitelli, G., Bonsignore, F., Del Conte, S., Novali, F., Pellegrino, I. & Vittuari, L. (2015). Integrated Use of Advanced InSAR and GPS Data for Subsidence Monitoring. pp. 147-150. https://doi.org/10.1007/978-3-319-09048-1_29.

17. Blachowski, J. (2016). Application of GIS spatial regression methods in assessment of land subsidence in complicated mining conditions: case study of the Walbrzych coal mine (SW Poland). Natural Hazards, 84, pp. 997-1014. https://doi.org/10.1007/s11069-016-2470-2.

18. Braun, A. (2021). Retrieval of digital elevation models from Sentinel-1 radar data – open applications, techniques, and limitations. Open Geosciences. https://doi.org/10.1515/geo-2020-0246.

19. Britannica. (n.d.). 'Rock (geology) - Mechanical Properties'. Available at: https://www.britannica.com/science/rock-geology/Mechanical-properties (Accessed: July 2021).

20. Bru, G., Portela, J.J., Ezquerro, P., Navarro, M., Staller, A., Béjar-Pizarro, M., Guardiola-Albert, C., Fernández-Merodo, J., López-Vinielles, J., Tomás, R. & Lopez-Sanchez, J. (2022). Imaging land subsidence in the Guadalentín River Basin (SE Spain) using Advanced Differential SAR Interferometry. 5th Joint International Symposium on Deformation Monitoring (JISDM), 20-22 June 2022, Valencia, Spain. pp. 227 – 233. https://doi.org/10.4995/JISDM2022.2022.13826

21.

22. Bulin, N.K. (1971). The Present Stress Field in the Upper Parts of the Crust. Geotectonics (Engl. Transl.), 3, pp. 133-139. https://doi.org/10.1016/0040-1951(75)90132-8

23. Buljak, V. & Ranzi, G. (2021). Calibration of constitutive models. Constitutive Modeling of Engineering Materials. Academic Press. pp. 43-53. https://doi.org/10.1016/B978-0-12-814696-5.00007-1.

24. Busch, A. (2014). Bergwerk Ost der RAG AG, Analyse von Senkungserscheinungen außerhalb des prognostizierten Einwirkungsbereiches, Institut für Geotechnik und Markscheidewesen, TU Clausthal, Germany.

25. Busch, A. (2017). Bergwerk Lippe der RAG AG, Analyse von Senkungserscheinungen außerhalb des prognostizierten Einwirkungsbereiches, Institut für Geotechnik und Markscheidewesen, TU Clausthal, Germany. Available at:https://www.bra.nrw.de/system/files/media/document/file/gutachten_bergwerk_lohberg-osterfeld_31.01.2017.pdf (Accessed: May 2020).

26. Cai, Y., Jin, Y., Wang, Z., Chen, T., Wang, Y., Kong, W., Xiao, W., Li, X., Lian, X. & Hu, H. (2023). A review of monitoring, calculation, and simulation methods for ground subsidence induced by coal mining. International Journal of Coal Science & Technology, 10. 32. Pp.1 – 23. https://doi.org/10.1007/s40789-023-00595-4.

27. Caro Cuenca, M., & Hanssen, R.F. (2008). Subsidence and uplift at Wassenberg, Germany due to coal mining using persistent scatterer interferometry. V.A. Gomez Garcia (Ed.), 13th FIG Symposium on deformation measurements and analysis, 4th IAG Symposium on Geodesy for Geotechnical and structural engineering, LNEC Measuring the changes, 12-15 May, Lisbon, Portugal. pp. 1-9. LNEC.

28. Chen, B., Deng, K., Fan, H., & Hao, M. (2013). Large-scale deformation monitoring in mining area by D-InSAR and 3D laser scanning technology integration. International Journal of Mining Science and Technology, 23(4), pp. 555–561.

29. Chen, Y., Tong, Y., & Tan, K. (2020). Coal mining deformation monitoring using SBAS-InSAR and offset tracking: a case study of Yu County, China. IEEE Journal of Selected Topics in Applied Earth Observations and Remote Sensing, 13, pp. 6077–6087. https://doi.org/10.1109/JSTARS.2020.3028083

30. Cheng, G., & Lu, L. (2000). Comparison of Spatial Interpolation Methods. Advances in Earth Science, 15, pp. 260-265.

31. Chi, S., Wang, L., & Yu, X. (2023). A New Method for Calculating Prediction Parameters of Surface Deformation in the Mining Area. Applied Sciences, 13(14), 8030. https://doi.org/10.3390/app13148030.

32. Chi, S., Wang, L., Yu, X., Fang, X., & Jiang, C. (2021). Research on Prediction Model of Mining Subsidence in Thick Unconsolidated Layer Mining Area. 9, pp. 23996-24010. https://doi.org/10.1109/ACCESS.2021.3056873.

33. Colesanti, C., Le Mouelic, S., Bennani, M., Raucoules, D., Carnec, C., & Ferretti, A. (2005). Detection of mining related ground instabilities using the Permanent Scatterers technique—a case study in the east of France. International Journal of Remote Sensing, 26(1), pp. 201-207. https://doi.org/10.1080/0143116042000274069.

34. Cremonesi, M., Franci, A., Idelsohn, S. & Oñate, E. (2020). A State of the Art Review of the Particle Finite Element Method (PFEM). Arch Computat Methods Eng, 27, pp. 1709-1735. https://doi.org/10.1007/s11831-020-09468-4.

35. Crosetto, M., Monserrat, O., Cuevas-González, M., Devanthéry, N., & Crippa, B. (2016). Persistent scatterer interferometry: A review. ISPRS Journal of Photogrammetry and Remote Sensing, 115, pp. 78-89. https://doi.org/10.1016/j.isprsjprs.2016.02.013.

36. Cross, P.A. & Thapa, K. (1979). The Optimal Design of Levelling Networks. Survey Review, 25(192), pp. 68-79. https://doi.org/10.1179/sre.1979.25.192.68.

37. Czaplewski, K., & Goward, D. (2016). Global Navigation Satellite Systems – Perspectives on Development and Threats to System Operation. TransNav, the International Journal on Marine Navigation and Safety of Sea Transportation, 10, pp. 183-192. https://doi.org/10.12716/1001.10.02.01.

38. Czerwonka-Schröder, D. & Klonowski, J. (2019). i²MON - Integrated monitoring for the detection of ground and surface displacements caused by coal mining. 4th Joint International Symposium on Deformation Monitoring (JISDM), 15-17 May 2019, Athens, Greece. Available at: https://api.semanticscholar.org/CorpusID:230102074 (Accessed: June 2020)

39. Díaz-Fernández, M.E., Álvarez-Fernández, M.I., & Álvarez-Vigil, A.E. (2010). Computation of influence functions for automatic mining subsidence prediction. Computers & Geosciences, 14(1), pp. 83-103.

40. DMT GmbH & Co. KG Geo Engineering & Exploration - Hydrogeologie & Wassermanagement. (2016). Kavernenspeicher Etzel: Auswirkungsanalyse für insgesamt 99 Kavernen. Essen, Germany. Available at: https://www.lbeg.niedersachsen.de/download/144445/Anhang_2_Auswirkungsana lyse_DMT_2018.pdf (Accessed: May 2022).

41. Dudek, M., Sroka, A., Tajduś, K., Misa, R., & Mrocheń, D. (2022). Assessment and Duration of the Surface Subsidence after the End of Mining Operations. Energies, 15(22), 8711. https://doi.org/10.3390/en15228711.

42. Eickemeier, R. (2005). Senkungsprognosen über Kavernenfeldern - Ein neues Modell -. 34. Geomechanik-Kolloquium Leipzig, Germany.

43. Eyo, E., Musa, T., Omar, K., Idris, K., Bayrak, T., Onuigbo, I., & Opaluwa, Y. (2014). Application of low-cost GPS tools and techniques for landslide monitoring: A review. Jurnal Teknologi, 71(4), pp. 71–78.

44. Fokker, P. (2002). Subsidence Prediction and Inversion of Subsidence Data. Proceedings of the SPE/ISRM Rock Mechanics in Petroleum Engineering Conference.78227. pp. 1-10. https://doi.org/10.2118/78227-MS.

45. Gabriel, A.K., Goldstein, R.M., & Zebker, H.A. (1989). Mapping small elevation changes over large areas: differential radar interferometry. Journal of Geophysical Research: Solid Earth, 94(B7), pp. 9183–9191.

46. Gambolati, G., & Teatini, P. (2021). Land Subsidence and its Mitigation. Groundwater Project. University of Padova, Italy. 92 pages. https://doi.org/10.21083/978-1-77470-001-3

47. Gargani, J., Geoffroy, L., Gac, S. and Cravoisier, S. (2006). Fault slip and Coulomb stress variations around a pressured magma reservoir: consequences on seismicity and magma intrusion. Terra Nova, 18(6), pp. 403-411.

48. Gasperini, D., Allemand, P., Delacourt, C., & Grandjean, P. (2014). Potential and limitation of UAV for monitoring subsidence in municipal landfills. International Journal of Environmental Technology and Management, 17, pp. 1-13. https://doi.org/10.1504/IJETM.2014.059456.

49. Gaul, L., Kögl, M., & Wagner, M. (2003). Boundary element methods for engineers and scientists: an introductory course with advanced topics. Springer Berlin, Heidelberg. 431 pages. https://doi.org/10.1007/978-3-662-05136-8.

50. Gazzola, L., Ferronato, M., Frigo, M. et al. (2021). A novel methodological approach for land subsidence prediction through data assimilation techniques. Comput Geosci, 25, pp. 1731-1750. https://doi.org/10.1007/s10596-021-10062-1.

51. Ge, L., Li, X., & Ng, A.H.M. (2016). UAV for mining applications: A case study at an opencut mine and a longwall mine in New South Wales, Australia. IGARSS 2016, pp. 5422–5425.

52. Geertsma, J. (1973) A basic theory of subsidence due to reservoir compaction: the homogeneous case. Verhandelingen Kon Ned. Geol. Mijnbouwk. Gen, 28 (1973), pp. 43-62

53. Ghilani, C.D. and Wolf, P.R. (2012). Elementary Surveying: An Introduction to Geomatics. Pearson Prentice Hall. Available at: https://cdn.prexams.com/10981/Solutions_-_Elementary_Surveying_13th_ed-libre.pdf (Accessed: November 2020).

54. Gledhill, K., Robinson, R., Webb, T., Abercrombie, R., Beavan, J., & Cousins, J. (2000). The Mw 6.2 Cass, New Zealand, earthquake of 24 November 1995: reverse faulting in a strike-slip region. New Zealand Journal of Geology & Geophysics, 43(2), pp. 255-269.

55. Goldstein, R., & Zebker, H. (1987). Interferometric radar measurement of ocean surface currents. Nature, 328, pp. 707–709. https://doi.org/10.1038/328707a0.

56. González-Rodríguez, G., Blanco, Á., Corral, N. & Colubi, A. (2007). Least squares estimation of linear regression models for convex compact random sets. ADAC, 1, pp. 67-81. https://doi.org/10.1007/s11634-006-0003-7.

57. Grafarend, E.W. (1974). Optimization of Geodetic Networks. Bollettino di geodesia e scienze affini, 33(4), pp. 351-406.

58. Grün, E. (1995). Analyse und Prognose von Unstetigkeiten als Folge bergbaubedingter Bodenbewegungen im linksniederrheinischen Steinkohlengebiet. [Doctoral dissertation, Technische Hochschule Aachen]. RWTH Aachen University Publications. 184 pages. Available at: https://publications.rwth-aachen.de/record/53553?ln=de (Accessed: August 2021)

59. Guzy, A., Hejmanowski, R. & Witkowski, W. (2021). Land Subsidence Modeling Due To Mining Drainage Using Monte Carlo-Modified Geographically Weighted Regression.World Multidisciplinary Earth Sciences Symposium (WMESS 2021), Prague, Czech Republic.

60. Guzy, A. & Witkowski, W.T. (2021). Land Subsidence Estimation for Aquifer Drainage Induced by Underground Mining. Energies, 14(15). 4658. https://doi.org/10.3390/en14154658.

61. Hastie, T., Tibshirani, R., & Friedman, J. (2009). The Elements of Statistical Learning: Data Mining, Inference, and Prediction, Second Edition. Springer Series in Statistics. Springer New York, NY. 745 pages. https://doi.org/10.1007/978-0-387-84858-7.

62. Hazen, G.A., & Sargand, S.M. (1988). Methods for assessing effects of longwall mining on surface subsidence. Mining Engineering, 40(6), pp. 451-454.

63. Hegemann, M. (2020). Die Trogtheorie von Karl Lehmann - ein Rück- und Ausblick nach 100 Jahren. Markscheidewessen, 127(2), pp. 28–34.

64. Heib, M., Linkov, A.M., & Zoubkov, V.V. (2001). On numerical modelling of subsidence induced by mining. Proceedings of the ISRM Regional Symposium EUROCK 2001. Espoo/FINLAND, June 4-7, pp. 795-799.

65. Helmut, F.S. (2008). The Role of Advanced Constitutive Models in Geotechnical Engineering. Geomechanic and Tunneling. https://doi.org/10.1002/geot.200800033.

66. Herget, G. (1974). Ground stress determinations in Canada. Rock Mechanics, 6, pp. 53-64. https://doi.org/10.1007/BF01238053.

67. Herget, G. (1986). Changes of Ground Stresses with Depth in the Canadian Shield. Proceedings of the International Symposium on Rock Stress and Rock Stress Measurements, Stockholm.pp. 61-68. Available at: https://onepetro.org/isrmis/proceedings-pdf/is86/all-is86/isrm-is-1986-006/2030486/isrm-is-1986-006.pdf (Accessed: June 2020).

68. Herget, G. (1993). Rock Stresses and Rock Stress Monitoring in Canada. Hudson JA (Ed.), Comprehensive Rock Engineering. Pergamon Press. pp. 617-648.

69. Hoek, E. (2016). 'The Art of Tunnelling in Rock - Dr. Evert Hoek Lecture Series'. YouTube video, added 20 April 2016. Available at: https://www.youtube.com/watch?v=RDDoBECOUf4&t=2s (Accessed: 1 April 2022).

70. Hoek, E. (1983). Strength of jointed rock masses. Géotechnique, 23(3), Presented at the Twenty-third Rankine Lecture, British Geological Society, London, 23 February 1983. pp. 187-223.

71. Hoek, E., & Brown, E.T. (1980a). Empirical Strength Criteria for Rock Masses. Journal of Geotechnical Engineering Division. pp. 1013 – 1035.

72. Hoek, E., & Brown, E.T. (1980b). Hoek, E. and Brown, E.T. (1980) Underground Excavations in Rock. London Institution of Mining and Metallurgy, London, 527 p.

73. Hoek, E., & Marinos, P. (2000). Predicting Tunnel Squeezing. Tunnels & Tunnelling International, 32(11), pp. 45-51.

74. Hoek, E., Carranza-Torres, C. & Corkum, B. (2002). Hoek-Brown failure criterion - 2002 Edition. Proc. NARMS-TAC Conference, Toronto, 2002, pp. 267-273.

75. Holdsworth, S. (2008). Constitutive Equations for Creep Curves and Predicting Service Life. Creep-Resistant Steels, Woodhead Publishing Series in Metals and Surface Engineering, pp. 403-420. https://doi.org/10.1533/9781845694012.2.40.

76. Holla, L. & Barclay, E. (2000). Mine subsidence in the southern coalfield, NSW, Australia. New South Wales Dept. of Mineral Resources.

77. Hong-dong FAN, Wei GU, Yong QIN, Ji-qun XUE, Bing-qian CHEN. (2014). A model for extracting large deformation mining subsidence using D-InSAR technique

and probability integral method. Transactions of Nonferrous Metals Society of China, Volume 24, Issue 4, pp. 1242-1247. https://doi.org/10.1016/S1003-6326(14)63185-X.

78. Hooker, J.N., Konyukhov, A.I., & Saks, V.N. (1972). Determination of in situ stresses in rock. Journal of Geotechnical and Geoenvironmental Engineering, 98(6), pp. 573-588.

79. Huang, G., Du, S., & Wang, D. (2023). GNSS techniques for real-time monitoring of landslides: a review. Satellite Navigation, 4(1), 5. https://doi.org/10.1186/s43020-023-00095-5.

80. Hurtado-Pulido, C. (2023). InSAR and airborne LiDAR for monitoring slow vertical land motion. Nature Reviews Earth & Environment 4. 679. https://doi.org/10.1038/s43017-023-00442-9.

81. Ike, C. (2019). Love Stress Function Method for Solving Axisymmetric Elasticity Problems of the Elastic Half-Space. Electronic Journal of Geotechnical Engineering, 24, pp. 663-707.

82. John, A. (2021). Monitoring of Ground Movements Due to Mine Water Rise Using Satellite-Based Radar Interferometry—A Comprehensive Case Study for Low Movement Rates in the German Mining Area Lugau/Oelsnitz. Mining, 1(1), pp. 35-58. https://doi.org/10.3390/mining1010004.

83. Jurisch, A. (1990). Grid optimisation in the finite-element method. Sebastian, H.J., Tammer, K. (Eds.), System Modelling and Optimisation. Lecture Notes in Control and Information Sciences, vol 143. Springer. https://doi.org/10.1007/BFb0008363.

84. Keilich, W., Seedsman, R., & Aziz, N.H. (2006). Numerical Modelling Of Mining Induced Subsidence. Aziz, N. (Ed.), Coal 2006: Coal Operators' Conference. University of Wollongong & the Australasian Institute of Mining and Metallurgy. pp. 313-326.

85. Kessler, T., Mugova, E., Jasnowski-Peters, H., Rinder, T., Stemke, M., Wolkersdorfer, C., Hilberg, S., Melchers, C., Struckmeier, W., Wieber, G., & Schafmeister, M.-Th. (2020). Grundwasser in ehemaligen deutschen Steinkohlenrevieren – ein wissenschaftlicher Blickwinkel auf Grubenflutungen. Grundwasser, 25. pp. 259-272. https://doi.org/10.1007/s00767-020-00460-0.

86. Khodaei, B., Hashemi, H., Salimi, S., & Berndtsson, R. (2023). Substantial carbon sequestration by peatlands in temperate areas revealed by InSAR. Environmental Research Letters, 18(4). 044012. https://doi.org/10.1088/1748-9326/acc194.

87. Kikuchi, N. (1987). Adaptive Grid Design for Finite Element Analysis In Optimisation: Part 1, Review of Finite Element Error Analysis. Mota Soares, C.A.

(Ed.), Computer Aided Optimal Design: Structural and Mechanical Systems. NATO ASI Series, vol 27. Springer. Pp. 493-562. https://doi.org/10.1007/978-3-642-83051-8_14.

88. Kim, T., & Jeon, S. (2019). Experimental Study on Shear Behaviour of a Rock Discontinuity Under Various Thermal, Hydraulic and Mechanical Conditions. Rock Mechanics and Rock Engineering, 52, pp. 2207-2226. https://doi.org/10.1007/s00603-018-1723-7.

89. Kirkpatrick, S., Gelatt Jr, C.D., & Vecchi, M.P. (1983). Optimisation by Simulated Annealing. Science, 220(4598), pp. 671-680. Available at: https://www2.stat.duke.edu/~scs/Courses/Stat376/Papers/TemperAnneal/KirkpatrickAnnealScience1983.pdf (Accessed: September 2022)

90. Knothe, S. (1953). Równanie profilu ostatecznie wykształconej niecki osiadania [A profile equation for a definitely shaped subsidence trough]. Archiwum Górnictwa i Hutnictwa 1, pp. 22–38 (in Polish).

91. Knothe, S. (2005). Asymetryczna funkcja rozkładu wpływów eksploatacji górniczej w ośrodku zmieniającym swoje własności [Asymmetric function of distribution of mining exploitation influences in the medium with changing properties]. Archives of Mining Sciences, 50 (4), pp. 401-415.

92. Kochmański, T. (1955) Obliczanie ruchów punktów górotworu pod wpływem eksploatacji górniczej [Calculating the movements of rock mass points under the influence of mining exploitation]. Polska Akademia Nauk, Komitet Geodezji, PWN, Warszawa (in Polish).

93. Konovalov, O. (2019). InSAR-based subsidence monitoring for Starobin potash deposit. Paper presented at the TerraSAR-X / TanDEM-X Science Team Meeting, October 21-24, 2019. Poster. doi:10.13140/RG.2.2.23564.33929.

94. Kowalski, A. (2020). Deformacje powierzchni na terenach górniczych kopalni węgla kamiennego [Surface deformations in the mining areas of hard coal mines]. GIG, Katowice. 300 pages.

95. Kratzch, H. (2013). Bergschadenkunde. Bochum: Deutschen Markscheider-Vereins, Aachen, Germany. 948 pages.

96. Kwinta, A. & Gradka, R. (2018). Mining exploitation influence range. Natural Hazards, 94, pp. 979-997. https://doi.org/10.1007/s11069-018-3450-5.

97. Lekhnitskii, S.G. (1981). Theory of Elasticity of An Anisotropic Body. 2nd ed. Holden-Day. 431 pages. Available at: https://archive.org/details/lekhnitskii-theory-of-elasticity-of-an-anisotropic-body-mir-1981/page/430/mode/2up (Accessed May 2020)

98. Li, C., Fernandez-Steeger, T., Link, J.Á.B., May, M., & Azzam, R. (2014). Use of MEMS Accelerometers/Inclinometers as a Geotechnical Monitoring Method for Ground Subsidence. Acta Geodynamica et Geomaterialia, 11, pp. 337-349. https://doi.org/10.13168/AGG.2014.0015.

99. Litwiniszyn, J. (1958). Statistical methods in the mechanics of granular bodies. Rheol Acta, 1, pp. 146-150. https://doi.org/10.1007/BF01968857.

100. Li, F., Liu, G., Tao, Q., & Zhai, M. (2022). Land subsidence prediction model based on its influencing factors and machine learning methods. PREPRINT (Version 1) Research Square. https://doi.org/10.21203/rs.3.rs-1881099/v1.

101. Lian, X., Liu, X., Ge, L., Hu, H., Du, Z., & Wu, Y. (2021). Time-series unmanned aerial vehicle photogrammetry monitoring method without ground control points to measure mining subsidence. Journal of Applied Remote Sensing, 15(2), 024505. pp. 1 – 15. https://doi.org/10.1117/1.JRS.15.024505.

102. Lin, S., Whittaker, B.N. and Reddish, D.J. (1992) 'Application of asymmetrical influence functions for subsidence prediction of gently inclined seam extractions', International Journal of Rock Mechanics and Mining Sciences & Geomechanics Abstracts, 29(5), pp. 479-490. https://doi.org/10.1016/0148-9062(92)92632-M.

103. Litwiniszyn, J. (1994). The Gauss function and the phenomena of rock mass subsidence and displacements of granular media. International Journal of Rock Mechanics and Mining Sciences & Geomechanics Abstracts. Vol 31. pp. 143-148, https://doi.org/10.1016/0148-9062(94)92804-5.

104. Liu, Z., Mei, G., Sun, Y. & Xu, N. (2021). Investigating mining-induced surface subsidence and potential damages based on SBAS-InSAR monitoring and GIS techniques: a case study. Environ Earth Sci, 80, 817. https://doi.org/10.1007/s12665-021-09726-z.

105. Lo, W., Purnomo, S.N., Dewanto, B.G., Sarah, D., & Sumiyanto. (2022). Integration of Numerical Models and InSAR Techniques to Assess Land Subsidence Due to Excessive Groundwater Abstraction in the Coastal and Lowland Regions of Semarang City. Water, 14(2), 201. https://doi.org/10.3390/w14020201.

106. Lubitz, C., Motagh, M., Wetzel, H.-U. & Kaufmann, H. (2013). Remarkable Urban Uplift in Staufen im Breisgau, Germany: Observations from TerraSAR-X InSAR and Leveling from 2008 to 2011. Remote Sensing, 5(6), pp. 3082-3100. https://doi.org/10.3390/rs5063082.

107. Luo, Y. (2015). An improved influence function method for predicting subsidence caused by longwall mining operations in inclined coal seams. International Journal

of Coal Science & Technology, 2, pp. 163–169. https://doi.org/10.1007/s40789-015-0086-x.

108. Makkonen, L. (2008). Bringing closure to the plotting position controversy. Communications in Statistics - Theory and Methods, 37(3), pp. 460-467. https://doi.org/10.1080/03610920701653094.

109. Marinos, P.G., & Hoek, E. (2001). Estimating the Geotechnical Properties of Heterogeneous Rock Masses such as Flysch. Bulletin of Engineering Geology and the Environment, 60, pp. 85-92.

110. Martin, C.D., & Chandler, N.A. (1993). Stress Heterogeneity and Geological Structures. Rock Mechanics and Rock Engineering, 26(5), pp. 401-420.

111. Marwan, A. (2008). State of the art of the prediction methods of short and long-term ground movements (subsidence and sinkhole) for the mines in France. Coal Geology Research Progress. Nova Science Publishers, Inc. pp. 53 – 77. Available at: https://www.researchgate.net/publication/278770539_State_of_the_art_of_the_prediction_methods_of_short_and_long-term_ground_movements_subsidence_and_sinkhole_for_the_mines_in_France (Accessed 08.2021).

112. Mendoza-Chavez, G., Martínez-Mártinez, L.H., Delgado-Hernandez, D.J., De León Escobedo, D., Alonso Guzmán, E.M., Martínez Molina, W., Arreygue-Rocha, E., Chavez-García, H.L., & Arteaga-Arcos, J.C., (2012) Mechanical Properties of Rocks Used for the Construction of Vehicular Bridges Supported by Pier Masonry. AMR 535–537, pp. 1881–1888. https://doi.org/10.4028/www.scientific.net/amr.535-537.1881

113. Meng, Z., Zhang, J., & Peng, S. (2006). Influence of sedimentary environments on mechanical properties of clastic rocks. Environmental Geology, 51, pp. 113-120. https://doi.org/10.1007/s00254-006-0309-y.

114. Morawietz, S., Heidbach, O., Reiter, K. et al. (2020). An open-access stress magnitude database for Germany and adjacent regions. Geotherm Energy, 8, 25. https://doi.org/10.1186/s40517-020-00178-5.

115. My, V., Thanh, N., Long, N. & Bui, L. (2014). Applicability of neural networks on surface subsidence prediction caused by underground mining. The 3rd International Conference on Advances in Mining and Tunneling, October 2014, Vung Tau, Vietnam. pp. 1 – 6.

116. Nocedal, J., & Wright, S.J. (2006). Numerical Optimisation. 2nd ed. Springer New York, NY: Springer Series in Operations Research and Financial Engineering. 664 pages. https://doi.org/https://doi.org/10.1007/978-0-387-40065-5.

117. Okal, E.A. (2009). The 1956 earthquake and tsunami in Amorgos, Greece. Geophysical Journal International, 178(3), pp. 1533-1554. https://doi.org/10.1111/j.1365-246X.2009.04237.x.

118. Oliver, M.A., & Webster, R. (2014). A tutorial guide to geostatistics: Computing and modelling variograms and kriging. Catena, 113, pp. 56-69. https://doi.org/10.1016/j.catena.2013.09.006.

119. Pal, A., Rošer, J., & Vulić, M. (2020). Surface Subsidence Prognosis above an Underground Longwall Excavation and Based on 3D Point Cloud Analysis. Minerals, 10(1), 82. https://doi.org/10.3390/min10010082.

120. Park, J., & Sandberg, I.W. (1991). Universal Approximation Using Radial-Basis-Function Networks. Neural Computation, 3(2), pp. 246-257. https://doi.org/10.1162/neco.1991.3.2.246.

121. Pawlik, M., Yin, X., Rudolph, T., Goerke-Mallet, P., Brune, J., & Benndorf, J. (2023). Modern methods of Geomonitoring in Post-Mining processes. Mining Engineering, pp. 23 - 29.

122. Pedregosa, F., Varoquaux, G., Gramfort, A., Michel, V., Thirion, B., Grisel, O., Blondel, M., Prettenhofer, P., Weiss, R., Dubourg, V., Vanderplas, J., Passos, A., Cournapeau, D., Brucher, M., Perrot, M., & Duchesnay, É. (2011). 'Scikit-learn: Machine Learning in Python'. Available at: https://scikit-learn.org/ (Accessed March 2023).

123. Peng, S. (2020). 'Surface Subsidence Engineering: Theory and Practice', 1st ed. CRC Press. 220 pages.

124. Petschko, H., Zehner, M., Fischer, P., & Goetz, J. (2022). Terrestrial and Airborne Structure from Motion Photogrammetry Applied for Change Detection within a Sinkhole in Thuringia, Germany. Remote Sensing, 14(13). 3058. https://doi.org/10.3390/rs14133058.

125. Polanin, P. (2015). Application of two parameter groups of the Knothe–Budryk theory in subsidence prediction. Journal of Sustainable Mining, 14(2), pp. 67-75. https://doi.org/10.1016/j.jsm.2015.08.010.

126. Przyłucka, M., Kowalski, Z. & Perski, Z. (2022). Twenty years of coal mining-induced subsidence in the Upper Silesia in Poland identified using InSAR. Int J Coal Sci Technol, 9, 86. https://doi.org/10.1007/s40789-022-00541-w.

127. Quasnitza, H. (1988). Eine Strategie zur Kallibrierung Markscheiderischer Bewegungsmodelle und zur Prädiktion von Bewegungselementen. Dissertation, TU Clausthal. (In German).

128. Ramírez, P. & Rambaud, C. (1986). Hundimientos mineros. Métodos de cálculo. [Mining subsidence. Calculation methods] Technological and Geological Institute of Spain, Madrid. 328 pages.

129. Radutu, A. & Vlad-Sandru, M. (2023). Review on the Use of Satellite-Based Radar Interferometry for Monitoring Mining Subsidence in Urban Areas and Demographic Indicators Assessment. Mining Revue, 29(1), pp. 42-62. https://doi.org/10.2478/minrv-2023-0004.

130. Richardson, R.M. (1992). Ridge forces, absolute plate motions, and the intraplate stress field. Journal of Geophysical Research: Solid Earth, Papers on Tectonophysics, pp. 13803–13872. https://doi.org/10.1029/91JB00475.

131. Rosner, P., Heitfeld, M., Spreckels, V., & Vosen, P. (2014). Auswirkungen von Geländehebungen im Zuge des Grubenwasseranstiegs im Ruhrrevier. Tagungsband RuhrGeo Tag Bochum, Germany, pp.153–177.

132. Ryaben'kii, V.S., & Tsynkov, S.V. (2006). A Theoretical Introduction to Numerical Analysis. CRC PRESS BocaRaton London NewYork Washington. 521 pages, Available at: https://stsynkov.math.ncsu.edu/book_sample_material/frontmatter.pdf (Accessed April 2020).

133. Saeidi, A., Deck, O., Marwan, A., Verdel, T., & Rouleau, A. (2013). Adjusting the Influence Function Method for Subsidence Prediction. Key Engineering Materials, 553, pp. 59-66. https://doi.org/10.4028/www.scientific.net/KEM.553.59.

134. Sanmiquel, L., Bascompta, M., Vintró, C., & Yubero, T. (2018). Subsidence Management System for Underground Mining. Minerals, 8(6), 243. https://doi.org/10.3390/min8060243.

135. Sashurin, A.D. (1999). Сдвижение горных пород на рудниках черной металлургии [Displacement of Rock in Black Metallurgy Mines]. IGD URO RAN, Ekaterinburg, Russia. p. 268. Available at: https://www.geokniga.org/bookfiles/geokniga-sdvizheniegornyhporodnarudnikahchernoymetallurgii.pdf (Accessed September 2020)

136. Bahuguna, P.P., Srivastava, A.M.C., & Saxena, N.C. (1991). A critical review of mine subsidence prediction methods. Mining Science and Technology, 13(3), 369-382. https://doi.org/10.1016/0167-9031(91)90716-P.

137. SciPy Community. (2019). 'SciPy optimise: Optimisation and Root Finding Routines'. Available at: https://docs.scipy.org/doc/scipy/reference/optimise.html (Accessed: January 2023).

138. Shadbolt, C.H. (1972). Subsidence engineering. University of Nottingham Mining Department Magazine, vol. 24, pp. 80-89.

139. Sheorey, P.R., Loui, J.P., Singh, K.B., & Singh, S.K. (2000). Ground subsidence observations and a modified influence function method for complete subsidence prediction. International Journal of Rock Mechanics and Mining Sciences, 37(5), pp. 801-818. https://doi.org/10.1016/S1365-1609(00)00023-X.

140. Shikakura, Y., Fukahata, Y., & Hirahara, K. (2014). Long-term changes in the Coulomb failure function on inland active faults in southwest Japan due to east-west compression and interplate earthquakes. J Geophys Res Solid Earth, 119, pp. 502-518. https://doi.org/10.1002/2013JB010156.

141. Shimada, H., Chen, Y., Hamanaka, A., Sasaoka, T., Shimada, H., & Matsui, K. (2013). Application of Highwall Mining System to Recover Residual Coal in End-walls. Procedia Earth Planet Sci, 6, pp. 311-318. https://doi.org/10.1016/j.proeps.2013.01.041.

142. Sidki-Rius, N., Sanmiquel, L., Bascompta, M., & Parcerisa, D. (2022). Subsidence management and prediction system: a case study in potash mining. Minerals, 12(9), 1155. https://doi.org/10.3390/min12091155.

143. Sikora, P. (2021). Simulation Possibilities of the Post-Mining Goafs Impact on the Deformations Induced by Next Underground Mining Operations with Use of the Cellular Automata Method. Geotech Geol Eng, 39, pp. 1923-1935. https://doi.org/10.1007/s10706-020-01595-w.

144. Simons, M., & Rosen, P.A. (2015). Interferometric Synthetic Aperture Radar Geodesy. Gerald Schubert (editor-in-chief) Treatise on Geophysics, 2nd edition, Vol 3. Oxford: Elsevier. pp. 339-385.

145. Skempton, A.W. (1960). Terzaghi's Discovery of Effective Stress. From Theory to Practice in Soil Mechanics - Selections from the Writings of Karl Terzaghi. John Wiley & Sons. 512 pages.

146. Skinner, B.F. (1984). The Shame of American Education. American Psychologist, 39, pp. 947-954.

147. Slowik, A., & Kwasnicka, H. (2020). Evolutionary algorithms and their applications to engineering problems. Neural Comput Appl, 32. pp. 12363–12379. https://doi.org/10.1007/s00521-020-04832-8.

148. Smith, R., & Knight, R. (2019). Modelling Land Subsidence Using InSAR and Airborne Electromagnetic Data. Geology, 27(6), pp. 483–486. https://doi.org/10.1029/2018WR024185.

149. Speck, R.C., & Bruhn, R.W. (1995). Non-Uniform Mine Subsidence Ground Movement and Resulting Surface-Structure Damage. Environmental & Engineering Geoscience, 1(1), pp. 61-74. https://doi.org/10.2113/gseegeosci.I.1.61.

150. Sroka, A., Knothe, S., Tajduś, K., & Misa, R. (2015). Point Movement Trace Vs. The Range Of Mining Exploitation Effects In The Rock Mass. Arch Min Sci. pp. 921 – 929. https://doi.org/10.1515/amsc-2015-0060.

151. Sroka, A. (2001). Die „sociale" Abbauverträglichkeit – der Grundgedanke der bergschadensminimierenden Abbauplanung. Das Markscheidewesen in der Rohstoff-, Energie- und Entsorgungswirtschaft, 43 wissenschaftliche Tagung des Deutschen Markscheider-Vereins, pp. 37-46.

152. Sroka, A., & Schober, F. (1982). Die Berechnung der maximalen Bodenbewegungen über kavernenartigen Hohlräumen unter Berücksichtigung der Hohlraumgeometrie. [Calculation of maximum ground movements above cavern-like voids considering cavity geometry]. Kali u. Steinsalz, 8, pp. 273-277.

153. Sroka, A. & Wittkopf, M. (1992). Deformationsmessungen und –analysen zur Parameteridentifikation geometrischer Bodenbewegungsmodelle im Markscheidewesen. Proceedings of the 6th International FIG-Symposium on Deformation Measurements, 24-28 February, 1992, Hannover, pp. 691-707.

154. Stewart, S. (2007). Rock Mass Strength and Deformability of Unweathered Closely Jointed New Zealand Greywacke. Doctoral thesis, University of Canterbury. 455 pages.

155. Stoica, P., & Selen, Y. (2004). Model-order selection: a review of information criterion rules. IEEE Signal Process Mag, 21(4), pp. 36-47. https://doi.org/10.1109/MSP.2004.1311138.

156. Storag Etzel. (2022a). 'Ergebnisse des nivellements 2022'. Storag Etzel. Available at: https://www.storag-etzel.de/verantwortung/umweltschutz-umweltmanagement/monitoring/ergebnisse-des-nivellements-2022 (Accessed: May 2023).

157. Storag Etzel. (2022b). 'History'. Available at: https://www.storag-etzel.de/en/company/history (Accessed: 07.2023).

158. Stow, R., & Wright, P. (1997). Mining subsidence Land Surveying by SAR Interferometry, 3rd ERS Symp., Florence, Italy. Pp. 525 – 530. Available at: https://earth.esa.int/eogateway/documents/20142/37627/3rd-ERS-Symposium-Space-at-the-Service-of-our-Environment.pdf. (Accessed: April 2023)

159. Suchowerska, I., Carter, A.M. and Hambleton, J.P. (2016). Geomechanics of subsidence above single and multi-seam coal mining. Journal of Rock Mechanics

and Geotechnical Engineering, pp. 304-313. https://doi.org/10.1016/j.jrmge.2015.11.007.

160. Tajduś, K., Sroka, A., & Misa, R. (2021a). Analysis of Mining-Induced Delayed Surface Subsidence. Minerals, 11(11), 1187. https://doi.org/10.3390/min11111187.

161. Tajduś, K., Sroka, A., Misa, R., Tajduś, A., & Meyer, S. (2021b). Surface Deformations Caused by the Convergence of Large Underground Gas Storage Facilities. Energies, 14(2), 402. https://doi.org/10.3390/en14020402.

162. Tang, Fq. (2011). Mining subsidence monitoring using the method of combining InSAR and GPS technology. J Coal Sci Eng China, 17, pp. 133-136. https://doi.org/10.1007/s12404-011-0205-2.

163. Terzaghi, K. (1936). The Shearing Resistance of Saturated Soils. Proc. First Int. Conf. Soil Mech. 1st International Conference on Soil Mechanics and Foundation Engineering, Harvard. Available at: https://www.issmge.org/publications/publication/the-shearing-resistance-of-saturated-soils-and-the-angle-between-the-planes-of-shear (Accessed: June 2021)

164. Thoms, R.L., & Gehle, R.M. (2000). A brief history of salt cavern use. In Proceedings of the 8th Conference on the Mechanical Behaviour of Salt, pp. 18-22. Trans Tech Publications Ltd.

165. Tsanakas, K. (2019). The Uplifted Terraces of the Arkitsa Region, NW Evoikos Gulf, Greece: A Result of Combined Tectonic and Volcanic Processes? Geomorphology of the Pieria Mtns, Northern Greece, Karymbalis E, Gaki-Papanastassiou K, Maroukian H. Journal of Maps, 15(22), pp. 499-508. https://doi.org/10.1080/17445647.2019.1619630.

166. Tunneling Experts. (2013). Variation of Intact Rock Properties. Available at: http://tunneling-experts.blogspot.com/2013/01/variation-of-intact-rock-properties.html (Accessed: June 2021).

167. Turk, G., & Ambrožič, T. (1999). Artificial neural networks in surface subsidence prediction. ZAMM. Zeitschrift für Angewandte Mathematik und Mechanik, 79.

168. Tzampoglou, P., Ilia, I., Karalis, K., Tsangaratos, P., Zhao, X. & Chen, W. (2023). Selected Worldwide Cases of Land Subsidence Due to Groundwater Withdrawal. Water, 15, 1094. https://doi.org/10.3390/w15061094.

169. Ulusay, R. (2015). The ISRM Suggested Methods for Rock Characterisation, Testing and Monitoring: 2007-2014. Springer International Publishing.

170. Van Sambeek, L. (1993). Evaluating Cavern Tests and Surface Subsidence Using Simple Numerical Models. Seventh Symposium on Salt, Vol. I, pp. 433-439.

171. Vasarhelyi, B. (2009). A possible method for estimating the Poisson's rate values of the rock masses. Acta Geodaetica et Geophysica Hungarica, 44, pp. 313-322. https://doi.org/10.1556/AGeod.44.2009.3.4.

172. Villegas, B. (2008). Numerical Analyses of the Hanging wall at the Kiirunavaara Mine, Sweden. Unpublished master's thesis, Department of Civil, Mining and Environmental Engineering, Division of Mining and Geotechnical Engineering, Luleå University of Technology, SE-971 87 Luleå, Sweden. 109 pages. Available at: http://www.diva-portal.org/smash/get/diva2:998827/FULLTEXT01.pdf (Accessed June 2021)

173. Villegas, T., Nordlund, E., & Dahner-Lindqvist, C. (2011). Hangingwall surface subsidence at the Kiirunavaara mine, Sweden. Engineering Geology, 121(1–2), pp. 18–27. https://doi.org/10.1016/j.enggeo.2011.04.010

174. Voight, B. (1966). Interpretation of In-situ Stress Measurements. Panel Report on Theme IV. Proceedings of the 1st Congress of the International Society for Rock Mechanics (ISRM), Lab. Nac de Eng. Civil, Lisbon.

175. Vušović, N., Vlahović, M. & Kržanović, D. (2021). Stochastic method for prediction of subsidence due to the underground coal mining integrated with GIS, a case study in Serbia. Environ Earth Sci, 80, 67. https://doi.org/10.1007/s12665-020-09349-w.

176. Vyazmensky, A., Elmo, D., Stead, D., & Rance, J. (2007). Combined finite-discrete element modelling of surface subsidence associated with block caving mining. Potvin Y, Carter J, eds. Proceedings of the 4th International Seminar on Deep and High Stress Mining, pp. 551-560. https://doi.org/10.1201/NOE0415444019-c58

177. Vyazmensky, A., Stead, D., Elmo, D., & Moss, A. (2010). Numerical Analysis of Block Caving-Induced Instability in Large Open Pit Slopes: A Finite Element/Discrete Element Approach. Rock Mech Rock Eng, 43, pp. 21-39. https://doi.org/10.1007/s00603-009-0035-3.

178. Wackerly, D., Mendenhall, W., & Scheaffer, R.L. (2008). Mathematical Statistics with Applications. 7th ed. Belmont, CA, USA: Thomson Higher Education.

179. Wales, D.J., & Doye, J.P.K. (1997). Global Optimisation by Basin-Hopping and the Lowest Energy Structures of Lennard-Jones Clusters Containing up to 110 Atoms. J Phys Chem A, 101(28), pp. 5111-5116. https://doi.org/10.1021/jp970984n.

180. Wang, G. (2022). Houston GNSS Network for Subsidence and Faulting Monitoring: Data Analysis Methods and Products. Journal of Surveying Engineering, 148, 20. https://doi.org/10.1061/(ASCE)SU.1943-5428.0000399.

181. Wang, R., Wu, K., He, Q., He, Y., Gu, Y., & Wu, S. (2022). A Novel Method of Monitoring Surface Subsidence Law Based on Probability Integral Model

Combined with Active and Passive Remote Sensing Data. Remote Sensing, 14(2), 299. https://doi.org/10.3390/rs14020299.

182. Wei, L., Yinping, L., Chunhe, Y., Deyi, J., Daemen, J., Jie, C. and Junfeng, K. (2016). A new method of surface subsidence prediction for natural gas storage cavern in bedded rock salts. Environ Earth Sci, 75. 800. https://doi.org/10.1007/s12665-016-5611-8.

183. Whittaker, B.N., & Reddish, D.J. (1989). Subsidence: Occurrence, Prediction and Control. Department of Mining Engineering, The University of Nottingham, University Park, Nottingham NG7 2RO (UK).

184. Moseley, P.T. & Garche, J. (2014) Electrochemical Energy Storage for Renewable Sources and Grid Balancing. 1st Edition, Elsevier. 492 pages.

185. Wong, R.H.C., Guo, Y., Li, L., Chau, K.T., Zhu, W., & Li, S. (2006). Anti-Wing Crack Growth from Surface Flaw in Real Rock under Uniaxial Compression. Onate E, Owen DRJ, Periaux J, Eurogen 2005 International Conference on Evolutionary Methods for Design, Optimisation and Control with Applications to Industrial and Societal Problems, Volume II, pp. 2609-2616. https://doi.org/10.1007/1-4020-4972-2_408.

186. World Stress Map Project. (n.d.). Available at: https://www.world-stress-map.org/ (Accessed: May 2021).

187. Xia, K., Chen, C., & Liu, X. (2016). Mining-induced ground movement in tectonic stress metal mines: a case study. Bulletin of Engineering Geology and the Environment, 75, pp. 1089–1115. https://doi.org/10.1007/s10064-016-0886-2.

188. Xia, Kz., Chen, Cx., & Liu, Xm., (2017). Ground movement mechanism in tectonic stress metal mines with steep structure planes. Journal of Central South University, 24, pp. 2092–2104. https://doi.org/10.1007/s11771-017-3618-2.

189. Yale, D.P. (2003). Fault and stress magnitude controls on variations in the orientation of in situ stress. Geological Society, London, Special Publications, 209, pp. 55-64. https://doi.org/10.1144/GSL.SP.2003.209.01.06.

190. Yan, W., Chen, J., Tan, Y., He, R., & Yan, S. (2022). Surface Dynamic Damage Prediction Model of Horizontal Coal Seam Based on the Idea of Wave Lossless Propagation. Int J Environ Res Public Health, 19(11), 6862. https://doi.org/10.3390/ijerph19116862.

191. Ye, L., Chen, F., Ma, H., Shi, X., Li, H. & Yang, C. (2022). Subsidence above rock salt caverns predicted with elastic plate theory. Environ Earth Sci, 81, 123. https://doi.org/10.1007/s12665-022-10232-z.

192. Yin, PF., & Yang, SQ. (2019). Discrete element modelling of strength and failure behaviour of transversely isotropic rock under uniaxial compression. J Geol Soc India, 93, pp. 235-246. https://doi.org/10.1007/s12594-019-1158-0.

193. Yetkin, M., Inal, C. & Yigit, C.O. (2009). Use of the particle swarm optimization algorithm for second order design of levelling networks. Vol. 3, No. 3, pp. 171-178. https://doi.org/10.1515/JAG.2009.018.

194. Zeitoun, D.G., & Wakshal, E. (2013). Land Subsidence Analysis in Urban Areas: The Bangkok Metropolitan Area Case Study. Springer Dordrecht. 269 pages. https://doi.org/https://doi.org/10.1007/978-94-007-5506-2.

195. Zhang, J., Ke, C., Shen, X., Lin, J., & Wang, R. (2023). Monitoring Land Subsidence along the Subways in Shanghai on the Basis of Time-Series InSAR. Remote Sensing, 15(4), 908. https://doi.org/10.3390/rs15040908.

196. Zhang, J., Yan, Y., Dai, H., Xu, L., Li, J., & Xu, R. (2022). Hyperbolic Secant Subsidence Prediction Model under Thick Loose Layer Mining Area. Minerals, 12(8), 1023. https://doi.org/10.3390/min12081023.

197. Zhang, X., Li, X., & Li, P. (2017). Review of GNSS PPP and Its Application. Acta Geodaetica et Cartographica Sinica, 46(10), pp. 1399–1407. Available at: http://xb.chinasmp.com/EN/Y2017/V46/I10/1399 (Accessed: April 2023)

198. Zhang, Y., Liu, Y., Jin, M., Jing, Y., Liu, Y., Liu, Y., Sun, W., Wei, J., & Chen, Y. (2019). Monitoring Land Subsidence in Wuhan City (China) using the SBAS-InSAR Method with Radarsat-2 Imagery Data. Sensors, 19(3), 743. https://doi.org/10.3390/s19030743.

199. Zhang. G., Liu. Y., Wang. T., Zhang. H., & Wang. Z. (2021). Ground Subsidence Prediction Model and Parameter Analysis for Underground Gas Storage in Horizontal Salt Caverns. Mathematical Problems in Engineering, vol. (2021a), Article ID 9504289, 16 pages. https://doi.org/10.1155/2021/9504289.

200. Zhao, B., Guo, Y., Mao, X., Zhai, D., Zhu, D., Huo, Y., Sun, Z., & Wang, J. (2022). Prediction Method for Surface Subsidence of Coal Seam Mining in Loess Donga Based on the Probability Integration Model. Energies, 15(6), 2282. https://doi.org/10.3390/en15062282.

201. Zhao, J., Konietzky, H., Herbst, M. & Morgenstern, R. (2021). Numerical simulation of flooding induced uplift for abandoned coal mines: simulation schemes and parameter sensitivity. Int J Coal Sci Technol, 8, pp. 1238–1249. https://doi.org/10.1007/s40789-021-00465-x.

202. Zienkiewicz, O.C., Taylor, R.L., & Zhu, J.Z. (2013). The finite element method: its basis and fundamentals. 7th ed. Elsevier Science Ltd. 714 pages. https://doi.org/10.1016/C2009-0-24909-9.

203. Zoback, M.L. (1992). First- and second-order patterns of stress in the lithosphere: The World Stress Map Project. Journal of Geophysical Research: Solid Earth, Papers on Tectonophysics.pp. 11703-11728. https://doi.org/10.1029/92JB00132.

Appendix A: Rock mass parameters

	Rock type	$\rho, \dfrac{kg}{m^3}$	E, Pa	ν	σ_i, Pa	m_b	Cluster
IGNEOUS	Andesite	2600	4.00E+10	0.28	1.38E+08	13	1
	Basalt	3000	6.00E+10	0.23	8.66E+08	13	2
	Diabase	2920	8.65E+10	0.24	2.97E+08	8	2
	Diorite	2900	6.50E+10	0.27	2.25E+08	13	0
	Dolerite	2900	6.50E+10	0.25	8.66E+08	8	2
	Gabbro	3100	7.00E+10	0.18	2.17E+08	14	2
	Granite	2655	5.00E+10	0.21	1.76E+08	16	0
	Norite	3000	8.36E+10	0.21	2.25E+08	10	2
	Rhyolite	2600	4.20E+10	0.20	5.77E+08	8	0
	Slate	2690	7.76E+10	0.25	1.74E+08	8	2
METAMORPHIC	Gneiss	2795	5.50E+10	0.25	1.67E+08	14	2
	Marble	2685	5.00E+10	0.28	1.40E+08	5	2
	Marl	2200	6.36E+09	0.22	1.23E+08	4	0
	Phyllite	2450	5.50E+10	0.26	1.33E+08	6	0
	Quartzite	2640	7.00E+10	0.20	2.21E+08	10	0
	Schist	2595	3.25E+10	0.17	7.75E+07	5	2
SEDIMENTARY	Claystone	2115	5.25E+10	0.33	8.00E+06	2	2
	Conglomerate (1)	2615	5.00E+10	0.25	1.27E+08	11	0
	Conglomerate (2)	2600	4.00E+10	0.10	4.00E+07	6	2
	Dolomite	2200	3.00E+10	0.23	2.30E+08	5	2
	Limestone	2415	4.50E+10	0.22	1.57E+08	4	2
	Mudstones (1)	2270	3.75E+10	0.15	1.88E+08	4	2
	Sandstone (1)	2185	2.55E+10	0.26	1.20E+08	9	0
	Sandstone (2)	2185	2.55E+10	0.10	1.20E+08	9	0
	Sandstone (3)	2050	3.00E+10	0.14	9.60E+07	10	2
	Sandstone (4)	2185	4.00E+10	0.26	1.20E+08	9	0
	Sandstone (5)	2185	2.55E+10	0.10	1.20E+08	2	0
	Shale (1)	2535	1.75E+10	0.17	2.10E+07	4	2
	Shale (2)	2300	2.00E+10	0.10	2.50E+07	6	1
	Siltstone	2000	1.65E+10	0.22	6.35E+07	4	2
	Tuff	2605	4.50E+10	0.19	6.10E+06	7	2

Appendix B: Experiment results: Subsidence profiles

Rock type	$\rho, \dfrac{kg}{m^3}$	E, Pa	v	σ_i, Pa	m_b
Andesite	2600	4.00E+10	0.28	1.38E+08	13
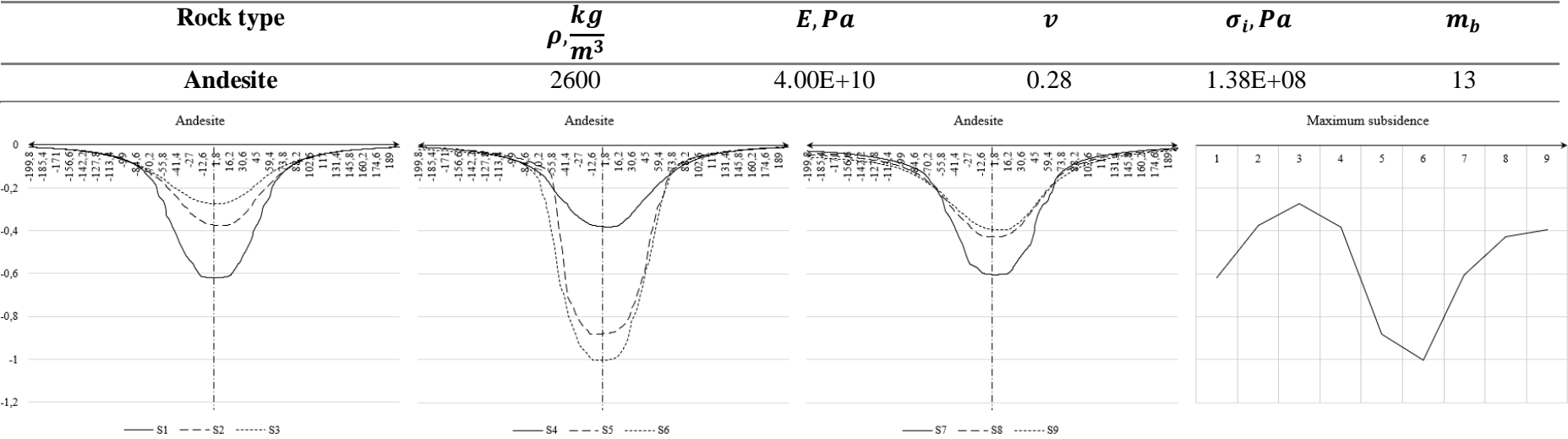
Rock type	$\rho, \dfrac{kg}{m^3}$	E, Pa	v	σ_i, Pa	m_b
Basalt	3000	6.00E+10	0.23	8.66E+08	13
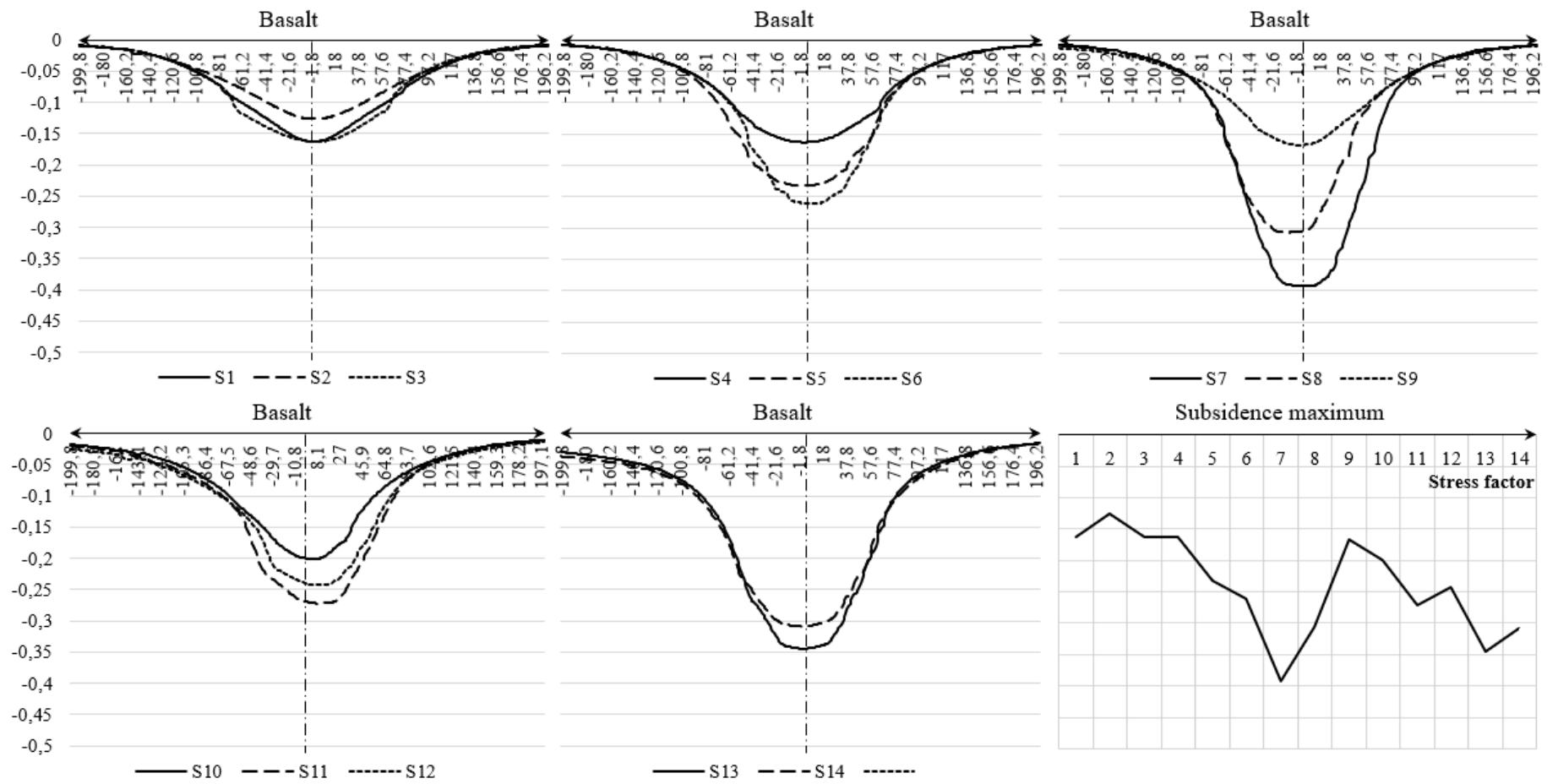
Rock type	$\rho, \dfrac{kg}{m^3}$	E, Pa	v	σ_i, Pa	m_b
Diabase	2920	8.65E+10	0.24	2.97E+08	8
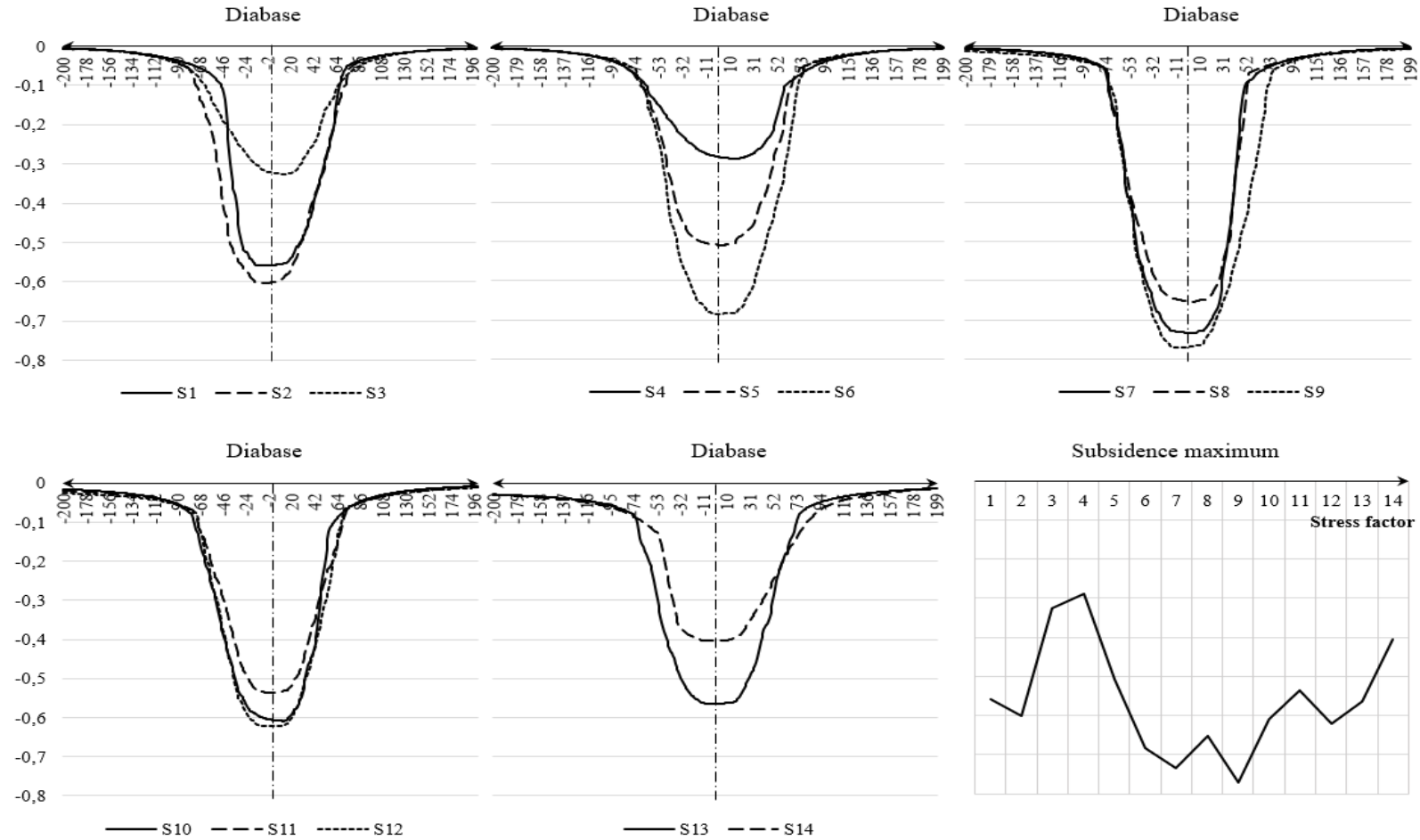
Rock type	$\rho, \dfrac{kg}{m^3}$	E, Pa	v	σ_i, Pa	m_b
Diorite	2900	6.50E+10	0.27	2.25E+08	13
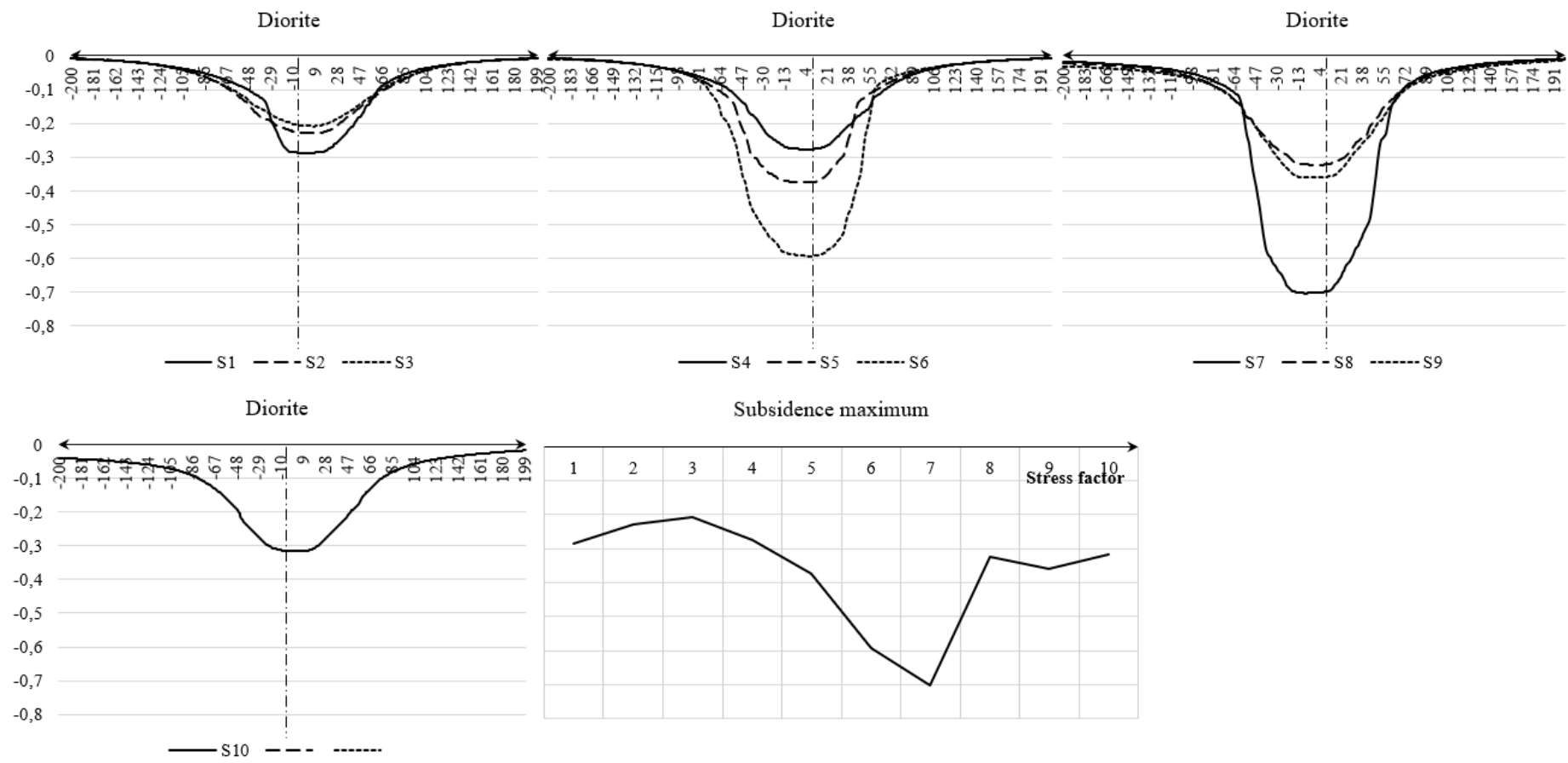
Rock type	$\rho, \dfrac{kg}{m^3}$	E, Pa	v	σ_i, Pa	m_b
Dolerite	2900	6.50E+10	0.25	8.66E+08	8
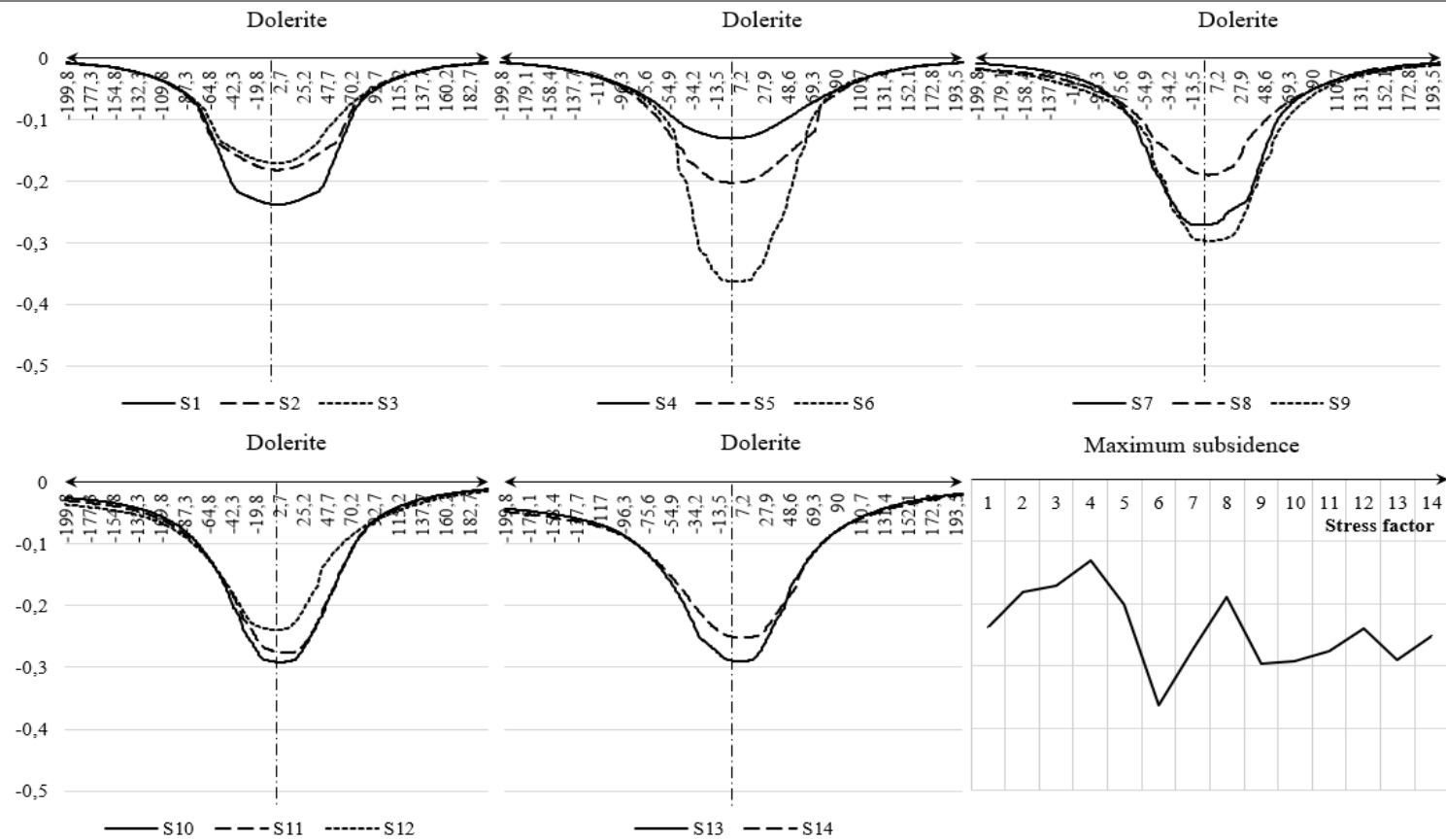
Rock type	$\rho, \dfrac{kg}{m^3}$	E, Pa	v	σ_i, Pa	m_b
Gabbro	3100	7.00E+10	0.18	2.17E+08	14

Gabbro · Gabbro · Gabbro · Gabbro · Gabbro · Subsidendce maximum
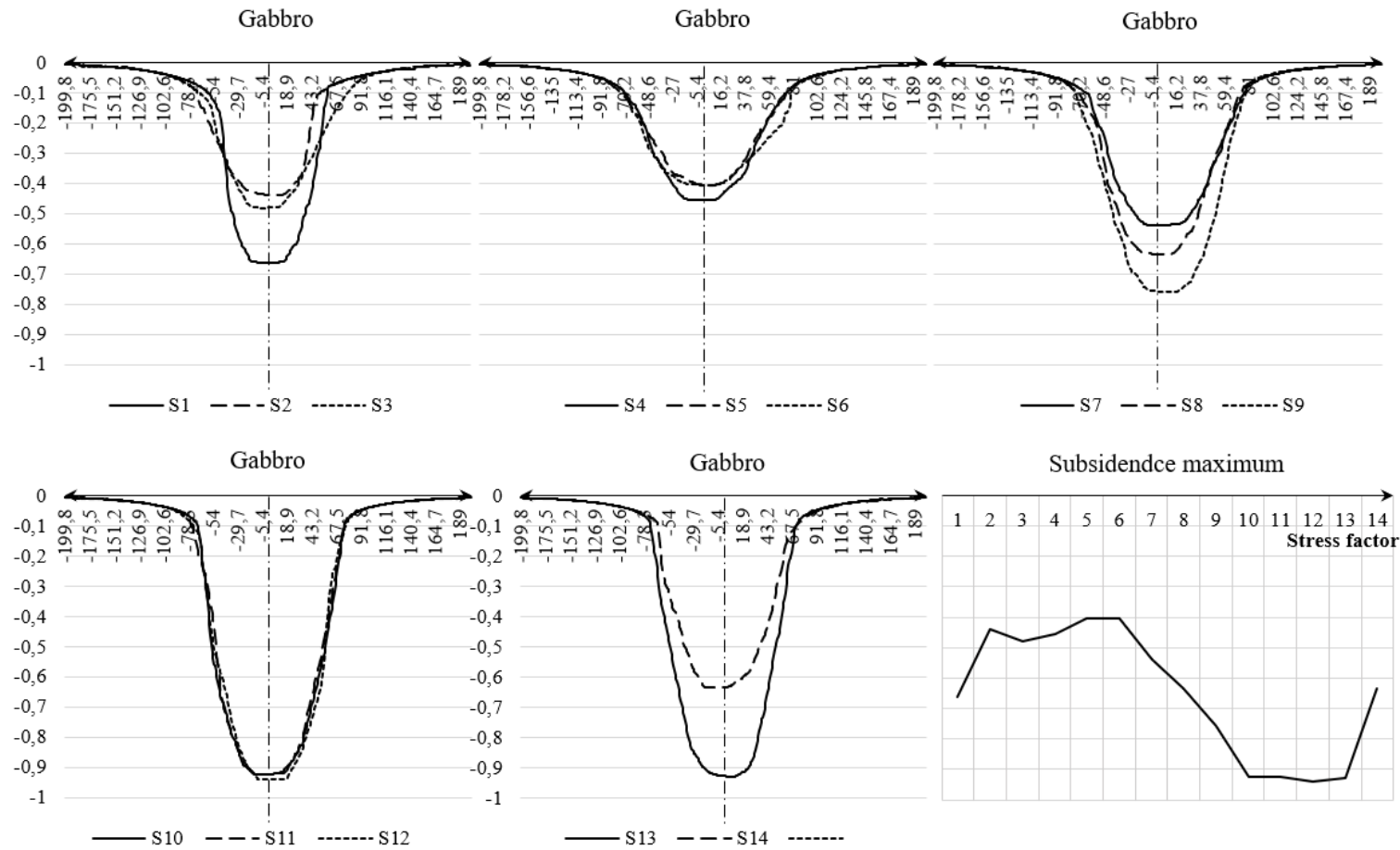
Rock type	$\rho, \dfrac{kg}{m^3}$	E, Pa	v	σ_i, Pa	m_b
Granite	2655	5.00E+10	0.21	1.76E+08	16
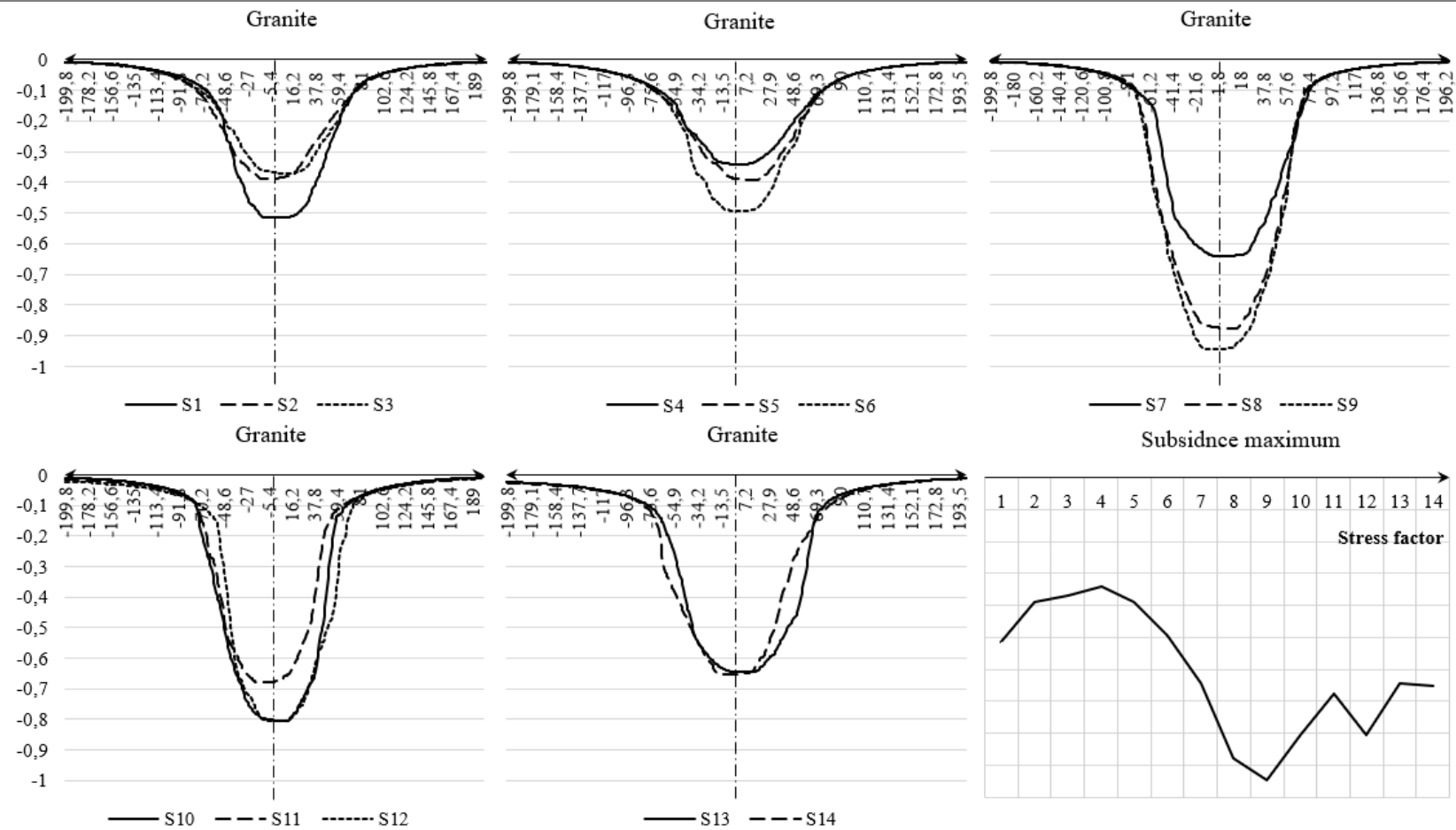
Rock type	$\rho, \dfrac{kg}{m^3}$	E, Pa	v	σ_i, Pa	m_b
Norite	3000	8.36E+10	0.21	2.25E+08	10

149
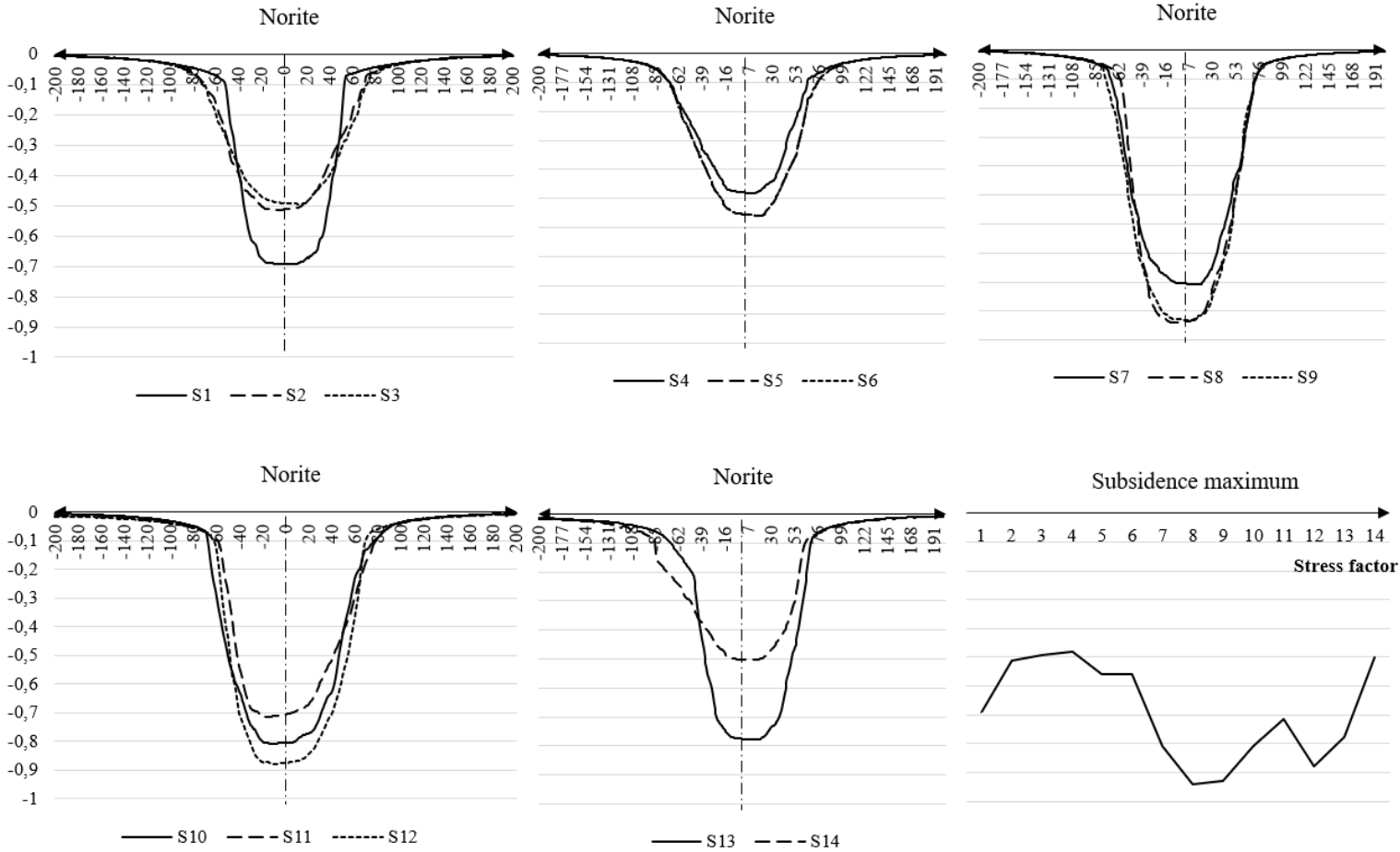
Rock type	$\rho, \dfrac{kg}{m^3}$	E, Pa	v	σ_i, Pa	m_b
Rhyolite	2600	4.20E+10	0.2	5.77E+08	8
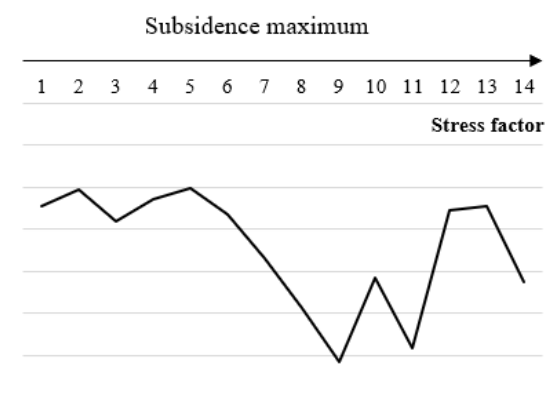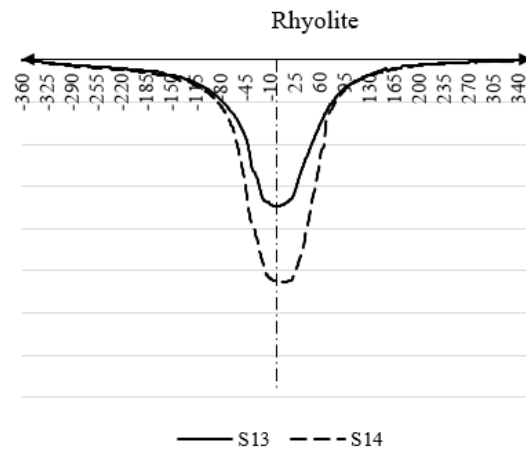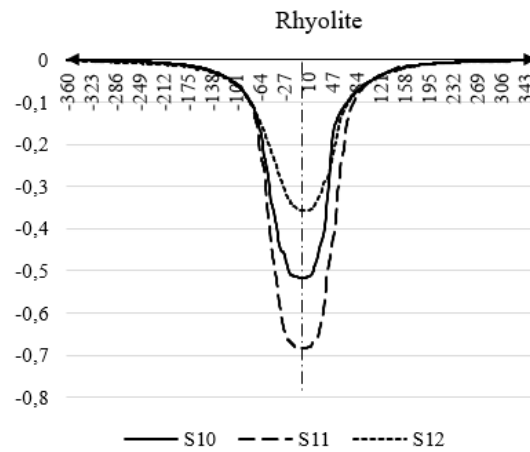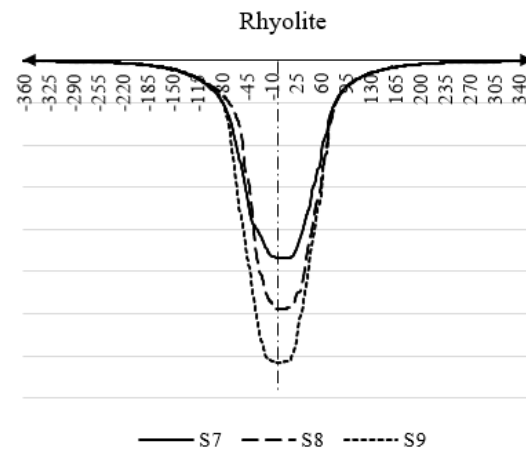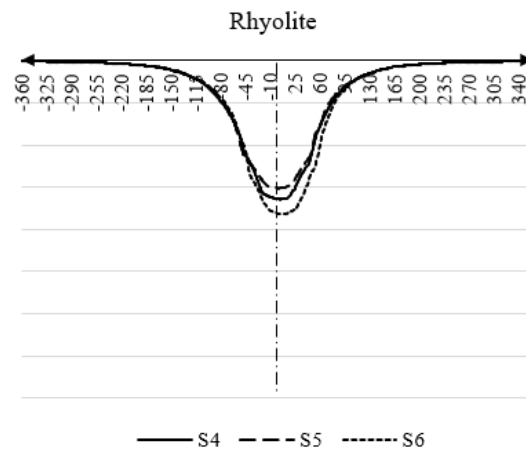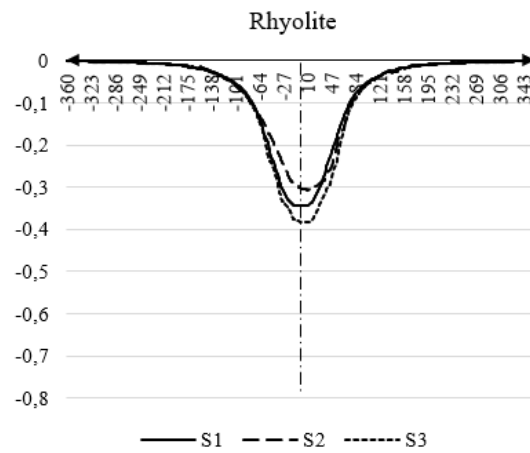
Rock type	$\rho, \dfrac{kg}{m^3}$	E, Pa	v	σ_i, Pa	m_b
Slate	2690	7.76E+10	0.25	1.74E+08	8
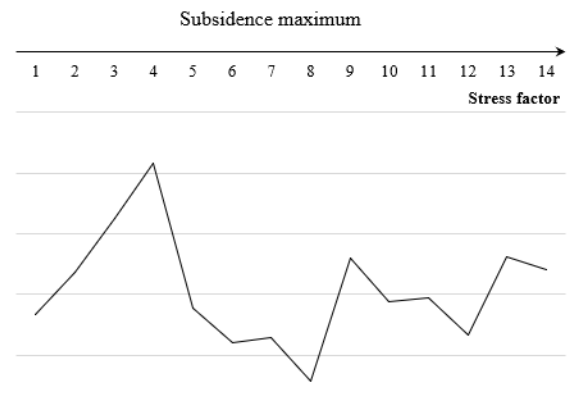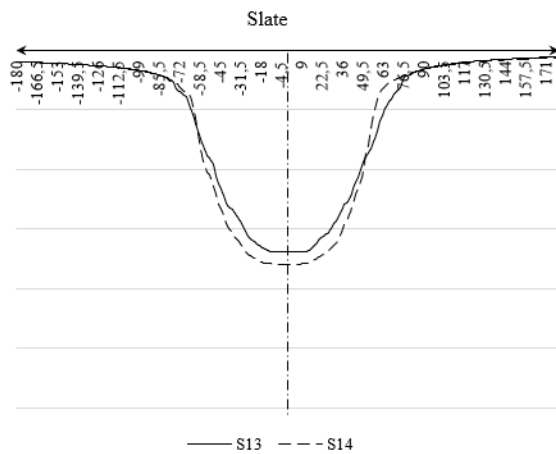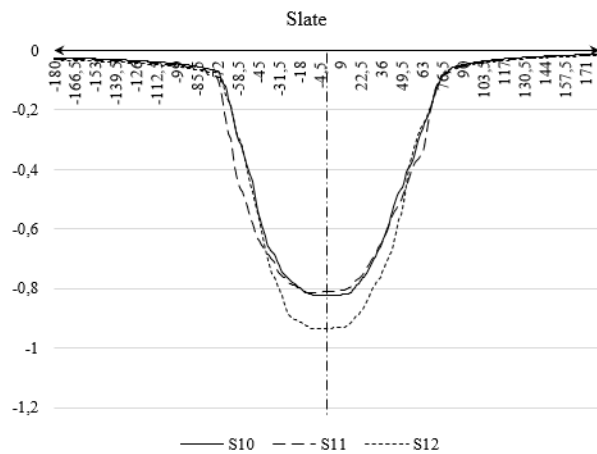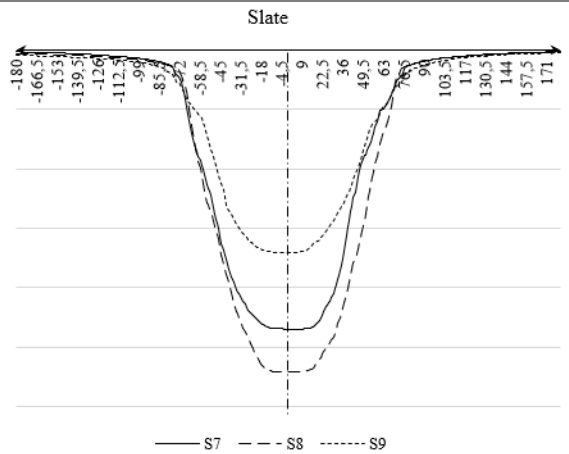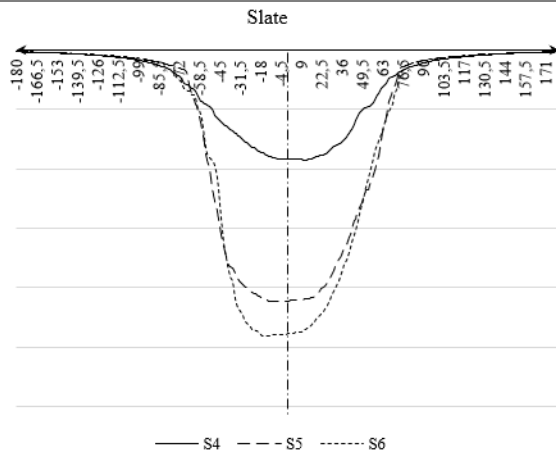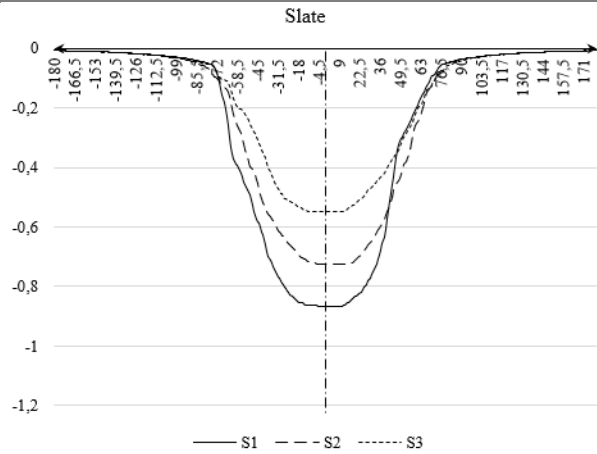
Rock type	$\rho, \dfrac{kg}{m^3}$	E, Pa	v	σ_i, Pa	m_b
Gneiss	2795	5.50E+10	0.25	1.67E+08	14

Rock type	$\rho, \dfrac{kg}{m^3}$	E, Pa	v	σ_i, Pa	m_b
Marble	2685	5.00E+10	0.28	1.40E+08	5

Marble

Marble

Marble

S1 — — S2 ------- S3

S4 — — S5 ------- S6

S7 — — S8 ------- S9

Marble

Marble

Subsidence maximum

Stress factor

S10 — — S11 ------- S12

S13 — — S14
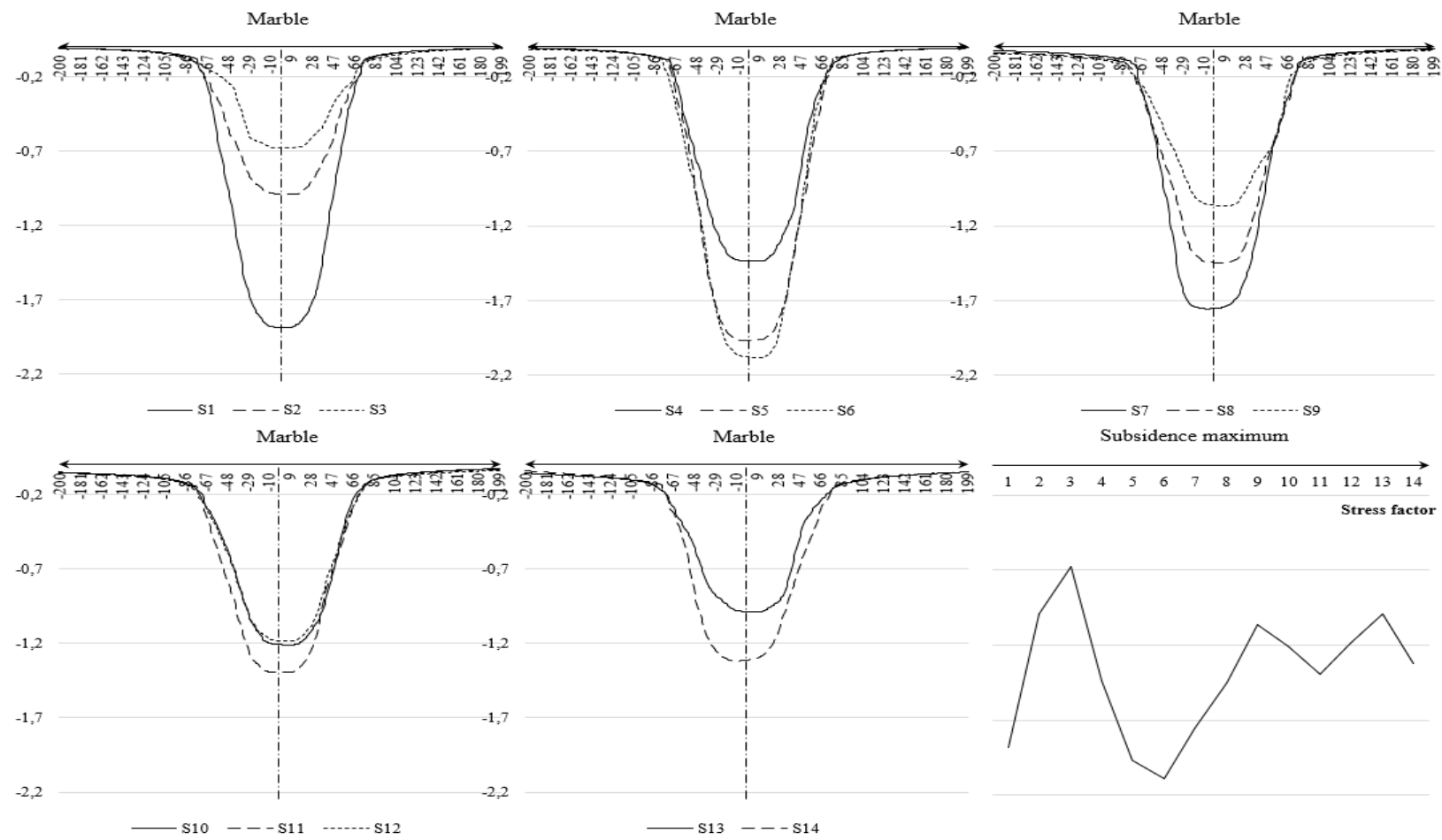
Rock type	$\rho, \dfrac{kg}{m^3}$	E, Pa	v	σ_i, Pa	m_b
Marl	2200	6.36E+09	0.22	1.23E+08	4

154
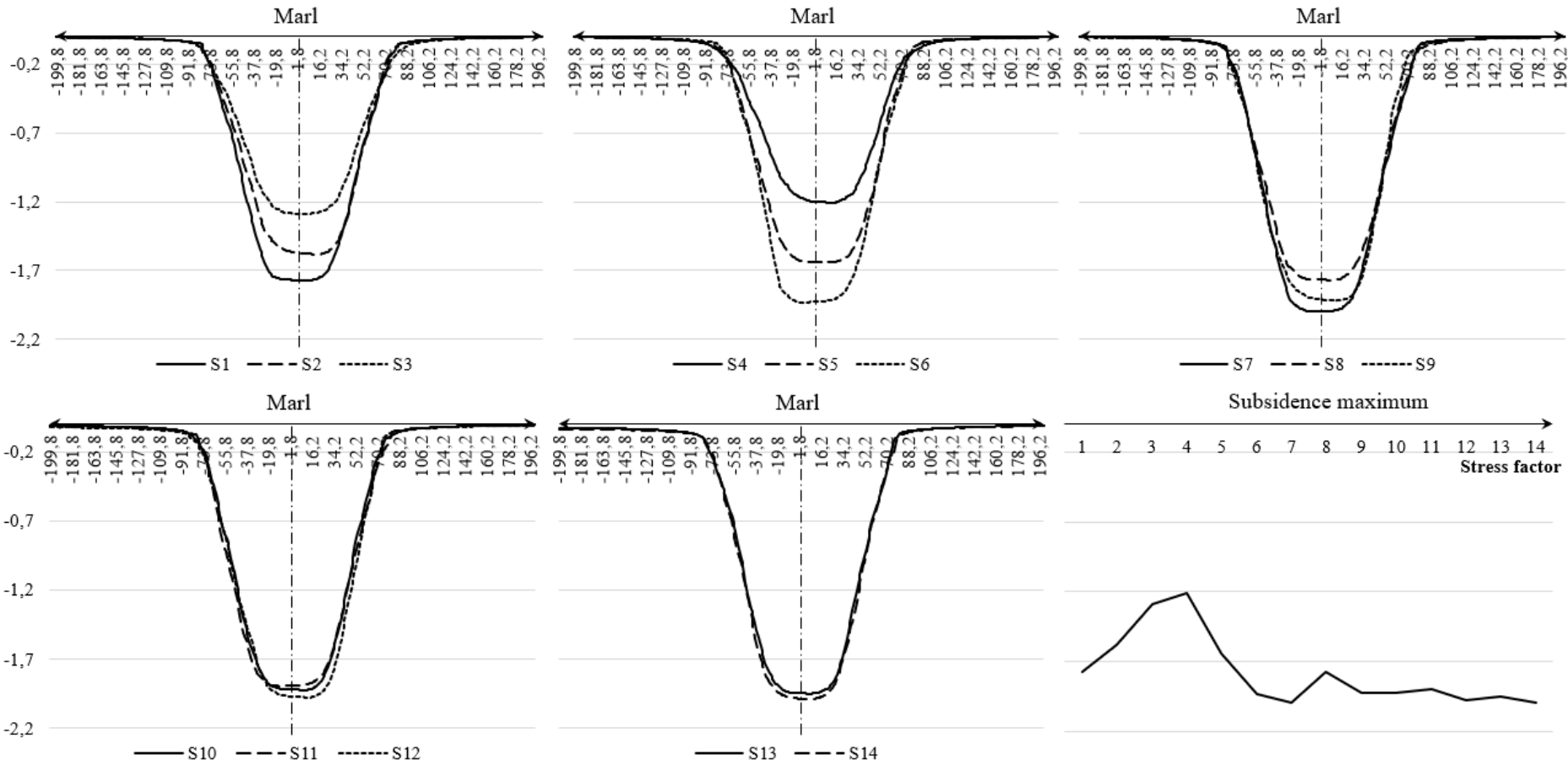
Rock type	$\rho, \dfrac{kg}{m^3}$	E, Pa	v	σ_i, Pa	m_b
Phyllite	2450	5.50E+10	0.26	1.33E+08	6

155
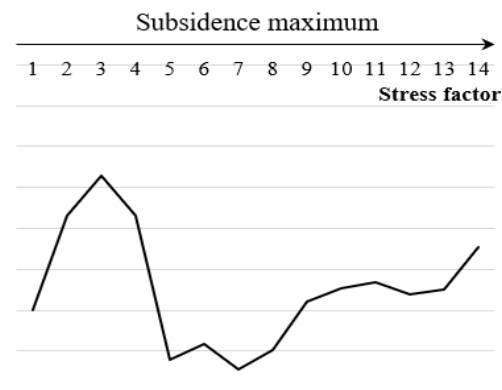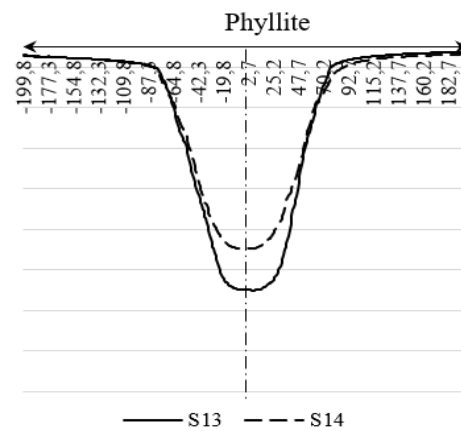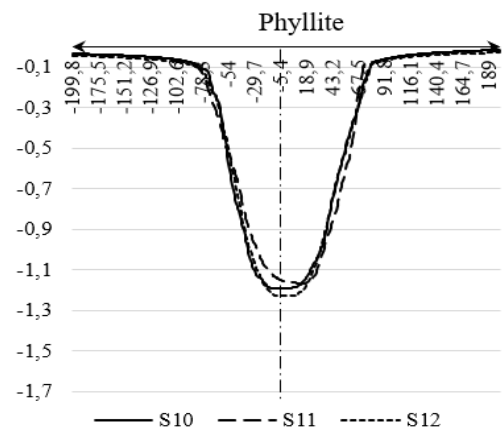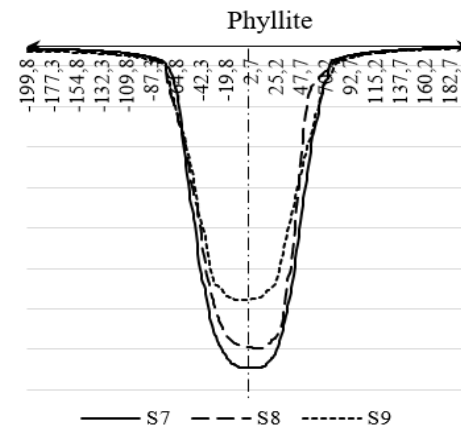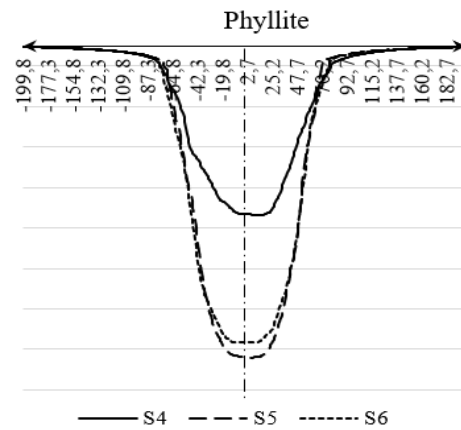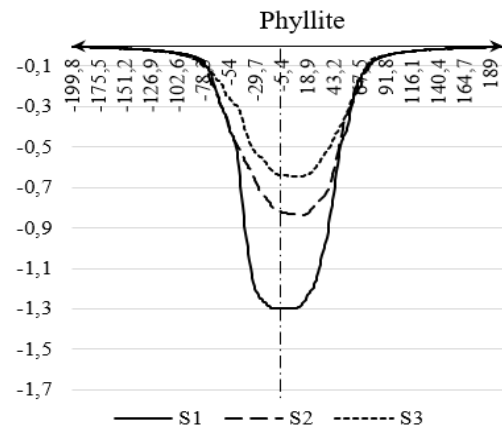
Rock type	$\rho, \dfrac{kg}{m^3}$	E, Pa	v	σ_i, Pa	m_b
Quartzite	2640	7.00E+10	0.2	2.21E+08	10
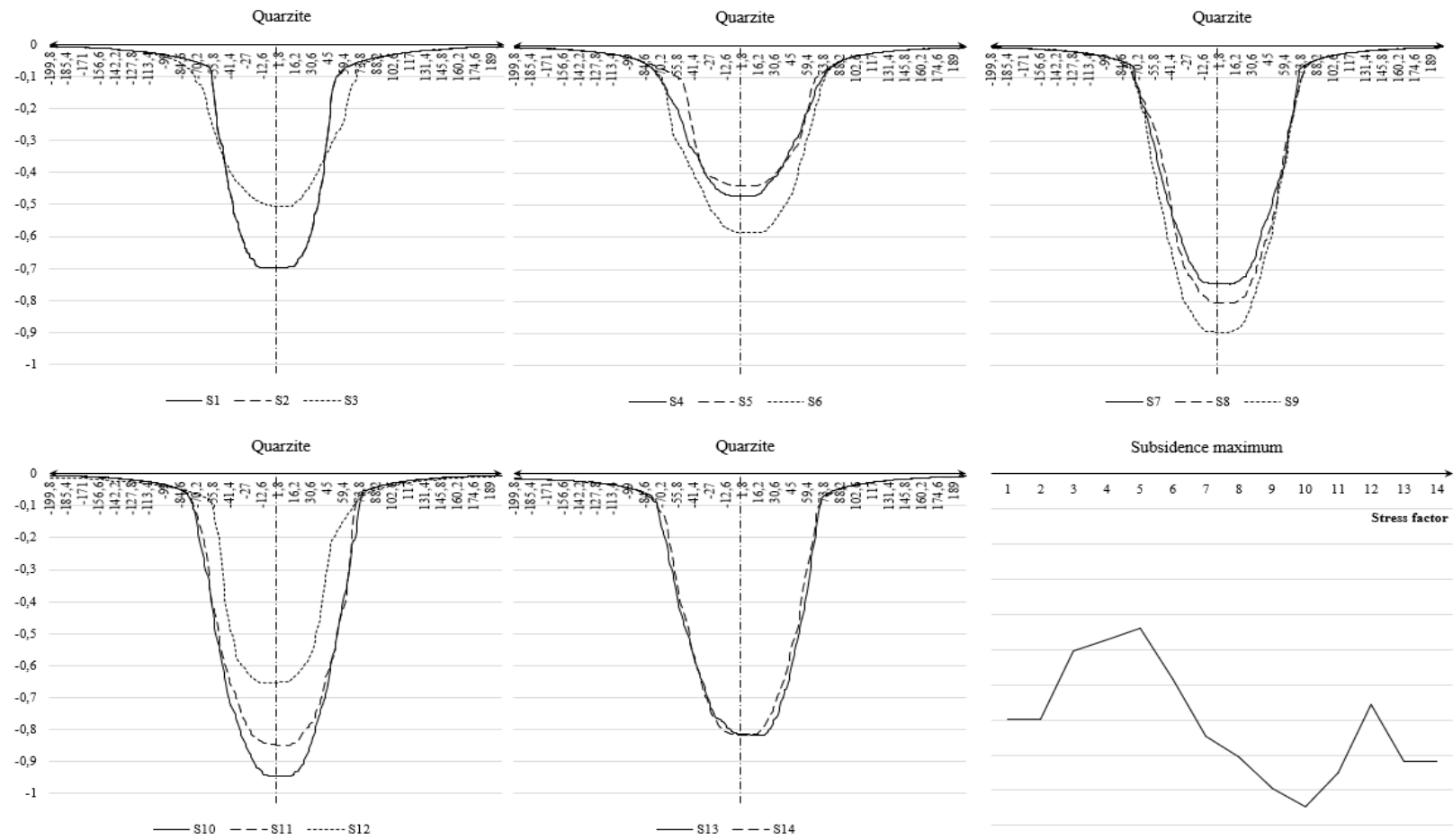
Rock type	$\rho, \dfrac{kg}{m^3}$	E, Pa	v	σ_i, Pa	m_b
Schist	2595	3.25E+10	0.17	7.75E+07	5
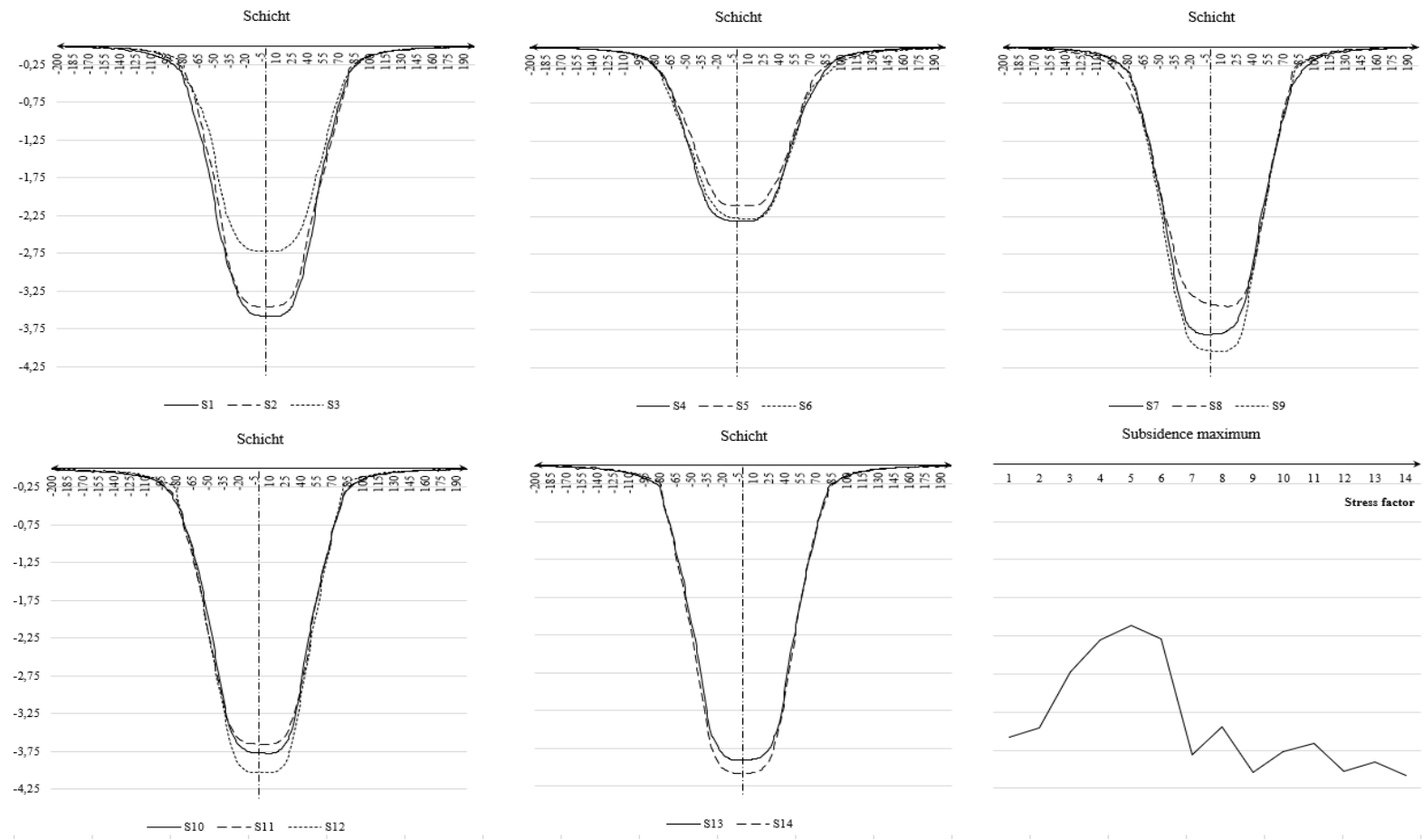
Rock type	$\rho, \dfrac{kg}{m^3}$	E, Pa	v	σ_i, Pa	m_b
Claystone	2115	5.25E+10	0.33	8.00E+06	2

Rock type	$\rho, \dfrac{kg}{m^3}$	E, Pa	v	σ_i, Pa	m_b
Conglomerate (1)	2615	5.00E+10	0.25	1.27E+08	11
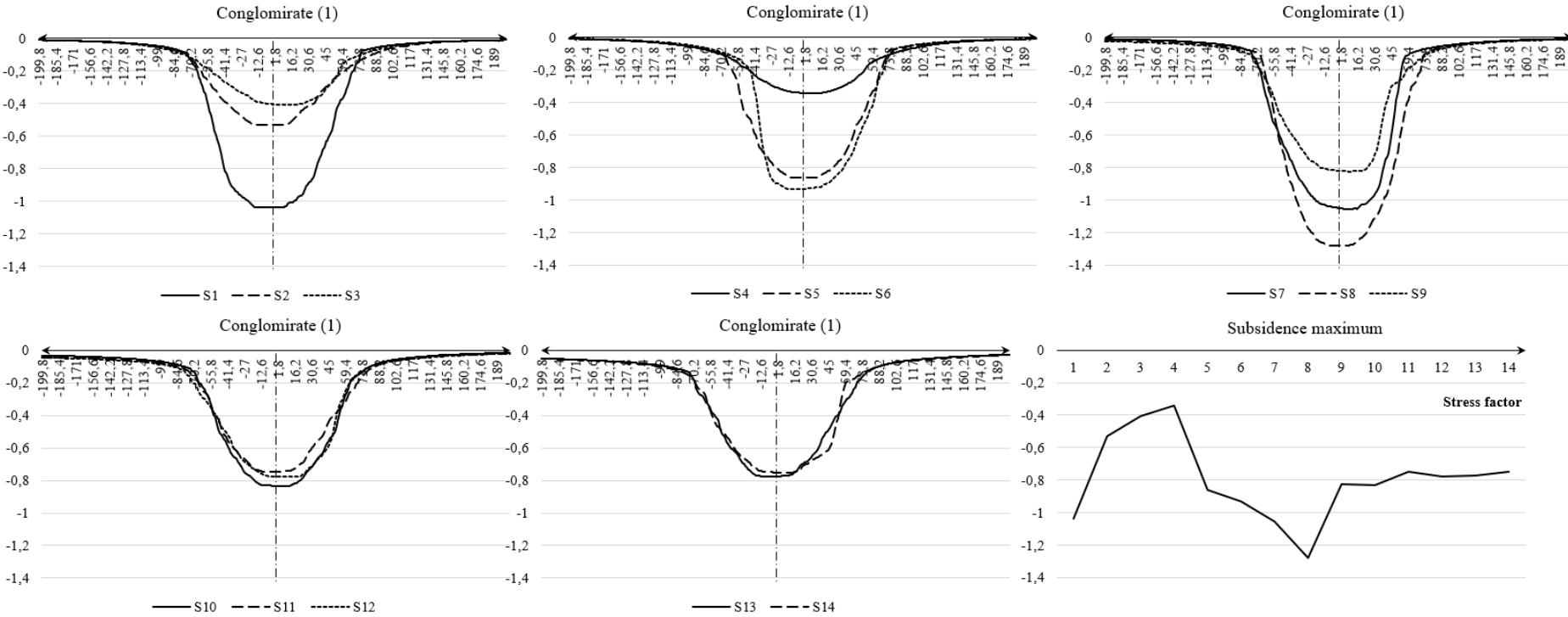
Conglomirate (1)

Conglomirate (1)

Conglomirate (1)

Conglomirate (1)

Conglomirate (1)

Subsidence maximum

Rock type	$\rho, \dfrac{kg}{m^3}$	E, Pa	v	σ_i, Pa	m_b
Conglomerate (2)	2600	4.00E+10	0.10	4.00E+07	6

Conglomirate (2)

Conglomirate (2)

Conglomirate (2)

Conglomirate (2)

Conglomirate (2)

Subsidence maximum
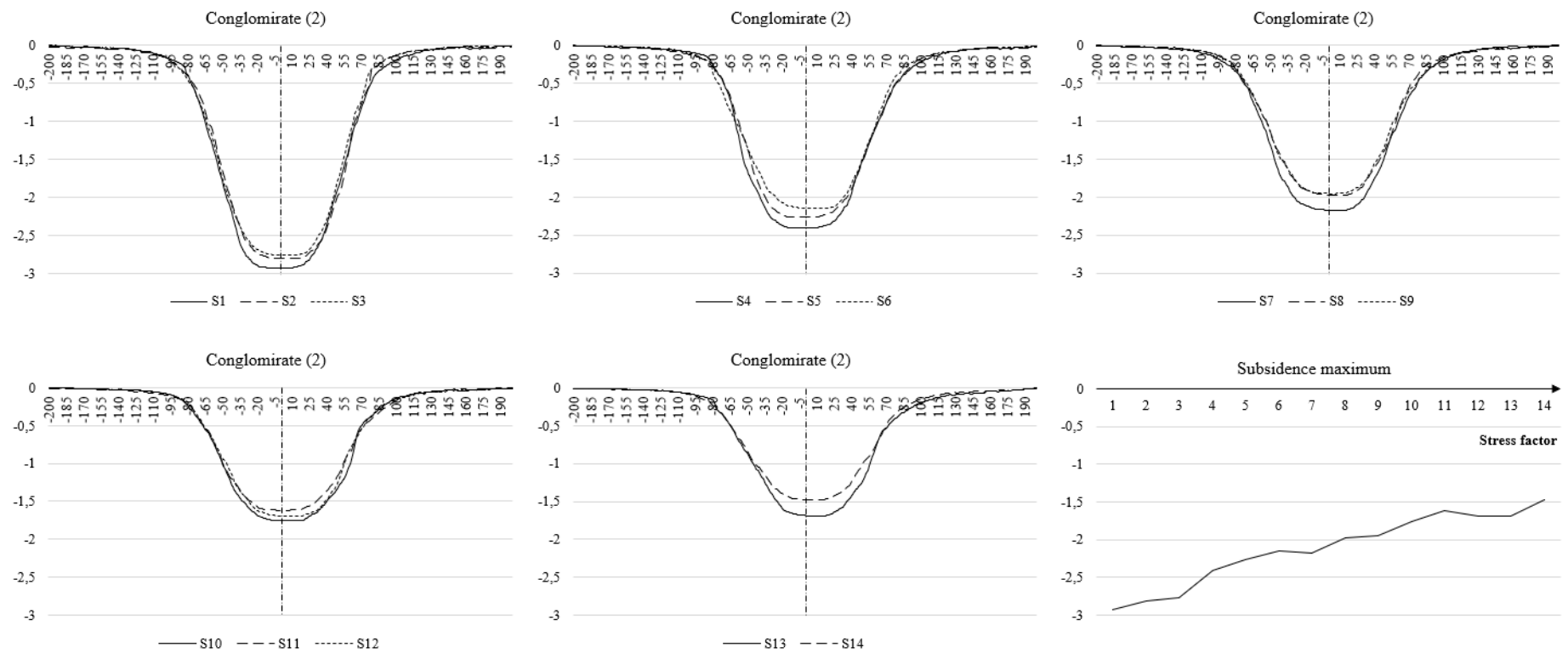
Rock type	$\rho, \dfrac{kg}{m^3}$	E, Pa	v	σ_i, Pa	m_b
Dolomite	2200	3.00E+10	0.23	2.30E+08	5

Rock type	$\rho, \dfrac{kg}{m^3}$	E, Pa	v	σ_i, Pa	m_b
Limestone	2415	4.50E+10	0.22	1.57E+08	4
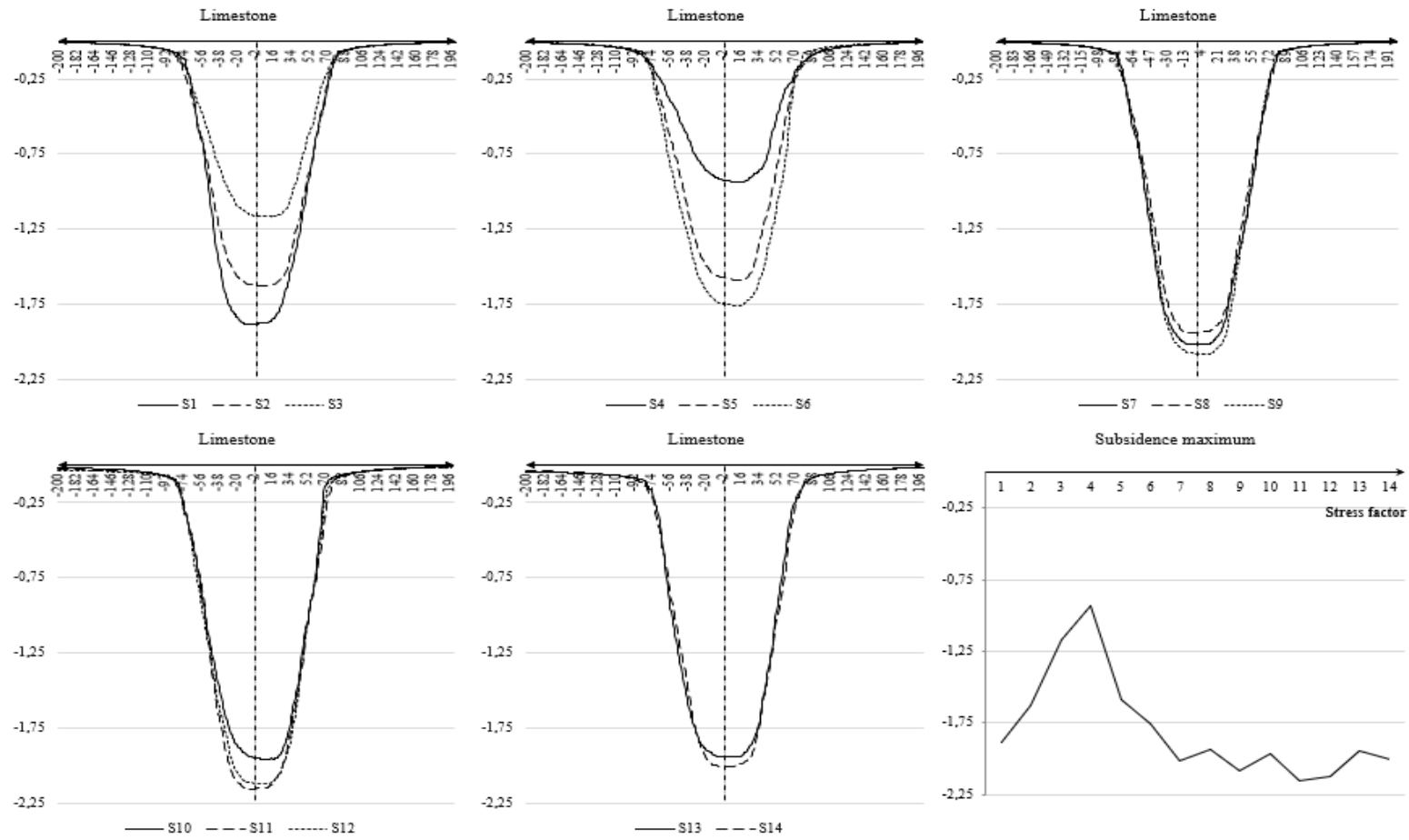
Rock type	$\rho, \dfrac{kg}{m^3}$	E, Pa	v	σ_i, Pa	m_b
Mudstones	2270	3.75E+10	0.15	1.88E+08	4
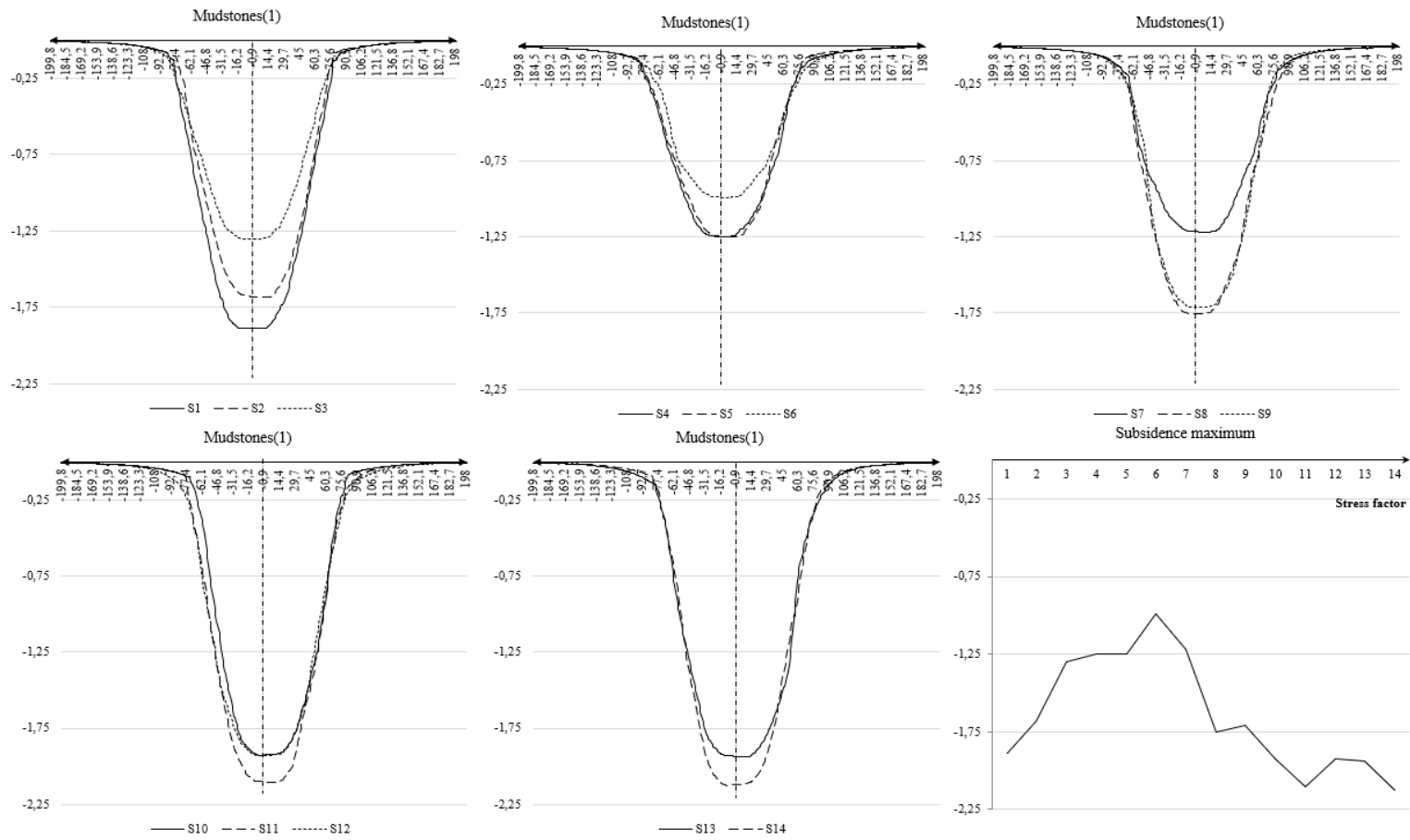
Rock type	$\rho, \dfrac{kg}{m^3}$	E, Pa	v	σ_i, Pa	m_b
Sandstone (1)	2185	2.55E+10	0.26	1.20E+08	9

164
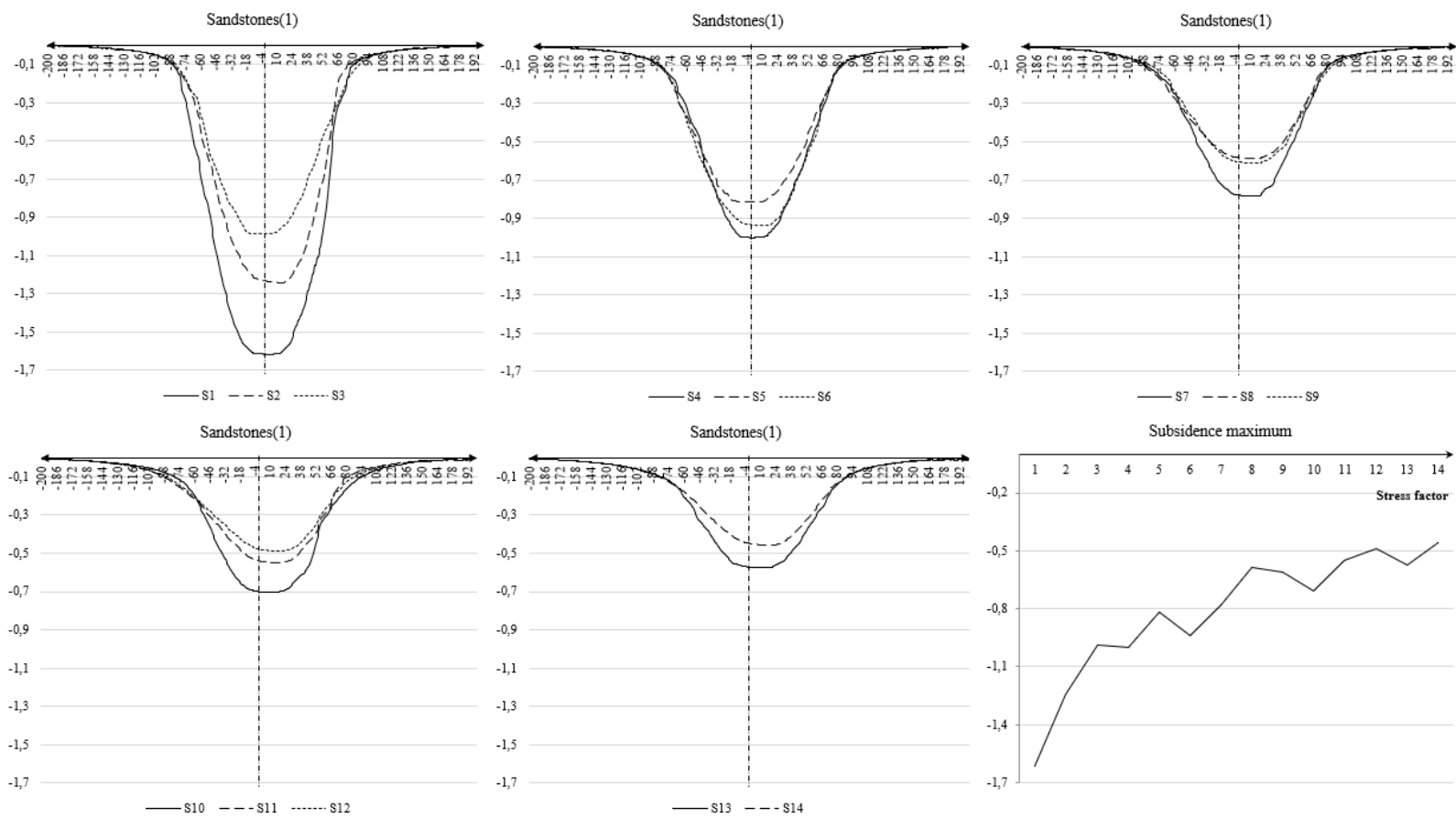
Rock type	$\rho, \dfrac{kg}{m^3}$	E, Pa	v	σ_i, Pa	m_b
Sandstone (2)/2_Sandstonee	2185	2.55E+10	0.10	1.20E+08	9
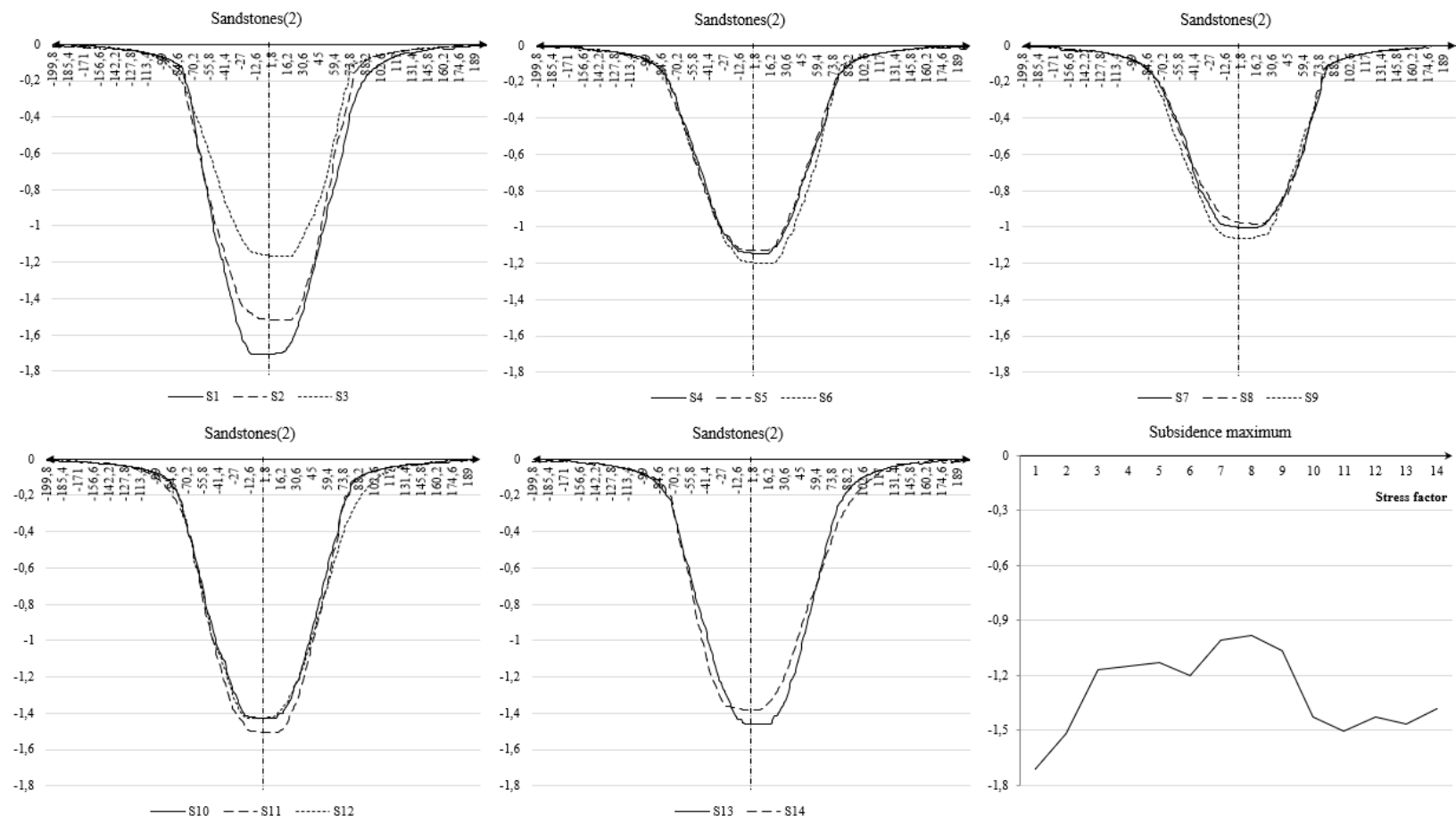
Rock type	$\rho, \dfrac{kg}{m^3}$	E, Pa	v	σ_i, Pa	m_b
Sandstone (3)/ Sandstone 1	2050	3.00E+10	0.14	9.60E+07	10
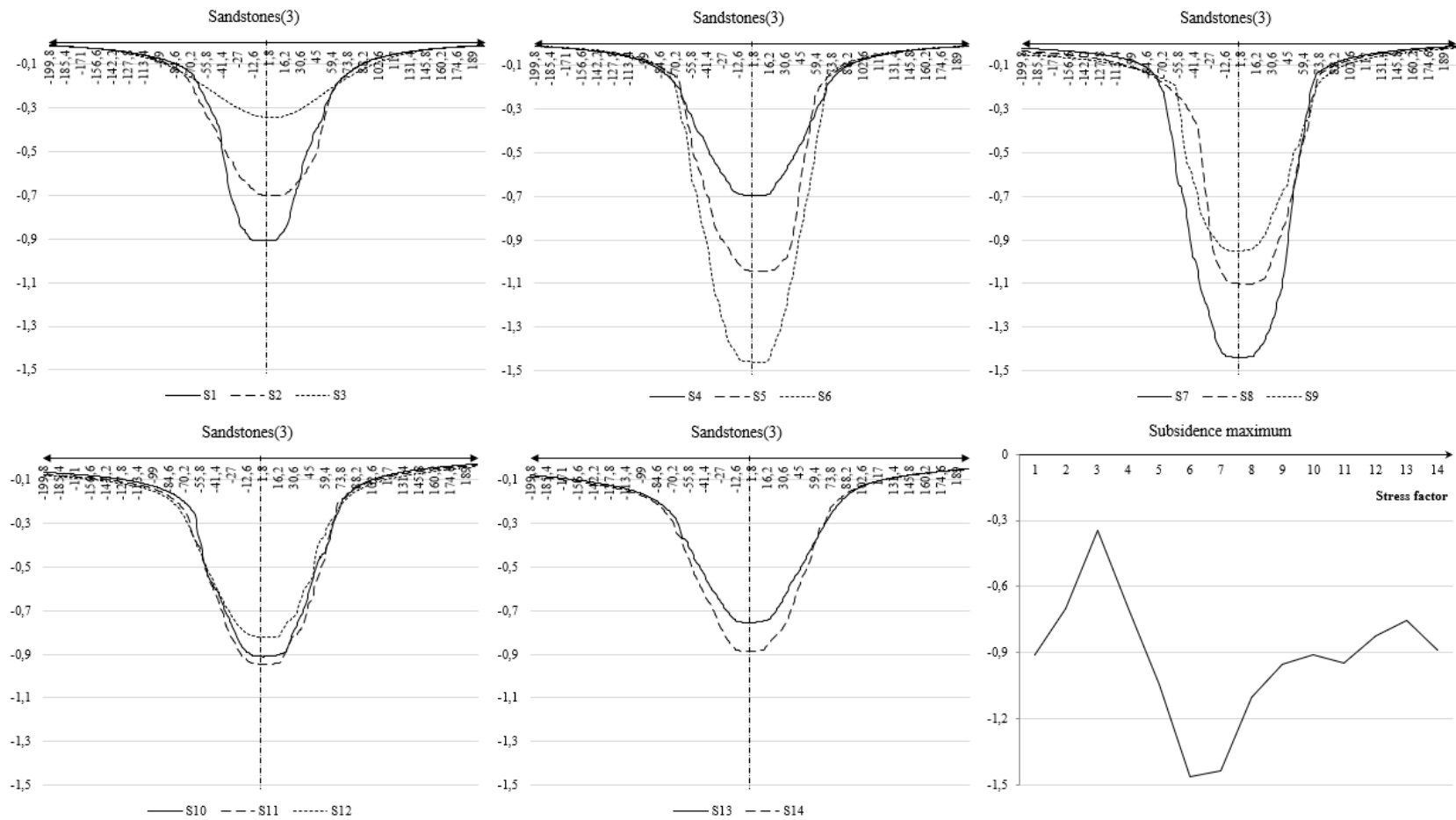
Rock type	$\rho, \dfrac{kg}{m^3}$	E, Pa	v	σ_i, Pa	m_b
Sandstone (4)/ 12,3	2185	4.00E+10	0.26	1.20E+08	9
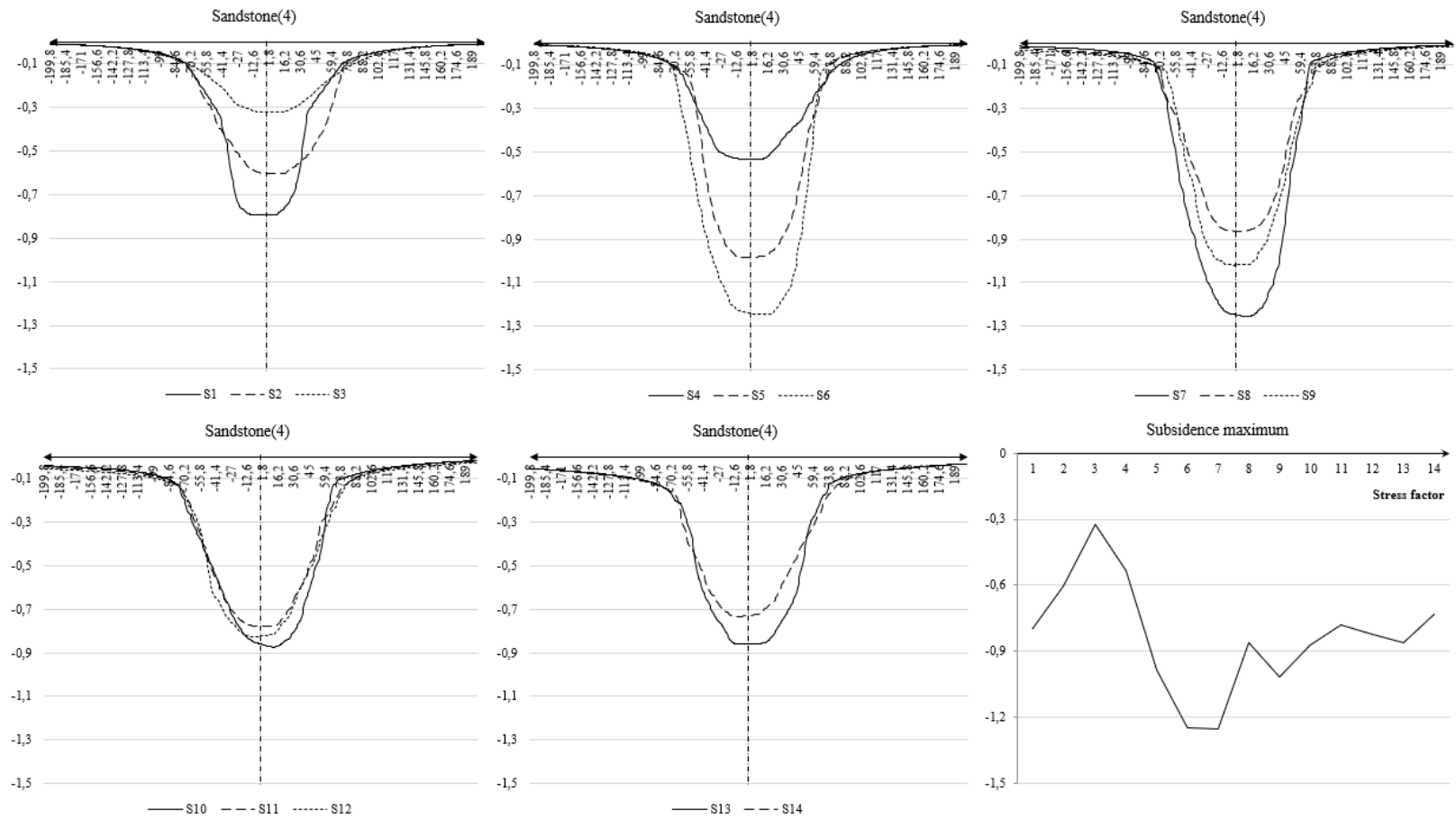
Rock type	$\rho, \dfrac{kg}{m^3}$	E, Pa	v	σ_i, Pa	m_b
Sandstone (5)/ 12,4	2185	2.55E+10	0.10	1.20E+08	2

168
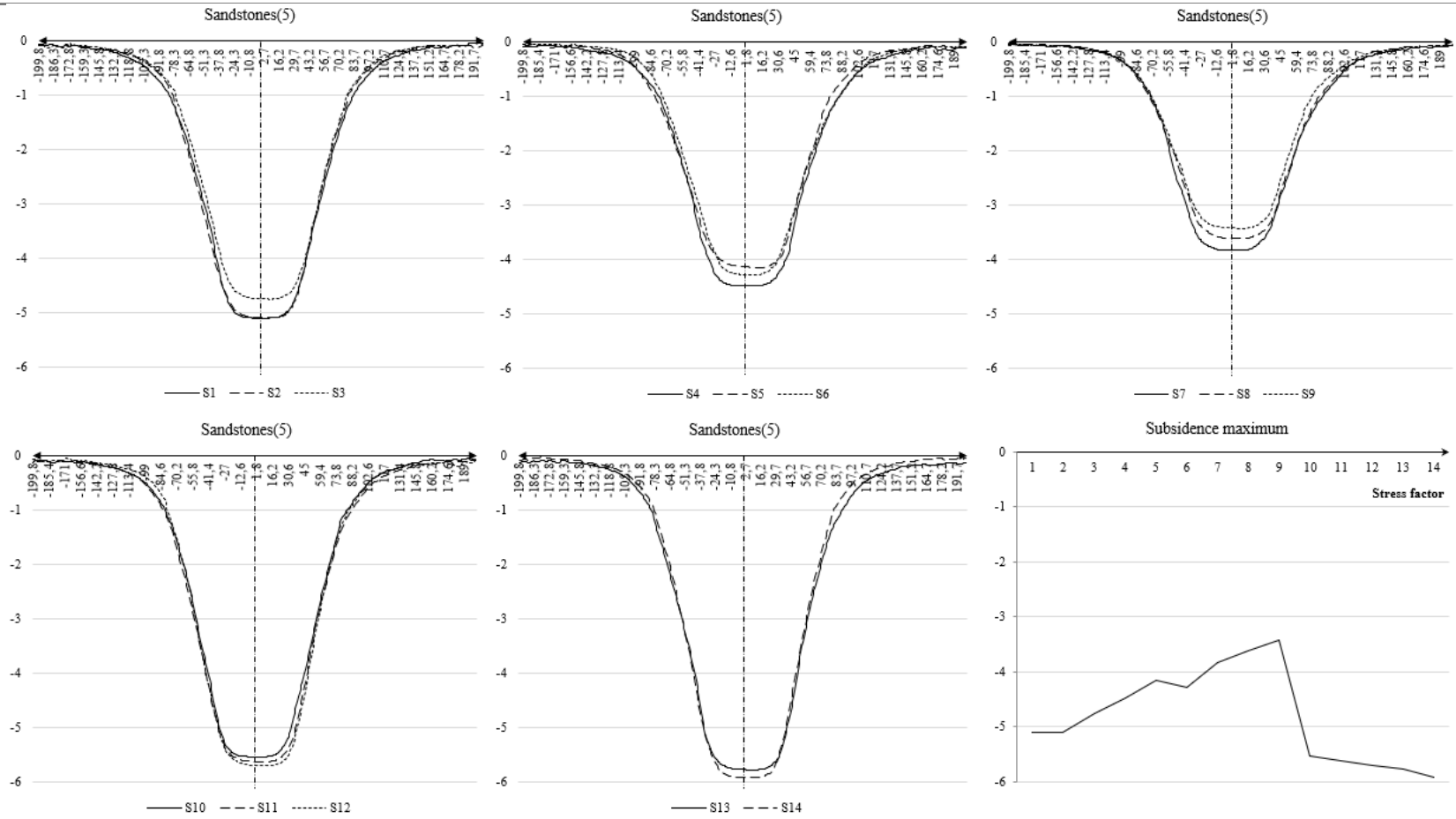
Rock type	$\rho, \dfrac{kg}{m^3}$	E, Pa	v	σ_i, Pa	m_b
Shale (1)	2535	1.75E+10	0.17	2.10E+07	4
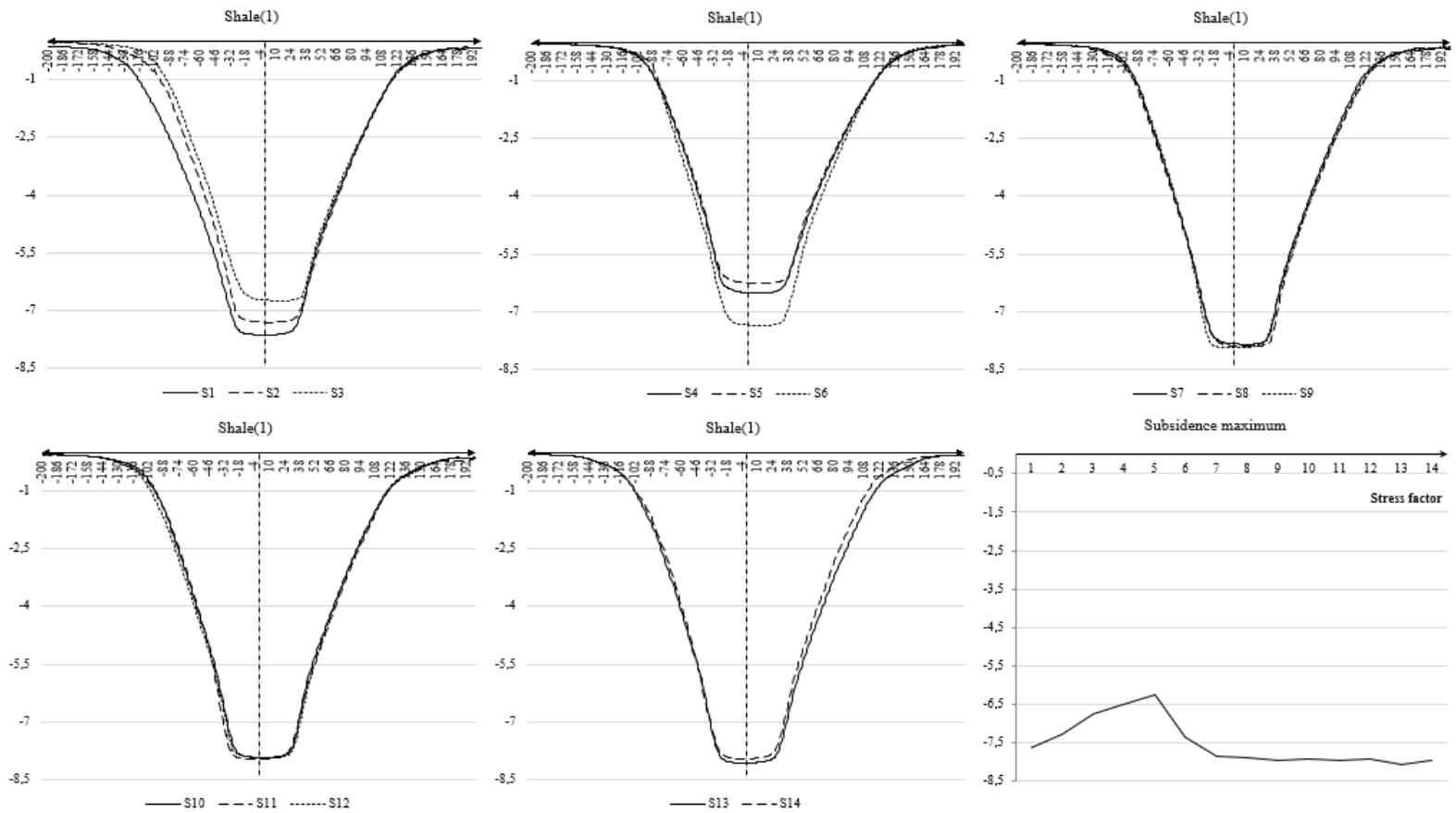
Rock type	$\rho, \dfrac{kg}{m^3}$	E, Pa	v	σ_i, Pa	m_b
Shale (2)	2300	2.00E+10	0.10	2.50E+07	6
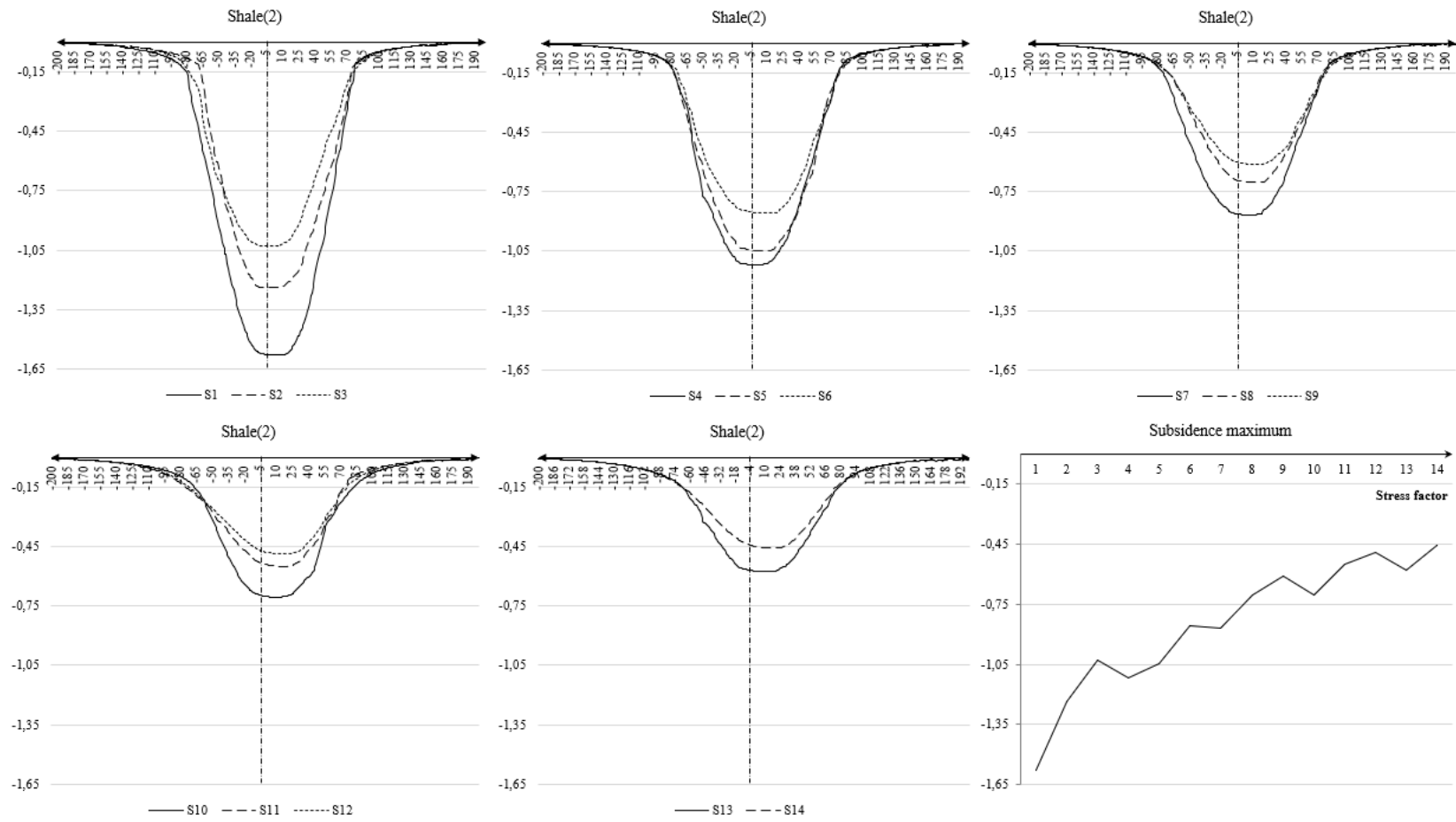
Rock type	$\rho, \dfrac{kg}{m^3}$	E, Pa	v	σ_i, Pa	m_b
Siltstone	2000	1.65E+10	0.22	6.35E+07	4
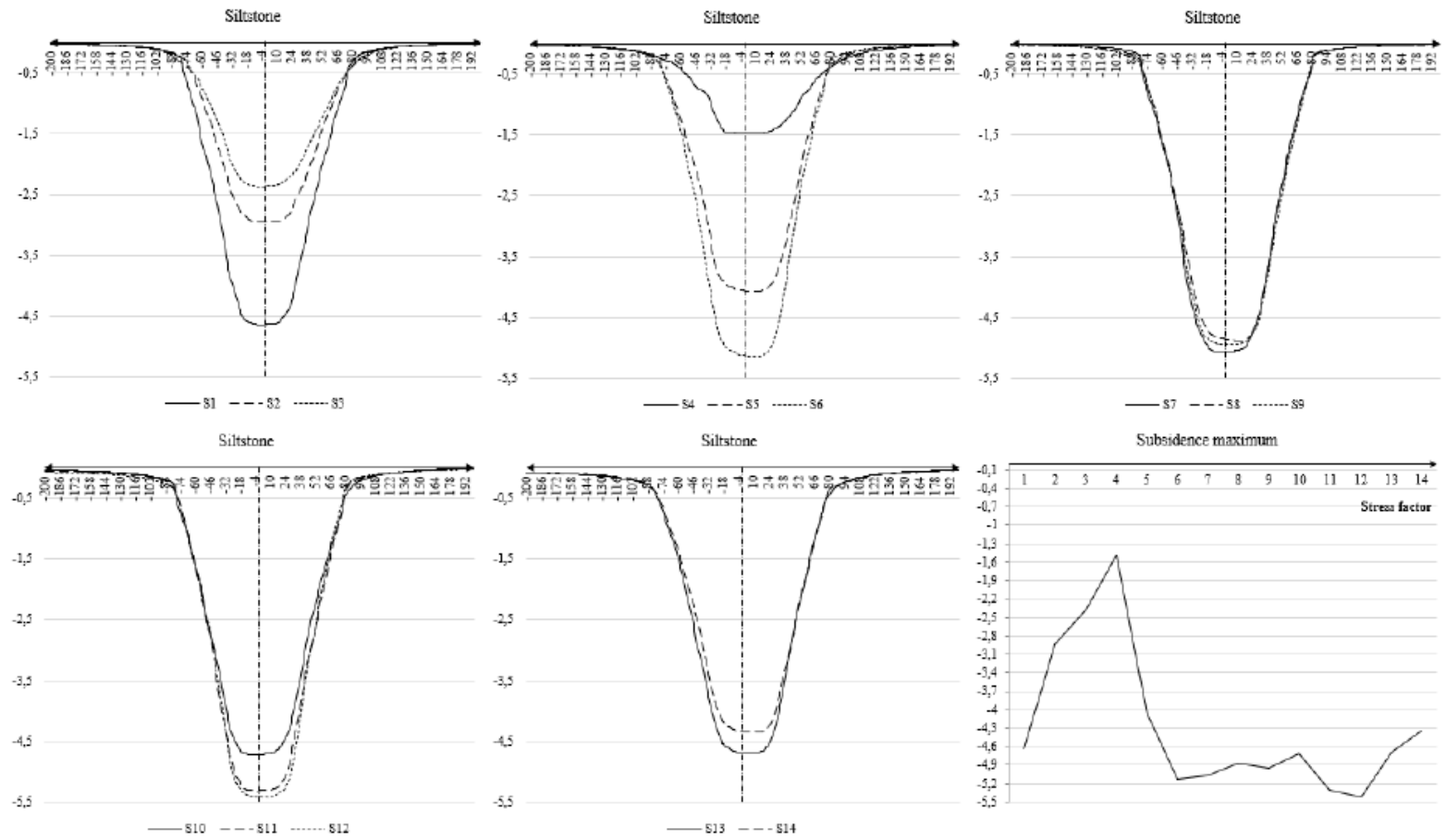
Rock type	$\rho, \dfrac{kg}{m^3}$	E, Pa	v	σ_i, Pa	m_b
Tuff	2605	4.50E+10	0.19	6.10E+06	7
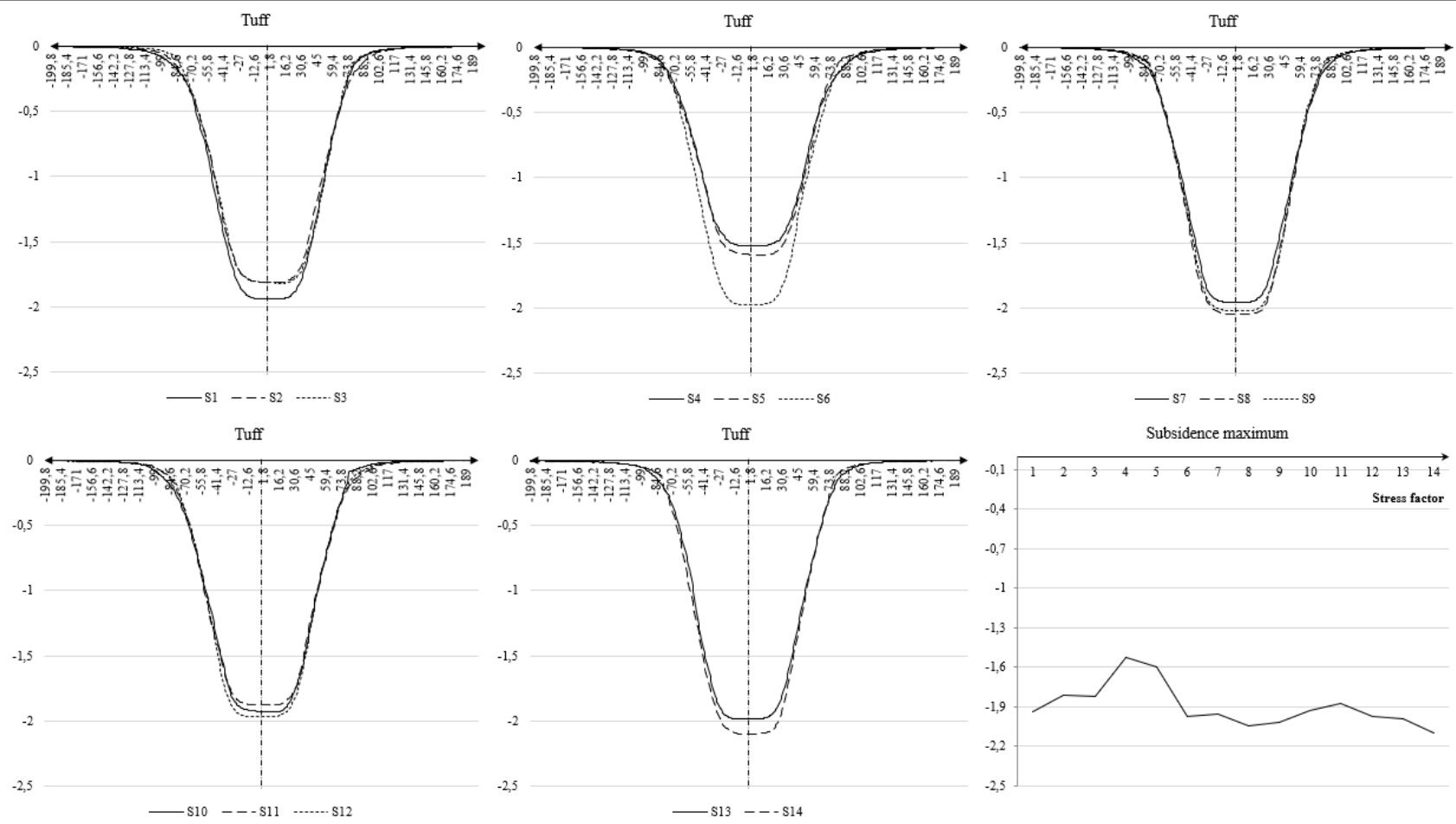
Appendix C: Correlation and rank correlation between rock properties and subsidence profile parameters

	ρ	E	v	σ_i	m_b	Stress factor	S_{max}	Inflection point (input)	Inflection point (release)	Skewness	Plateau angle (input)	Plateau angle (release)	Influence angle (Input)	Influence angle (release)
ρ	1.00	0.77	0.19	0.50	0.57	-0.02	0.35	-0.03	-0.10	0.38	-0.04	0.14	0.29	-0.35
E	0.80	1.00	0.40	0.39	0.46	-0.01	0.50	0.00	-0.24	0.12	-0.01	0.08	0.42	-0.41
v	0.17	0.41	1.00	0.19	0.15	-0.03	0.28	0.26	-0.37	-0.13	0.07	-0.01	0.43	-0.36
σ_i	0.63	0.61	0.25	1.00	0.31	0.00	0.41	-0.12	-0.02	0.52	0.03	0.09	0.47	-0.49
m_b	0.56	0.50	0.15	0.43	1.00	-0.03	0.60	0.01	-0.17	0.23	0.10	0.02	0.42	-0.43
Stress factor	-0.02	-0.01	-0.04	-0.01	-0.03	1.00	-0.06	0.05	-0.01	0.01	-0.01	0.02	0.22	-0.12
S_{max}	0.58	0.56	0.32	0.70	0.75	-0.09	1.00	-0.06	-0.08	-0.02	0.17	0.14	0.41	-0.32
Inflection point (input)	-0.03	0.01	0.26	-0.07	0.01	0.03	0.09	1.00	-0.18	-0.31	0.15	-0.10	0.10	-0.14
Inflection point (release)	-0.09	-0.26	-0.39	-0.07	-0.12	-0.05	-0.10	-0.17	1.00	0.12	0.06	0.04	-0.35	0.31
Skewness	0.26	0.07	-0.24	0.31	0.19	0.02	0.28	-0.27	0.10	1.00	-0.06	0.16	0.31	-0.45
Plateau angle (input)	-0.12	-0.09	0.03	-0.12	-0.03	-0.02	-0.02	0.16	0.02	-0.14	1.00	0.04	0.06	-0.06
Plateau angle (release)	0.18	0.22	0.25	0.26	0.15	-0.04	0.19	-0.01	-0.16	-0.03	-0.33	1.00	0.05	-0.08
Influence angle (input)	0.32	0.43	0.43	0.55	0.41	0.27	0.57	0.13	-0.37	0.26	-0.11	0.25	1.00	-0.90
Influence angle (release)	-0.35	-0.42	-0.39	-0.51	-0.44	-0.12	-0.64	-0.18	0.35	-0.42	0.13	-0.23	-0.89	1.00

Normal correlation coefficient (by Pearson method)

Rank correlation coefficient (by Spearman method)

Appendix D: Caverns map

Caverns map with data
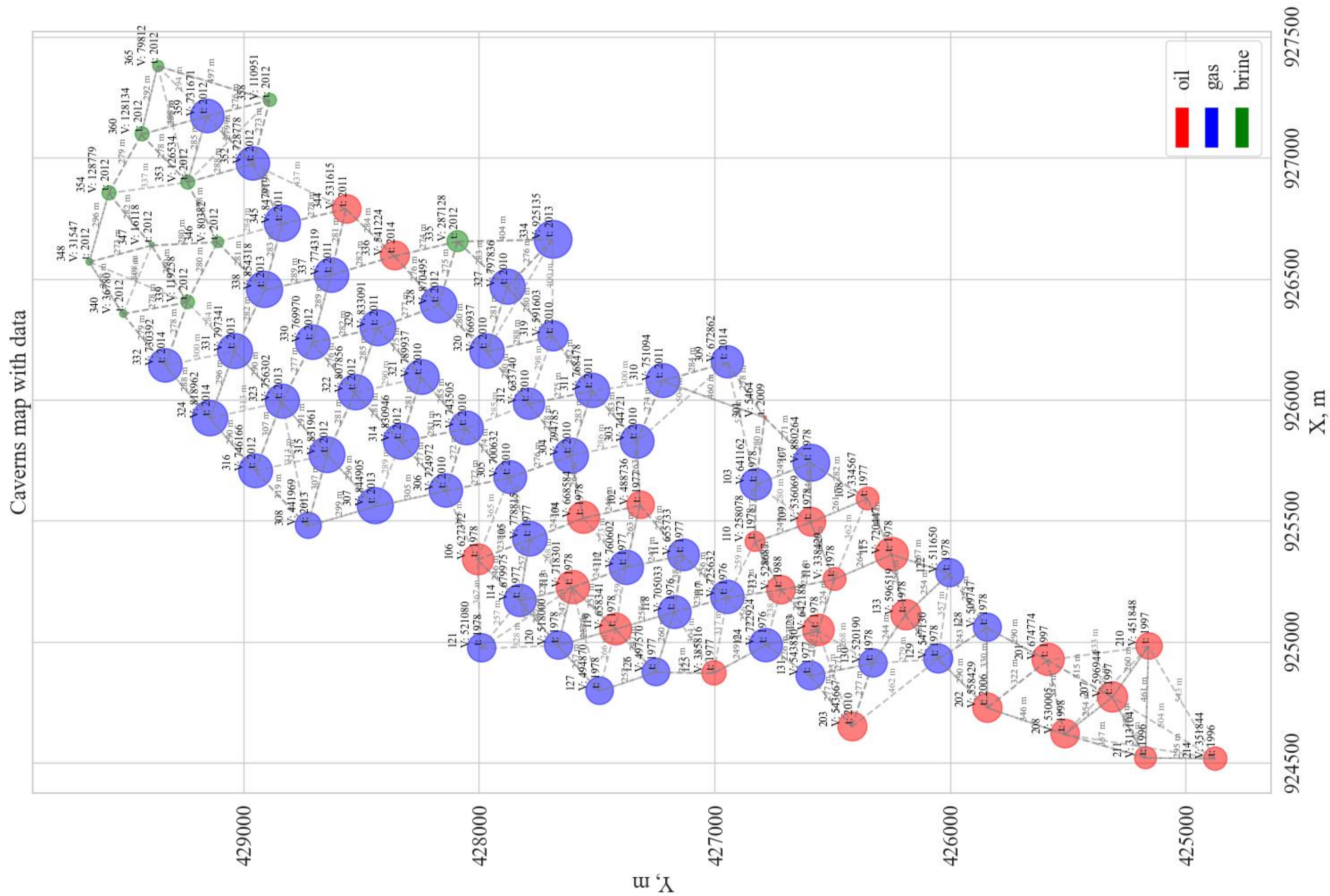
Appendix E: Caverns data for 2022.

	Name	X	Y	z_r	z_f	Year	Type	Volume
1	102	925566	427317	848	1500	1977	Oil	488736
2	103	925652	426824	855	1500	1978	Gas	641162
3	104	925514	427557	855	1500	1978	Oil	668584
4	105	925426	427783	836	1500	1977	Gas	778815
5	106	925342	428006	883	1500	1978	Oil	627372
6	107	925742	426592	878	1500	1978	Gas	880264
7	108	925595	426351	896	1300	1977	Oil	334567
8	109	925496	426592	874	1320	1978	Oil	536069
9	110	925415	426828	870	1500	1978	Oil	258078
10	111	925360	427134	830	1500	1977	Gas	655733
11	112	925310	427376	860	1500	1977	Gas	760602
12	113	925227	427604	826	1500	1978	Oil	718301
13	114	925173	427827	1019	1680	1977	Gas	679975
14	115	925363	426248	871	1450	1978	Oil	720447
15	116	925261	426491	844	1200	1978	Oil	338429
16	117	925185	426946	818	1470	1976	Gas	725632
17	118	925125	427172	830	1490	1976	Gas	705033
18	119	925055	427420	903	1550	1978	Oil	658341
19	120	924987	427664	1077	1750	1978	Gas	518000
20	121	924975	427992	1208	1850	1978	Gas	521080
21	122	925285	426003	905	1500	1978	Gas	511650
22	123	925048	426560	905	1580	1978	Oil	642188
23	124	924989	426782	888	1482	1976	Gas	722924
24	125	924873	427003	838	1200	1977	Oil	385816
25	126	924877	427250	1015	1650	1977	Gas	497570
26	127	924799	427490	1169	1759,8	1978	Gas	494870
27	128	925060	425844	896	1548,8	1978	Gas	509747
28	129	924931	426050	903	1490	1978	Gas	547130

	Name	X	Y	z_r	z_f	Year	Type	Volume
29	130	924914	426329	928	1529,4	1978	Gas	520190
30	131	924863	426595	1065	1699	1977	Gas	543850
31	132	925218	426718	845	1500	1988	Oil	528687
32	133	925114	426190	875	1450	1978	Oil	596519
33	201	924927	425587	975	1449,1	1997	Oil	674774
34	202	924730	425842	945	1558	2006	Oil	558429
35	203	924651	426417	1080	1690	2010	Oil	543667
36	207	924774	425311	1050	1479,7	1997	Oil	596944
37	208	924621	425514	955	1494	1998	Oil	530005
38	210	924984	425158	1384	1762,3	1997	Oil	451848
39	211	924523	425171	1047	1233,4	1996	Oil	313104
40	214	924520	424875	1156	1393,4	1996	Oil	351844
41	301	925930	426787	1035	1300	2009	Oil	5464
42	303	925829	427330	1190	1650	2010	Gas	744721
43	304	925772	427610	1140	1550	2010	Gas	794785
44	305	925681	427870	1190	1600	2010	Gas	700632
45	306	925626	428141	1190	1600	2010	Gas	724972
46	307	925562	428440	1245	1660	2013	Gas	844905
47	308	925481	428727	1255	1619,8	2013	Gas	441969
48	309	926157	426947	1245	1570	2014	Gas	672862
49	310	926081	427221	1190	1689,6	2011	Gas	751094
50	311	926040	427518	1190	1600	2011	Gas	768478
51	312	925986	427788	1190	1600	2010	Gas	633740
52	313	925884	428055	1190	1600	2010	Gas	743505
53	314	925829	428330	1245	1660	2012	Gas	830946
54	315	925776	428644	1245	1660	2012	Gas	831961
55	316	925709	428949	1255	1675	2012	Gas	746166
56	319	926266	427687	1100	1520	2010	Gas	591603
57	320	926201	427967	1190	1600	2010	Gas	766937

	Name	X	Y	z_r	z_f	Year	Type	Volume
58	321	926097	428244	1190	1600	2010	Gas	789937
59	322	926031	428526	1245	1660	2012	Gas	807856
60	323	925995	428836	1245	1660	2013	Gas	756302
61	324	925927	429142	1245	1660	2014	Gas	818962
62	327	926468	427881	1190	1600	2010	Gas	797836
63	328	926394	428171	1190	1605,1	2012	Gas	870495
64	329	926299	428431	1190	1605	2011	Gas	833091
65	330	926240	428706	1245	1660,8	2012	Gas	769970
66	331	926204	429037	1245	1660	2013	Gas	797341
67	332	926144	429331	1245	1660	2014	Gas	730392
68	334	926666	427687	1245	1660	2013	Gas	925135
69	335	926657	428091	1200	1600	2012	Brine	287128
70	336	926597	428358	1050	1273	2014	Oil	541224
71	337	926518	428628	1245	1665	2011	Gas	774319
72	338	926457	428911	1245	1660	2013	Gas	854318
73	339	926406	429237	1265	1680	2012	Brine	119258
74	340	926358	429511	1230	1560	2012	Brine	36780
75	344	926792	428564	1010	1410,3	2011	Oil	531615
76	345	926730	428835	1245	1659,9	2011	Gas	847919
77	346	926655	429109	1230	1550	2012	Brine	80382
78	347	926641	429389	1075	1390	2012	Brine	16118
79	348	926572	429654	1230	1560	2012	Brine	31547
81	352	926978	428959	1310	1580	2012	Gas	728778
82	353	926902	429237	1230	1550	2012	Brine	126534
83	354	926857	429571	1230	1550	2012	Brine	128779
85	358	927241	428887	1005	1282,8	2012	Brine	110951
86	359	927175	429155	1230	1550	2012	Gas	731671
87	360	927099	429433	1230	1550	2012	Brine	128134
88	365	927383	429363	1010	1250	2012	Brine	79812